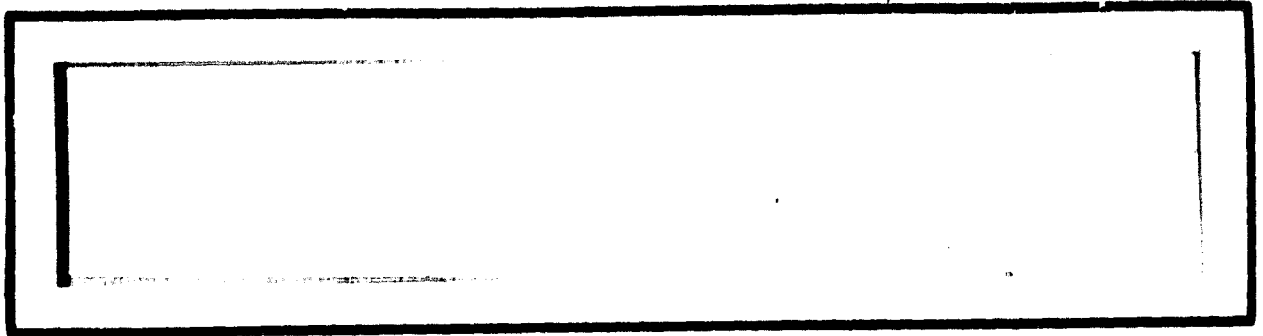


General Disclaimer

One or more of the Following Statements may affect this Document

- This document has been reproduced from the best copy furnished by the organizational source. It is being released in the interest of making available as much information as possible.
- This document may contain data, which exceeds the sheet parameters. It was furnished in this condition by the organizational source and is the best copy available.
- This document may contain tone-on-tone or color graphs, charts and/or pictures, which have been reproduced in black and white.
- This document is paginated as submitted by the original source.
- Portions of this document are not fully legible due to the historical nature of some of the material. However, it is the best reproduction available from the original submission.



Axiomatix

(NASA-CR-161007) PAYLOAD/ORBITER
SIGNAL-PROCESSING AND DATA-HANDLING SYSTEM
EVALUATION Final Report (Axiomatix, Los
Angeles, Calif.) 198 p HC A09/MF A01

N82-12107 .

CSCL 17B G3/16 08444

Unclass



PAYLOAD/ORBITER SIGNAL-PROCESSING AND DATA-HANDLING
SYSTEM EVALUATION *NASA CR-161007*

FINAL REPORT

Contract No. NAS 9-15240G

Technical Monitor: William E. Teasdale

Prepared for

NASA Lyndon B. Johnson Space Center
Houston, Texas 77058

Prepared by

Gaylord K. Huth
Andreas Polydoros

Axiomatix

9841 Airport Blvd., Suite 912
Los Angeles, California 90045

Axiomatix Report No. R8012-5
December 22, 1980

TABLE OF CONTENTS

	<u>Page</u>
LIST OF TABLES	iii
LIST OF FIGURES	iv
1.0 EXECUTIVE SUMMARY	1
1.1 Purpose of Effort and Degree of Performance	1
1.2 General Approach to the Activity	2
1.3 Organization of the Final Report	4
2.0 INTRODUCTION	6
2.1 Statement of Work	6
2.1.1 Objectives	6
2.1.2 Stipulated Tasks	6
2.1.3 General Approach	6
2.2 Organization of the Final Report	10
2.3 Recommendations for Future Effort	11
3.0 PAYLOAD SIGNAL-PROCESSING AND DATA-HANDLING SYSTEM	12
3.1 Detached Payload/Orbiter Functional Signal Flow	12
3.2 Payload RF Communication System	15
3.2.1 Generic Payload Transponder	15
3.2.2 IUS SGLS Transponder	18
3.2.3 IUS STDN/TDRS Transponder	21
3.2.4 Payload Interrogator (PI)	25
3.2.5 IUS/Orbiter RF Communication Links	31
3.3 Payload Signal-Processing System	34
3.3.1 Payload Signal Processor	34
3.3.2 Communication Interface Unit	39
3.3.3 Ku-Band Signal Processor	40
3.4 Payload Data-Handling System	48
3.4.1 Payload Experiment Recorder (PR)	48
3.4.2 Multiplexer/Demultiplexer	49
3.4.3 PCM Master Unit (PCMMU)	57
3.4.4 Payload Data Interleaver (PDI)	59
3.4.5 Network Signal Processor (NSP)	51
3.5 Orbiter Network Communication System	65
3.5.1 S-Band PM Links	65
3.5.2 S-Band FM Links	67
3.5.3 Ku-Band Links	71

	<u>Page</u>
4.0 DETACHED PAYLOAD COMMUNICATION SYSTEM STUDY	75
4.1 PI Phase Noise Spectral Characteristics	77
4.2 IUS Transponder Phase Noise Spectral Characteristics . .	91
4.3 PI/IUS Two-Way Communication Phase Noise Spectral Characteristics	93
4.4 Performance of PI in the Presence of Mismatched Wideband Detector Phase and Phase Noise	97
5.0 PAYLOAD/ORBITER/TDRSS INTERFACE STUDY	107
5.1 Payload User Constraints Derived from TDRSS User Constraints	111
5.2 Analysis of Cumulative Effect of TDRSS User Constraint Parameters on Bit Error Probability Performance	115
5.3 Payload Data Performance Degradation due to Payload Data Asymmetry with an UQPSK Modulator	118
5.4 Payload Data Performance Degradation due to the Ku-Band System Digital Phase Modulator Phase Asymmetry	122
REFERENCES	130
APPENDIX I Phase Noise Spectral Calculations for the PI/IUS Two-Way Communication Link	
APPENDIX II Mean-Square Error Approximation to Phase Noise Spectra	
APPENDIX III Performance of a Wideband Phase Detector in the Presence of Mismatched Phase Shift and Phase Noise	
APPENDIX IV The Effect of Transmitter Phase Asymmetry on UQPSK Systems with Noisy Receiver Phase Reference	

LIST OF TABLES

	<u>Page</u>
3.1 Typical Payload Transponder Receiver Characteristics	17
3.2 Typical Payload Transponder Transmitter Characteristics . .	18
3.3 Principal PI Transmitter Characteristics	27
3.4 Principal PI Receiver Characteristics	28
3.5 PSP Telemetry Signal-Processing Capabilities	36
3.6 PSP Command Signal Characteristics	36
3.7 Ku-Band Signal Processor Data Characteristics	43
3.8 Payload Recorder Record/Playback Capabilities	49
3.9 Network Signal Processor Performance	63
3.10 Data Rates for Network PM Links	67
3.11 S-Band Transponder Performance Specifications	68
3.12 S-Band FM Performance Specifications	69
3.13 Input and Output Signal Characteristics of FMSP for Payload Data	72
3.14 Ku-Band Forward Link RF Signal Characteristics	74
4.1 PI Frequency Division Constants	80
4.2 PI Transfer Function Parameters	89
4.3 Allowed Values of Phase Noise and Phase Offset for 2 dB . Performance Degradation at $P_b = 10^{-5}$	104
5.1 Ku-Band Signal Processor Return Link Data Characteristics .	109
5.2 TDRSS User Constraints on Data Characteristics	112
5.3 Payload User Constraints for Data on Ku-Band Channel 3 . . (Mode 1)	114
5.4 Payload User Constraints for Clock to KuSP (Channel 3, Mode 1)	114

LIST OF FIGURES

	<u>Page</u>
1.1 Schedule of Subtasks for Payload/Orbiter Interface Assessments	3
2.1 Schedule of Subtasks for Payload/Orbiter Interface Assessments	8
3.1 Orbiter/Payload Functional Command Signal Flow	13
3.2 Payload/Orbiter Functional Telemetry Signal Flow	14
3.3 Typical Payload Transponder Diagram	16
3.4 IUS SGLS Transponder Functional Block Diagram	20
3.5 IUS STDN/TDRS Transponder Functional Block Diagram	22
3.6 Payload Interrogator Functional Diagram	26
3.7 IUS Received Power versus Range for Each PI Output Power Setting	33
3.8 PI Received Power versus Range from IUS	35
3.9 PSP Functional Block Diagram	37
3.10 Command Tone Modulation Envelope	41
3.11 Communication Interface Unit Functional Block Diagram	42
3.12 Ku-Band Signal Processor Forward Link Functional Block Diagram	44
3.13 Ku-Band Mode 1 Three-Channel Modulation	46
3.14 Ku-Band Mode 2 Three-Channel Modulation	47
3.15 MDM System Block Diagram	50
3.16 Serial Digital Input/Output Channel Interface	52
3.17 Rise and Fall Times	53
3.18 Serial Word Format	54
3.19 Data Code	54
3.20 Data Word Synchronization, Nonvalid Manchester Code	55
3.21 Serial Channel Data Transfer	56
3.22 PCMMI Block Diagram	58
3.23 PDI Block Diagram	60
3.24 Forward Link Network Signal Processor Block Diagram	62
3.25 Return Link Network Signal Processor Functional Block Diagram	64
3.26 Network Transponder Functional Block Diagram	66
3.27 FM Signal Processor Functional Block Diagram	70
3.28 Ku-Band Forward Link Function	73
4.1 A Simple Block Diagram of the IUS/Orbiter Two-Way Coherent Communication System	76
4.2 Functional Block Diagram of IUS Transponder and PI	78
4.3 Phase Noise Spectrum of the PI TCXO	82
4.4 Measured Transmitter Single-Sided Phase Noise Spectral Density	83
4.5 Approximations to the Measured Transmitter Single-Sideband Phase Noise Spectral Density	84
4.6 Aximatrix Approximation for the Transmitter Phase Noise Spectral Density	85

	<u>Page</u>
4.7 VCXO Measured Phase Noise Power Spectral Density	87
4.8 VCO Phase Noise Power Spectra after Filter Extraction	90
4.9 Total Standard Deviation σ_A versus Damping Factor ζ_1	98
4.10 Functional Block Diagram of a PI Receiver with Wideband Phase Detector	99
4.11 Bit Error Probability versus E_b/N_0 for No Phase Offset as a Function of Phase Noise	101
4.12 Bit Error Probability versus E_b/N_0 for 5° Phase Offset as a Function of Phase Noise	102
4.13 Bit Error Probability versus E_b/N_0 for 20° Phase Offset as a Function of Phase Noise	103
4.14 Performance Degradation versus Phase Offset at $P_b = 10^{-3}$ as a Function of Noise	105
4.15 Performance Degradation versus Phase Noise at $P_b = 10^{-5}$ as a Function of Phase Offset	106
5.1 Payload/Orbiter Functional Telemetry Signal Flow	108
5.2 Data Transition Time Definition	113
5.3 Variation of Degradation in SNR as a Function of Asymmetry when Data Transition Time Dominates Data Asymmetry	119
5.4 Variation of Cumulative Degradation in SNR as a Function of Asymmetry when Data Transition Time Dominates Data Asymmetry	120
5.5 Payload Data Performance Degradation as a Function of Data Asymmetry with var $\phi = 0$	123
5.6 Payload Data Performance Degradation as a Function of Data Asymmetry with var $\phi = 4$	124
5.7 Payload Data Performance Degradation as a Function of Data Asymmetry with var $\phi = 9$	125
5.8 SNR Loss Versus S_θ for the Payload Data Channel 2	127
5.9 SNR Loss Versus S_θ for the Operational Data Channel 1	128

1.0 EXECUTIVE SUMMARY

1.1 Purpose of Effort and Degree of Performance

The overall objective of this work has been to identify and resolve potential incompatibilities between Orbiter subsystems and payload communication systems to assure that acceptable end-to-end system performance will be achieved. The potential incompatibilities can be associated with either attached payloads in the payload bay or detached payloads communicating with the Orbiter via an RF link.

Assessment of the payload signal-processing and data-handling system was made by investigating interface problems experienced between the Inertial Upper Stage (IUS) and the Orbiter since similar problems could be expected for other payloads. Some of the principal accomplishments made by Axiomatix during this assessment are listed below.

(1) Identification of potential detached payload interface problem due to phase noise generated by the Orbiter payload interrogator (PI) and turned around by the payload transponder. The phase noise problem was definitized by the following:

- (a) Measurement of the PI and IUS transponder phase noise spectral characteristics using a test procedure defined by Axiomatix
- (b) Analysis of the phase noise spectral characteristics and formulation of an analytical model for both the PI and IUS transponder
- (c) Analysis of combined PI/IUS two-way communication link performance degradation. This analysis included the PI transmitted phase noise turned around by the IUS transponder in addition to the IUS transponder generated phase noise
- (d) Analysis of the performance degradation due to a static phase error at the PI wideband phase detector along with the two-way communication link phase noise.
- (e) Recommendation for tightening of phase noise specifications on the PI and IUS transponder

(2) Identification of potential attached payload interface problem due to TDRSS user constraints not being met by payloads. This problem was definitized by the following:

- (a) Definition of payload user constraints based on appropriate TDRSS user constraints

(b) Analysis of bit error probability (BEP) performance degradation as a function of payload compliance with the user constraints

(3) Identification of potential attached payload interface problem due to implementation of the Ku-band system digital phase modulator. This problem was definitized by the following:

(a) Analysis of the performance degradation due to payload data asymmetry

(b) Analysis of the performance degradation due to phase asymmetry of the Orbiter Ku-band system digital phase modulator

(4) Recommendation of approach to resolve payload/Orbiter interface problems.

(a) Identify payload user constraints

(b) Assess performance degradation for varying compliance with the payload user constraints

(c) Develop payload/Orbiter interface design handbook.

1.2 General Approach to the Activity

While performing the activities required by this contract, Axiomatix has worked closely with the cognizant NASA personnel, the Orbiter prime contractor (Rockwell International), the IUS prime contractor (Boeing Aerospace Co.), and the IUS and Orbiter payload communication equipment subcontractor (TRW Defense and Space Group). Figure 1.1 presents the subtasks which Axiomatix undertook to accomplish the assessments of the payload signal-processing and data-handling system. The subtasks shown in this figure follow the principal accomplishments listed in the previous section.

The work performed under this contract was strongly related to the parallel efforts. Axiomatix support for the detailed implementations review and critiques of the payload communication equipment, the Ku-band communication system and the IUS transponder was provided through Contract No. NAS 9-16067, Exhibit A. This Axiomatix support to the hardware development yielded an invaluable background to the details of the hardware design for evaluating potential interface problems. The overall payload/Orbiter/TDRSS (GSTDN) system support for Axiomatix was provided through Contract No. NAS 9-16067, Exhibit B. This Axiomatix support to the overall system ties together the various payload-related equipment as well as

Subtasks	Calendar Year											
	1979						1980					
	S	O	N	D	J	F	M	A	M	J	J	A
Detached Payload Communication System Study Review of PI Design Analysis of PI Phase Noise Spectral Characteristics Review of IUS Transponder Design Analysis of IUS Phase Noise Spectral Characteristics Analysis of Combined PI/IUS Two-Way Phase Noise Spect. Char. Performance Analysis of PI in the Presence of Mismatched Wideband Detector Phase and Phase Noise												
Payload/Orbiter/TDRSS Interface Study Review of Payload/Orbiter/TDRSS Interface Requirements Definition of Payload User Constraints Derived from TDRSS User Constraints Analysis of TDRSS User Constraints on Payload Data Bit Error Probability Performance Analysis of Payload Data Performance Degradation due to Payload Data Asymmetry with an UQPSK Modulator Analysis of Payload Data Performance Degradation due to the Ku-Band System Digital Phase Modulator Phase Asymmetry												

Figure 1.1. Schedule of Subtasks for Payload/Orbiter Interface Assessments

yielding an extensive insight into the total system. Hence, Axiomatix is in a unique position to recommend resolution to payload/Orbiter interface problems for either a design change or an operational workaround. Finally, through Contract No. NAS 9-15604C, Axiomatix suggested revisions to the interface control document (ICD) #2-19001 to define the detached payload interfaces as well as to better define the attached payload interfaces where IUS/Orbiter interface problems were encountered. The detailed review of ICD 2-19001 during Contract No. NAS 9-15604C provided Axiomatix with an excellent background to both past and current IUS/Orbiter interface problems so that Axiomatix could recommend design changes or operational workarounds to avoid these problems with future payloads attempting to interface with Orbiter subsystems.

1.3 Organization of the Final Report

Following the introductory section 2, there are three sections and four appendices which address various aspects and details of the payload signal-processing and data-handling system.

Section 3 contains a detailed description of the payload signal-processing and data-handling system. The primary concern of this section is with detached payloads. Therefore, the description of the payload signal-processing and data-handling system is presented from the detached payload point of view. Both Orbiter subsystems and IUS transponders are described in detail. In addition, the IUS/Orbiter communication link performance is analyzed.

Section 4 assesses the effect of phase noise on the performance of the two-way RF communication link between the IUS transponders and the Orbiter PI. Sections 4.1 and 4.2, along with Appendices I and II, formulate the phase noise spectral characteristics of the PI and IUS transponders, respectively, based on phase noise measurements by TRW using a test procedure defined by Axiomatix. Section 4.3 combines the results of sections 4.1 and 4.2 and formulates the PI/IUS two-way communication link phase noise spectral characteristics. Finally, section 4.4 and Appendix III analyze the performance of the PI due to phase noise along with static phase error at the wideband detector resulting from phase mismatch.

The payload/Orbiter/TDRSS interface requirements and system end-to-end performance is analyzed in Section 5. The processing of the payload data by the Orbiter Ku-band system for transmission through the

TDRSS is delineated in Section 5. The TDRSS user constraints that apply to payload data unmodified by the Orbiter Ku-band system are presented in section 5.1. Section 5.2 analyzes the bit error probability (BEP) performance degradation as a function of compliance with defined payload user constraints. Sections 5.3 and 5.4, in conjunction with Appendix IV, analyze the BEP performance degradation due to the interaction between imperfections in the payload data or timing in the Ku-band system and the digital phase modulator used to modulate the payload data on an UQPSK subcarrier for transmission through the TDRSS.

2.0 INTRODUCTION

2.1 Statement of Work

2.1.1 Objectives

The objectives of this contract were to identify and resolve potential incompatibilities between Orbiter subsystems and payload interface requirements to assure that acceptable end-to-end system performance will be achieved.

2.1.2 Stipulated Tasks

The contract statement of work calls out the following tasks:

"Task #1 - Detailed Payload Signal Processing and Data Handling System Assessment - The contractor shall review current Orbiter payload data handling and signal processing system specifications and identify potential incompatibilities between Orbiter LRU's and between Orbiter hardware characteristics and payload interface requirements. The contractor shall propose necessary changes to system implementations, operational requirements, or interface configurations that will resolve identified problem areas. The contractor shall also propose appropriate tests, as required to identify potential problems and to demonstrate adequate resolution of identified problems."

"Task #2 - Problem Area Analysis and Resolution - The contractor shall analyze current and potential problem areas and shall recommend to NASA Management appropriate corrective action to resolve payload/Orbiter interface problem areas."

2.1.3 General Approach

Potential interface compatibility problems can be associated with either attached payloads in the payload bay or detached payloads communicating with the Orbiter via an RF link. The effort under this contract was divided between an assessment of the attached payload/Orbiter interfaces and the detached payload/Orbiter interfaces. Assessments of these interfaces were made by investigating interface problems experienced between the Inertial Upper Stage (IUS) and the Orbiter. To this end, Axiomatix worked closely with the cognizant NASA personnel, the Orbiter prime contractor (Rockwell International), the IUS prime contractor (Boeing Aerospace Co.) and the IUS, CIU and Orbiter payload communication equipment subcontractor (TRW Defense and Space Group).

Figure 2.1 presents the subtasks which Axiomatix undertook to accomplish the assessments of the payload signal-processing and data-handling system. Following the review of the Payload Interrogator (PI) and IUS transponder designs, a potential system interface problem due to phase noise generated by the PI and turned around by the IUS transponder was found. Therefore, Axiomatix undertook an analysis task to better define the potential problem and assess the system ramifications of the resulting performance degradation. First, the PI and IUS transponder phase noise spectral characteristics were measured using a test procedure defined by Axiomatix. Second, Axiomatix analyzed the phase noise spectral characteristics and formulated an analytical model for both the PI and IUS transponder. Third, Axiomatix analyzed the performance degradation of the combined PI/IUS two-way communication link with the PI transmitted phase noise turned around by the IUS transponder in addition to the IUS transponder generated phase noise. Finally, Axiomatix analyzed the performance degradation of having a static phase error at the PI wideband phase detector along with the phase noise resulting from the two-way communication link. As a result of the Axiomatix effort, the specification on transmitted phase noise by the PI has been tightened to minimize the overall system performance degradation of the PI/IUS two-way communication link.

A second potential system interface problem was found during the review of the payload/Orbiter/TDRSS interface requirements. Since the Orbiter Ku-band system transmits the low rate payload data unmodified through the TDRSS, some of the TDRSS user constraints must be applied to the payload data as payload user constraints. Axiomatix defined the payload user constraints from the appropriate TDRSS user constraints, then analyzed the bit error probability performance degradation as a function of compliance with the defined payload user constraints. In the process of determining the payload data performance degradation for the payload user constraint parameters, Axiomatix discovered two additional sources of performance degradation in the Ku-band system. The first source of performance degradation is due to the effect of payload data asymmetry (one of the defined payload user constraint parameters) on the Orbiter Ku-band system digital phase modulator used to modulate the payload data on an unbalanced quadriphase-shift-keyed (UQPSK) subcarrier. Axiomatix analyzed the performance degradation due to payload data asymmetry at

Subtasks	Calendar Year											
	1979						1980					
	S	O	N	D	J	F	M	A	M	J	J	A
Detached Payload Communication System Study												
Review of PI Design												
Analysis of PI Phase Noise Spectral Characteristics												
Review of IUS Transponder Design												
Analysis of IUS Phase Noise Spectral Characteristics												
Analysis of Combined PI/IUS Two-Way Phase Noise Spect. Char.												
Performance Analysis of PI in the Presence of Mismatched Wideband Detector Phase and Phase Noise												
Payload/Orbiter/TDRSS Interface Study												
Review of Payload/Orbiter/TDRSS Interface Pequirements												
Definition of Payload User Constraints Derived from TDRSS User Constraints												
Analysis of TDRSS User Constraints on Payload Data Bit Error Probability Performance												
Analysis of Payload Data Performance Degradation due to Payload Data Asymmetry with an UQPSK Modulator												
Analysis of Payload Data Performance Degradation due to the Ku-Band System Digital Phase Modulator Phase Asymmetry												

Figure 2.1. Schedule of Subtasks for Payload/Orbiter Interface Assessments

this payload/Orbiter interface so that a payload user can trade off the amount of data asymmetry with the resulting performance degradation. The second source of payload data performance degradation is due to phase asymmetry of the Orbiter Ku-band system digital phase modulator. While this source of payload data performance degradation is beyond the control of the payload, Axiomatix analyzed the effect of the digital modulator phase asymmetry to determine the overall payload/Orbiter/TDRSS end-to-end system performance degradation.

2.1.4 Continuity with Previous Work

The previous stages of this contract (i.e., NAS 9-15240 A-F) have analyzed implementations of the Orbiter Ku-band system, the network S-band communication system and the Orbiter S-band payload communication systems. The performance degradation due to phase noise was first analyzed for two-way communication links under NAS 9-15240 E/F. The performance degradation due to individual TDRSS user constraints was first analyzed in NAS 9-15240A. In NAS 9-15240C, the cumulative performance degradation due to multiple TDRSS user constraints was analyzed. The performance of the Ku-band system UQPSK modulation was first analyzed in NAS 9-15240A.

2.1.5 Relationship to Parallel Work

The work performed under this contract was strongly related to the parallel efforts. Axiomatix support for the detailed implementations review and critiques of the payload communication equipment, the Ku-band communication system and the IUS transponder was provided through Contract NAS 9-16067, Exhibit A. This Axiomatix support to the hardware development yielded an invaluable background to the details of the hardware design for evaluating potential interface problems. The overall payload/Orbiter/TDRSS (GSTDN) system support for Axiomatix was provided through Contract NAS 9-16067, Exhibit B. This Axiomatix support to the overall system ties together the various payload-related equipment as well as yielding an extensive insight into how the payload/Orbiter interface issues relate to the total system. Hence, Axiomatix is in a unique position to recommend resolution to payload/Orbiter interface problems for either a design change or an operational workaround. Finally, through

Contract NAS 9-15604C, Axiomatix suggested revisions to the interface control document (ICD) #2-19001 to define the detached payload interface as well as to better define the attached payload interfaces where IUS/Orbiter interface problems were encountered. The detailed review of ICD 2-19001 during Contract NAS 9-15604C provided Axiomatix with an excellent background to both past and current IUS/Orbiter interface problems so that Axiomatix could recommend design changes or operational workarounds to avoid these problems with future payloads attempting to interface with Orbiter subsystems.

2.2 Organization of the Final Report

There are three sections and four appendices which address various aspects and details of the payload signal-processing and data-handling system.

Section 3 contains a detailed description of the payload signal-processing and data-handling system. The primary concern of this section is with detached payloads. Therefore, the description of the payload signal-processing and data-handling system is presented from the detached payload point of view. Both Orbiter subsystems and IUS transponders are described in detail. In addition, the IUS/Orbiter communication link performance is analyzed.

Section 4 assesses the effect of phase noise on the performance of the two-way RF communication link between the IUS transponders and the Orbiter PI. Sections 4.1 and 4.2, along with Appendices I and II, formulate the phase noise spectral characteristics of the PI and IUS transponders, respectively, based on phase noise measurements by TRW using a test procedure defined by Axiomatix. Section 4.3 combines the results of sections 4.1 and 4.2 and formulates the PI/IUS two-way communication link phase noise spectral characteristics. Finally, section 4.4 and Appendix III analyze the performance of the PI due to phase noise along with static phase error at the wideband detector resulting from phase mismatch.

The payload/Orbiter/TDRSS interface requirements and system end-to-end performance is analyzed in Section 5. Processing of the payload data by the Orbiter Ku-band system for transmission through the TDRSS is delineated in Section 5. The TDRSS user constraints which apply to payload data unmodified by the Orbiter Ku-band system are presented in

section 5.1. Section 5.2 analyzes the bit error probability (BEP) performance degradation as a function of compliance with defined payload user constraints. Sections 5.3 and 5.4, in conjunction with Appendix IV, analyze the BEP performance degradation due to interactions between imperfections in the payload data or timing in the Ku-band system and the digital phase modulator used to modulate the payload data on an UQPSK subcarrier for transmission through the TDRSS.

2.3 Recommendations for Future Effort

As a result of the payload signal-processing and data-handling system assessment, Axiomatix recommends that the results presented in this report be extended to an overall system study which will provide the payload communication system designer with the following:

- (1) Payload user constraints derived from Orbiter subsystem design requirements and capabilities and from TDRSS user constraints
- (2) Performance degradation based on varying user constraint compliance
- (3) "Designer's Handbook" which will show in detail methods of designing interface circuitry to meet all Orbiter and TDRSS user constraints.

3.0 PAYLOAD SIGNAL-PROCESSING AND DATA-HANDLING SYSTEM

The Orbiter avionics equipment serving payloads in the attached and detached modes perform two major functions. First, there are avionic equipment that perform payload RF and baseband signal-processing functions. Second, there are avionic equipment that perform the payload data-handling functions. The equipment in the first category are the Payload Interrogator (PI), Payload Signal Processor (PSP), Communication Interface Unit (CIU), and Ku-Band Signal Processor (KuSP). The equipment in the second category are the Payload Experiment Recorder (PR), Multiplexer/Demultiplexer (MDM), Payload Data Interleaver (PDI), PCM Master Unit (PCMMU), Network Signal Processor (NSP), and various DOD encryptor/decryptor units.

The primary concern of this report is with detached payloads. Therefore, the description of the payload signal-processing and data-handling system will be presented from the detached payload point of view. For a detailed description and analysis of the payload signal-processing and data-handling system interfaces with an attached payload, see the Axiomatix report entitled "Shuttle/Payload Communications and Data System Interface Analysis"¹.

3.1 Detached Payload/Orbiter Functional Signal Flow

Figure 3.1 presents the command signal flow from the Orbiter to the payload in a functional form. For NASA missions, the PSP sends commands through the PI. The NASA commands come to the PSP from the general-purpose computer (GPC) through a MDM. For DOD missions, the CIU sends commands through the PI. The DOD commands come to the CIU from the GPC through the MDM or directly from the KuSP. The commands from the KuSP and the NSP, which are passed through the GPC, are generated on the ground and transmitted to the Orbiter using direct S-band network communication link or the S-band or Ku-band communication links through the tracking and data relay satellite system (TDRSS).

The payload/Orbiter functional telemetry signal flow is presented in Figure 3.2. In the detached mode, telemetry is transmitted by the payload transponder to the PI. For NASA missions with standard data formats, the telemetry data passes from the PI to the PSP, which sends it

¹Gaylord K. Huth, "Shuttle/Payload Communications and Data Systems Interface Analysis," (Final Report on Contract No. NAS 9-15604C), Axiomatix Report No. R8012-4, December 31, 1980.

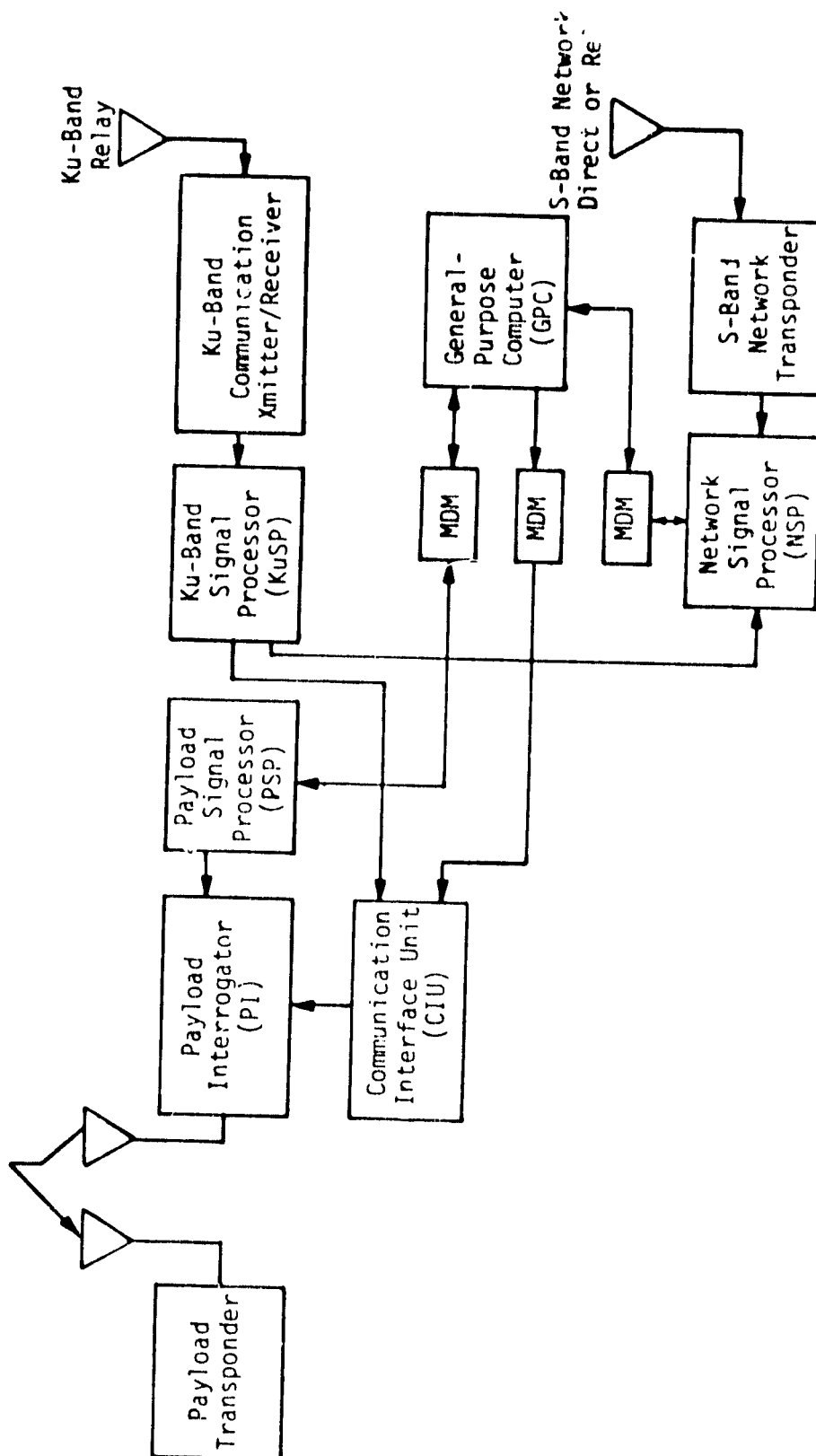


Figure 3.1. Orbiter/Payload Functional Command Signal Flow

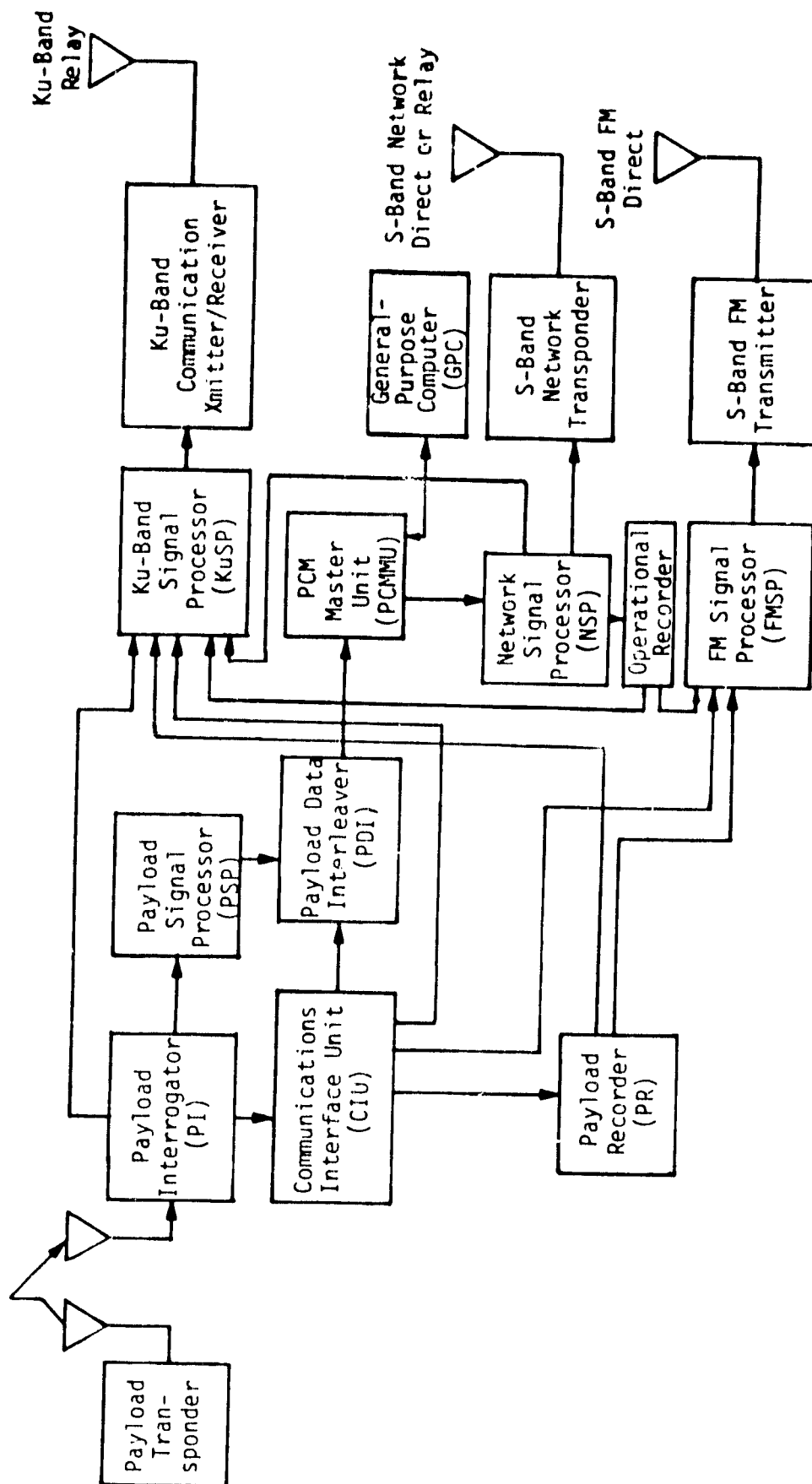


Figure 3.2. Payload/Orbiter Functional Telemetry Signal Flow

to the PDI for data handling. For DOD missions with standard data formats, the telemetry data passes from the PI to the CIU, which distributes the processed data to the PR, PDI, FMSP or KuSP for data handling. When nonstandard telemetry data formats are used in the detached mode, the PI strips off the RF carrier and sends the unprocessed data to the KuSP for transmission to the ground. This mode is called the "bent-pipe" mode since the Orbiter performs no processing of the telemetry data other than carrier translation.

3.2 Payload RF Communication System

The payload RF communication system includes the payload transponder and the PI. The payload transponders considered in this report are generic and those used on the Inertial Upper Stage (IUS).

3.2.1 Generic Payload Transponder

NASA and DOD payload transponders are generically quite similar in terms of their functions and architectures. NASA transponders are standardized, with three mission-oriented types available: deep-space transponders [for use with the Deep Space Network (DSN)], near-Earth transponders [for use with the space tracking and data network ground stations (GSTDN)], and TDRSS transponders (for use with TDRSS or GSTDN). DOD transponders interface with the USAF Satellite Control Facility (SCF).

Conspicuous differences between NASA and DOD transponders are the forward link frequency bands and transponding ratios. The NASA receive frequency range is S-band (2025 - 2120 MHz), while the DOD receive frequency range is L-band (1760 - 1840 MHz). The transmitter frequency is related to the receiver frequency by a ratio of integers, called the coherency (or turn-around) ratio. Both the NASA and DOD transmitter frequency ranges are S-band (2200 - 2300 MHz). The corresponding coherency ratios are, for NASA, 240/221, and for DOD, 256/205.

Figure 3.3 is a block diagram of the typical payload transponder. The forward link RF input is preselected, filtered for the frequency band utilized [S-band for NASA and L-band for IUS and DOD], and the input is then mixed down to the first IF. Further mixing translates the first IF signal to the second IF, where the output from the second IF amplifier is distributed to four phase detector/demodulator functions.

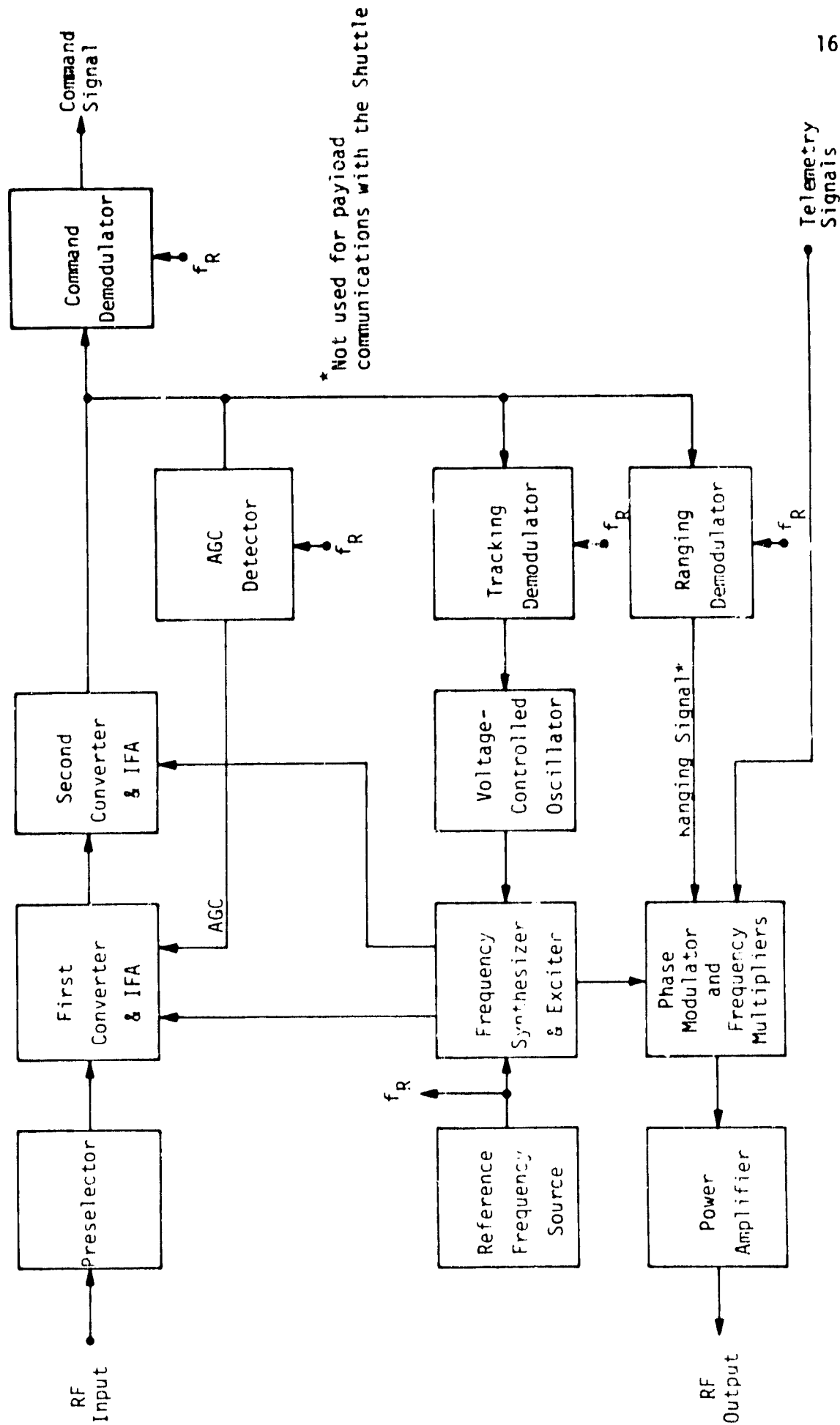


Figure 3.3. Typical Payload Transponder Diagram

The carrier-tracking loop functions to acquire and track the residual carrier component of the input signal. A second-order tracking loop is employed. Frequency and phase coherence are supplied from the VCO to the synthesizer/exciter, where the coherent reference frequencies are derived for the demodulation functions.

AGC is obtained through in-phase demodulation of the residual carrier. The AGC voltage is filtered and applied to the first IF amplifier to control the gain of the receiver. The AGC voltage is also filtered and compared with a threshold to determine whether the carrier-tracking loop is in or out of lock.

The command demodulator coherently recovers the command phase modulation from the carrier. Spectral conditioning (in most cases, limited to lowpass filtering) is usually provided in the output to the signal processor command detector. Typical transponder receiver operating and performance parameters for commands are indicated in Table 3.1.

Table 3.1. Typical Payload Transponder Receiver Characteristics

Item	Parameter and Range
Receive Frequency Range:	
L-Band Frequency (DOD)	1760 - 1840 MHz
S-Band Frequency (NASA)	2025 - 2120 MHz
Tracking Loop Bandwidth	18, 60, 200 or 2000 Hz
Tracking Loop Order	Second
AGC Dynamic Range	100 db
Command Channel Frequency Response	1 - 130 kHz
Noise Figure	5 - 8 dB

The synthesizer/exciter provides all reference frequencies to the transponder. A reference oscillator supplies standard frequencies to the receiver synthesizer, and coherence is provided by the receiver VCO. Synthesized frequencies are distributed to the receiver mixers and phase

detectors and to the transmitter phase modulator through a frequency multiplier.

The phase modulator provides the means of modulating the return link carrier with telemetry and ranging signals. Its output drives the transmitter frequency multiplier, producing the required modulated carrier signal in the S-band frequency range.

Finally, the power amplifier raises the modulated S-band transmitter signal to the level required by the return link. For near-Earth spacecraft, the power levels may range from a few hundred milliwatts to several watts, while deep-space vehicles employ power levels on the order of 100 W.

Typical transponder transmitter operating and performance parameters are indicated in Table 3.2.

Table 3.2. Typical Payload Transponder Transmitter Characteristics

Item	Parameter and Range
Transmitter Frequency Range	2200 - 2300 MHz
Ranging Channel Frequency Response	1 kHz to 1.2 MHz
Transmitter Phase Deviation	Up to 2.5 radians
Transmitter Output Power	200 mW to 5W*

*Up to 200 watts with external power amplifiers.

3.2.2 IUS SGLS Transponder

The telemetry, tracking and command (TT&C) SGLS transponder acquires and tracks, with a phase-locked-loop, an incoming S-band signal and provides demodulated spacecraft commands to the decoder. The transponder also receives data and telemetry from the spacecraft and phase modulates this information and the internally demodulated ranging tones onto an S-band 3W carrier which is provided to the antenna for downlink transmission.

The transponder shown in Figure 3.4, a functional block diagram, is a single unit consisting of an S-band receiver, a transmitter, and the auxiliary circuitry. This transponder configuration performs the following functions:

- Searches and acquires an SGLS-compatible S-band signal with modulation
- Provides a coherent link, when in the VCXO mode, with a fixed 256/205 transmit-to-receiver frequency ratio
- Provides a noncoherent stable return link signal when in the auxiliary oscillator mode
- Receives and demodulates command signals, outputting commands and clock signals
- Receives, demodulates to baseband, and remodulates ranging signals on the return link carrier to provide coherent turnaround ranging
- Accepts, modulates and transmits various analog and digital telemetry data on the return link
- Provides telemetry outputs of key transponder parameters and operational status of the transponder
- Operates in the receive and transmit modes independently by way of having separate dc-to-dc converters

The receiver utilizes a dual-downconversion, fully phase-coherent design, incorporating a second-order phase-lock loop. S-band input signals in the frequency range of 1763-1840 MHz are amplified in a low noise pre-amplifier before downconversion to a first IF frequency of approximately 44 MHz. Amplification, gain control and bandwidth limiting are accomplished in the first IF circuits before further downconversion to 12.515 MHz. Then the signal is further amplified and sent to the demodulator module circuits. Here four functions are performed:

(1) Acquisition. Operates in conjunction with the discriminator module to acquire an SGLS signal (including modulation).

(2) Phase detection. A predetection filter (30 kHz crystal filter) reduces the noise spectrum before phase detection takes place in the carrier-tracking phase-lock loop. Loop bandwidth (B_L) is 2 kHz.

(3) Coherent amplitude detection. Another detector, using a 90° phase-shifted reference, produces an output proportional to the RF carrier amplitude. This output forms the correction signal in the automatic gain control (AGC) loop and signal strength information for telemetry.

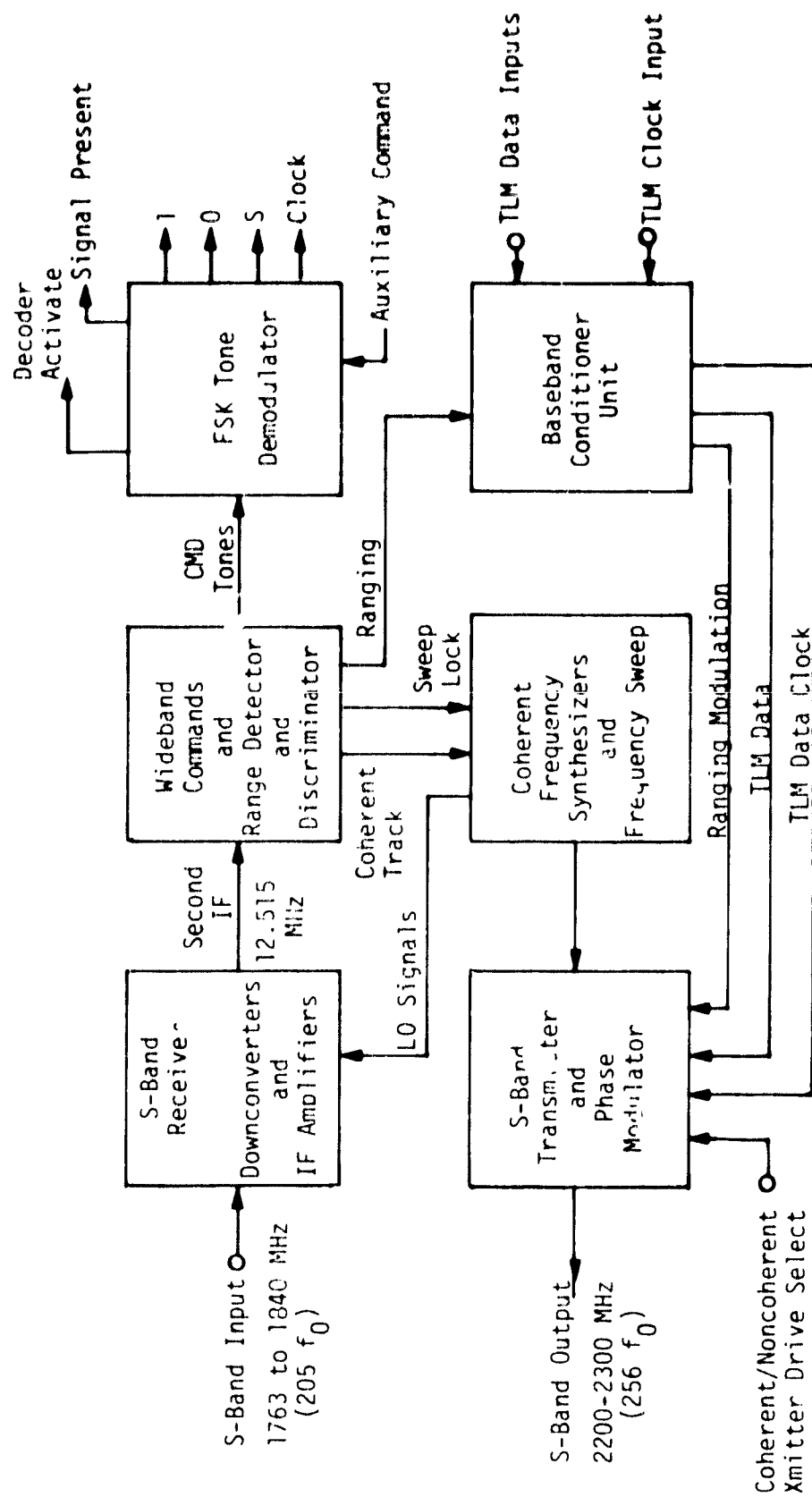


Figure 3.4. IUS SGLS Transponder Functional Block Diagram

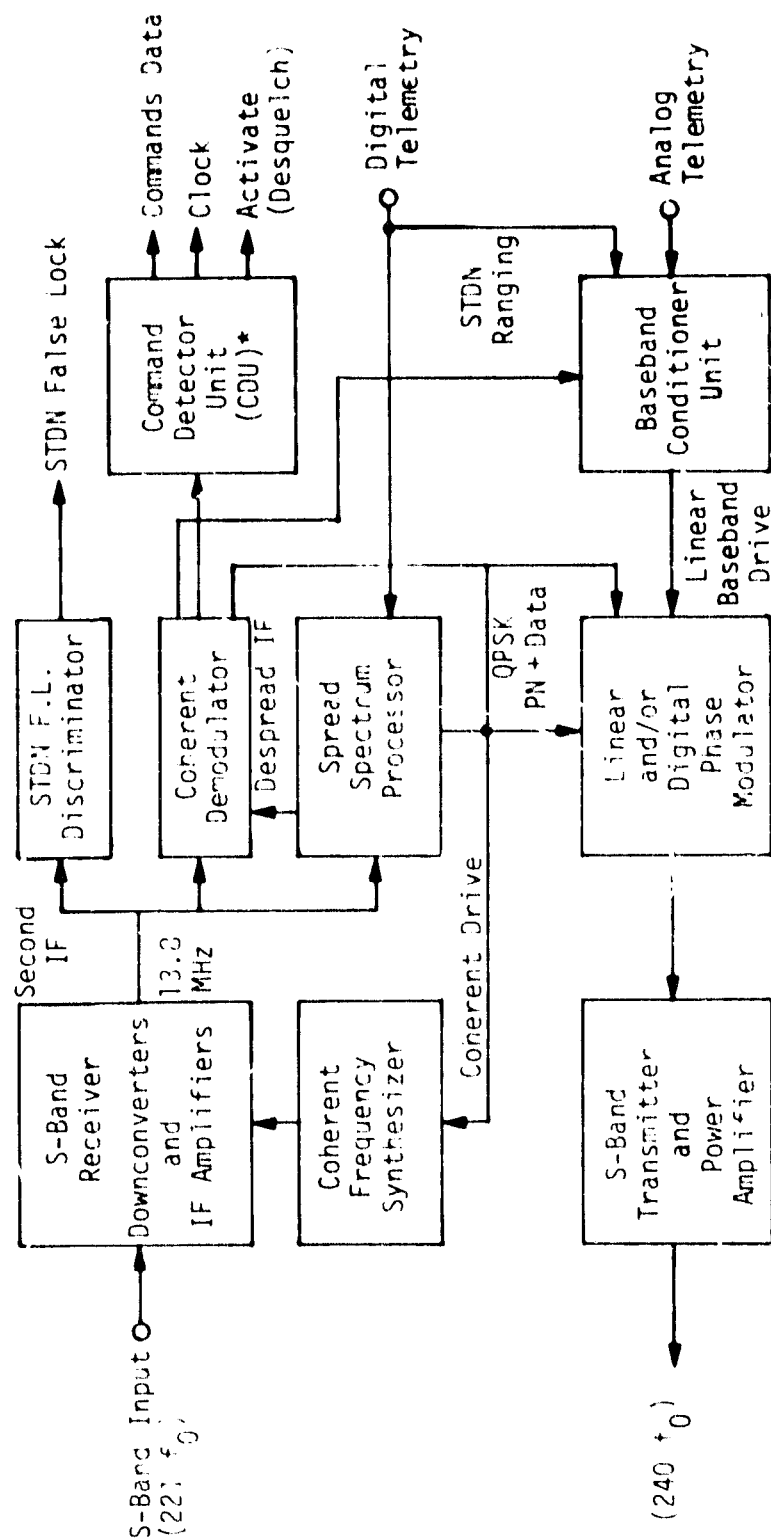
(4) Wideband detection. A wideband detector/frequency discriminator which, unlike the above two detectors, is not preceded by a narrowband filter, is used to demodulate the phase modulation from the uplink carrier. The output of this demodulator provides the wideband data output to the baseband circuits, where filtering separates ranging and command data. The discriminator function of this module does not allow the receiver to acquire to a sideband and, upon carrier acquisition, commands the sweep off in the demodulator. The module supplies the command tones to the FSK tone demodulator and the ranging information to the baseband conditioner.

The S-band transmitter operates from an internal auxiliary oscillator in the noncoherent mode or from a VCXO output provided by the receiver (coherent mode). Selection of the source can be determined by command or will be automatically set by the phase lock status of the receiver. Both sources are at a frequency of $2f_0$, approximately 17.5 MHz. Frequency multipliers utilizing SAW filters increase the output frequency to S-band at $256 f_0$. Phase modulation is performed at $1/4$ the output frequency, approximately 560 MHz. The modulator utilizes a quadrature hybrid terminated in voltage variable reactances to achieve linear phase modulation.

Digital telemetry and data are biphase modulated on a 1.024 MHz subcarrier while the analog data is FM modulated onto a 1.7 MHz subcarrier. These signals are summed with the turn-around ranging tones before they are provided to the linear phase modulator. An option is available to replace the 1.7 MHz FM subcarrier with a 1.7 MHz biphase modulated subcarrier. The transmitter also provides variable modulation indices of the subcarrier automatically when either of the subcarriers are commanded off. The S-band power amplifiers are wideband circuits culminating in a circulator protecting the 2.5 to 3.5W output from shorted or open loads. A separate high-efficiency dc-dc power converter provides operating power to the transmitter upon command.

3.2.3 IUS STDN/TDRS Transponder

The STDN/TDRS transponder is a multimode device capable of receiving and transmitting signals compatible with both the STDN and TDRS operational modes and signal formats. An abbreviated block diagram of the transponder is shown in Figure 3.5. A summary of transponder functions follows.



* Includes Bit Synchronizer

Figure 3.5. IUS STDN/TOPS Transponder Functional Block Diagram

- Provides two-way coherent communications with the Orbiter, STDN ground station or TDRS satellites at the appropriate S-band frequency
- Transponds with a coherency ratio of 240/221
- Acquires and demodulates STDN signals in 1/2-second (> -117 dBm) when commanded to the STDN ONLY false acquisition mode
- Recognizes, acquires and demodulates either STDN or TDRS signals when commanded to the DUAL mode; transponder recognizes signals based on the signal structure rather than on the signal level
- Incorporates a command decoder unit which demodulates the STDN subcarrier and recovers the 2 kbps clock and data signals in either mode; a data squelch circuit based on the measurement of E_b/N_0 is also included
- Removes the 3 Mbps spread spectrum code from the TDRS command channel signal and recovers the range synchronization from the TDRS spread spectrum range channel signal
- QPSK or PM modulates the coherent S-band transmit carrier with telemetry and ranging data; in TDRS, the carrier is also coherently spread at about 3 Mbps
- Provides noncoherent telemetry transmission in the absence of received signals or when commanded.

The basic transponder configuration is the same for both the STDN and TDRS modes; that is, both are configured to utilize the same frequency plan, receiver and transmitter RF and IF modules. When communicating with the Orbiter, the transponder is configured to the STDN mode.

The received signal is amplified by a low noise preamplifier to a first downconversion to approximately 47 MHz. A second coherent downconversion brings the signal to the second IF ($F_R = 13.8$ MHz); due to the design of the frequency plan, this second IF operates at a fixed frequency regardless of the input frequency. The second IF signal is divided three ways and is simultaneously sent to the discriminator, the carrier (coherent) demodulator and the spread spectrum processor. The discriminator is employed as an aid to fast acquisition of modulated STDN signals; its sole purpose is to prevent the receiver from locking onto the STDN 16 kHz subcarrier.

The coherent demodulator is employed to recover the data signals which are modulated onto the received carrier. It can be configured as either a linear demodulator (STDN signals) or a Costas PSK demodulator (TDRS signals). Demodulation also generates the phase error signal used

to lock up the receiver VCXO; it also generates the coherent amplitude detector (CAD) signal which indicates receiver lock. The TDRS signals are demodulated using a conventional linear phase-lock-loop.

In the normal configuration, the demodulated data (baseband) signals are sent to the command detector unit. This unit contains a sub-carrier demodulator and a bit synchronizer. The subcarrier demodulator recovers the 2 kbps data from the STDN 16-kHz PSK subcarrier; it employs a frequency-doubling subcarrier recovery loop. The bit synchronizer is an advanced design capable of recovering and reclocking data at three different selectable data rates (2 kbps, 2 kbps/N and 2 kbps/M), where N and M may be an integer from 1 to 16. Only 2 kbps is used for the IUS program.

The bit synchronizer also includes a combined squelch and bit synchronization lock circuit which is insensitive to bit transition density. The outputs of the CDU are the data and clock and an ACTIVATE (desquelch) signal. Upon command, the CDU is also capable of demodulating an auxiliary 16-kHz PSK subcarrier signal.

The return link signal is provided by the transmitter, shown in the lower portion of Figure 3.5. The STDN mode service consists of a 1.024 MHz PSK subcarrier for digital telemetry, a 1.7 MHz subcarrier for analog telemetry, and the ranging signal. These signals are assembled at baseband in the baseband conditioner unit and are used to modulate a linear phase modulator operating at 1/4 the output frequency. This signal is frequency multiplied x4; in the STDN mode, the inputs to the digital modulator are held to a logical one. The signal is amplified to 3.0W nominal and passed through an isolator to the output.

One of the salient features of the STDN/TDRS transponder is the capability to automatically identify the format of the received signal (i.e., STDN versus TDRS) and to configure the transponder to the appropriate mode. For example, if an STDN (or Orbiter) signal appears and is recognized, the receiver VCXO select switch is switched to allow the carrier loop to commence tracking. In either event, the receiver control algorithm configures the command detector unit (CDU) to match the received signal (TDRS or STDN), and also sends the lock-up information to the transmitter control algorithm circuit. The transmitter is then reconfigured and switched to coherent, assuming that the external TXR command is COHERENT. In the TDRS mode, this does not occur until long (range) code lockup is verified.

In the STDN (and Orbiter) mode only, the requirement is to correctly acquire an STDN signal modulated with a 16-kHz command subcarrier (but no range tones) and to achieve this within 1/2 second at signal levels ≥ -117 dBm. The STDN signal may be swept or it may be stationary. In this mode, the receiver VCXO select switch is set to permit the receiver to sweep ± 150 kHz every 300 ms. The demodulator is configured for LINEAR. A true lock indication is declared when both of the following conditions are achieved:

- The demodulator CAD indicates the presence of a CW signal within the acquisition loop bandwidth (± 4 kHz)
- The discriminator indicates that this CW signal is not a sideband of the received carrier.

The discriminator is thus used to prevent false lock on the STDN (or Orbiter) subcarrier. It is equipped with a dual (\pm) threshold which indicates if the incoming carrier is ± 16 kHz from the true receiver center frequency, as it would be if the receiver was attempting to lock on to a subcarrier sideband. If both of the above conditions are satisfied, the Receiver Select switch is positioned so that coherent tracking commences. When tracking is verified, the carrier loop bandwidth is narrowed to 800 Hz to prevent tracking out the 4 kHz range tone when it is turned on.

3.2.1 Payload Interrogator (PI)

Basically, the PI is a transceiver consisting of a receiver and a transmitter which are frequency excited or referenced to a universal frequency synthesizer that allows the PI to operate on any of 861 channel pairs. The transmitter operates on two distinct bands--1763 - 1840 MHz (L-band) and 2025 - 2120 MHz (S-band) and the receiver covers the band 2200 - 2300 MHz (S-band). Tables 3.3 and 3.4 list the principal operating characteristics of the transmitter and receiver, respectively.

Figure 3.6 shows a functional block diagram for the PI. A single RF port connects the PI to the payload antenna cable as the payload antenna serves to simultaneously receive and transmit signals. This port connects into the receiver input and transmitter output through an assembly known as the triplexer. The triplexer consists of six cavity-based band-pass filters which divide the receiver band and both transmic bands approximately in half. The two band assignments, designated "high" and "low," are

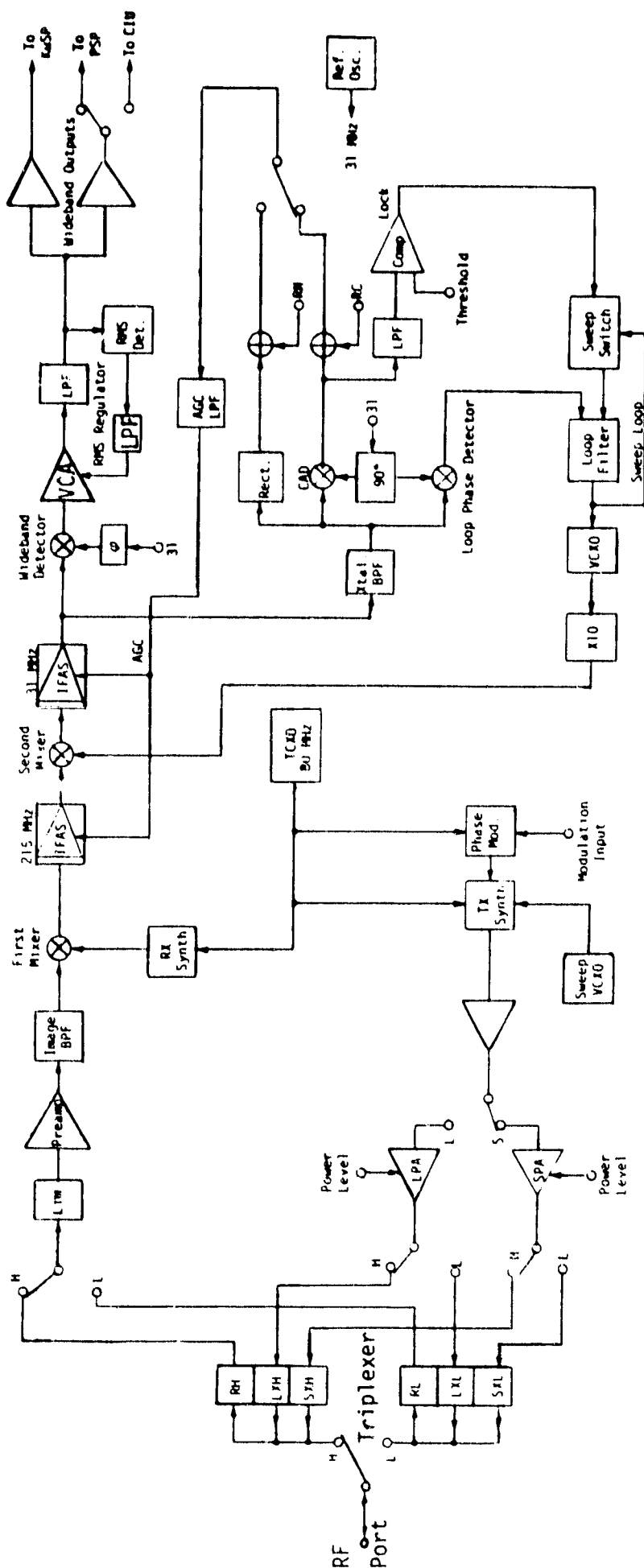


Figure 3.6. Payload Interrogator Functional Diagram

Table 3.3. Principal PI Transmitter Characteristics

Parameter	Value	Units
L-Band Frequency Range	1763 - 1840	MHZ
S-Band Frequency Range	2025 - 2120	MHz
Carrier Frequency Tolerance	± 0.001	%
Carrier Phase Noise	10 max	degrees-RMS
Output Spurs	< -65	dBc
Phase Modulator	0.2 to 2.5	radians
Frequency Sweep Ranges	75 \pm 5	kHz
	55 \pm 5	kHz
	33 \pm 3	kHz
Frequency Sweep Rates	10 \pm 3	kHz/sec
	250 \pm 75	Hz/sec
Power Level: High Medium Low	37 to 42	dBm
	27 to 32	dBm
	4 to 9	dBm

used to provide payload communication with minimum interference to network communications. When the PI is transmitting to a DOD payload in the frequency band of 1763.7 - 1799.7 MHz and receiving in the frequency band of 2202.4 - 2247.5 MHz, the S-band network transponder transmits at 2287.5 MHz and receives DOD operational signals at 1831.787 MHz. Alternately, when the PI is transmitting to a DOD payload in the 1803.7 - 1839.79 MHz band and receiving in the 2252.4 - 2297.5 MHz band, the the S-band network transponder transmits at 2217.5 MHz and receives DOD operational signals at 1775.773 MHz. Similarly, when the PI is transmitting to a NASA payload in the 2025.8 to 2072.56 MHz band and receiving in the 2200 - 2250.75 MHz band, the network transponder then transmits at 2287.5 MHz and receives NASA operational signals at 2106.406 MHz. Alternately, when the PI is transmitting to a NASA payload in the 2072.68 - 2119.79 MHz band and receiving in the 2250.875 to 2300.875 MHz band, the network transponder transmits at 2217.5 MHz and receives NASA operational signals at 2041.947 MHz.

Table 3.4. Principal PI Receiver Characteristics

Parameter	Value	Units
Input Frequency Range	2200 - 2300	MHz
Input Signal Level Operating Range	-124 to +36	dBm
AGC Range	-127 to -27	dBm
Noise Figure	7.0 max	dB
Thresholds: Acquisition	-120.0	dBm
Tracking	-124.0	dBm
Acquisition Sweep Range: Minimum	± 112	kHz
Maximum	± 132	kHz
Nominal Acquisition Sweep Range	330	kHz/sec
Frequency Rate Tracking	17	kHz/sec
False Lock Immunity	Sidebands < -26	dBc
Tracking Bandwidth	3200	Hz
Maximum Phase Noise	15	Degrees-RMS
Throughput Bandwidth: Minimum	4.3	MHz
Maximum	5.5	MHz
Output Signal Regulation	2.0 ± 0.4	VRMS
Throughput SNR Losses	2.1 max	dB

Frequency synthesis for both the receiver and the transmitter is based upon a master 80 MHz temperature-controlled crystal oscillator (TCXO). Transmitter carrier phase modulation takes place at a fixed frequency which is subsequently translated to the proper output frequency

within the transmitter synthesizer (TX). In order to frequency sweep the transmitter carrier, a VCXO sweep circuit is used, with its output also being input to the transmitter synthesizer. Thus, the output of the transmitter synthesizer is a discrete carrier, phase-modulated and frequency-swept signal with a nominal (no sweep) carrier frequency corresponding to the designated channel.

The transmitter synthesizer output is amplified to a level that is necessary to drive either of the output power amplifiers. Separate power amplifiers are used for L-band and S-band channels (respectively, LPA and SPA). Only one amplifier may be on or active at a given time. Either amplifier is capable of providing three selectable output power levels, as listed in Table 3.3. Power amplifier output is switched into the appropriate triplexer subband.

As shown in Figure 3.6, a single RF port connects the PI to the payload antenna cable as the Orbiter payload antenna serves to simultaneously receive and transmit signals. This port connects into the receiver input through the triplexer. Immediately following the triplexer receive switch and located at the input to the preamplifier is a power overload limiter. This limiter functions to protect the FET preamplifier itself from any damage for applied power levels as large as +36 dBm. The preamplifier output is input through an image frequency-rejecting BPF to the first mixer.

The function of the first mixer is to downtranslate the received signal to a fixed intermediate frequency (IF) of 215 MHz. Since the input signal carrier frequency may correspond to any one of the designated channels on the 2200 - 2300 MHz range, the mixer reference supplied by the receiver synthesizer (RX) must also cover a 100-MHz range (1985-2085 MHz). Following this mixer is a wideband IF amplifier assembly (IFAS) consisting of several stages of gain-controllable (AGC) amplification and bandpass filters.

A second mixer further downconverts the 215 MHz first IF signal to the 31 MHz second IF. The reference for this second mixer is derived from the tracking loop VCXO, so the second mixer represents the input to a quasilong loop phase-locked-loop (PLL) architecture. The second mixer is followed by an IFAS. At the output of the IFAS, the signal is effectively split into two principal channels.

The wideband channel provides for modulation receiver and output to the appropriate processing units. A wideband phase demodulator referenced to a 31 MHz oscillator (which becomes phase coherent with respect to the signal carrier component by virtue of the carrier-tracking loop discussed subsequently) translates all of the signal first-order sidebands to the lowpass or baseband frequency region. The baseband waveform (which generally consists of signal-plus-noise) is then regulated to a fixed RMS value prior to being output.

A second 31 MHz channel is narrowband (approximately 30 kHz IF bandwidth) by virtue of the placement of a crystal BPF prior to two quadrature reference-driven demodulators. One of these demodulators, known as the loop phase detector, produces a carrier frequency/phase error voltage which is subsequently filtered and applied to the voltage control input of the PLL VCXO. The VCXO output is frequency multiplied by a factor of 10, whence it becomes the reference to the second mixer, thus completing the PLL circuit. For the conditions of proper PLL tracking, the frequency and phase of the received signal discrete carrier component at the input to the loop phase detector is in frequency-synchronous phase-quadrature with the 31 MHz derived reference.

Prior to achieving a condition of phase lock, the frequency difference between the received signal and the receiver references may be very large ($> \pm 100$ kHz). Thus, as an aid to attaining lock, the VCXO frequency is swept over the uncertainty range by means of the sweep loop. Once a state of lock is established, the sweep loop is disabled by the lock detector circuit.

The second demodulator of the narrowband quadrature pair is known as the coherent amplitude detector (CAD). If, when the PLL is locked, the input and reference to the loop phase detector have a 90° phase difference, the input and reference to the CAD then have a 0° phase relationship. As a result, the CAD output is a direct (zero frequency) voltage with amplitude proportional to the level of the received carrier. Such a voltage has two distinct uses: (1) as a means of indicating phase lock, and (2) the basis for receiver automatic gain control (AGC).

To implement a lock detector, the CAD output is input to a two-pole small bandwidth LPF which is followed by a comparator referenced to a fixed threshold. When the PLL is out of lock, any direct signal component and noise voltage appearing at the LPF output are essentially smaller

than the threshold so that the comparator output will indicate a "false" or out-of-lock status. Conversely, if the PLL is locked, the direct voltage appearing at the LPF output is sufficiently greater than the threshold so that the comparator output becomes "true," indicating a state of in-lock.

An AGC voltage is formed by simply offsetting the CAD output (i.e., adding a reference voltage, RC), lowpass filtering, and feeding the result back to the voltage-controllable gain amplifiers within the first and second IFAS's. Since AGC is also needed for receiver acquisition conditions when the PLL is out of lock and no direct voltage is produced at the CAD output, a noncoherent AGC voltage is derived and used in this state. The implementation involves rectifying the 31 MHz output of the crystal BPF to obtain the AGC measure, adding a reference voltage RN, and switching the result into the AGC LPF (in lieu of the CAD output). Switching between noncoherent and coherent AGC is dependent upon which of the respective voltages is the largest.

3.2.5 IUS/Orbiter RF Communication Links

One of the requirements for the RF link between the IUS and the Orbiter is that the link be operational from a minimum range equivalent to IUS being in the payload bay of the Orbiter to a range of 10 nmi. The resulting wide range in the RF signal levels requires special considerations for protecting the STDN/TDRS and the SGLS transponder when they are in the payload bay. Conversely, the PI receiver must also be protected.

The transmitter for the PI has the capability of being switched to a power output compatible with the distance to the IUS. The Orbiter payload antenna EIRP is +29.7 dBm, +19.7 dBm, and -3.3 dBm. For the case of the IUS in the payload bay, the output power should be set at the lowest power level (-3.3 dBm) to avoid the possibility of saturating or damaging any of the IUS SGLS or STDN/TDRS transponders. At this level, the received power at the SGLS receiver is -56.8 dBm, which is within the operating dynamic range of threshold (approximately -120 dBm) to -40 dBm maximum. However, the other two output power levels are -23.8 and -33.8 dBm, which exceed the upper limit of the SGLS transponder specified dynamic range. Similar examination of the received signal power for the NASA IUS with the STDN/TDRS transponder shows that the lowest PI output power level must be used so that the IUS received power (-52.5 dBm) is less than -40 dBm (i.e., the upper limit of the specified dynamic range for the STDN/TDRS transponder).

Figure 3.7 presents the received power at the IUS SGLS and STDN/TDRS transponders versus range for the three PI output power levels. The IUS transponders are specified to achieve acquisition at a received power level of -117 dBm in 0.5 seconds with a probability of 0.9 for a modulated signal. In terms of the Orbiter acquisition procedure, a modulated signal would be present only during reacquisition. Therefore, the reacquisition threshold for the SGLS transponder is reached at 5 nmi in the low-power mode, while the STDN/TDRS transponder reaches the reacquisition threshold at 8.5 nmi in the low-power mode. In the medium-power mode, the SGLS and STDN/TDRS transponders reach the reacquisition threshold at 24 nmi and 36 nmi, respectively. Considering the range limitations due to performance, one determines the received power at which the system operates with zero margin. We call such points ZPMO in Figure 3.7. Thus, as seen from Figure 3.7, the ZPMO for the STDN transponder is outside the range for acquisition. Thus, the STDN range is reacquisition-limited rather than performance-limited. For the SGLS, we have a ZPMO range of 14 nmi with medium-power PI transmission. Therefore, for either transponder, the 10 nmi operating range requirement can be met with medium-power PI transmissions.

No adjustments are possible for controlling the output power of the IUS transmitter so that the 20W (13 dBW) from the TWT results in 13.2W (11.2 dBW) being radiated into the bay. Above -20 dBm, however, the receiver IF amplifier circuits begin to saturate. At input signal levels of +10 dBm and higher, a preamplifier protective diode breakdown limiter becomes operative. Thus, intentional receiver operation above +10 dBm is not recommended.

The PI received power from the IUS SGLS transponder at 3 m is estimated at -19.4 dBm. Thus, the receiver IF amplifier will begin to saturate. Furthermore, this estimate of the received power was calculated based on a -4.0 dB IUS pointing loss (worst case). If there is no pointing loss, the received power is -15.4 dBm and the PI IF amplifier could be in saturation but there will be no damage to the PI receiver. Similarly, the PI received power from the IUS STDN/TDRS transponder at 3 m is estimated to be at -13.6 dBm including a -3.4 dB IUS pointing loss. Therefore, when at close range, the antenna selection on IUS will be such as to keep the PI receiver out of saturation. Thus, there will be no damage to the PI receiver at close ranges.

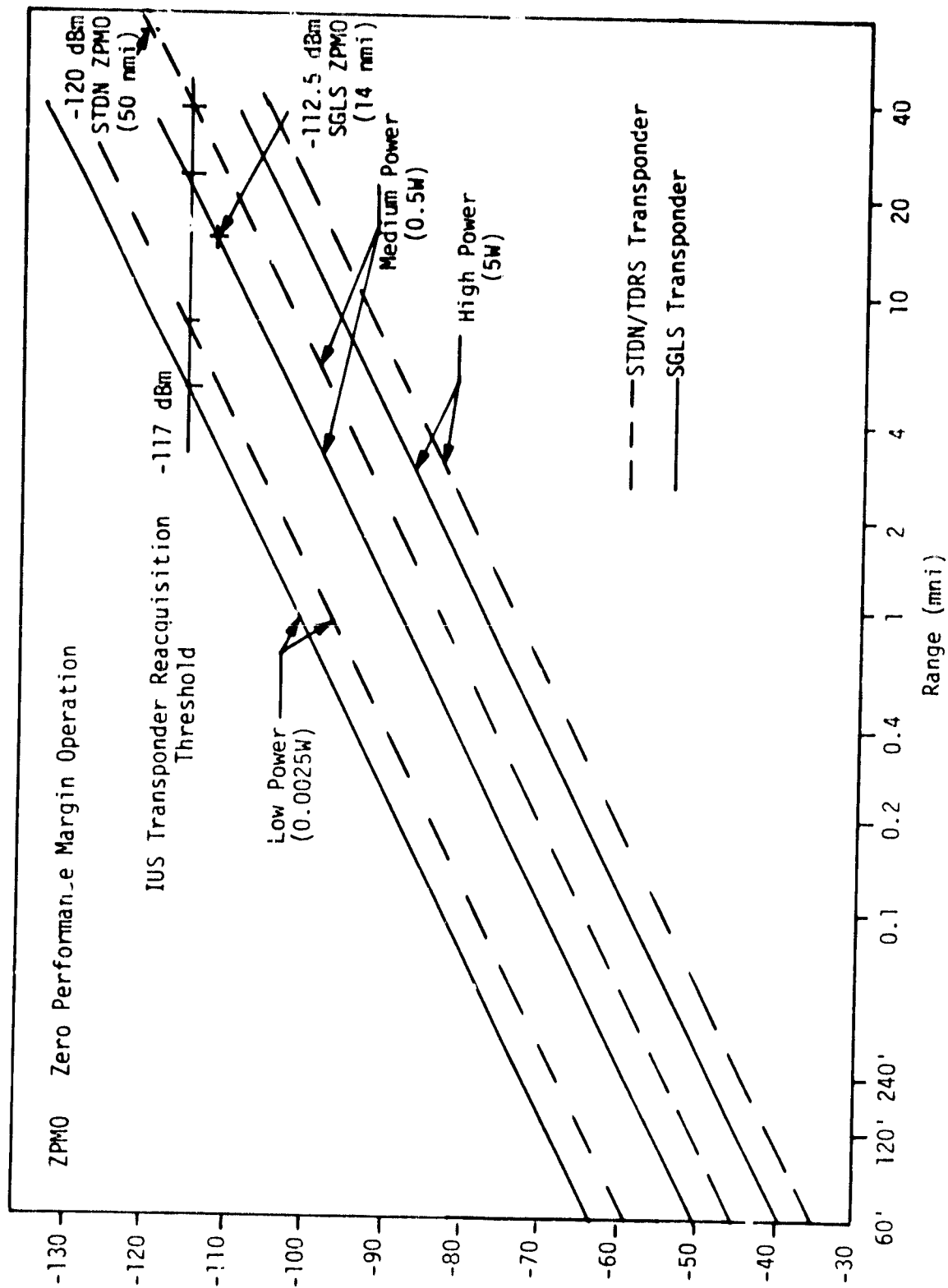


Figure 3.7. IUS Received Power versus Range for Each PI Output Power Setting

The power received by the PI versus the range to the IUS is presented in Figure 3.8. As can be seen from the figure, the reacquisition threshold is far above the zero margin performance (ZPMO) for both the SLGS and STDN/TDRS transponder transmissions. It can also be seen from Figure 3.8 that the 10 nmi operating range requirement is met for both transponders in the digital telemetry mode. In the analog FM mode, the performance is limited to 7 nmi.

3.3 Payload Signal-Processing System

The payload signal-processing system provides two basic functions: (1) process commands to be transmitted by the PI, and (2) process telemetry received by the PI. The Orbiter subsystems comprising a part of the payload signal-processing system are the PSP, CIU and KuSP.

3.3.1 Payload Signal Processor

The PSP consists of two basic processors--one to handle telemetry data and the second to process and encode command messages. Telemetry input is in the form of data biphase modulated onto a subcarrier which is serially processed in such a manner as to (1) PSK demodulate the data from the subcarrier, (2) bit synchronize and matched-filter detect the data, and (3) frame synchronize the data. Table 3.5 lists the principal PSP telemetry signal-processing capabilities.

Commands are handled by the PSP in such a manner as to: (1) accept command messages in "burst" form and buffer store, (2) perform a validation check, (3) rate convert to the appropriate bit rate and prefix with an idle pattern, and (4) biphase modulate the serial command word onto a subcarrier. Data rates and signal characteristics for the command signal generation portion of the processor are tabulated in Table 3.6.

A telemetry functional block diagram of the PSP appears in the upper part of Figure 3.9. Telemetry signal input may be derived from either the PI, which represents the operational input, or ground support equipment (GSE) for preflight test purposes. As the input signal is a biphase-modulated suppressed subcarrier waveform, the PSK demodulator functions to regenerate a coherent subcarrier reference which is used to phase demodulate the data from the subcarrier. Thus, the output from the PSK demodulator is composed of the telemetry bits. Subcarrier regeneration and tracking is accomplished by means of a polarity-type Costas loop.

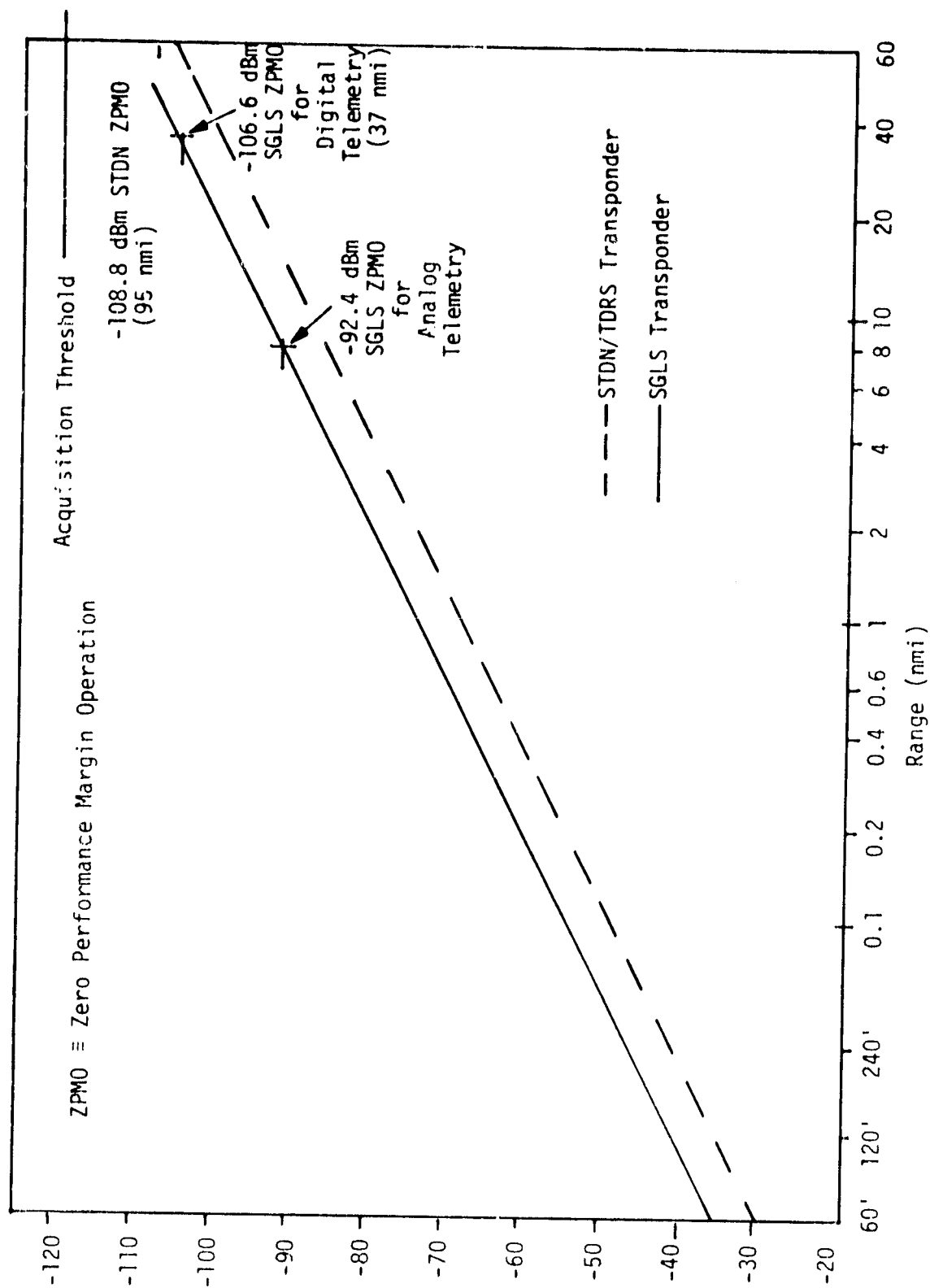


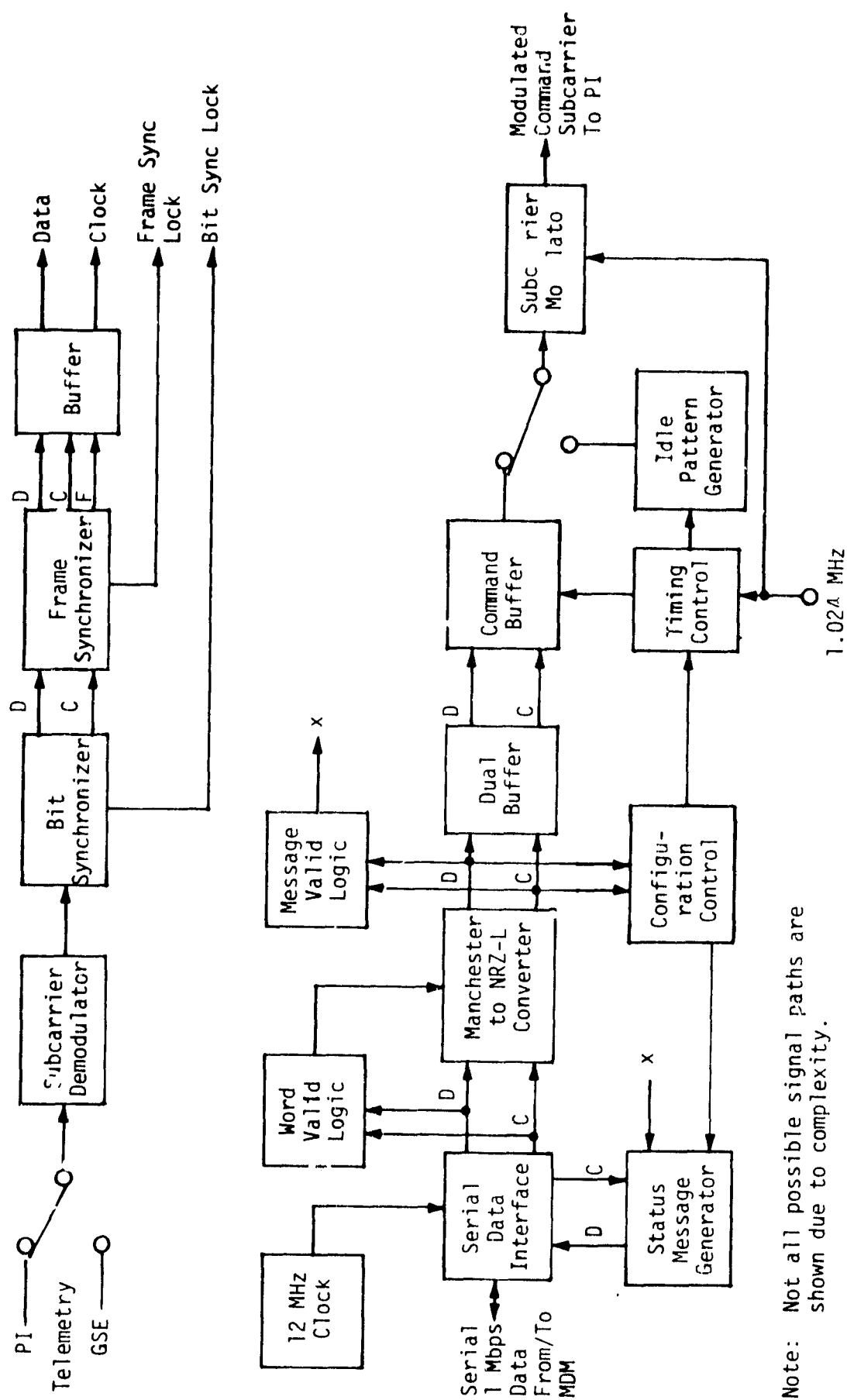
Figure 3.8. PI Received Power versus Range from IUS

Table 3.5. PSP Telemetry Signal-Processing Capabilities

Parameter	Value	Units
Subcarrier Waveform	Sinusoidal	-
Subcarrier Modulation	PSK, ± 90	Degrees
Subcarrier Frequency	1.024	MHz
Bit Rates	$16 + 2^N$, $N = 0, 1, 2, 3, 4,$	kbps
Bit Format	NRZ-L, M, or S, or Manchester-L, M, or S	-
Word Length	8	Bits
Minor Frame Length	8 to 1024	Words
Master Frame Length	1 to 256	Minor Frames
Transition Density	≥ 64 transitions in 512 bits ≤ 64 consecutive bits w/o transition	

Table 3.6. PSP Command Signal Characteristics

Parameter	Value	Units
Subcarrier Waveform	Sinusoidal	-
Subcarrier Modulation	PSK, ± 90	Degrees
Subcarrier Frequency	16	kHz
Idle Pattern	Alternating "ones" & "zeros"	
Bit Rates	2000 ± 2^N , $N = 0, 1, 2, \dots, 8$	bps



Note: Not all possible signal paths are shown due to complexity.

Figure 3.9. PSP Functional Block Diagram

The bit synchronizer is a digital data transition tracking loop (DTTL) of proven design and performance. Data detection itself is performed by integrating across an entire bit (in-phase integration or averaging) and taking the resulting polarity as representative of the bit value (+1 or -1). Bit clock synchronization is accomplished by means of integrating between bits (mid-phase integration or averaging) and using the resulting measure as an error signal which subsequently corrects the local bit timing clock source phase to maintain proper alignment with the received bits.

At the output of the bit synchronizer, a received serial telemetry data bit stream exists and is identical to that generated by the payload, with the exception of occasional bit errors. This data stream consists of random (insofar as processing is concerned) telemetry information plus regularly inserted frame synchronization words. It is these frame synchronization words that the frame synchronization processor searches for and locks onto so that the telemetry stream output by the PSP is frame synchronized.

A PSP command functional block diagram is presented in the lower part of Figure 3.9. As shown in this figure, PSP control/mode information and command data are transferred to the PSP from the general-purpose computer (GPC) via a MDM interface. For this purpose, a serial bilateral data bus operating at a rate of 1 Mbps is employed. Also, over this same bus, the PSP is able to transmit a status message to the GPC for the purpose of configuration and command data validation. Input/output in the proper mode is established to the PSP from the MDM using discrete (one-bit message) lines.

Within the PSP, a 1 MHz serial data interface is provided which performs data word detection and synchronization. All timing is generated from a master 12 MHz clock. The word validation logic examines the serial interface output to (1) check the integrity of the Manchester data waveform, (2) check parity, and (3) look for end-of-data identification. Failure to pass any of these tests results in inhibiting the Manchester-to-NRZ conversion operation.

All word-valid Manchester data is converted to serial NRZ-L data, after which it is clocked into the dual buffer. The dual buffer consists of two storage memories: one which receives current data at the 1 Mbps rate while the other is clocked out at a rate proportional to the

1.024 MHz clock. Thus, new command messages from the GPC/MDM may be received and stored at the 1 Mbps rate while, at the same time, command data may be transferred to the command subcarrier modulator at the selected payload command bit rate.

The message-valid logic examines all messages received from the GPC/MDM for illegal codes. Any illegal form detected is sufficient to inhibit further processing operations. A failure-to-pass message validation is transmitted through the status message generator back to the GPC, and a message repeat is requested.

The portion of the GPS message which corresponds to the PSP configuration information is processed by the configuration control which, in turn, is responsible for setting the PSP mode/operating parameters. Configuration status is transmitted back to the GPC via the status message generator. Command message verification is also made using status message reportback to the GPC.

Valid command bits to be transmitted to the payload are clocked from the command buffer at the proper bit rate. Each command is prefixed with a command idle pattern of alternating "ones" and "zeros." (In fact, the command idle pattern can be transmitted any time when requested and in lieu of actual command bits.) Command bits or idle pattern bits biphasic modulate a 16 kHz sinusoidal subcarrier which is output to the PI.

3.3.2 Communication Interface Unit

The primary function of the CIU is to provide command and telemetry data conditioning between the Orbiter and the IUS transponder. The CIU physically consists of four boxes and two control panels mounted in an Orbiter standard console. The four boxes consist of two GFE units (KGT-60 and KGR-60), a CIU BLACK unit, and a CIU RED unit. The CIU/KG control and display panels control the operating mode of the CIU. The CIU BLACK unit performs command and telemetry processing of BLACK (encrypted and clear) data. The CIU RED unit performs command and telemetry processing of RED (unencrypted) data.

The CIU accepts command data from one of five sources:

- (1) S-band MDM
- (2) KuSP
- (3) GN&C MDM
- (4) Crew-generated data from control panel
- (5) T-0 umbilical.

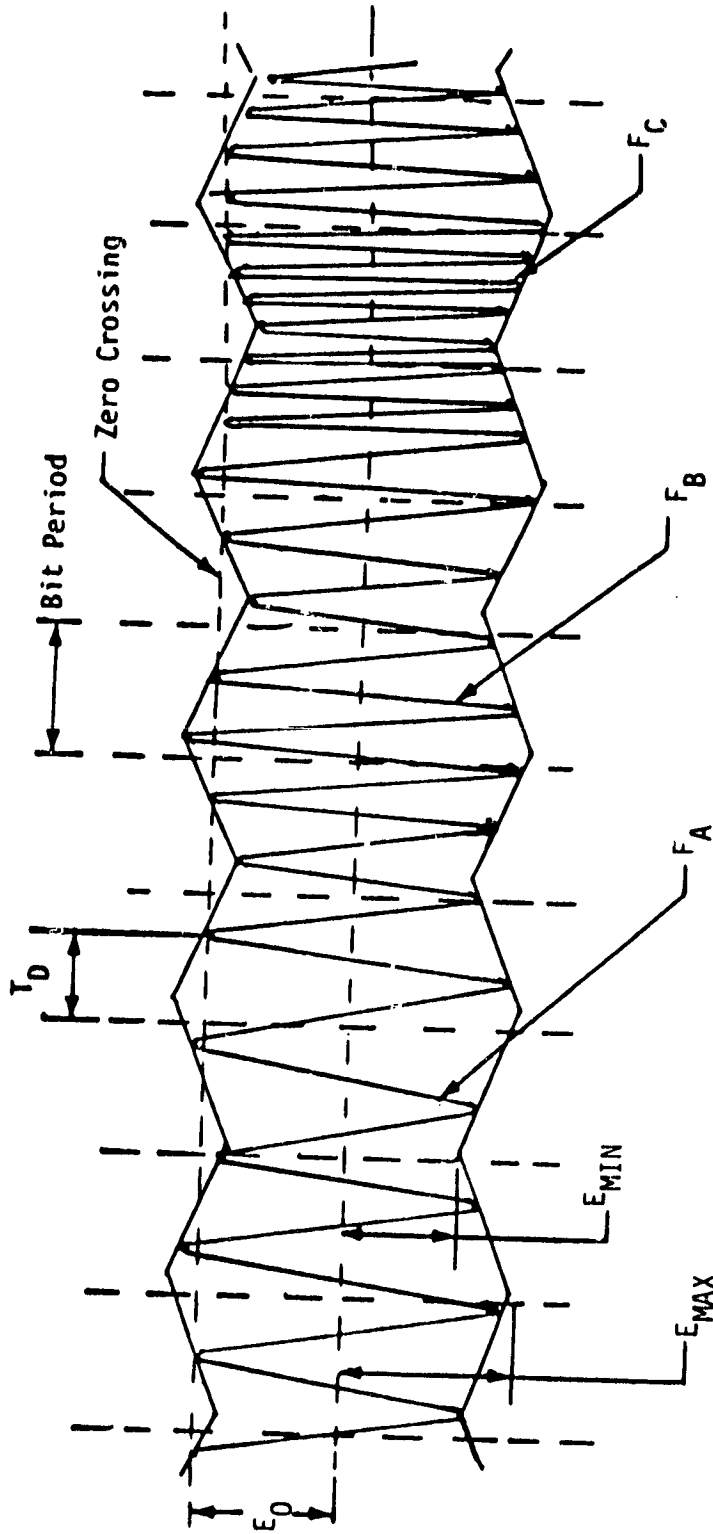
Input command data is validated, formatted, modulated on an SGLS baseband carrier (see Figure 3.10) at 1k baud, and forwarded to one of six destinations. The CIU forwards the conditioned command data to one of two redundant PI's for RF transmission to the IUS transponder.

The CIU receives telemetry data from one of the two PI's as a PSK subcarrier (1.024 MHz), frequency multiplexed with FM/FM environmental data on a 1.7 MHz subcarrier. The CIU performs PSK demodulation and bit synchronization to generate NRZ-L telemetry data and clock for selection to the KGR-60 or the PDI. The same telemetry data is NRZ-L to biphas-L converted for selection to the PR, FMSP or KuSP. The CIU performs FM demodulation on the 1.7 MHz subcarrier to generate three-channel FM (16, 24 and 32 kHz). The CIU provides the three-channel FM plus a 100 kHz reference for selection to the PR.

Figure 3.11 shows a simplified block diagram of the CIU. Microprocessor technology is fundamental to the CIU operation. The microprocessor performs the bit synchronization function on the telemetry data for processing by the KGR-60, then receives telemetry data (NRZ-L) and clock from the KGR-60. The microprocessor performs frame synchronization, VCC extraction (required for DOD commands) and command authentication, and determines command rejection. The microprocessor also accepts GN&C data and provides the command generator function to send GN&C or crew-generated command data to the FM/AM modulator via the KGT-60. The required binary-to-ternary conversion on the command data is also performed by the microprocessor. Additional functions performed by the microprocessor are CIU mode control and status display.

3.3.3 Ku-Band Signal Processor

The KuSP receives IUS and payload data from the PI, PSP, CIU and PR. Similarly, the KuSP transmits data to the IUS and payload via the CIU or NSP/GPC/PSP (or CIU). Table 3.7 presents the characteristics of the data that are handled by the KuSP. The 216 kbps data shown for the forward link originates at the TDRSS ground station and can be 72 kbps command data to the NSP, 128 kbps DOD command data to the CIU, 128 kbps text and graphics data, and 216 kbps data containing 72 kbps command data plus digital voice data that is sent directly to the NSP. Figure 3.12 illustrates the functional processing of the KuSP for data to be transmitted to the IUS and payload (i.e., the forward link). When the forward



T_D = Delay Time = 600 microseconds

$$\text{Percent Modulation} = \frac{E_{MAX} - E_{MIN}}{E_{MAX} + E_{MIN}} \times 100 = 50\% \pm 10\%$$

F_A = 65 kHz nominal = "S"

F_B = 76 kHz nominal = "0"

F_C = 95 kHz nominal = "1"

Figure 3.10. Command Tone Modulation Envelope

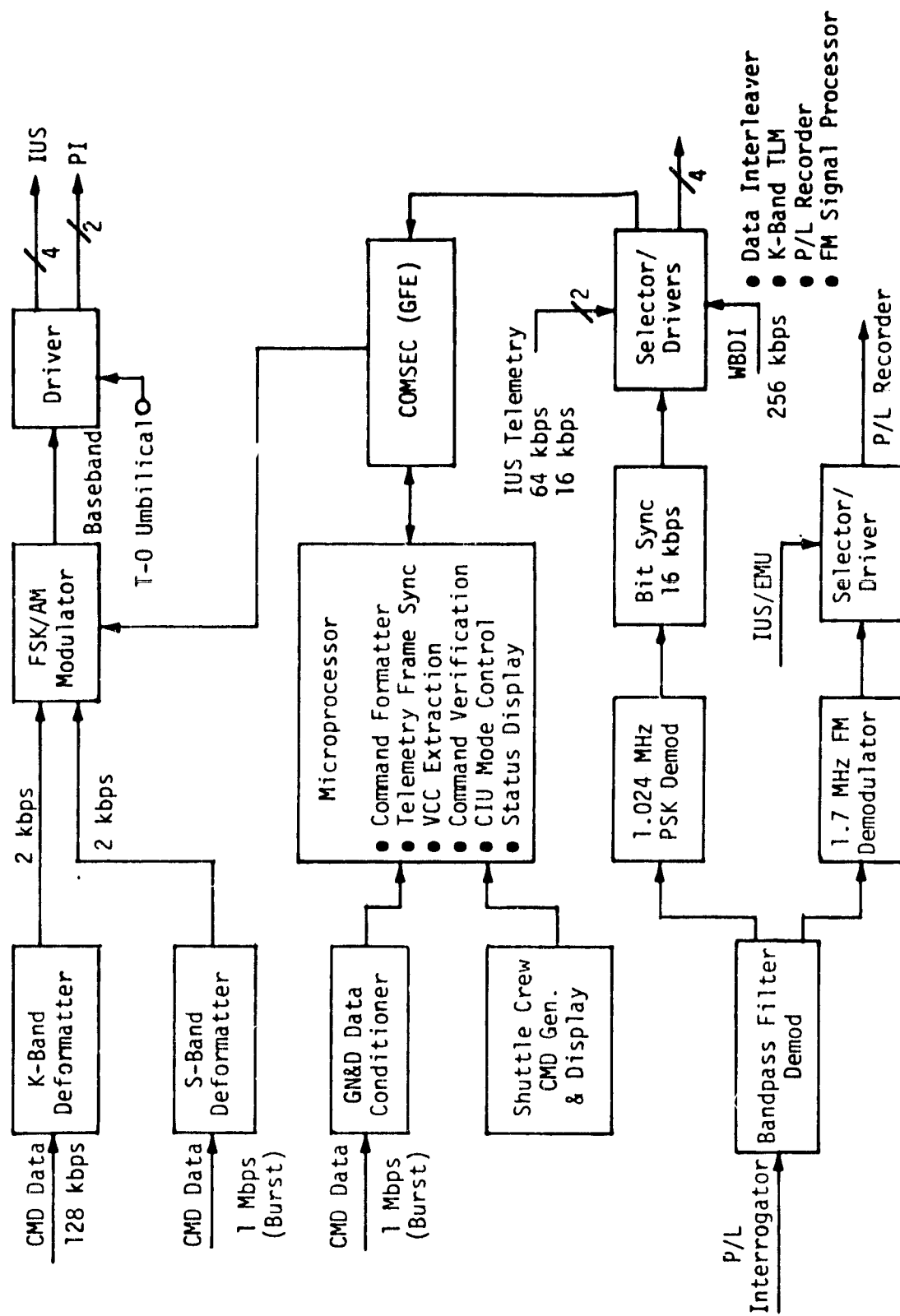


Figure 3.11. Communication Interface Unit Functional Block Diagram

Table 3.7. Ku-Band Signal Processor Data Characteristics

Processor Interface	Type	Rate or Bandwidth
FORWARD LINK		
Operations Data - NSP(1,2)	Digital	32,72,96,219 kbps (Manchester)
Command/Text & Graphics - NSP(1,2) and Test & Graphics	Digital	72 kbps Command 128 kbps Text & Graphics 16 kbps Frame Sync (Manchester)
Command/DOD Payload Command Data - NSP(1,2)/CIU	Digital	72 kbps Command 128 kbps DOD Payload 16 kbps Frame Sync (Manchester)
RETURN LINK		
CHANNEL 1 (MODE 1/MODE 2)		
Operations Data - NSP(1,2)	Digital	129 kbps (Manchester)
CHANNEL 2 (MODE 1/MODE 2)		
Payload Recorder (PR)	Digital	25.4-1024 kbps (Manchester)
Payload low data rate - PSP(1,2)	Digital	16-2000 kbps (NRZ) 16-1024 kbps (Manchester)
PI(1,2) low data rate	Digital/Analog	16-2000 kbps (NRZ) 16-1024 kbps (Manchester) 0-2 MHz
CHANNEL 3 (MODE 2)		
PI(1,2) high data rate	Digital/Analog	16-4000 kbps (NRZ) 0-4.5 MHz
Video Interface Unit	Analog	0-4.5 MHz

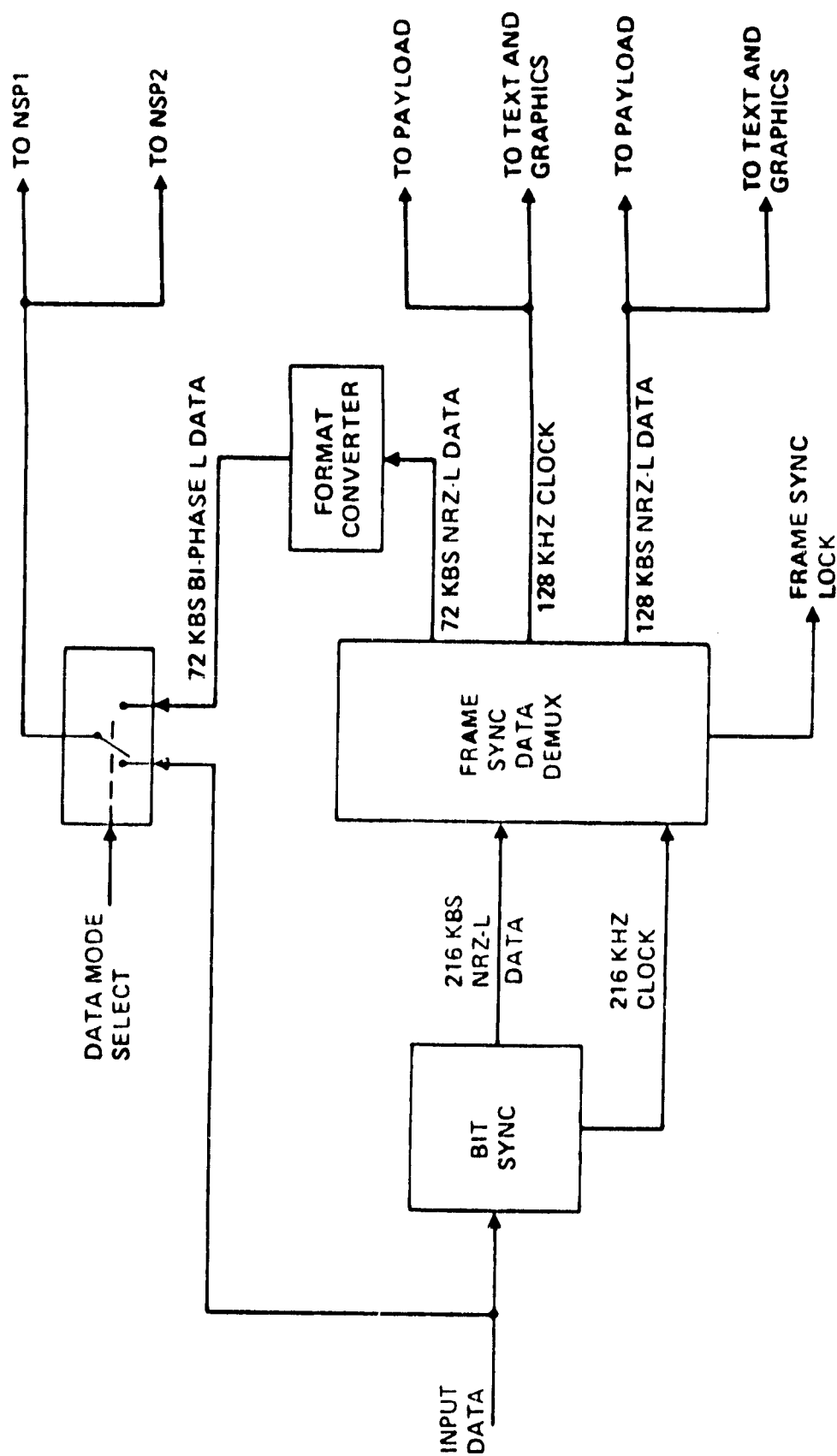


Figure 3.12. Ku-Band Signal Processor Forward Link Functional Block Diagram

link contains the normal S-band 216 kbps operational data of the 72 kbps command data plus digital voice data, the data mode select is set to transfer the data directly to NSP1 and NSP2 without any processing in the KuSP. Note that, in this data select position, the possible data rates are 32, 72, 96 and 216 kbps. When the 216 kbps forward link data contains either text-and-graphics data or DOD command data, then data mode select is set to transfer the 72 kbps command data to NSP1 and NPS2. The 128 kbps DOD command data is actually 2 kbps which has been coded to use the available 128 kbps data rate without having to modify the KuSP bit synchronizer or frame synchronizer design.

The characteristics of the data that must be processed by the KuSP on the return link are quite varied, as shown in Table 3.7. The return link is transmitted in one of two modes which are identified by the type of carrier modulation utilized. Mode 1 implements unbalanced quadriphase-shift-keying (UQPSK) while Mode 2 implements FM. In both modes of operation, two of the channels (1 and 2) UQPSK modulate a subcarrier. Mode 1 utilizes this modulated subcarrier along with the third channel to UQPSK the carrier, as shown in Figure 3.13. Mode 2 linearly sums the modulated subcarrier with the third channel and frequency modulates the carrier with the resultant summed signal, as shown in Figure 3.14.

Channel 1 always (Modes 1 and 2) carries the operations data of 192 kbps consisting of 128 kbps telemetry data and two 32 kbps delta-modulated voice channels. Similarly, the data on Channel 2 does not change from Mode 1 to Mode 2. Channel 2 carries the output from the PR and the PSP as well as narrowband bent-pipe data from the PI. The range of data rates handled by the KuSP Channel 2 is shown in Table 3.7 to be 16-1024 kbps Manchester-coded data, 16-2000 kbps NRZ-coded data, or DC-2 MHz analog bent-pipe data.

In Mode 2, the UQPSK-modulated 8.5 MHz subcarrier is filtered, as shown in Figure 3.14, by a bandpass filter with -3 dB points at 4.75 and 12.8 MHz. This BPF has extremely sharp low-frequency skirts (-40 dB point \geq 4.0 MHz) to minimize spectral spillover of the modulated subcarrier into the Channel 3 frequency band (DC-4.5 MHz). The Channel 3 input is passed through a lowpass filter with specified amplitude responses of -3 dB at 5.5 MHz and -20 dB at 8.1 MHz. Differential delay is no more than 20 ns due to equalization. Although the combination of these two filters will provide excellent performance of the linear Channel 3, their selection is suboptimum for Channel 2 performance since the bandpass necessarily has a high bandwidth-to-center frequency ratio and the lowpass filter provides only nominal skirt

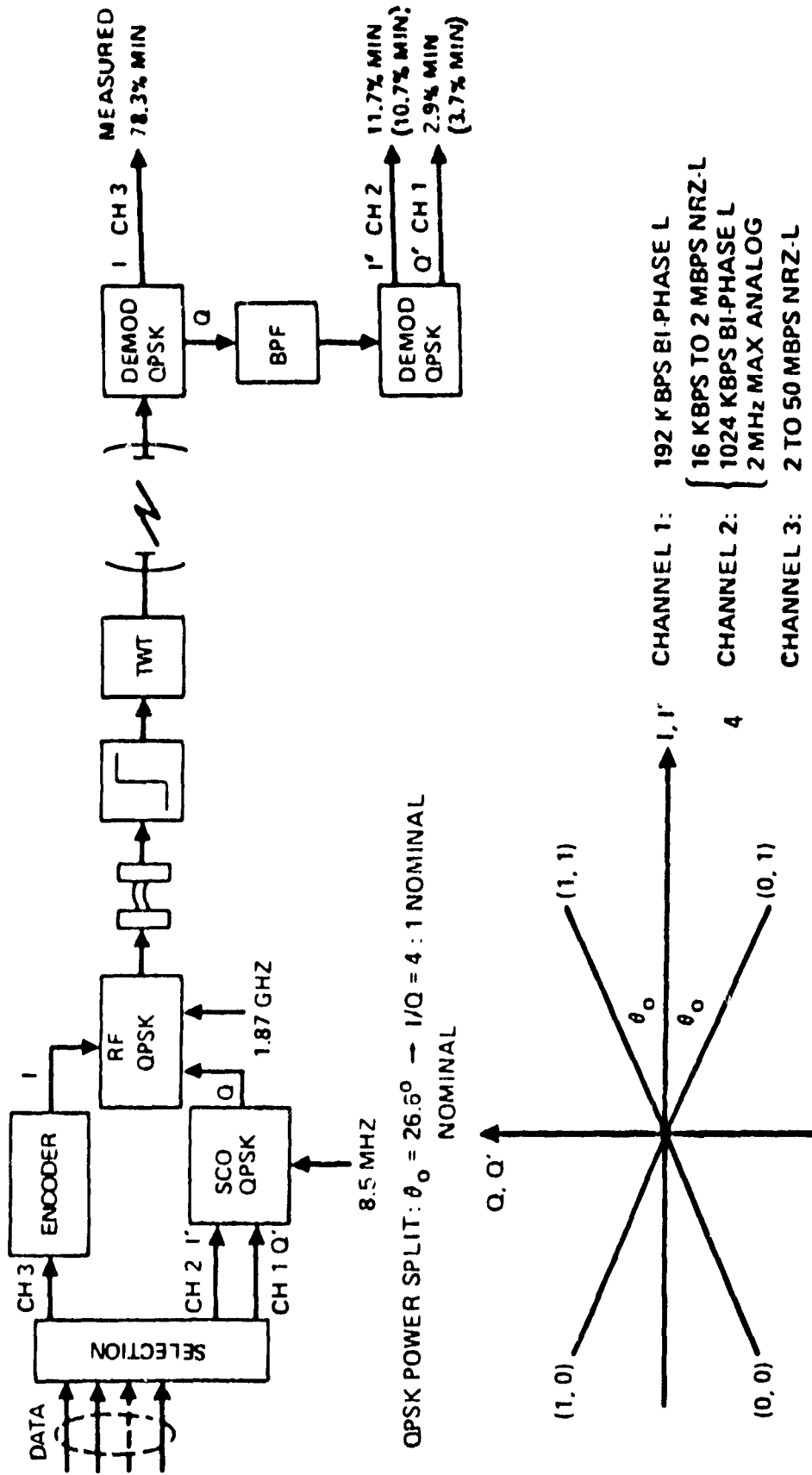
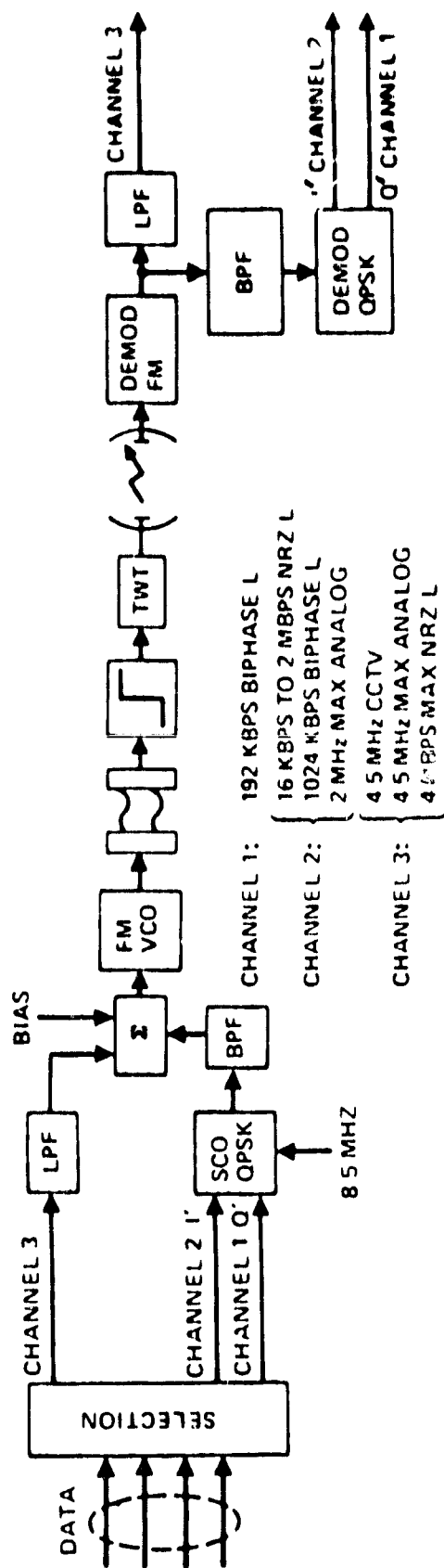


Figure 3.13. Ku-Band Mode 1 Three-Channel Modulation



QPSK POWER SPLIT: $I/Q = 4:1$ NOMINAL

FM POWER SPLIT: CHANNEL 3 FM DEVIATION: 11 MHz NOMINAL

SUB C_x FM DEVIATION: 6 MHz NOMINAL

Figure 3.14. Ku-Band Mode 2 Three-Channel Modulation

rejection. Note that the degradation to Channel 2 due to spectral spillover from Channel 3 depends on the type of data on Channels 2 and 3. The worst degradation occurs when Channel 2 is 2 Mbps NRZ digital data and Channel 3 has a flat spectrum greater than 8 MHz. Table 3.7 presents the type of data present in Channel 3 for Mode 2. The data with the greatest spectral bandwidth and, hence, the most potential degradation to Channel 2 is the 4.0 Mbps NRZ digital data, but it is unlikely that Mode 2 would be used to transmit this data. More likely, Mode 1 would be used to transmit digital data at this high rate. The analog data from the PI can range from DC to 4.5 MHz but, since the PI contains a lowpass filter with effective noise bandwidth equal to 5 MHz, it can be expected that this signal will cause little degradation to Channel 2. The video interface unit (VIU) outputs a television signal with spectral bandwidth of approximately 4.5 MHz. Here again, there will be little spectral spillover into Channel 2 and there should be little degradation.

3.4 Payload Data-Handling System

The payload data-handling system distributes the data received from the payload and throughout the Orbiter and distributes the data received from the ground (and crew) to the payload. The Orbiter subsystems which are a part of the payload data-handling system are the PR, MDM, PCMMU, PDI and NSP.

3.4.1 Payload Experiment Recorder (PR)

The data-recording system uses wideband digital and analog magnetic tape recorders to record and reproduce digital and analog signals. The magnetic tape recorder data storage system consists of two components. The first component comprises the multitrack coaxial reel-to-reel tape transport and its associated electronics. The tape transport features negator spring tension and contains a minimum of 2400 usable feet of 0.5-inch by 1-mil magnetized tape. The transport can store a minimum of 3.4×10^9 bits of digital data. The second component contains additional data conditioning circuitry and all other control logic and associated electronics.

Payload experiment data recording is provided via the payload station panel. Predetermined patch panel wiring permits digital data recording in either parallel (up to 14 tracks) or a combination of

parallel-serial. Data rates from 25.5 kbps (lowest rate for a tape speed of six inches-per-second (ips)) to 1024 kbps (highest rate for a tape speed of 120 ips) can be selected from four tape speeds provided by pre-mission wiring of recorder program plugs.

Analog data can be recorded on up to 14 tracks in parallel with frequencies from 1.9 kHz (lowest frequency for 6 ips tape speed) to 1.6 MHz (highest frequency for 120 ips tape speed) by premission program wiring. The basic recorder has the record/playback capabilities presented in Table 3.8 below.

Table 3.8. Payload Recorder Record/Playback Capabilities

Data Range (kbps)	Frequency Range (kHz)	Selectable Tape Speed (ips)	Time Per Track (min)
64- 128	1.9 - 250	15	32
128- 256	3.8 - 500	30	16
256- 512	7.5 -1000	60	8
512-1024	1.5 -1600	120	4

3.4.2 Multiplexer/Demultiplexer

The primary interface unit between the GPC and other subsystems is an MDM, shown in Figure 3.15. The MDM's act as a GPC-to-Orbiter format conversion unit. They accept serial digital information from the GPC's and convert or format this information into analog, discrete or serial digital form for transfer to Space Shuttle subsystems. The MDM's can also receive analog, discrete or serial digital information from the Space Shuttle subsystems and convert and format these data into serial digital words for transfer to the GPC. In addition, MDM's are used by the instrumentation subsystems, but only in a receive mode. Each MDM is controlled through either the primary port connected to the primary serial data bus or through the secondary port connected to the backup serial bus if failure is encountered with the primary system. The input and output of the MDM are via a multiplexer interface adapter (MIA).

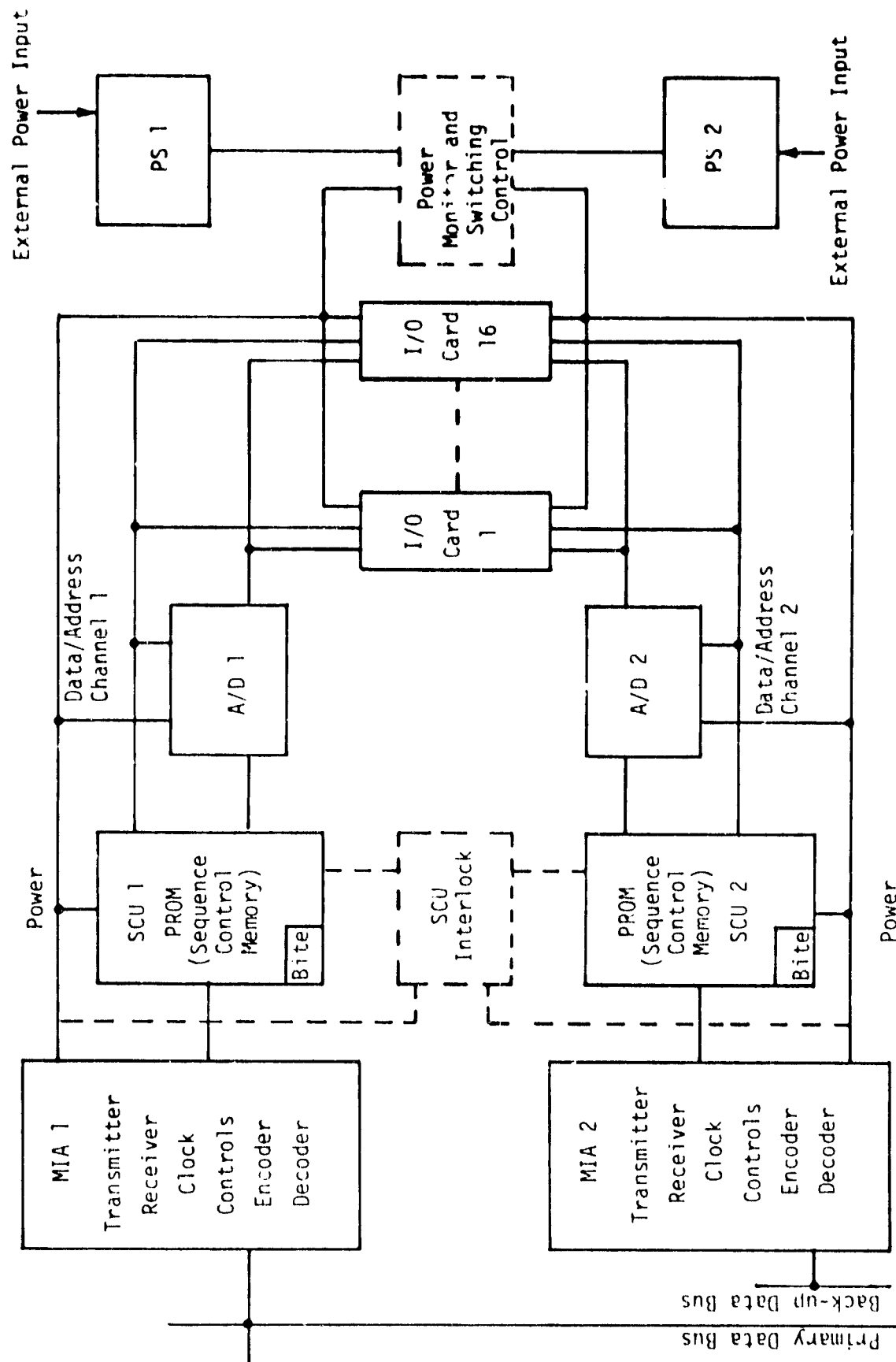


Figure 3.15. MDM System Block Diagram

The characteristics of the serial digital data input/output channels between the Orbiter subsystem (e.g., NSP, PSP, CIU) I/O buffer and the MDM are shown in Figure 3.16. The Word and Message Discretes are in the "0" states when the voltage level is between -0.6 V to +0.6 V and in the "1" states when the voltage level is between +2.1 V to +5.9 V. These discretes have differential signal termination with an impedance of 71 ± 7 ohms and a rise and fall time between 10 and 90% of 100 - 1000 ns, as shown in Figure 3.17.

When the Word Discrete is switched to a logical "1" state, the Orbiter subsystem is enabled to transmit individual words to the MDM. Figures 3.18 through 3.20 present the format for individual words to the MDM. Figure 3.18 illustrates the overall data format and shows the various parts of the MDM word. Figure 3.19 presents the specifications for the data coding. Note that the burst data rate to the MDM is 1 Mbps. The first three bits of each MDM word are used for word synchronization and are different from the normal Manchester-coded bits. Figure 3.20 presents the specifications for the nonvalid Manchester code used for word synchronization.

When the Message Discrete is switched to a logical "1" state, the Orbiter subsystem is initiated to transfer multiple words under the control of the Word Discrete, beginning with the first word. Figure 3.21 presents the specifications for the Message Discrete and the relationship between the Message Discrete and Word Discretes in the transfer of multiple MDM words.

Single-Ended Discretes are also shown in Figure 3.16. These discretes have the same logical state specifications as Word and Message Discretes; however, Single-Ended Discretes have rise and fall times of 20 μ s (max). The power-off impedance and load impedance must be 10 kohms (max) with a line drive capacitance of 35 pf/ft (min). The corresponding input current is 2.5 mA in the "0" state and 1.25 mA in the "1" state.

The characteristics of the analog interfaces with the MDM are a voltage range of 0 - 5 V (peak), a source impedance of 100 ohms (max), a load impedance of 500 kohms (min), a load "OFF" impedance of 100 kohms (min) and a line drive of 35 pf/ft (min). There can be only one analog interface per return.

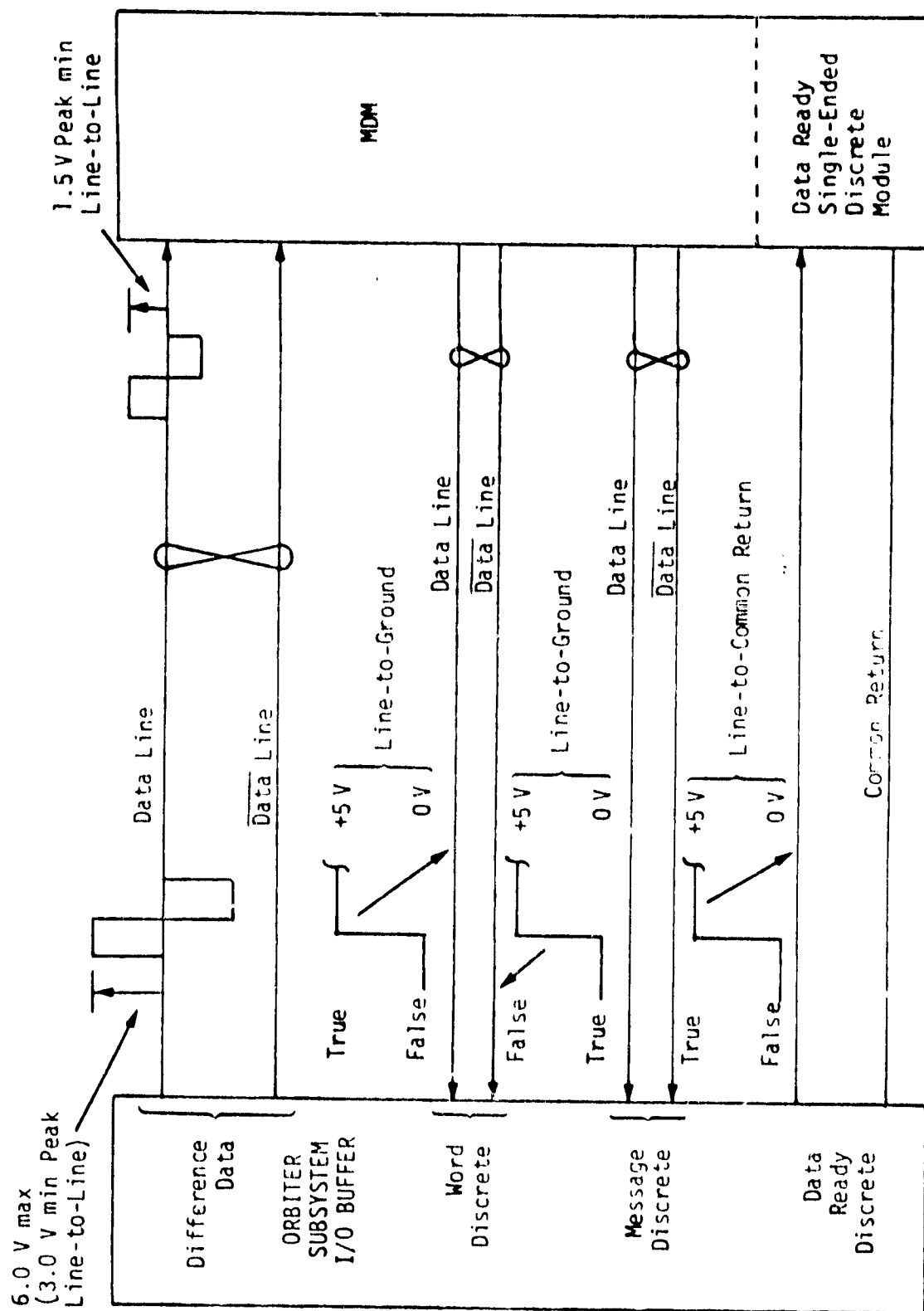
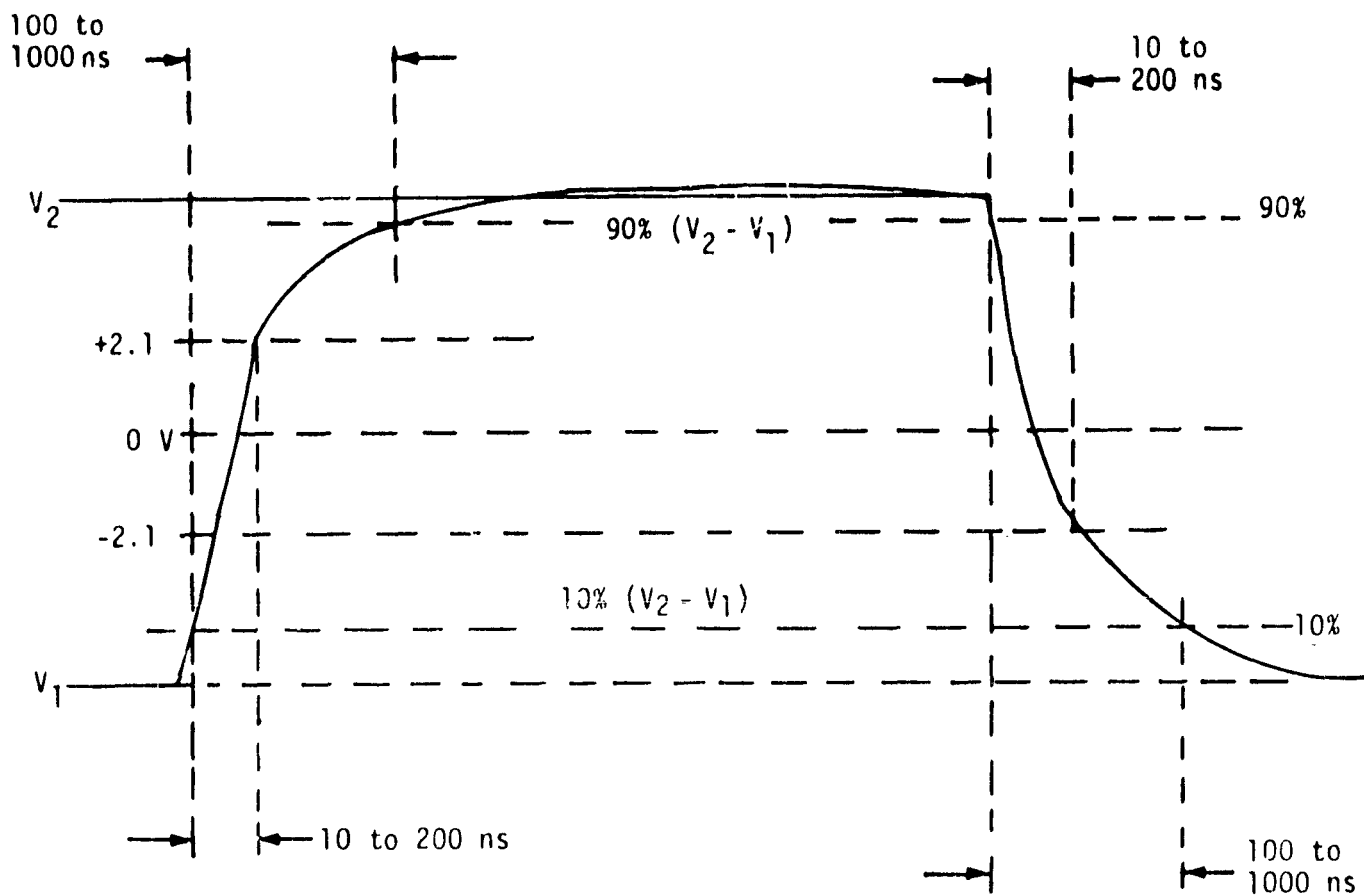


Figure 3.16. Serial Digital Input/Output Channel Interface



$$-5.9 \text{ volts} \leq V_1 \leq -2.1 \text{ volts}$$

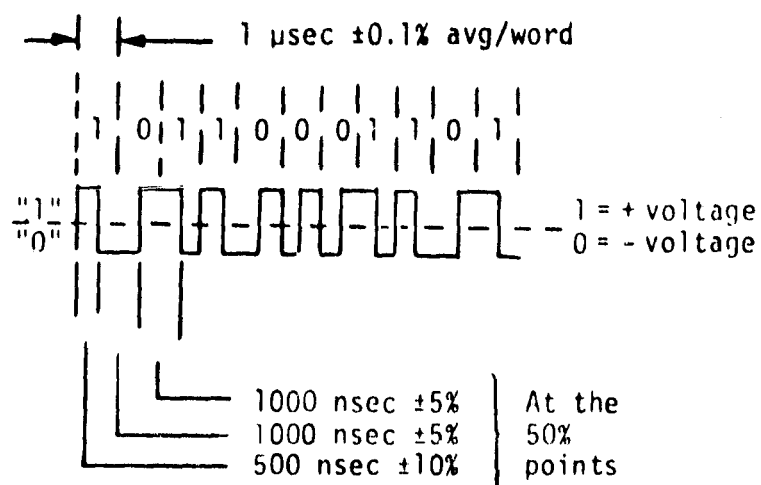
$$+2.1 \text{ volts} \leq V_2 \leq +5.9 \text{ volts}$$

NOTE: Waveform represents line-to-line voltage excursion.

Figure 3.17. Rise and Fall Times

3	16		1
SYNC	SIGN OR MSB	DATA	PARITY

Figure 3.18. Serial Word Format



NOTE: Biphase Level (Manchester II)

"1" represented by 10
 "0" represented by 01 for Data

"1" represented by 01
 "0" represented by 10 for $\overline{\text{Data}}$

Figure 3.19. Data Code

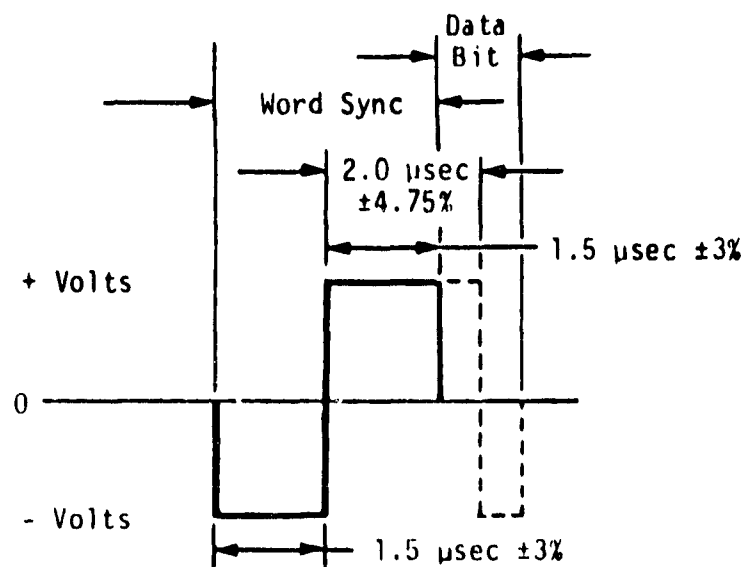


Figure 3.20. Data Word Synchronization, Nonvalid Manchester Code

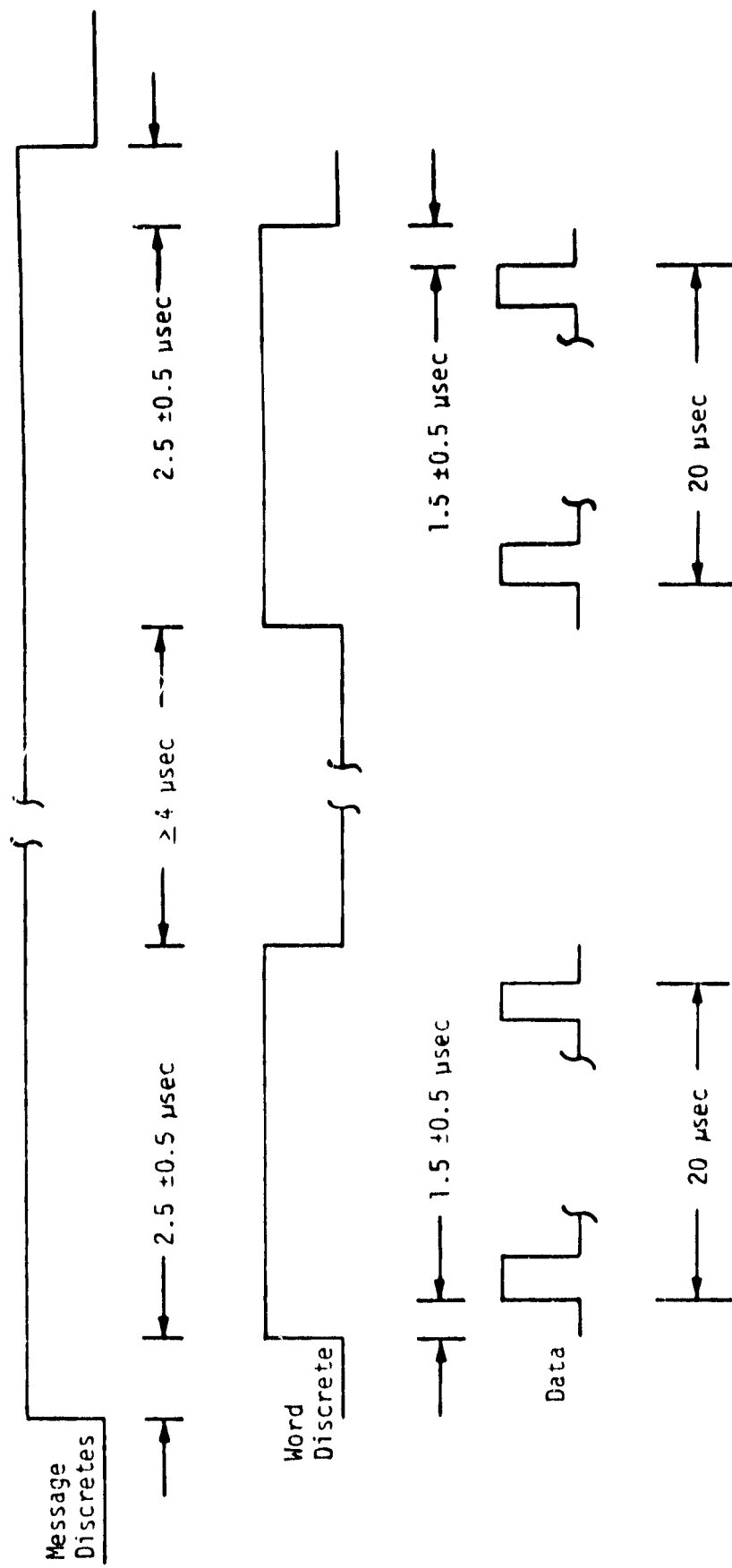


Figure 3.21. Serial Channel Data Transfer

3.4.3 PCM Master Unit (PCMMU)

The block diagram of the PCMMU is presented in Figure 3.22. Operational instrumentation (OI) sensor data (designated as downlink data) are acquired by the PCMMU in conjunction with MDM's. The MDM's under control of the PCMMU's accept, encode and store the data in a random-access memory (RAM) located within the PCMMU. The stored data are "refreshed" (updated) periodically under the control of a preprogrammed read-only memory. This module is known as a "fetch PROM."

GPC sensor and derived data (designated as downlist data) are acquired by GPC's and sent by a data bus to the PCMMU's. The PCMMU provides a unique double-buffer memory for each computer input, which allows data reception asynchronously while synchronously outputting previously received data. This guarantees the homogeneity of the data (i.e., output data are not overlaid by incoming data). Payload data are processed through the PCMMU in the same manner as the OI sensor data except that the PCMMU interfaces with the PDI.

The OI PCMMU, after accepting data from the MDM, computers and PDI, formats the data into a serial digital output stream for telemetry, recording and GSE. Format control is provided by the output formatter, which is programmable and can be modified by a set of instructions from the computers.

The PCMMU has a maximum output capability of 128 kbps for purposes of telemetry and on-board recording. The PCMMU, on command from the crew, can send 64 kbps of information. This mode is primarily used in conjunction with the low bit rate of the transmission system (S-band or Ku-band) and the TDRSS.

Formats have been developed for the ascent, on-orbit and entry phases and ground checkout. As noted in Figure 3.22, one of the format memories is a 128 kbps PROM having a fixed format and cannot be modified by the GPC. This format is used during power-up of the Orbiter and during the ascent phase. A fixed format is necessary because loss of power to the PCMMU would result in loss of information from 64/128 kbps RAM's (volatile memory).

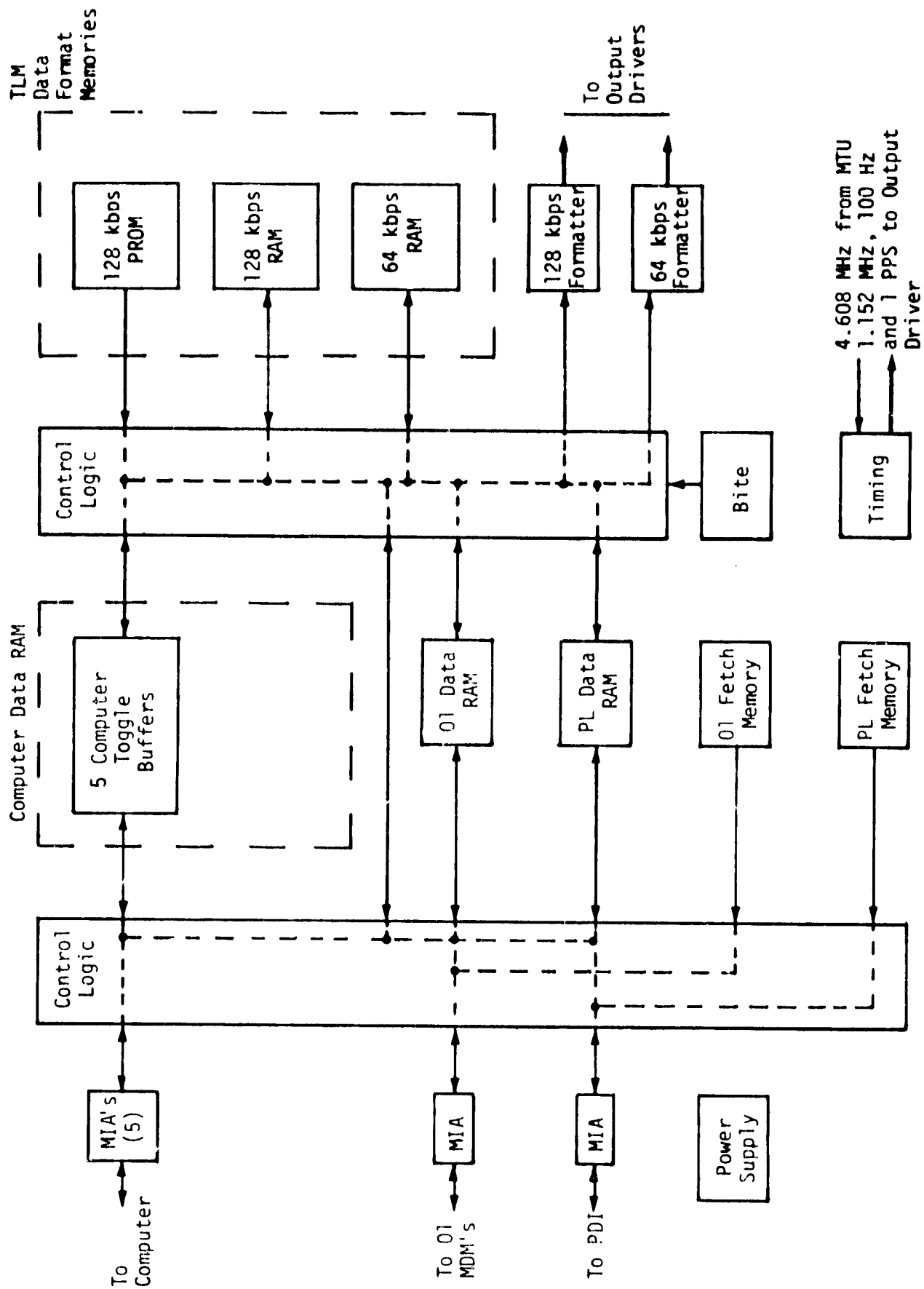


Figure 3.22. PCMMU Block Diagram

3.4.4 Payload Data Interleaver (PDI)

The programmable PCMMU can be modified from one flight to the next. Since the Shuttle provides transportation for many types of payloads, a programmable PDI was designed to interface with the PCMMU. The PDI (Figure 3.23) can accept data simultaneously from five different attached payloads, including the IUS/CIU and an input from the PSP, then select and individually decommutate the data for storage in a buffer memory. This memory is accessible to the PCMMU and the data are included with the Orbiter PCM stream. The PDI is programmed onboard from the mass memory through the GPC, which is used to select specific data from each payload PCM signal and transfer them to buffer memory locations. An input switch matrix selects four of the inputs for the bit synchronizers. The "chain" functions of bit synchronization, decommutation and word selection are provided for up to four simultaneous PCM streams in two possible modes, as listed below.

Mode 1. In this mode, a chain bit synchronizes, master-frame synchronizes, minor-frame synchronizes and word synchronizes to the incoming data stream. The word selector blocks data into proper words for storage in the data RAM and/or toggle buffer. PCM code type, bit rate, PCM format, synchronization codes and word selection are programmable under control of the decommutator format memories. Two word selection capabilities for this mode of operation are as follows: Type I--The first type selects all, or a subset of, the words in a payload PCM format minor frame (or master frame for formats without minor frames) for storage in the toggle buffer. Type II--The second type of word selection is by parameter. The specification of a parameter consists of its word location within a minor frame, the first minor frame in which it appears, and its sample rate. The specification is provided as part of the decommutator control memory format load.

Mode 2. In this mode, a chain bit synchronizes to the incoming data, clocks it into eight-bit words, blocks the eight-bit words into frames, supplies synchronization pattern at the start of each frame and includes the status register as the last three 16-bit words of each frame. A homogeneous data set for this mode of operation is defined as all information within this PDI-created frame. Code type, bit rate, frame length

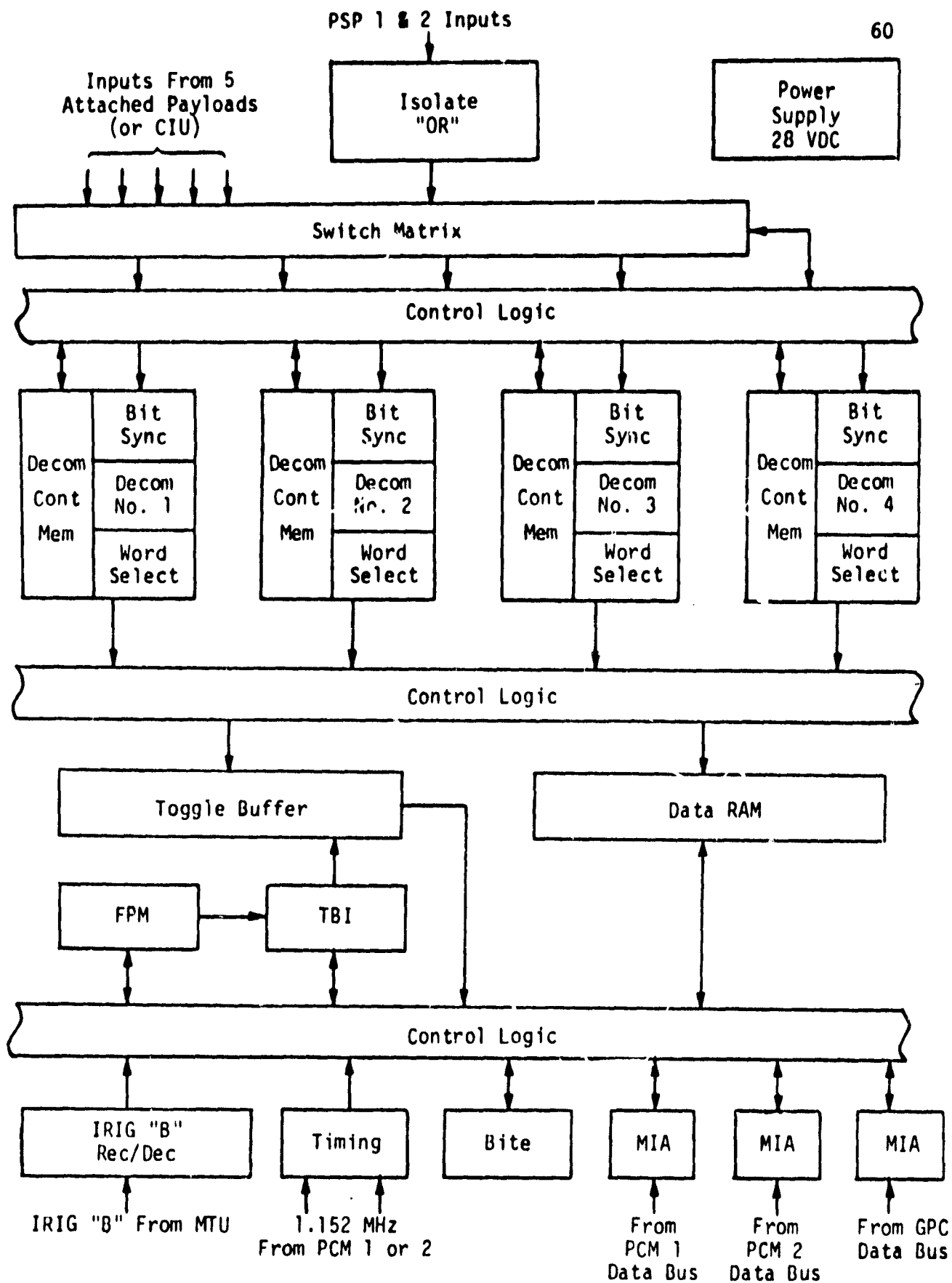


Figure 3.23. PDI Block Diagram

and synchronization pattern are programmable under control of the decommutator format memories. The frames are supplied to the toggle buffer for storage as homogeneous data sets. No data is supplied to the data RAM in this mode of operation.

A status register containing the status and time for a given chain operation is provided by the word selector to the Toggle Buffer (TB) control logic. This logic regulates access to and from the half buffers by the word selectors and data busses. All requests for TB data by the data ports are processed through the Fetch Pointer Memory (FPM) and the Toggle Buffer Identifier (TBI). The TB control logic also partitions data from the word selector into homogeneous data sets for access by the data bus ports.

The FPM is used to identify which TB is to be accessed by a data bus port. It also allows access to any location in the data RAM by any of the PDI data bus ports at any time. FPM control logic routes all requests for TB data to the location in the FPM identified by the data bus command word. It further provides for loading and reading of formats to and from the FPM at any time by the data bus ports.

A data RAM for storage of data from the word selector by parameter is provided. The data RAM control logic steers data provided by the word selector into addresses in the data RAM specified by the decommutator control memory.

There are three data bus ports for interface with the Orbiter GPC that have read and write access into the switch matrix, decommutator control memory, FPM, PDI and data RAM.

An IRIG "B" receiver/decoder accepts an IRIG "B" codes from an external source, decodes time and supplies it to the four status registers.

3.4.5 Network Signal Processor (NSP)

The NSP performs the digital-processing functions for the operational data. A block diagram of the forward command link is shown in Figure 3.24. All receiver input data first passes through the symbol synchronizer. Convolutionally encoded TDRSS-relayed data passes to the Viterbi decoder, and encrypted DOD data are output to an external COMSEC device, the output of which then goes to the frame synchronizer decoder. Unencrypted input data go directly to the frame synchronization decoder,

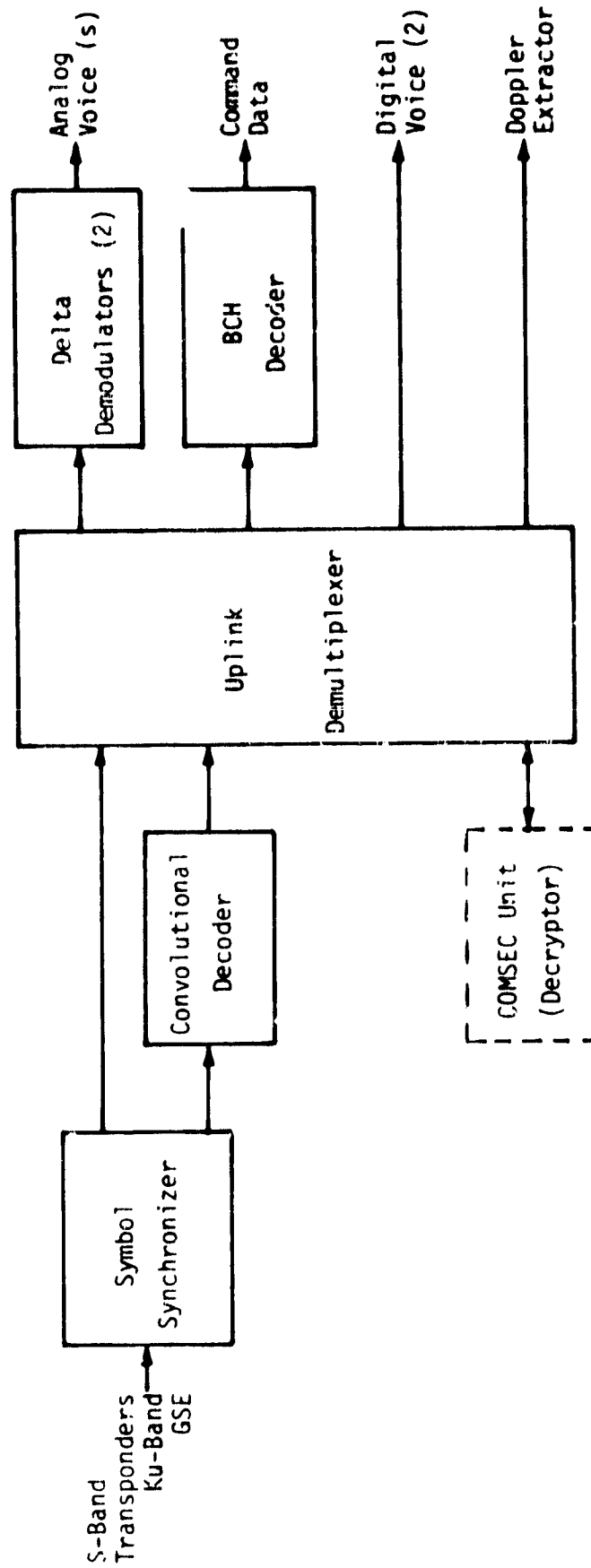


Figure 3.24. Forward Link Network Signal Processor Block Diagram

the output of which drives the demultiplexer (demux). Voice data from the demux are rate-buffered to either 24 k bits/s or 32 k bits/s to the delta demodulators or the payload station when receiving digital voice data in the DOD mode. Command data are buffered to a BCH (Bose-Chaudhuri-Hocquenghem) error detection/correction decoder at a net 6.4 k bits/s rate. The performance parameters for the network signal processor are shown in Table 3.9 below.

Table 3.9. Network Signal Processor Performance

NSP Bit Synchronizer	
Acquisition and Tracking Threshold SNR	-5 dB
Hard Decision Uncoded Data Detection (-5 dB \leq SNR \leq 10.6 dB)	< 0.6 dB from theory
Acquisition Time:	
Uncoded, SNR > 0 dB	1 s max
Coded, SNR > -3 dB	2 s max
NSP Viterbi Decoder	
For BER 10^{-1} to 10^{-6}	< 1 dB from theory
NSP BCH Command Decoder	
Probability of Undetected Error	10^{-18} max

The NSP performs the digital-processing functions for the operational data. An NSP block diagram of the return telemetry link is shown in Figure 3.25. On-board analog voice signals are delta modulated using a modified ABATE algorithm and multiplexed with telemetry data. Data to be TDRSS relayed are convolutionally encoded (rate 1/3, constraint length 7). All digital output data are converted from NRZ-L to biphasic-L prior to being transferred to the S-band transponder, Ku-band system or GSE umbilical.

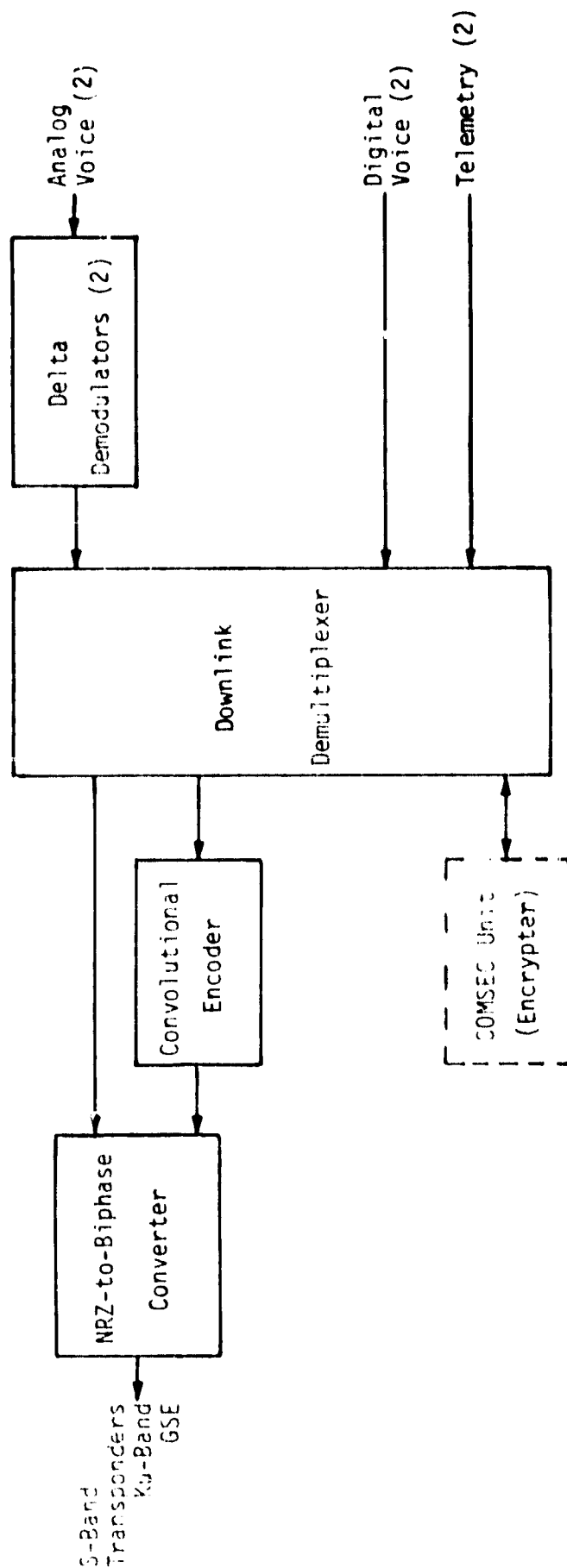


Figure 3.25. Return Link Network Signal Processor Functional Block Diagram

3.5 Orbiter Network Communication System

The payload command data transmitted from the ground through the Orbiter and the payload telemetry data transmitted from the Orbiter to the ground are processed by the Orbiter network communication system. The Orbiter network communication system includes S-band phase-modulated (PM) links, S-band frequency-modulated (FM) links, and Ku-band links.

3.5.1 S-Band PM Links

The S-band PM transponder is a multimode communications unit that operates in three primary modes (DOD direct, GSTDN direct, and GSTDN Hi-Power/TDRS relay) and several secondary modes. The transponder supports full-duplex communication in any of the primary modes, provides Doppler turn-around during coherent operation, and provides tone ranging turn-around. Turn-around ranging is accomplished exclusively with tones on the 1.7 MHz subcarrier.

A block diagram of the network transponder is shown in Figure 3.26. The transponder receiver searches for, acquires, tracks and coherently demodulates either residual carrier PM signals in the DOD or GSTDN modes or suppressed carrier PSK signals in the TDRSS mode. Acquisition of the spread spectrum code in the TDRSS mode is accomplished prior to carrier acquisition. The receiver is configured as a Costas loop for carrier acquisition and tracking. Symbol synchronization is performed in the NSP after carrier acquisition.

In normal operation, the transmit frequency is coherently related to the received frequency by either the DOD 256/205 or the NASA 240/221 transponding (turnaround) ratio. On the power-limited TDRSS relay links, convolutional encoding is required, resulting in a symbol rate three times the information rate. The composite link data rates are shown in Table 3.10. The spectrum of the forward TDRS link is further spread to reduce the power spectral density impinging on the earth's surface by combining the coded data symbols with an 11.232 Mc/s pseudo-noise (PN) sequence of length 1023. The performance parameters for the transponder are presented in Table 3.11. The power amplifier assembly supplies high-power amplification of the network transponder output for TDRS/GSTDN (high power) modes, providing a minimum of 100 W RF output power.

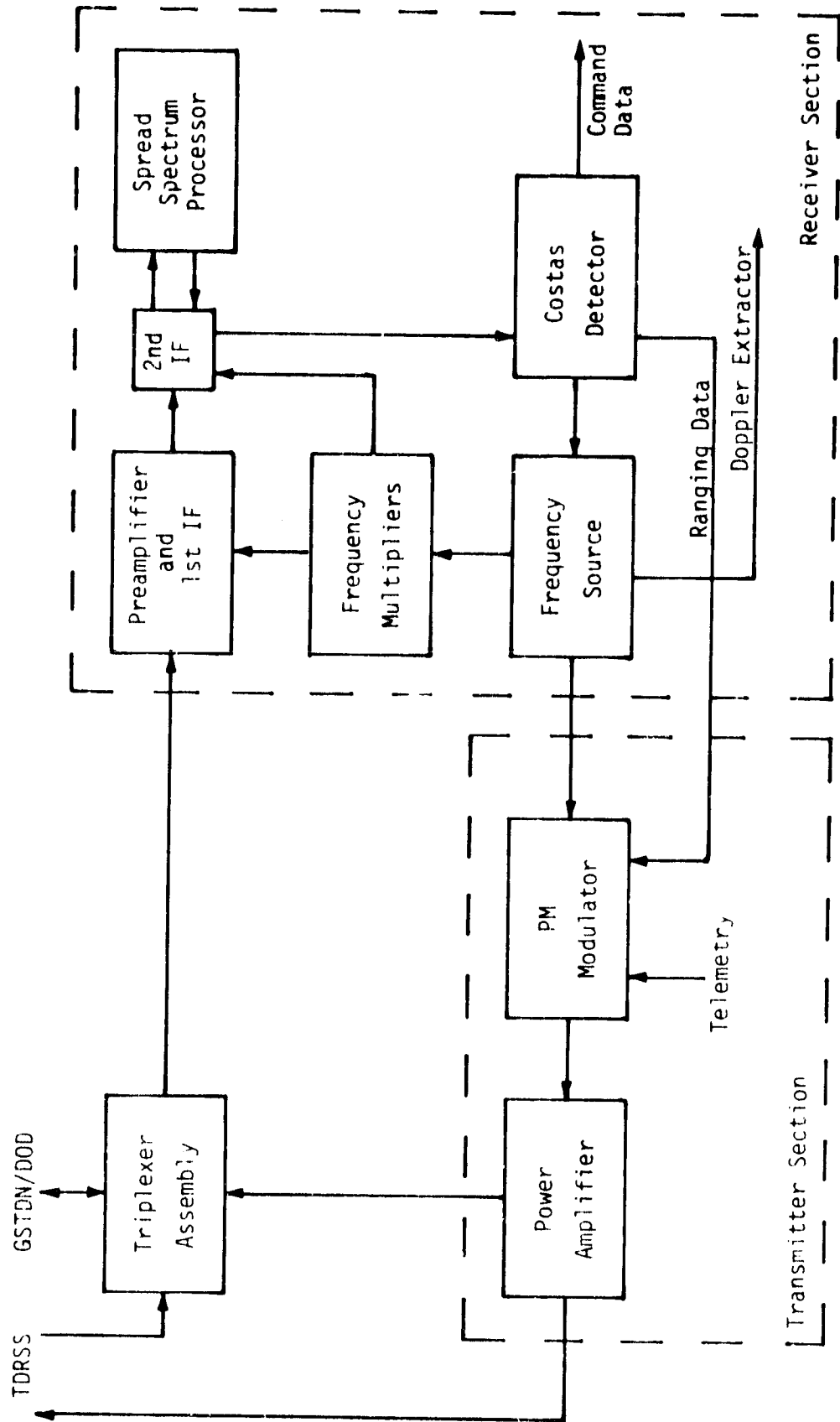


Figure 3.26. Network Transponder Functional Block Diagram

Table 3.10. Data Rates for Network PM Links

Link	Rate	Channels Available	Composite Link Rate	
			Direct (Bit Rate)	Relay (Rate 1/3 coded) (Symbol Rate)
Forward (Ground to Orbiter)	High	Two 32 kbps voice One 8 kbps command	72 kbps	216 ksps
	Low	One 24 kbps voice One 8 kbps command	32 kbps	96 ksps
Return (Orbiter to Ground)	High	Two 32 kbps voice One 128 kbps telemetry	192 kbps	576 ksps
	Low	One 32 kbps voice One 64 kbps telemetry	96 kbps	288 ksps

3.5.2 S-Band FM Links

The FM Signal Processor (FMSP) and FM transmitter provide a capability for transmission of data not amenable for incorporation into the limited-rate PCM telemetry data stream. The data to be transmitted via FM include television, digital data from the main engines during launch, wideband payload data, or digital data from the PI or attached payload interface (API). The characteristics of the data and the performance specifications for the FMSP and FM transmitter are presented in Table 3.11.

Conditioning and multiplexing for FM transmission occur in the FMSP, as shown in Figure 3.27. Video and wideband digital and analog signals are routed to the FM transmitter with only matching and filtering, but narrowband digital engine data are placed on subcarriers at 576, 768, and 1024 kHz.

The FM transmitter operates at 2250 MHz with an output power of 10 W. Both baseband and RF filtering are provided to reduce out-of-channel interference to the PM and payload receivers. The nominal RF bandwidth is 10 MHz.

Table 3.11. S-Band Transponder Performance Specifications

RECEIVER (AMBIENT TEMPERATURE)			
Noise Figure		8	dB Max
Doppler Accommodated		± 55	kHz
Doppler Rate Accommodated		± 5	kHz/s Max
Tone-Ranging Response (± 1 db)		1.5 to 1.9	MHz
Tone-Ranging Delay		1.1	μ s Max
Tone-Ranging Delay Variation		78.0	ns Max
Dynamic Range		-30 to -122	dBm Min
ACQUISITION PROBABILITY > 0.9 IN 6 SECONDS			
		MINIMUM SIGNAL LEVEL INTO TRANSPONDER	
MODE	MODULATION	32 kbps	72 kbps
STDN/SGLS	Bi- ϕ -L, PSK (No Ranging)	-117.0 dBm	-116.0 dBm
STDN Hi Power	Bi- ϕ -L, PSK* (No Tone Ranging)	-102.0 dBm	-101.0 dBm
TDRS*	Bi- ϕ -L, PSK	-103.0 dBm	-98.8 dBm
TDRS*	Carrier Only	-104.5 dBm	-100.3 dBm
<p>The tone ranging uplink signal shall be turned off during acquisition. Center frequency ± 50 kHz.</p> <p>* Input noise power spectral density of -151 dBm/Hz, acquisition probability > 0.9 in 12s for TDRS LO & HI data.</p>			
PN ACQUISITION TIMES			
P_r/N_0 (dB-Hz)	Average Acquisition Time (Seconds)		Average Time To Unlock (Seconds)
	96 ksps	216 ksps	
49.5	≤ 60	\leq N/A	≥ 3600
51	≤ 20		≥ 3600
53		≤ 30	≥ 3600
54	≤ 10.0	≤ 10.0	≥ 3600

Table 3.12. S-Band FM Performance Specifications

FM Signal Processor	
TV Channel Input	FIA TV Standard RS 170
TV Channel Gain	19 dB ± 0.8 dB to -0.25 dB
TV Channel Dynamic Range	51 dB ± 0.25 dB
Frequency Response ± 0.25 dB and Phase Ripple $\pm 1.0^\circ$	DC to 4.5 MHz
CCIR K Factor	<2%
Main Engine	
Data in 3 Channels	60 kbps BPL
Subcarrier Frequencies	576 kHz, 768 kHz, 1024 kHz
Subcarrier Modulation	$\pm 180^\circ$ at $\pm 15^\circ$
Analog Data Bandwidth	300 Hz to 4 MHz
Wideband Digital Data Rate	200 bps to 5 Mbps NRZ, or 200 bps to 2 Mbps Manchester Coded
Recorded Data - 2 Channels Data Rate	25.5 kbps to 1024 kbps
Narrowband DOD Digital Data Rate	250 bps to 256 kbps
Input Common Mode Voltage (DC to 2 MHz)	1V max
FM Transmitter	
Frequency	2250.0 MHz $\pm 0.003\%$
Output Power (into 1.5:1 load)	10W min, 15W max
Deviation Sensitivity (for deviation up to ± 4.5 MHz peak)	1 MHz/V peak $\pm 10\%$
Frequency Response ± 1 dB	DC to 5.0 MHz
Incidental AM	5% max over input range
Incidental PM	<5 kHz RMS over modulation BW
Intermodulation Distortion (2-tone equal amplitude)	<40 dB with frequency deviation ± 1 MHz

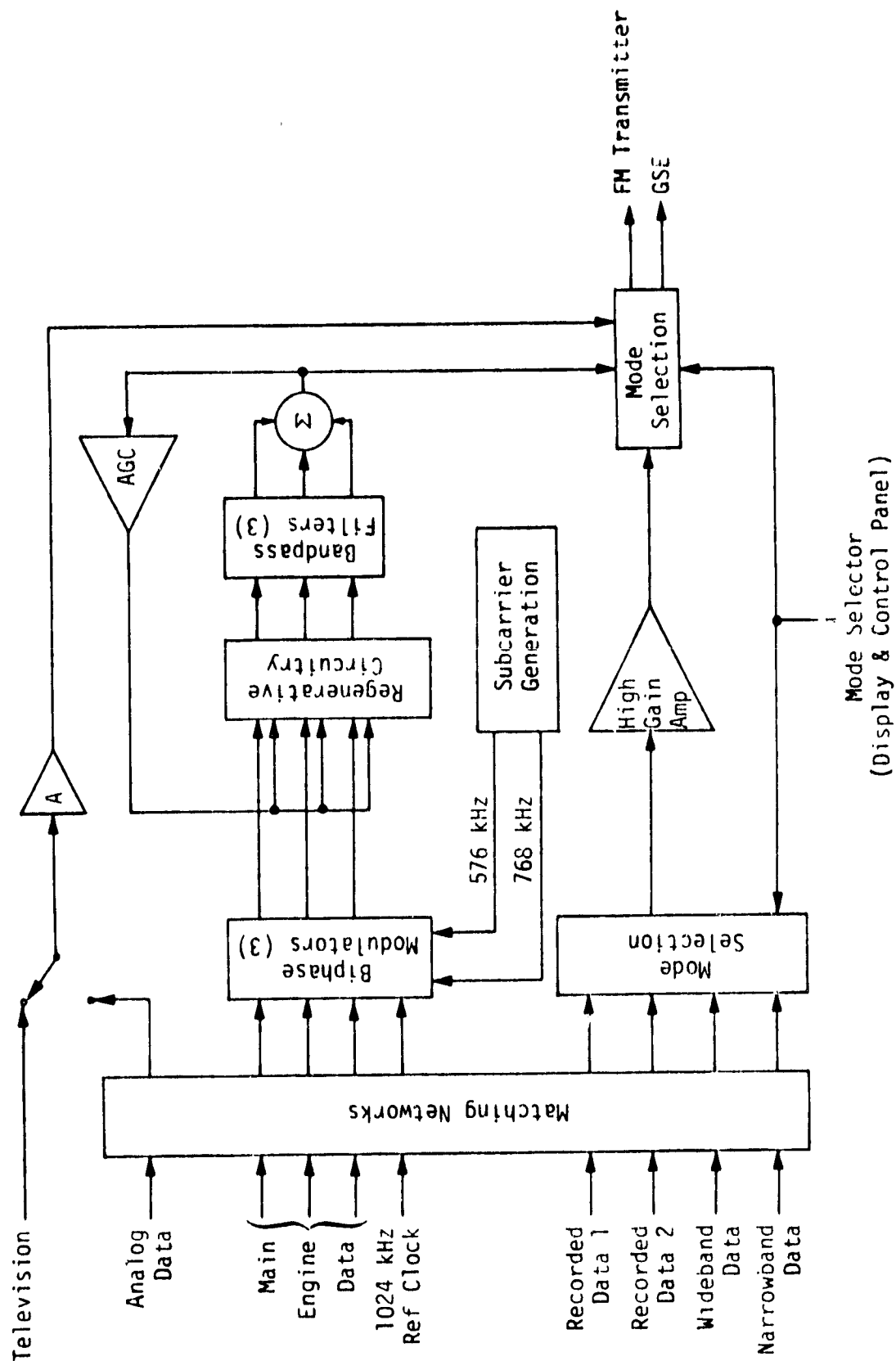


Figure 3.27. FM Signal Processor Functional Block Diagram

To further identify the interface between the payload system (i.e., the API and PR) and the FMPS, Table 3.13 presents the requirements of the input signals to the FMSP. As additional information concerning the data processing, Table 3.13 also presents the characteristics of the data signals output to the FM transmitter. Corresponding to each type of input signal, the signal source (i.e., API or PR) is identified. The signal type is either digital or analog, with the digital data further specified by the type of data coding. Note that, for the NASA wideband payload data, the data coding can be either Manchester II (biphase-L) or NRZ-L, but the Manchester-coded data is limited to data rates less than 2 Mbps rather than 5 Mbps for NRZ-L coded data. The signal level voltages are all peak-to-peak (p/p) and line-to-line for differential coupling and line-to-common for single-ended coupling. The impedance for all the signals is $75\ \text{ohms} \pm 10\%$, except the recorded data from the PR, which is $71\ \text{ohms} \pm 10\%$.

The rise and fall times for the digital data are also presented in Table 3.13. It is desirable to keep the rise and fall times less than 10% but, in some cases, absolute times are specified which determine the type of output drivers required at the PR, API and payload. Note that there is an additional specification of $\pm 2\%$ data asymmetry and $\pm 0.1\%$ bit jitter on the PR output signal to reduce the degradation associated with these types of signal distortion. The output of the FMSP for the PR signal has a specification of $\pm 0.25\%$ bit jitter which is expected due to the multiplication of the jitter through the FMSP buffering. Actually, each of the input signals to the FMSP should have these specifications but, typically, these are not difficult specifications to meet except from tape recorders.

3.5.3 Ku-Band Links

An overall block diagram of the Ku-band forward link data subsystem is shown in Figure 3.28. The characteristics of the received RF signal are given in Table 3.14. The forward link RF carrier transmitted by the TDRS is normally biphase-modulated with a modulo-two sum of data and PN code where the data and PN clocks are asynchronous. The data format is biphase-L (Manchester) and the PN code is NRZ-L. The PN code is a 1023-symbol Gold Code.

Table 3.13. Input and Output Signal Characteristics of FMSP for Payload Data

Signal	Signal Type	Data Coding	Data Rate	Signal Level	Rise/Fall Time	Coupling	Impedance
INPUT SIGNALS							
Recorded Data (PR)	Digital	Manchester II	22.5 kbps (min) 1024 kbps (max)	3-9V p/p line/line	<100 nsec < $\pm 2\%$ asymmetry <0.1% bit jitter	Balanced Differential	71 ohms $\pm 10\%$
Wideband Payload (API)	Digital	Manchester II NRZ-L	200 bps-2 Mbps 200 bps-5 Mbps	5V ± 0.5 V p/p line/line	<50 nsec	Balanced Differential	75 ohms $\pm 10\%$
Wideband Payload (API)	Analog	---	300 Hz-4 MHz	1V $\pm 10\%$ p/p line/line	---	Balanced Differential	75 ohms $\pm 10\%$
DOD Payload (API or CIU)	Digital	Manchester II or NRZ-L	250 bps-250 kbps	1V ± 0.6 V p/p line/line	<100 nsec	Balanced Differential	75 ohms $\pm 10\%$
OUTPUT SIGNALS							
Recorded Data	Digital	Manchester II	22.5 kbps (min) 1024 kbps (max)	1.27V $\pm 5\%$ p/p	10% of bit duration; $\pm 0.25\%$ bit jitter	Single Ended	71 ohms $\pm 10\%$
Wideband Payload	Digital	Manchester II NPZ-L	200 bps-2 Mbps 200 bps-5 Mbps	4V $\pm 5\%$ p/p	<10%	Single Ended	75 ohms $\pm 10\%$
Wideband Payload	Analog	---	300 Hz-4 MHz	4V $\pm 15\%$ p/p	---	Single Ended	75 ohms $\pm 10\%$
DOD Payload	Digital	Manchester II or NRZ-L	250 bps-250 kbps	1.27V $\pm 5\%$	<100 nsec	Single Ended	75 ohms $\pm 10\%$

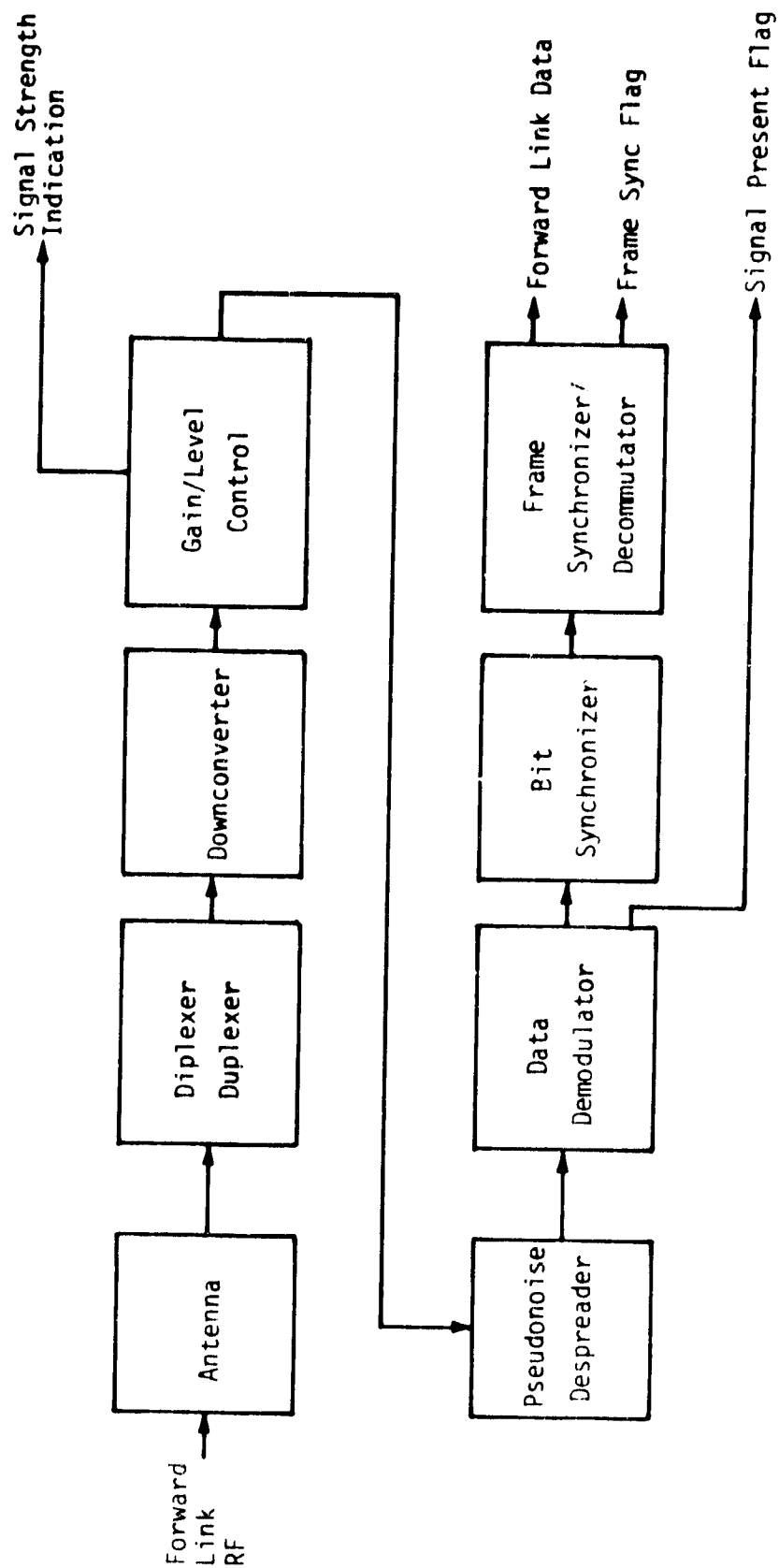


Figure 3.28. Ku-Band Forward Link Function

Table 3.14. Ku-Band Forward Link RF Signal Characteristics

Carrier frequency	13.775 GHz \pm 10 kHz
Received wave polarization	Right-hand circular
Received wave axial ratio	1 dB max
Dynamic range of incident	-113.5 dBW/m ² max
Flux density	-126.9 dBW/m ² min
PN code length	1023 symbols
PN code rate	3.028031 Mchips/s \pm 1 chip/s
PN code format	NRZ-L
Mode 1 data rate	216 kbps \pm 22 bps
Mode 2 data rate	32 or 72 or 96 or 216 kbps
Data format (all modes)	Biphase-L (Manchester)
Modulation (when present)	Biphase

The return link output of the KuSP modulators is upconverted by the exciter of the Ku-band transmitter to 15.0034 GHz. The upconverter output is amplified to 10 mW by a four-stage GaAs FET limiting amplifier. The low AM-to-PM conversion of the limiting amplifier permits a significant relaxation of the TWT AM-to-PM conversion specification. The TWT in the transmitter amplifies the exciter output to 50 W minimum and sends it to the antenna through the diplexer/duplexer. The total return link EIRP is about 53 dBW.

4.0 DETACHED PAYLOAD COMMUNICATION SYSTEM STUDY

In assessing the performance of one-/two-way coherent communication links, one must consider the many sources of random fluctuations present in the overall system and their individual degrading effects. While it is most common to consider only those degradations which are due to the additive thermal noise on the link(s), a complete characterization of system performance should also include the effects of such phase noise sources as transmitter and receiver local and reference oscillators, mixer (multiplier) logic noise, AM-to-PM conversion due to link nonlinearities, and possible vibration effects. All of these phase noise components degrade carrier-tracking-loop performance, and those which are not tracked by the loop(s) have an additional harmful effect on overall system error probability performance.

To assess the effect of phase noise on the performance of an actual payload/Orbiter link, the link between the IUS transponders and the Orbiter PI was analyzed. Figure 4.1 presents a simple block diagram of the IUS/Orbiter communication link. Regardless of the analysis technique employed, the first step in assessing tracking-loop and bit error performance degradations due to phase noise effects is to introduce appropriate mathematical models for the carrier (discrete or suppressed) tracking loop(s) which include the various sources of phase noise referred to above. These models ordinarily take the form of equivalent linear loop block diagrams with phase noise sources described by power spectral densities characterized by inverse power law behavior as a function of frequency away from some nominal value. A complete discussion of the various phase and frequency instabilities present in precision frequency sources, along with their characterization, is given in [1]. For our purposes, it is convenient (as was done in [2]) to represent the equivalent two-sided lowpass power spectral density $S_{\psi}(f)$ of the various phase noise instabilities by the (inverse) power series*

$$S_{\psi}(f) = \sum_{k=0}^3 \frac{h_k}{|f|^k} \quad (1)$$

*We shall ignore any discrete frequency components in the spectrum such as those caused by spurs or vibration effects.

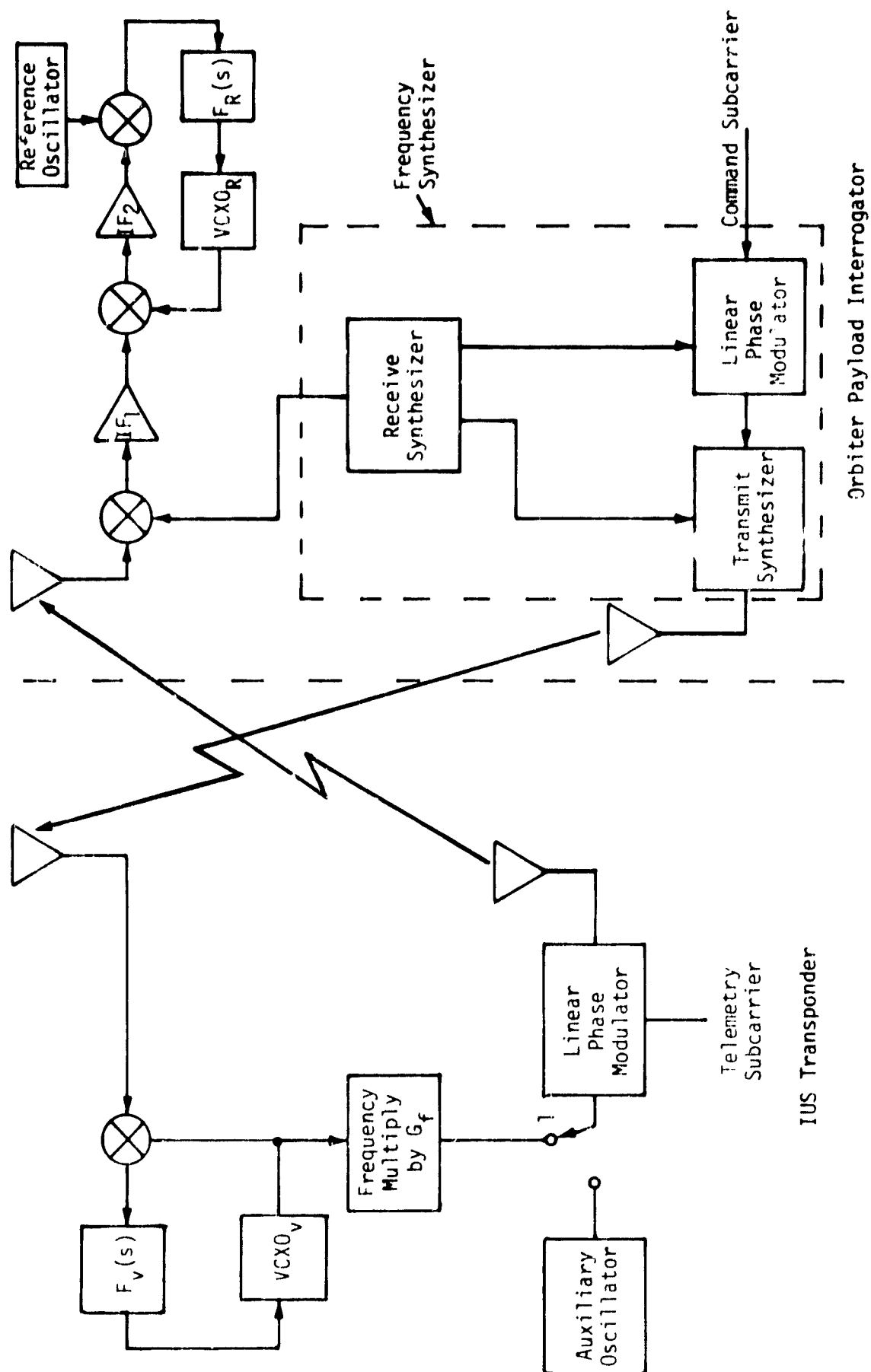


Figure 4.1. A Simple Block Diagram of the IUS/Orbiter Two-Way Coherent Communication System

The $|f|^0$ term corresponds to white phase noise, $|f|^{-1}$ corresponds to flicker phase noise, $|f|^{-2}$ corresponds to white frequency noise, and $|f|^{-3}$ corresponds to flicker frequency noise.

An equivalent linear baseband model of the IUS/Orbiter communication link, including various phase noise sources, is illustrated in Figure 4.2. To define the effect of phase noise on performance, the phase noise spectrum $\phi_e(s)$ at the PI receiver must be evaluated based on the VCO, VCXO and TCXO phase noise processes, entering in both the PI and IUS transponder. In the following discussion, K_{PI} , K_{IUS} , G_f , K_1 , D , N , E and F represent constants. All other parameters represent either Laplace transforms or transfer functions, whichever is evident from Figure 4.2, with the variable s being suppressed. First consider the PI receiver.

4.1 PI Phase Noise Spectral Characteristics

From Figure 4.2, it follows that

$$\phi_e = \phi_1 - \theta_{r2} \quad (2)$$

where, from Appendix I,

$$\phi_1 = \frac{G_3 G_4 (\theta_{IUS} - \theta_{RX}) - \left[10 \psi_{PI} - 10 \frac{K_{PI} F_{PI} \theta_{r2}}{s} \right] G_4}{1 + \frac{10 G_4 F_{PI} K_{PI}}{s}} \quad (3)$$

combining (2) and (3) and defining

$$H_{PI} = \frac{10 K_{PI} F_{PI}(s)}{s + 10 K_{PI} F_{PI}(s)} \quad (4)$$

then (2) simplifies to

$$\phi_e = (\theta_{IUS} - \theta_{RX}) G_3 G_4 (1 - H_{PI}) - 10 \psi_{PI} G_4 (1 - H_{PI}) - \theta_{r2} (1 - H_{PI}) \quad (5)$$

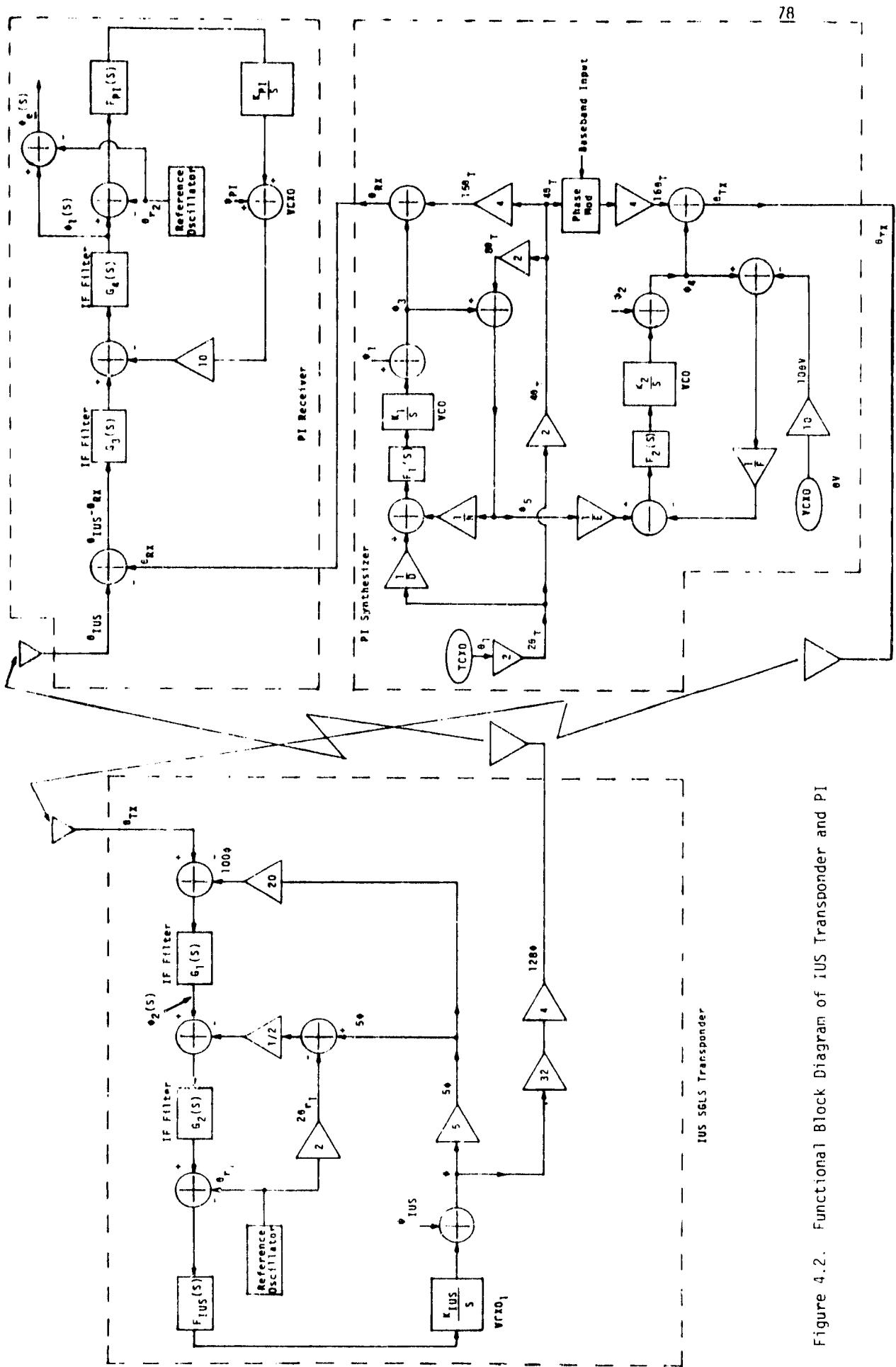


Figure 4.2. Functional Block Diagram of IUS Transponder and PI

where $G_4(s)$ has been assumed to be much wider than the loop filter $F_{PI}(s)$. That is, $G_4(s)$ bandwidth is of the order of megahertz, while the loop filter bandwidth is of the order of kilohertz. Therefore, whenever the product $G_4(s)F_{PI}(s)$ appears, it is assumed to be equal to $F_{PI}(s)$.

The PI synthesizer phase noise outputs denoted by θ_{RX} and θ_{TX} in Figure 4.2 are found in Appendix I to be given by

$$\theta_{RX} = \psi_1 (1 - H_1) + 2 \left[8 + \left(\frac{N}{D} + 4 \right) H_1 \right] \theta_T \quad (6)$$

where H_1 is defined as

$$H_1 = \frac{K_1 F_1(s)/N}{s + K_1 F_1(s)/N} \quad (7)$$

Similarly,

$$\begin{aligned} \theta_{TX} = & \psi_2 (1 - H_2) + \left(\frac{F}{E} \right) H_2 (1 - H_1) \psi_1 + 10 H_2 \theta_v \\ & + 2 \left[8 + \left(\frac{F}{E} \right) H_2 \left[\frac{N}{D} H_1 - 4 (1 - H_1) \right] \right] \theta_T \end{aligned} \quad (8)$$

where H_2 is defined as

$$H_2 = \frac{K_2 F_2(s)/F}{s + K_2 F_2(s)/F} \quad (9)$$

Note that ψ_1 and θ_T are common to the phase noise expressions of both θ_{RX} and θ_{TX} . In a two-way communication system, the question can be asked: when is the transmitted phase noise correlated with the receiver phase noise? If the round-trip time delay is short enough, then the same phase noise components ψ_1 and θ_T appear in the expression of θ_{RX} and θ_{TX} . Alternatively, if the round-trip time delay is long enough, then denote ψ_1^T and θ_T^T for the transmitted phase noise and ψ_1^R and θ_T^R for the received phase noise. For this case, ψ_1^T is assumed independent of ψ_1^R and, similarly, θ_T^T is assumed independent of θ_T^R . Therefore, in this case,

$$\theta_{RX} = \psi_1^R (1 - H_1) + 2 \left[8 + \left(\frac{N}{D} + 4 \right) H_1 \right] \theta_T^R \quad (10)$$

and

$$\begin{aligned} \theta_{TX} = & \psi_2 (1 - H_2) + \left(\frac{F}{E} \right) H_2 (1 - H_1) \psi_1^T + 10 H_2 \theta_V \\ & + 2 \left[8 + \left(\frac{F}{E} \right) H_2 \left[\left(\frac{N}{D} \right) H_1 - 4 (1 - H_1) \right] \right] \theta_T^T \end{aligned} \quad (11)$$

The frequency division constants E, F, N and D of Figure 4.2 and (6), (8), (10) and (11) depend on the operating mode of the vehicle transponder (IUS) and the channel number, CN, assigned to the particular frequency selected in the frequency band corresponding to this mode, as shown in Table 4.1 below.

Table 4.1. PI Frequency Division Constants

Frequency Division Multiple	STDN	DSN	SGI S
E	240	240	256
F	222	221	205
N	CN + 519	CN - 431	40CN - 35460
D	1280	432	1280
CN	1 - 808	850 - 882	900 - 919
G_f	240/222	240/221	256/205

From Table 4.1, note that, for all three modes,

$$G_f \left(\frac{F}{E} \right) = 1 \quad (12)$$

Also, the worst-case (largest) phase error would occur for the maximum value of N which corresponds to the highest channel number. Thus,

$$G_f\left(\frac{FN_{\max}}{DE}\right) = \frac{N_{\max}}{D} = \begin{cases} \left(\frac{1372}{1280}\right) = 1.0367 & \text{STDN} \\ \left(\frac{451}{432}\right) = 1.044 & \text{DSN} \\ \left(\frac{1300}{1280}\right) = 1.0156 & \text{SGLS} \end{cases} \quad (13)$$

To determine the phase noise spectrum of θ_{RX} and θ_{TX} , it is necessary to determine the phase noise spectrum of ψ_1 , ψ_2 , θ_v and θ_i . The TCXO phase noise θ_T has a spectrum shown in Figure 4.3. The spectrum S_{TX} of the phase noise θ_{TX} was measured by TRW in the SGLS mode and is shown in Figure 4.4. Both TRW and Axiomatix integrated the spectrum S_{TX} to determine the total number of degrees of phase noise. The TRW and Axiomatix integrations for the piecewise linear PI transmitter synthesizer output spectrum were checked and both were found to be correct. The difference between these results lies in the assumed models, as illustrated in Figure 4.5. For example, the area $TRW_I = 2.25 \times 10^{-3}$ while $AXIOM_I = 1.29 \times 10^{-3}$, and $TRW_{II} = 2.5 \times 10^{-3}$ while $AXIOM_{II} = 0.8 \times 10^{-3}$. Hence, the difference between total $\sigma_\phi = (3.94^\circ)_{TRW}$ versus $(2.62^\circ)_{AXIOM}$ is attributed to the difference approximations of the same spectrum.

The Axiomatix model was based on the phase noise spectrum shown in Figure 4.4, which is 3 dB lower than that currently used by TRW. If these 3 dB are added back to the Axiomatix model, the integrated total deviation will be $2.62 \times \sqrt{2} = 3.7^\circ$, which closely approximates the 3.9° of the TRW calculations. In the following discussion, we show the calculations which lead to the 2.62° number (prior to adding the 3 dB).

For the region $30 \text{ Hz} < f < 800 \text{ Hz}$ shown in Figure 4.6,

$$S_{TX}(f) = \frac{C_L}{f^{1/2}} \quad (14)$$

or -5 dB/decade slope. For the region $800 \text{ Hz} < f < 2 \text{ MHz}$,

$$S_{TX}(f) = \frac{C_2}{f^2} \quad (15)$$

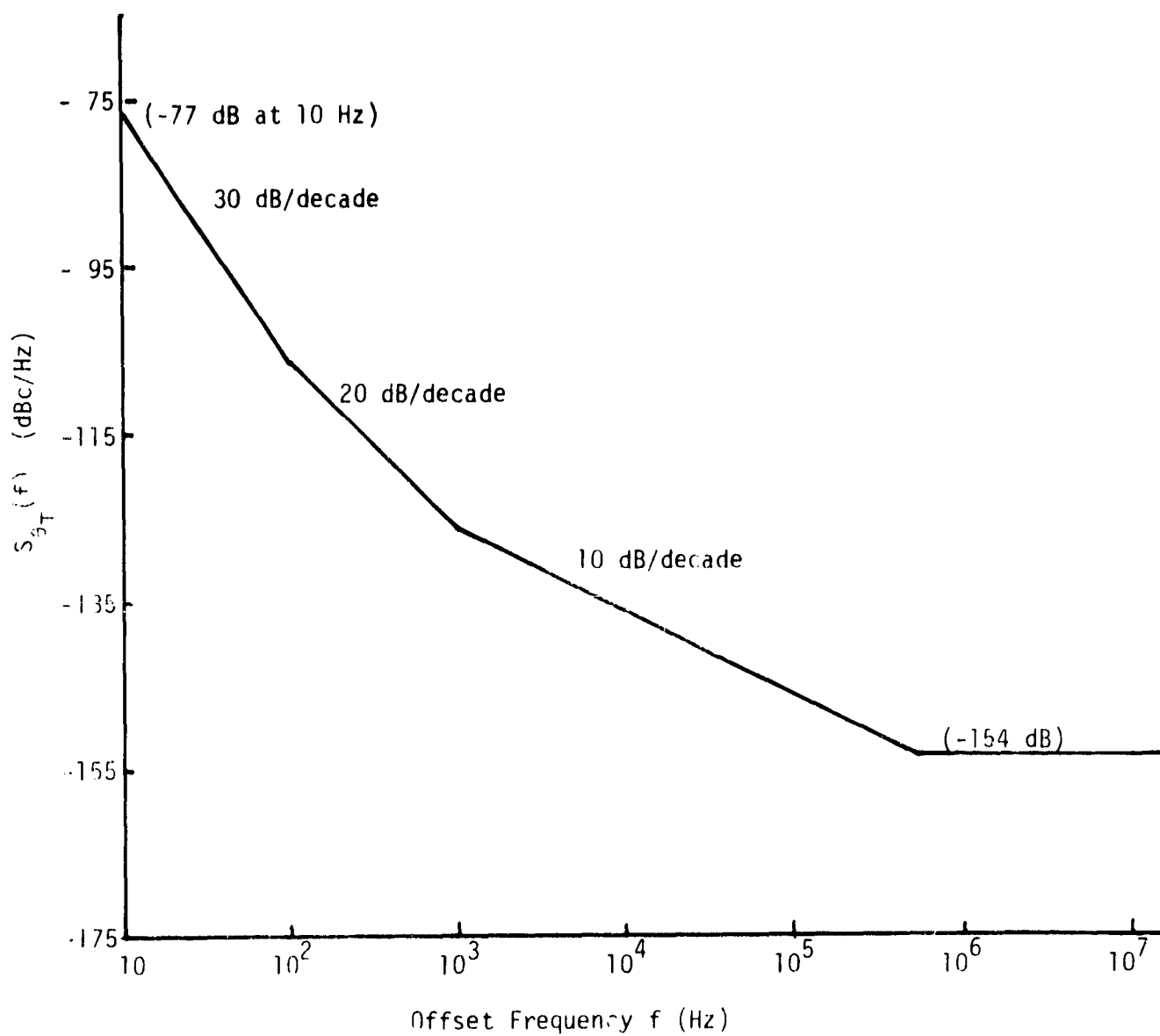


Figure 4.3. Phase Noise Spectrum of the PI TCX0

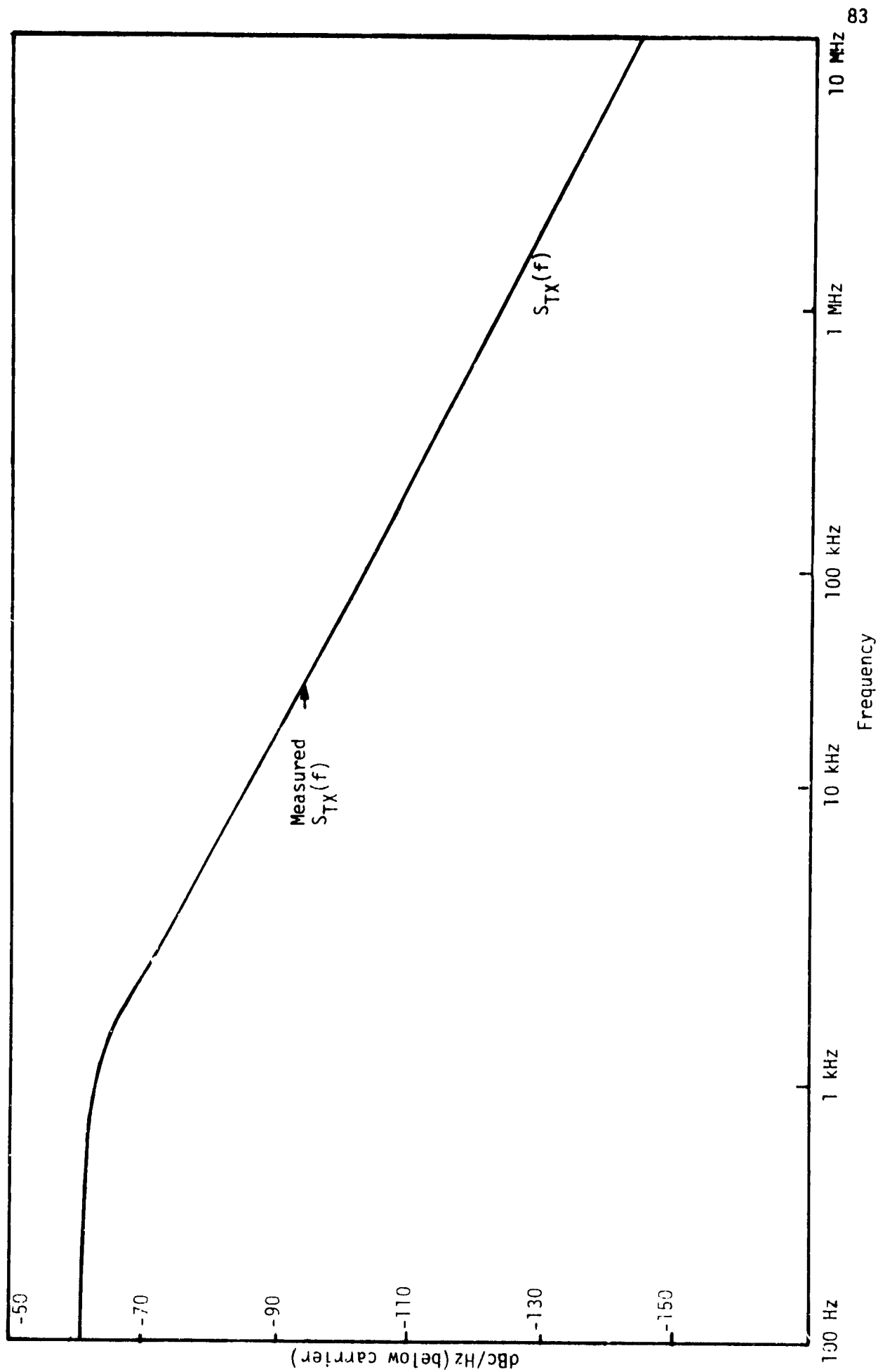


Figure 4.4. Measured Transmitter Single-Sided Phase Noise Spectral Density

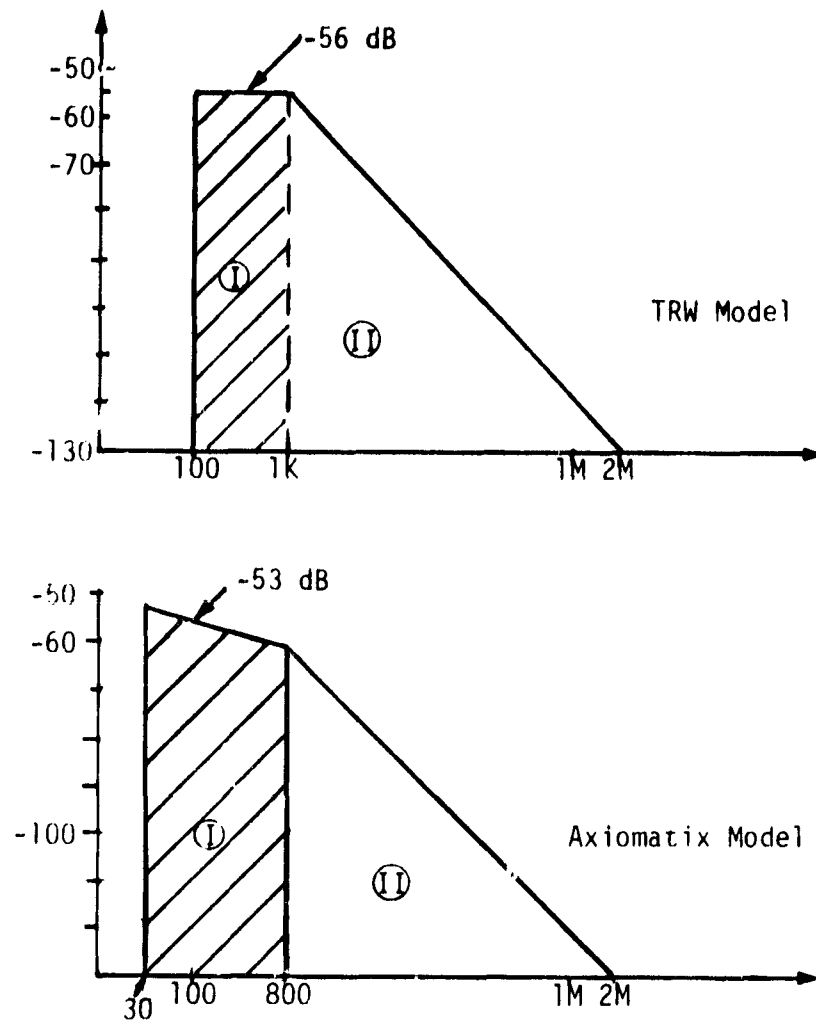


Figure 4.5. Approximations to the Measured Transmitter Single-Sided Phase Noise Spectral Density

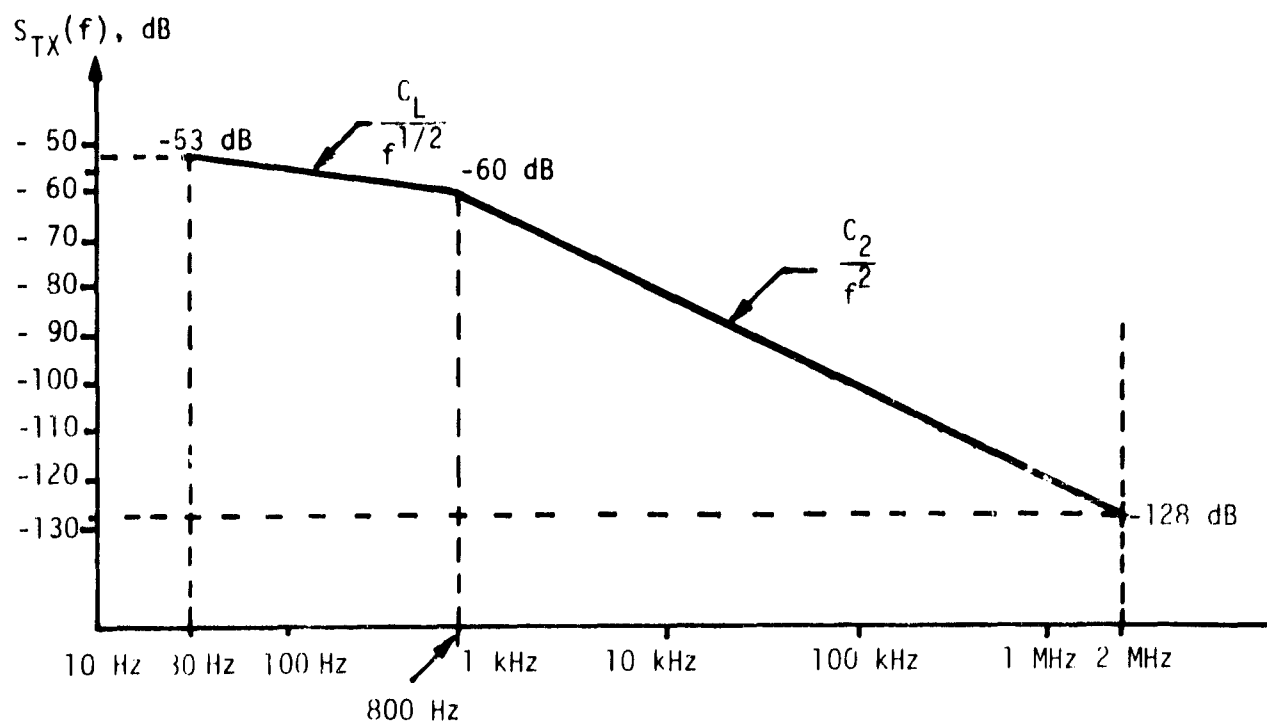


Figure 4.6. Aximatrix Approximation for the Transmitter Phase Noise Spectral Density

or -20 dB/decade slope. Constants C_1 and C_2 are adjusted such that

$$S_{TX}(30) = \frac{C_1}{\sqrt{30}} = -53 \text{ dB} = 10^{-5.3} \Rightarrow C_1 = 2.83 \times 10^{-5} \quad (16)$$

and

$$S_{TX}(800) = \frac{C_2}{(800)^2} = -60 \text{ dB} = 10^{-6} \Rightarrow C_2 = 6.4 \times 10^{-1} \quad (17)$$

Then,

$$\begin{aligned} \sigma_{TX}^2 &= \int_{30 \text{ Hz}}^{2 \text{ MHz}} S(f) df = C_1 \int_{30}^{800} \frac{df}{\sqrt{f}} + C_2 \int_{800}^{2 \times 10^6} \frac{df}{f^2} \\ &= C_1 \left[\sqrt{800} - \sqrt{30} \right] + C_2 \left[\frac{1}{800} - \frac{1}{2 \times 10^6} \right] \\ &= \underbrace{2 \times 2.83 \times 10^{-5} \left[\sqrt{800} - \sqrt{30} \right]}_{1.29 \times 10^{-3}} + \underbrace{6.4 \times 10^{-1} \left[\frac{1}{800} - \frac{1}{2 \times 10^6} \right]}_{8 \times 10^{-4}} \quad (18) \end{aligned}$$

or

$$\begin{aligned} \sigma_{TX}^2 &= 2.09 \times 10^{-3} \Rightarrow \sigma_{TX} = 4.57 \times 10^{-2} \text{ rad} \\ &= \left[\sigma_{TX} = 2.62^\circ \right] \quad (19) \end{aligned}$$

The spectrum of the phase noise processes ψ_1 and ψ_2 can be determined from S_{TX} if it is assumed that ψ_1 and ψ_2 possess the spectral density $S_{II}(f)$ and if $S_{\theta_V} = 0$ and $S_{\theta_T}(f) = 0$ (i.e., their contribution is negligible). The assumption concerning $S_{\theta_T}(f)$ can be verified by comparing Figure 4.3 with Figure 4.4 or 4.6. The spectrum of θ_V is a VCXO spectrum, as shown in Figure 4.7. Note that the VCXO phase noise spectrum $S_I(f)$ was measured at 2211 MHz, while θ_V is at 68 MHz. Therefore,

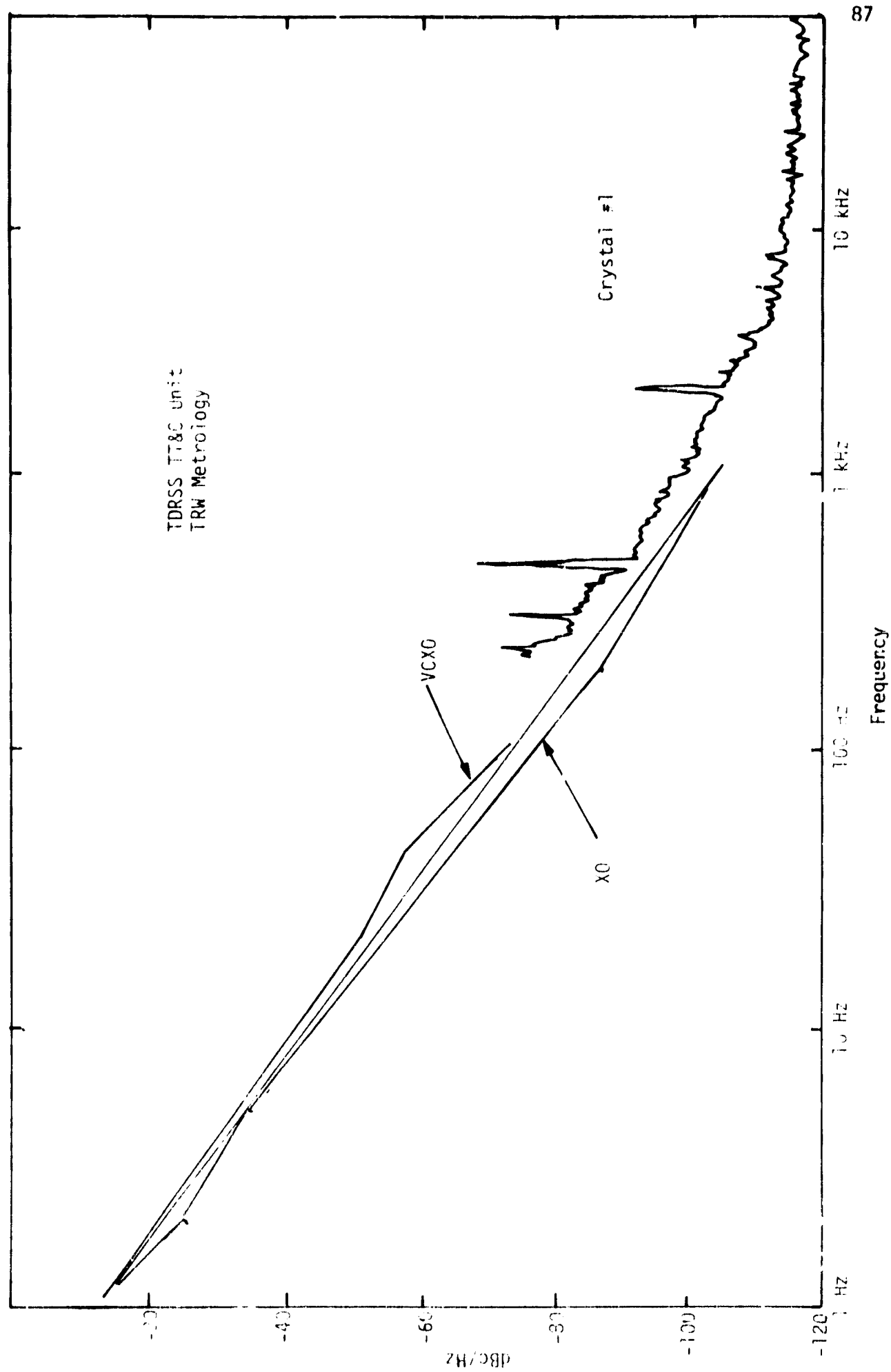


Figure 4.7. VCXO Measured Phase Noise Power Spectral Density

$$S_{\theta_V}(f) = \left(\frac{68}{2277}\right)^2 S_I(f) \quad (20)$$

Comparing $S_I(f)$ in Figure 4.7, including the factor to convert to θ_V , with Figure 4.4 or 4.6 shows that $S_{\theta_V}(f)$ can be considered negligible with respect to $S_{TX}(f)$. With S_{θ_V} and S_{θ_T} neglected, then from (11),

$$S_{TX}(f) = S_{\psi_2}(f) |1 - H_2(f)|^2 + S_{\psi_1}(f) |1 - H_1(f)|^2 |H_2(f)|^2 \left(\frac{F}{E}\right)^2 \quad (21)$$

Letting

$$S_{II}(f) = S_{\psi_1}(f) + S_{\psi_2}(f) \quad (22)$$

and from noting that

$$|H_2|^2 = \frac{f_{n_2}^2 (f_{n_2}^2 + r_2 f^2)}{f^4 + R_2 f_{n_2}^2 f^2 + f_{n_2}^4} \quad (23)$$

and

$$|1 - H_i|^2 = \frac{f^4}{f^4 + R_i f_{n_i}^2 f^2 + f_{n_i}^4} \quad ; \quad i=1,2 \quad (24)$$

where $R_1 = r_1^2 + 2$ and $r_i = 4r_i^2$. Then,

$$S_{II}(f) = \frac{S_{TX}(f)}{T(f)} \quad (25)$$

where

$$\begin{aligned}
 T(f) &= \left(\frac{F}{E}\right)^2 |1 - H_1|^2 |H_2|^2 + |1 - H_2|^2 \\
 &= \left(\frac{F}{E}\right)^2 \left(\frac{f^4}{f^4 + R_1 f_{n_1}^2 f^2 + f_{n_1}^4} \right) \left(\frac{f_{n_2}^2 (f_{n_2}^2 + r_2 f^2)}{f^4 + R_2 f_{n_2}^2 f^2 + f_{n_2}^4} \right) + \left(\frac{f^4}{f^4 + R_2 f_{n_2}^2 f^2 + f_{n_2}^4} \right) \quad (26)
 \end{aligned}$$

Simplifying,

$$\begin{aligned}
 T(f) &= \frac{f^8 + \left(r_2 \left(\frac{F}{E}\right)^2 f_{n_2}^2 + R_1 f_{n_1}^2 \right) f^6 + \left(\left(\frac{F}{E}\right)^2 f_{n_2}^4 + f_{n_1}^4 \right) f^4}{f^8 + \left(R_1 f_{n_1}^2 + R_2 f_{n_2}^2 \right) f^6 + \left(f_{n_1}^4 + f_{n_2}^4 + R_1 R_2 f_{n_1}^2 f_{n_2}^2 \right) f^4 + f_{n_1}^4 f_{n_2}^4} \quad (27)
 \end{aligned}$$

The transfer function parameters (natural frequency f_n , damping factor ζ) which were used in the computation of the integrals are given in Table 4.2. Using (27) and Figure 4.4, the spectrum $S_{11}(f)$ is found for the SGLS mode and is presented in Figure 4.8.

Table 4.2. PI Transfer Function Parameters

Parameters \ H	H_{PI}	$H_{1\text{ synthesizer}}$	$H_{2\text{ synthesizer}}$
f_n (Hz)	328	1000	560
ζ	0.82	1.0	5.0

Returning to (5), the remaining phase noise spectrum associated with the PI are ψ_{PI} , which is the VCXO phase noise process, and θ_{r2} , a local oscillator phase noise process. The spectra of ψ_{PI} and θ_{r2} are the same (VCXO spectrum) as those given in Figure 4.7. Since the spectrum in Figure 4.7, $S_1(f)$, is measured with respect to a 2211 MHz carrier and ψ_{PI} is measured at 1.84 MHz, then

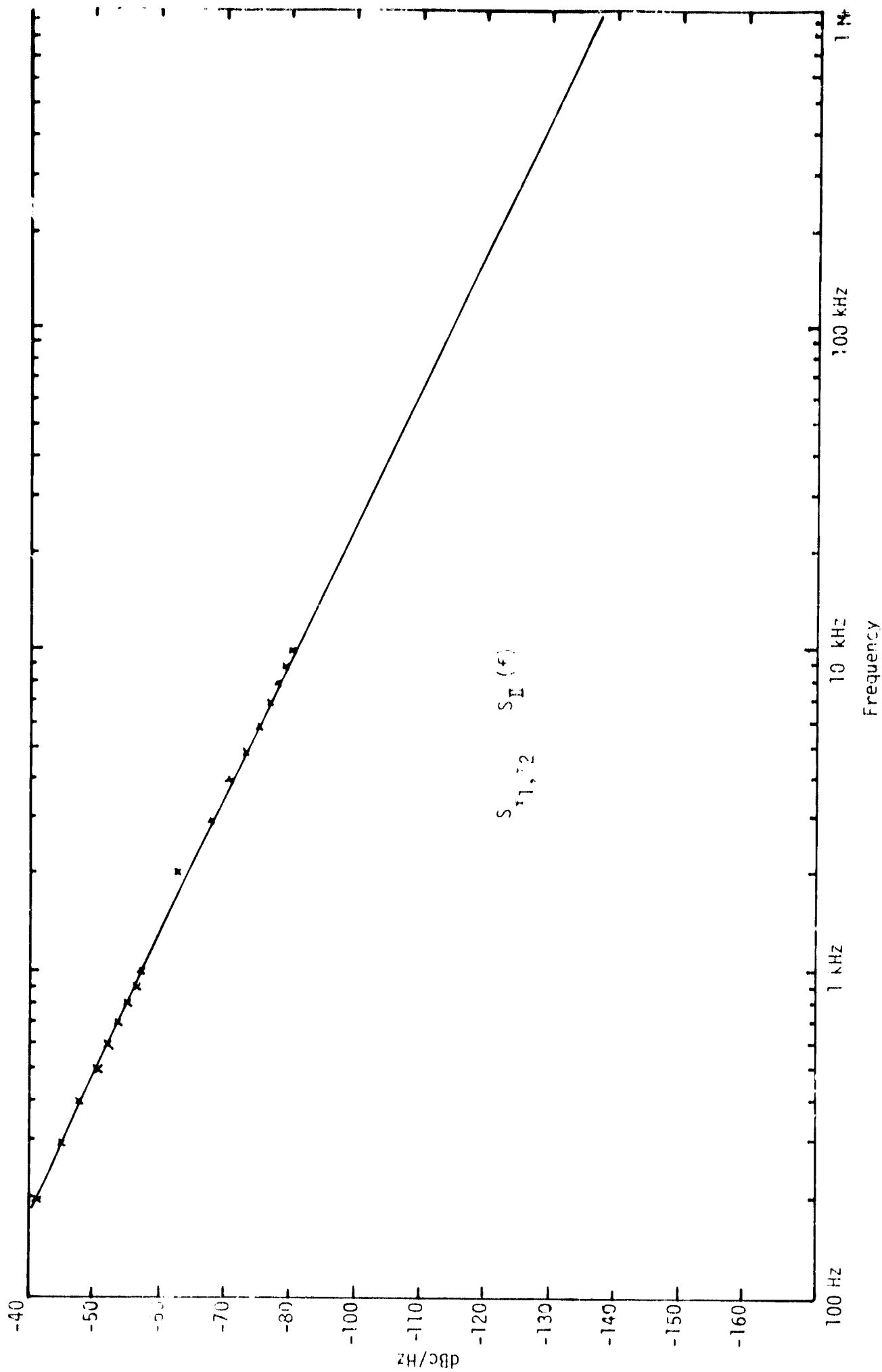


Figure 4.8. VCO Phase Noise Power Spectra after Filter Extraction

$$S_{10_{\psi_{PI}}}(f) = \left(\frac{18.4}{2211} \right)^2 S_I(f) \quad (28)$$

Similarly, since θ_{r_2} is measured at 31 MHz, then

$$S_{\theta_{r_2}}(f) = \left(\frac{31}{2211} \right)^2 S_I(f) \quad (29)$$

4.2 IUS Transponder Phase Noise Spectral Characteristics

The functional block diagram of the IUS transponder in terms of phase noise is presented in Figure 4.2. Note that the output phase noise of the IUS transponder is

$$\theta_{IUS} = 128\phi \quad (30)$$

Therefore, the spectrum of ϕ must be determined. From Appendix I,

$$\phi \left[1 + \frac{s}{2} \frac{K_{IUS} F_{IUS} G_2}{s} \right] = \psi_{IUS} + \frac{K_{IUS} F_{IUS} G_2 \phi_2}{s} + \frac{(G_2 - 1) K_{IUS} F_{IUS}}{s} \theta_{r_1} \quad (31)$$

Assuming that the bandwidth of G_2 is much greater than the bandwidth of F_{IUS} , then the product $F_{IUS} G_2$ simplifies to F_{IUS} . Also, within the bandwidth of F_{IUS} , the difference $G_2 - 1$ is zero for all s . Hence,

$$\phi \left[1 + \frac{s}{2} \frac{K_{IUS} F_{IUS}}{s} \right] = \psi_{IUS} + \frac{K_{IUS} F_{IUS}}{s} \phi_2 \quad (32)$$

From Figure 4.2, note that

$$\phi_2 = G_1 \left| \theta_{TX} - 100\phi \right| \quad (33)$$

Combining (32) and (33),

C - 2

$$\Phi \left[1 + \frac{5}{2} \frac{K_{IUS} \psi_{IUS}}{s} + \frac{100 G_1 K_{IUS} F_{IUS}}{s} \right] = \psi_{IUS} + \frac{G_1 K_{IUS} F_{IUS}}{s} \theta_{TX} \quad (34)$$

Assuming that the bandwidth of G_1 is much greater than the bandwidth of F_{IUS} , then the product $F_{IUS} G_1$ also simplifies to F_{IUS} . Therefore,

$$\Phi = \frac{s \psi_{IUS} + K_{IUS} F_{IUS} \theta_{TX}}{s + 102.5 \frac{K_{IUS} F_{IUS}}{K_{IUS} F_{IUS}}} \quad (35)$$

Define H_{IUS} to be

$$H_{IUS} = \frac{102.5 \frac{K_{IUS} F_{IUS}}{K_{IUS} F_{IUS}}}{s + 102.5 \frac{K_{IUS} F_{IUS}}{K_{IUS} F_{IUS}}} \quad (36)$$

Thus,

$$\Phi = (1 - H_{IUS}) \psi_{IUS} + \frac{1}{102.5} H_{IUS} \theta_{TX} \quad (37)$$

The output phase noise, θ_{IUS} , for the IUS transponder is, from (30) and (37), given by

$$\theta_{IUS} = 128 \psi_{IUS} (1 - H_{IUS}) + G_f H_{IUS} \theta_{TX} \quad (38)$$

where G_f is the coherent turnaround ratio for the SGLS mode given in Table 4.1 to be

$$G_f = \frac{256}{205} \quad (39)$$

The spectrum of the phase noise process θ_{TX} was determined in the previous section. The phase noise process ψ_{IUS} is due to a VCXO, so its spectrum can be from Figure 4.7. Since $128 \psi_{IUS}$ is measured at the same frequency as $S_I(f)$, then

$$S_{IUS}(f) = S_I(f) \quad (40)$$

To further define H_{IUS} , the transfer function can be written in terms of natural frequency and damping factor. Thus,

$$|H_{IUS}|^2 = \frac{f_n^2 (f_n^2 + 4\zeta^2 f^2)}{f^4 + (4\zeta^2 - 2)f_n^2 f^2 + f_n^4} \quad (41)$$

and

$$|1 - H_{IUS}|^2 = \frac{f^4}{f^4 + (4\zeta^2 - 2)f_n^2 f^2 + f_n^4} \quad (42)$$

For the IUS SGLS transponder,

$$\zeta = 0.707 \quad ; \quad f_n = 3774 \text{ Hz} \quad (43)$$

4.3 PI/IUS Two-Way Communication Phase Noise Spectral Characteristics

The PI/IUS two-way communication phase noise can be found by substituting into (5). For short round-trip time delay, the expressions for θ_{RX} and θ_{TX} are given by (6) and (8). Combining these results with (38) for the IUS transponder phase noise, the total two-way phase noise for short range is

$$\begin{aligned} \phi_e = & 128 \tilde{\psi}_{IUS}(1 - H_{IUS})(1 - H_{PI}) - 10 \tilde{\psi}_{PI}(1 - H_{PI}) - \theta_{r_2}(1 - H_{PI}) \\ & + G_f \psi_2 H_{IUS}(1 - H_2)(1 - H_{PI}) + 10 G_f \theta_v H_2 H_{IUS}(1 - H_{PI}) \\ & - \tilde{\psi}_1 [1 - H_2 H_{IUS}] (1 - H_1)(1 - H_{PI}) \\ & - 2\tilde{\theta}_T \left[8 + 4 H_2 H_{IUS} - 8 G_f H_{IUS} - \left(\frac{N}{D} + 4 \right) (H_{IUS} H_2 - 1) H_1 \right] (1 - H_{PI}) \end{aligned} \quad (44)$$

where the quantities with a \sim represent phase noise spectra that have been bandlimited by the 12 MHz IF bandwidth of the PI. Also, from (12), $G_f(F/E) = 1$, which has been used in (44) to simplify the result.

For the case of long round-trip time delay, the expressions for θ_{RX} and θ_{TX} are given by (10) and (11). The total two-way phase noise for long range is

$$\begin{aligned} \phi_e = & 128 \tilde{\psi}_{IUS}(1 - H_{IUS})(1 - H_{PI}) - 10 \tilde{\psi}_{PI}(1 - H_{PI}) - \theta_{r_2}(1 - H_{PI}) \\ & + G_f \psi_2 H_{IUS}(1 - H_2)(1 - H_{PI}) + 10 G_f \theta_v H_2(1 - H_{PI}) \\ & - \psi_1^T H_2 H_{IUS}(1 - H_1)(1 - H_{PI}) + 2\theta_T^T \left[8 G_f + H_2 \left(\frac{N}{D} H_1 - 4(1 - H_1) \right) \right] H_{IUS}(1 - H_{PI}) \\ & - \tilde{\psi}_1^R(1 - H_1)(1 - H_{PI}) - 2\theta_T^R \left[8 + \left(\frac{N}{D} + 4 \right) H_1 \right] (1 - H_{PI}) \end{aligned} \quad (45)$$

To evaluate the mean-square (variance) of the phase noise, note that

$$\sigma_\phi^2 = \frac{1}{2\pi j} \int_{-j\infty}^{j\infty} \overline{\phi_e(s) \phi_e(-s)} ds \quad (46)$$

where the overbar denotes statistical expectation. But,

$$S_\phi(s) = \overline{\phi_e(s) \phi_e(-s)} \quad (47)$$

denotes the power spectral density (in Laplace transform notation) of the phase noise process ϕ_e . Using (44) and the power spectral densities $S_{\theta_T}(f)$ in Figure 4.3, $S_I(f)$ in Figure 4.7 with the relationships of (20), (28) and (29), and $S_{II}(f)$ in Figure 4.8, then, for short range,

$$\begin{aligned}
S_{\phi} = S_I & \left\{ |1-H_{IUS}|^2 |1-H_{PI}|^2 + 2.658 \times 10^{-4} |1-H_{PI}|^2 + 9.46 \times 10^{-2} G_f^2 |H_2|^2 |H_{IUS}|^2 |1-H_{PI}|^2 \right\} \\
& + S_{II} \left\{ G_f^2 |H_{IUS}|^2 |1-H_2|^2 |1-H_{PI}|^2 + |1-H_2 H_{IUS}|^2 |1-H_1|^2 |1-H_{PI}|^2 \right\} \\
& + S_{\theta_T} \left\{ 256 |1-H_{PI}|^2 + 64 |H_2|^2 |H_{IUS}|^2 |1-H_{PI}|^2 + 2 G_f^2 |H_{IUS}|^2 |1-H_{PI}|^2 \right. \\
& \quad \left. + 4 \left(\frac{N}{D} + 4 \right)^2 |H_{IUS} H_2 - 1|^2 |H_1|^2 |1-H_{PI}|^2 \right\} \quad (48)
\end{aligned}$$

For long range, the expression for ϕ_e in (45) is used instead of (44) and the spectral density is given by

$$\begin{aligned}
S_{\phi} = S_I & \left\{ |1-H_{IUS}|^2 |1-H_{PI}|^2 + 2.658 \times 10^{-4} |1-H_{PI}|^2 + 9.46 \times 10^{-2} G_f^2 |H_2|^2 |H_{IUS}|^2 |1-H_{PI}|^2 \right\} \\
& + S_{II} \left\{ G_f^2 |H_{IUS}|^2 |1-H_2|^2 |1-H_{PI}|^2 + |H_2|^2 |H_{IUS}|^2 |1-H_1|^2 |1-H_{PI}|^2 + |1-H_1|^2 |1-H_{PI}|^2 \right\} \\
& + S_{\theta_T} \left\{ 256 G_f^2 + 4 \left(\frac{N}{D} \right)^2 |H_1|^2 |H_2|^2 |H_{IUS}|^2 |1-H_{PI}|^2 + 64 |1-H_1|^2 |H_2|^2 |H_{IUS}|^2 |1-H_{PI}|^2 \right. \\
& \quad \left. + 256 |1-H_{PI}|^2 + 4 \left(\frac{N}{D} + 4 \right)^2 |H_1|^2 |1-H_{PI}|^2 \right\} \quad (49)
\end{aligned}$$

In order to determine σ_{ϕ}^2 for short or long range, each term in (48) and (49) must be integrated as indicated by (46). Note that there are five different types of integrals to be evaluated. That is, there is an integration of: (1) a phase noise spectrum only, (2) a spectrum multiplied by a single transfer function, (3) a spectrum multiplied by two transfer functions, (4) a spectrum multiplied by three transfer functions, and (5) a spectrum multiplied by four transfer functions. The evaluation of each of these integral types has been derived and presented in Axiomatix Report R8005-3, "Shuttle Ku-Band and S-Band Communications Implementation Study," [3] for the case where the phase noise spectrum can be written in the form given in (1). Appendix II presents the spectrum of the TCXO and VCXO of Figures 4.3 and 4.7 in terms of a sum of the form

$$S_I(f) \cong 1.58 \times 10^{-12} - \frac{1.5 \times 10^{-8}}{f} + \frac{5.44 \times 10^{-5}}{f^2} + \frac{1.984 \times 10^{-2}}{f^3} \quad (50)$$

and

$$S_{\theta_T}(f) = 3.16 \times 10^{-16} + \frac{3.98 \times 10^{-10}}{f} - \frac{1.476 \times 10^{-8}}{f^2} + \frac{3.174 \times 10^{-4}}{f^3} \quad (51)$$

The spectrum of $S_{II}(f)$ presented in Figure 4.8 has the form

$$S_{II}(f) = \frac{0.5}{f^2} \quad (52)$$

The exact expressions for S_ϕ given in (48) and (49) could be used to evaluate σ_ϕ^2 by integrating from $-\infty$ to $+\infty$, but the evaluation of the integrals having products of three or four transfer functions are troublesome. In the evaluation of these integrals using the derivations in [3], a number of matrices must be employed. For the particular values of the spectra and transfer function parameters involved, the matrices are very "illconditioned." That is, the eigenvalues of the matrices differ by many orders of magnitude. To avoid this problem, note that, using Table 4.2 and (43), the integrals involving three or four transfer functions are upper bounded by the integration of the two-way integrals

$$\int_{-\infty}^{\infty} S_I(f) |H_{IUS}(f)|^2 |1 - H_{PI}(f)|^2 df \quad (53)$$

$$\int_{-\infty}^{\infty} S_{II}(f) |1 - H_I(f)|^2 |1 - H_{PI}(f)|^2 df \quad (54)$$

$$\int_{-\infty}^{\infty} S_{\theta_T}(f) |H_I(f)|^2 |1 - H_{PI}(f)|^2 df \quad (55)$$

and

$$\int_{-\infty}^{\infty} S_{\theta_T}(f) |1 - H_I(f)|^2 |1 - H_{PI}(f)|^2 df \quad (56)$$

With these approximations, the total phase noise contribution was

$$\sigma_{\phi} = 1.51^{\circ} \quad (57)$$

for short or long range, using (48) and (49), respectively. The value of σ_{ϕ} was found to be quite sensitive to the actual damping factors. Figure 4.9 shows the dependence of σ_{ϕ} on the parameter ζ_1 (damping factor for the transfer function H_1) with all other parameters kept constant.

4.4 Performance of PI in the Presence of Mismatched Wideband Detector Phase and Phase Noise

The PI, as discussed in subsection 3.2.4, employs a wideband phase detector outside of the phase-lock-loop (PLL) used to recover the carrier. Figure 4.10 shows the use of the wideband phase detector in a functional block diagram of that portion of the PI receiver. A narrow bandwidth crystal filter is used in front of the PLL. Hence, a phase-shift network must be used between the PLL and the wideband phase detector to compensate for an unwanted phase shift introduced by the crystal filter. Due to initial alignment and long-term drift, the phase-shift network introduces a constant mean phase offset at the wideband phase detector. This mean phase offset and phase noise variance due to the PI/IUS two-way communication cause a performance degradation of the data detector. Appendix III analyzes this performance degradation for data phase modulation directly onto the carrier and for data phase modulated onto a suppressed subcarrier.

For data phase-modulated directly onto the carrier, Appendix III obtains the average bit error probability \bar{P}_b by integrating the following expression:

$$\bar{P}_b = \frac{1}{2} \int_{-\infty}^{\infty} \frac{d\phi}{\sigma_{\phi} \sqrt{2\pi}} \exp \left\{ -\frac{(\phi - m_{\phi})^2}{2\sigma_{\phi}^2} \right\} \left[Q \left[\sqrt{\frac{2E_b}{N_0}} \cos \left(\phi + \frac{\pi}{2} - \beta \right) \right] + Q \left[\sqrt{\frac{2E_b}{N_0}} \cos \left(\phi - \frac{\pi}{2} + \beta \right) \right] \right] \quad (58)$$

where m_{ϕ} is the mean phase offset at the wideband phase detector, σ_{ϕ}^2 is phase noise variance and β is the angle modulation index given by

$$\beta = \cos^{-1} m \quad (59)$$

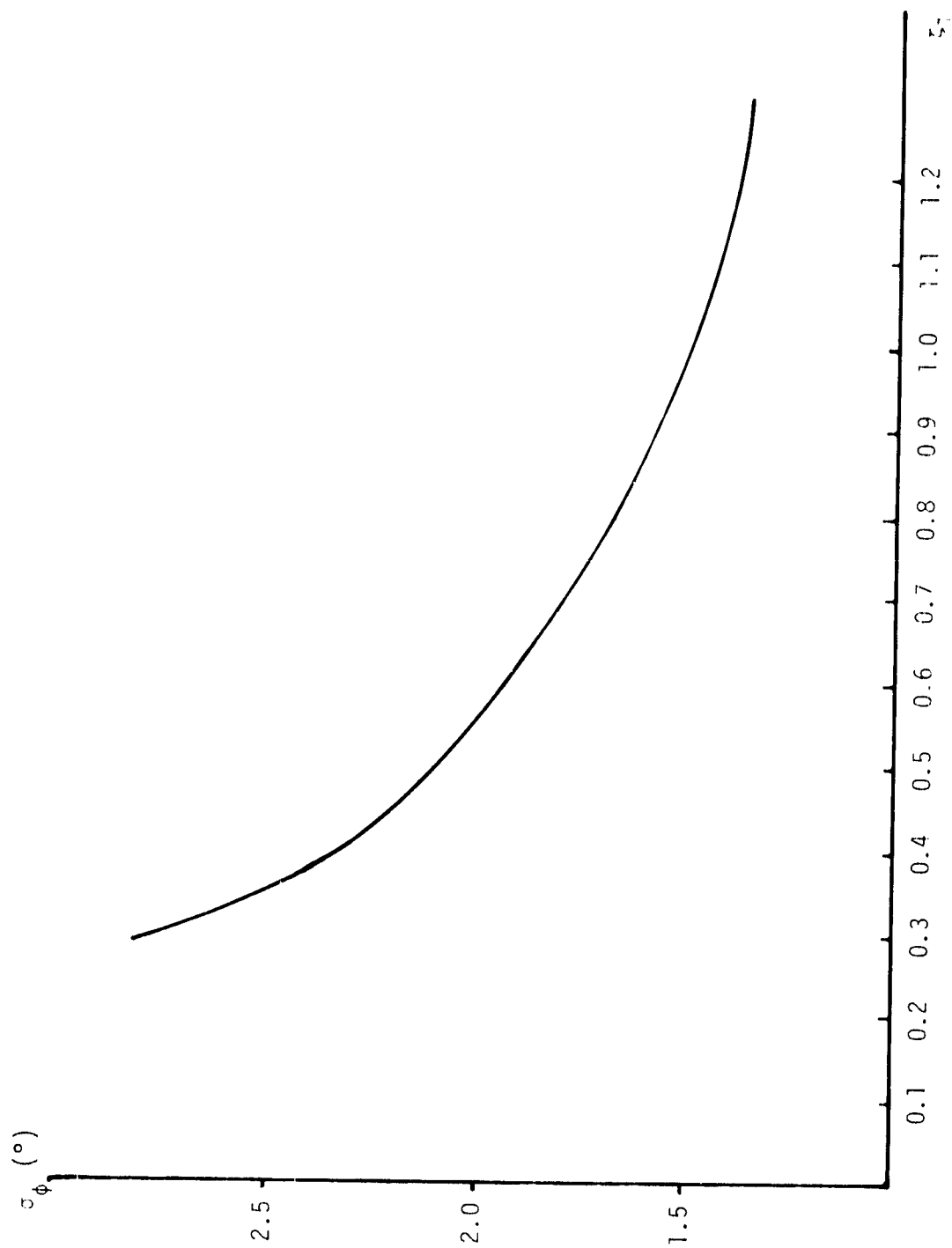


Figure 4.9. Total Standard Deviation σ_ϕ versus Damping Factor ζ_1

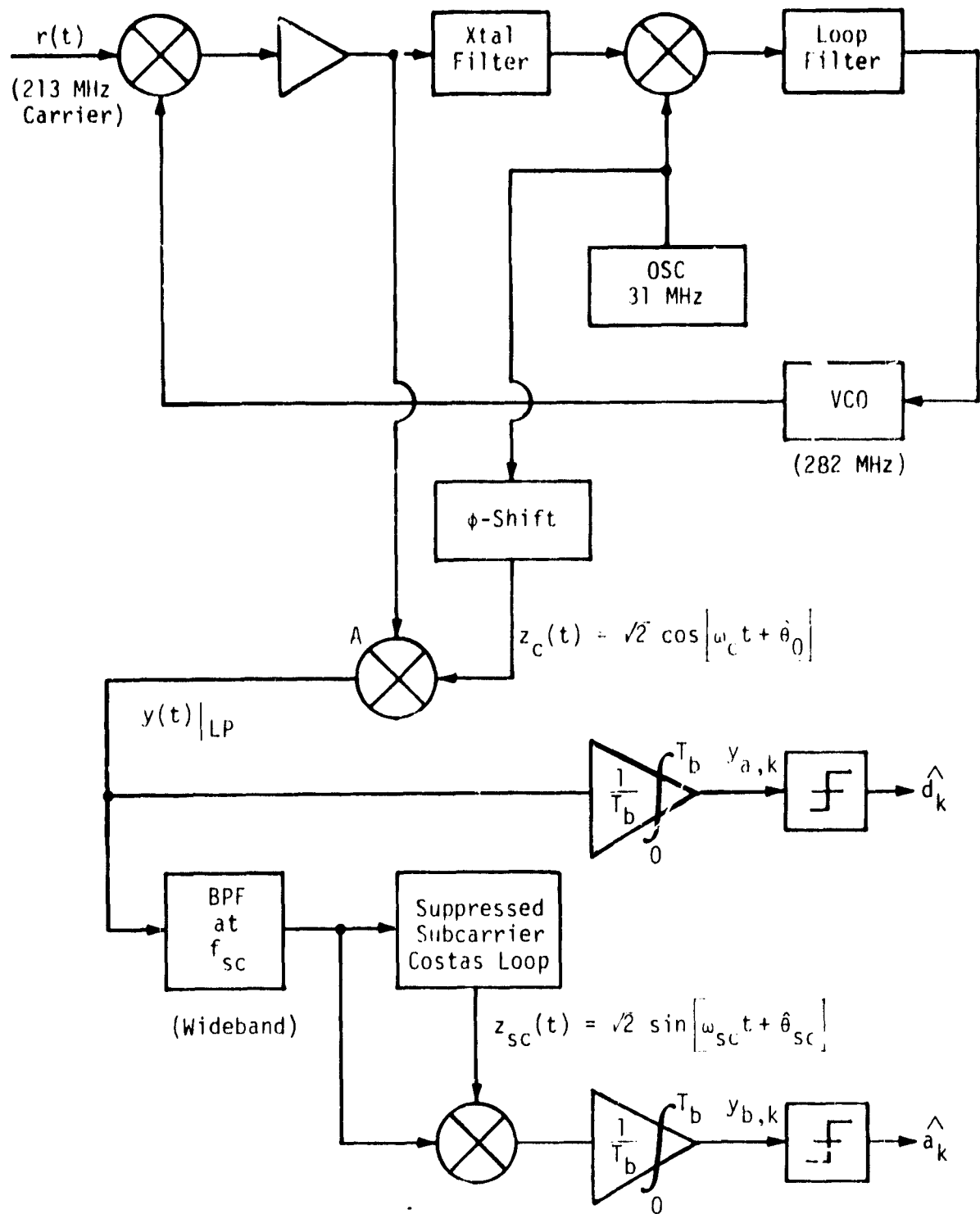


Figure 4.10. Functional Block Diagram of a PI Receiver with Wideband Phase Detector

with m equal to the modulation factor. Note that the nature of the phase noise process has been assumed to be Gaussian in (58).

With data phase modulated onto a suppressed subcarrier, Appendix III obtains the average bit error probability $P_{b,sc}$ for perfect subcarrier tracking by integrating the following expression:

$$\bar{P}_{b,sc} = \frac{1}{\sigma_{\phi_c} \sqrt{2\pi}} \int_{-\infty}^{\infty} Q \left[\sqrt{\frac{2E^*}{N_0}} \cos \phi_c \right] \exp \left\{ -\frac{\phi_c - m\phi_c^2}{2\sigma_{\phi_c}^2} \right\} d\phi_c \quad (60)$$

where ϕ_c is the carrier phase error including the phase offset $m\phi_c$ at the wideband phase detector and $\sigma_{\phi_c}^2$ is the sum of the variances of the phase noise and the PLL tracking error. Also,

$$E^* = E_b (1 - m^2) \quad (61)$$

where m is again the modulation factor. The assumption of perfect subcarrier tracking is very reasonable for the PSP design which, under worst-case conditions, exhibits only 0.8 dB* SNR performance degradation for the combined subcarrier and bit synchronizer tracking loops. In fact, the PSP degradation based on breadboard tests varies between 0.002 and 0.6 dB for most conditions.

The standard NASA and DOD modulation formats have data phase modulated onto a subcarrier. Therefore, to assess the performance degradation of the PI due to phase noise and phase offset at the wideband phase detector, the integration in (60) was carried out. Figures 4.11 through 4.13 present the bit error probability versus E_b/N_0 for various combinations of phase noise σ_ϕ and phase offset m_ϕ . Figure 4.11 illustrates the performance degradation as a function of σ_ϕ , with $m_\phi = 0$. Note that the performance degradation is small until $\sigma_\phi = 20^\circ$. In fact, at $\sigma_\phi = 20^\circ$, the performance degradation is beginning to get very large by $\bar{P}_b = 10^{-4}$. Figure 4.12 illustrates the performance degradation for $m_\phi = 5^\circ$ as a function of σ_ϕ . With $m_\phi = 5^\circ$, the performance degradation is about the same as $m_\phi = 20^\circ$ until $\sigma_\phi = 20^\circ$. Figure 4.13 illustrates the performance degradation for $m_\phi = 20^\circ$ as a function of σ_ϕ . With $m_\phi = 20^\circ$, $\sigma_\phi = 10^\circ$ shows

*Based on PSP breadboard measurements

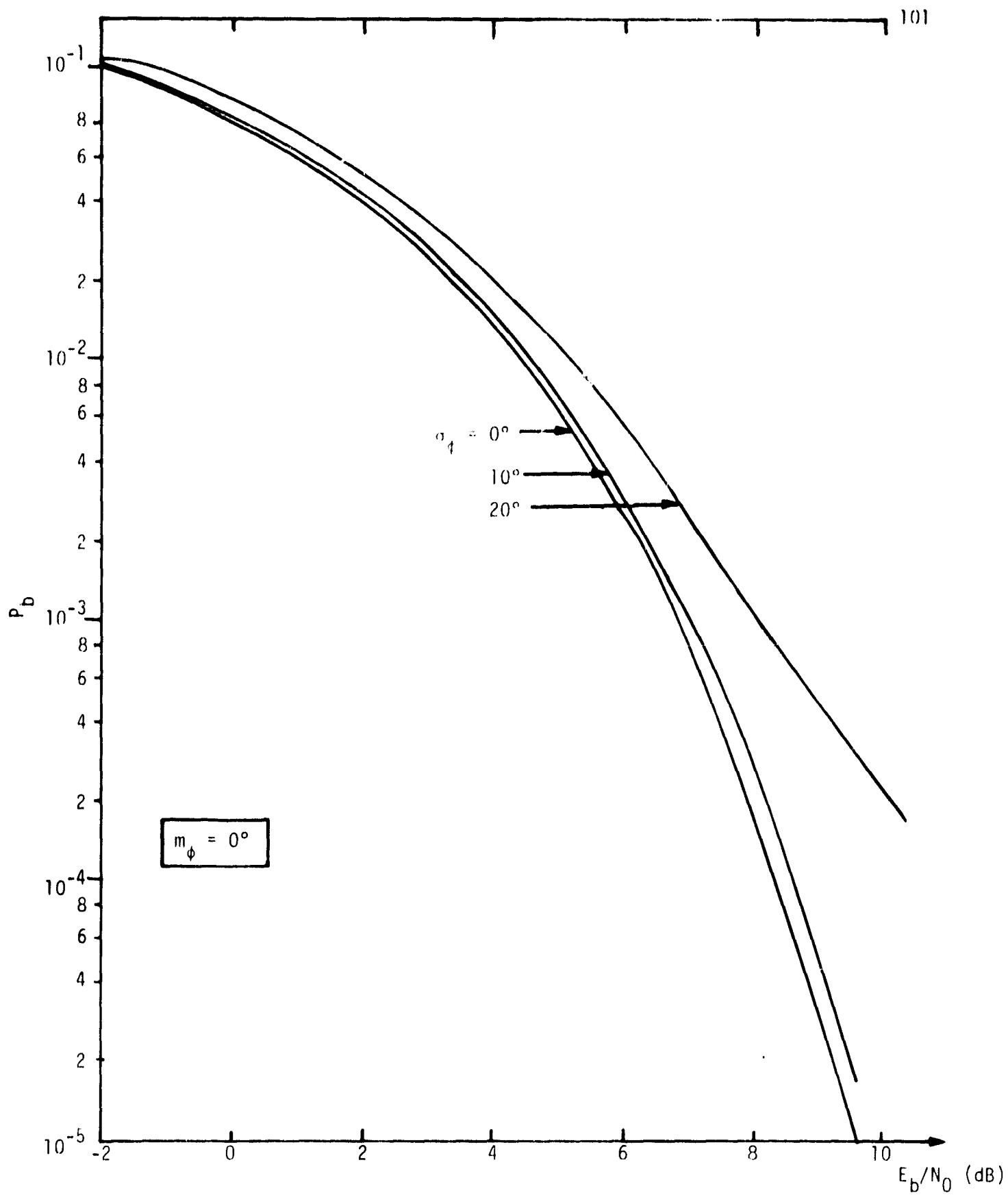


Figure 4.11. Bit Error Probability versus E_b/N_0 for No Phase Offset as a Function of Phase Noise

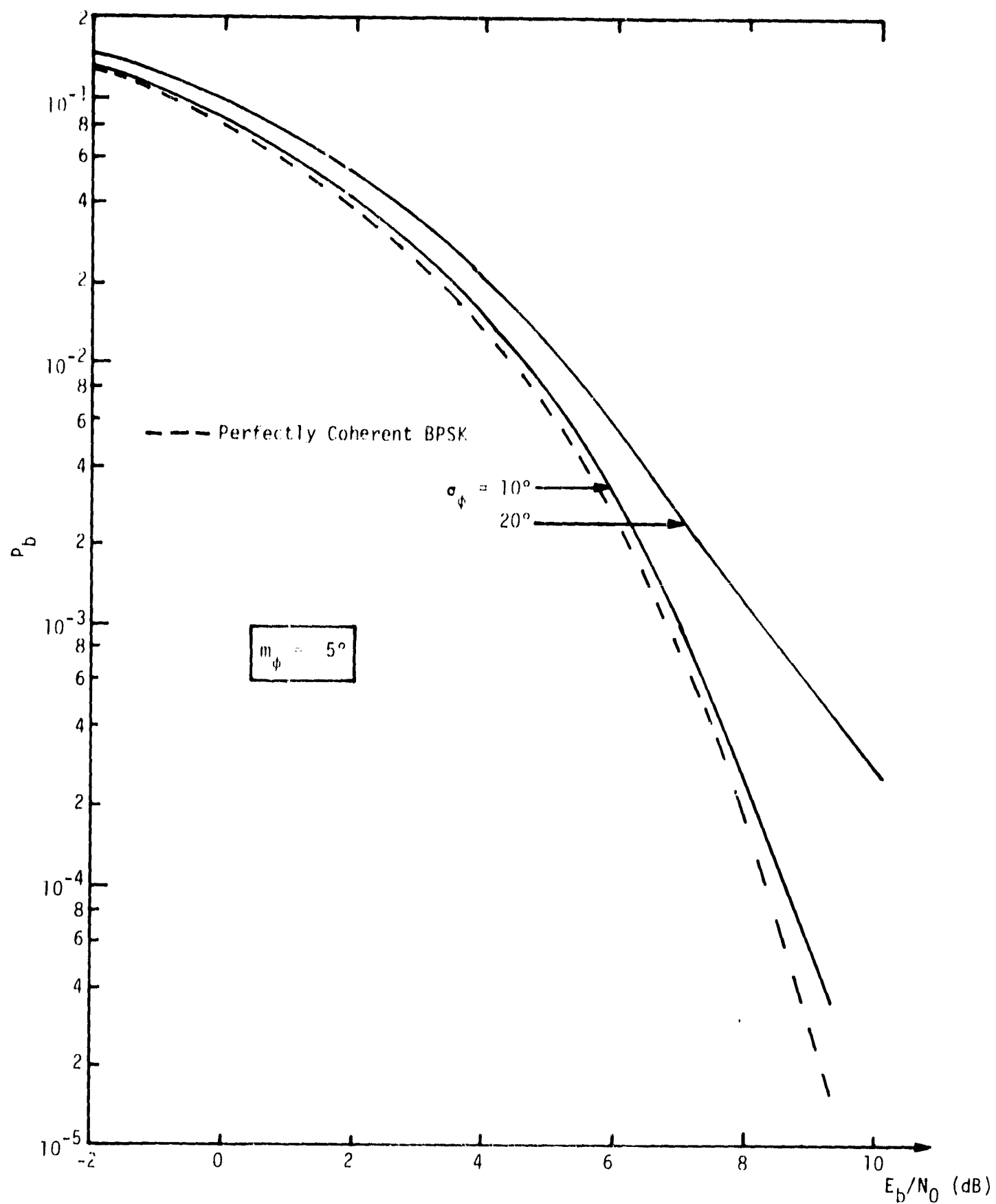


Figure 4.12. Bit Error Probability versus E_b/N_0 for 5° Phase Offset as a Function of Phase Noise

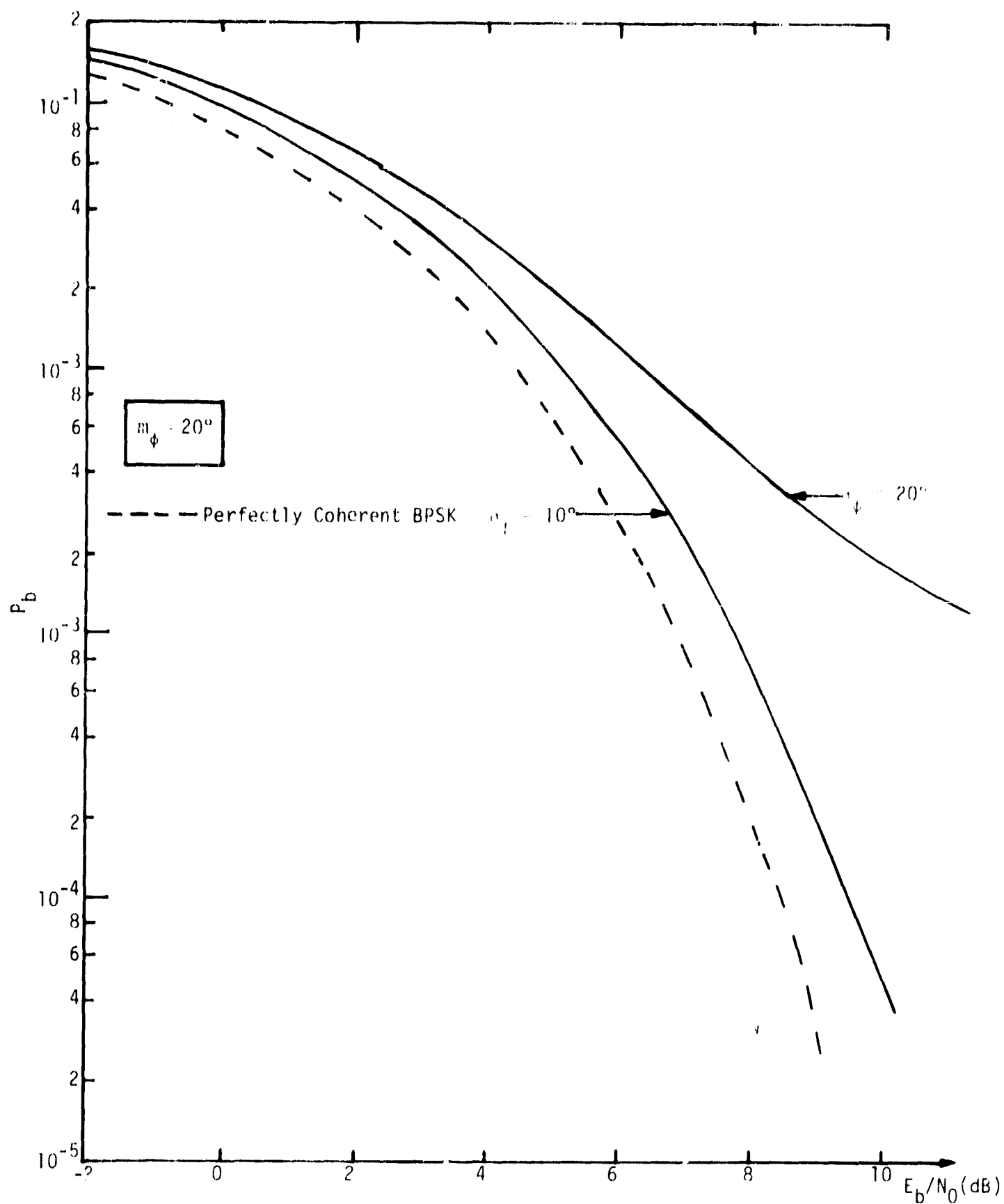


Figure 4.13. Bit Error Probability versus E_b/N_0 for 20° Phase Offset as a function of Phase Noise

significant performance degradation and $\sigma_\phi = 20^\circ$ shows an irreducible bit error probability of about 10^{-3} . That is, no matter how large E_b/N_0 becomes, the system bit error probability will not be less than 10^{-3} .

Figures 4.14 and 4.15 illustrate the performance degradation at a given bit error probability. Figure 4.14 plots performance degradation versus m_ϕ as a function of σ_ϕ . The performance degradation of Δ dB losses are the difference in decibels between the curves for the various values of m_ϕ and σ_ϕ in Figures 4.11 through 4.13 at $P_b = 10^{-3}$ and the theoretical curve for perfectly coherent BPSK. Note that, with $\sigma_\phi = 0^\circ$, the integral in (60) does not exist because the value of ϕ_c is a fixed deterministic number--not a random variable. In this case, the performance degradation from the theoretical curve for coherent BPSK is given by

$$\Delta \text{ dB} = 20 \log_{10}(\cos m_\phi) \quad (62)$$

At $\bar{P}_b = 10^{-3}$, the performance degradation rapidly becomes significant as m_ϕ and σ_ϕ become larger than 10° . Figure 4.15 plots the performance degradation versus σ_ϕ as a function of m_ϕ at $\bar{P}_b = 10^{-5}$. When σ_ϕ is greater than 15° , even with $m_\phi = 0^\circ$, the performance degradation is significant. For $m_\phi = 15^\circ$, the performance degradation rapidly becomes significant above $\sigma_\phi = 8^\circ$. The total allowed performance degradation for the PI at $\bar{P}_b = 10^{-5}$ is 2 dB. Table 4.3 presents some of the allowed values of m_ϕ and σ_ϕ if all the allowed 2 dB was used in accommodating the phase noise and phase offset at the wideband phase detector.

Table 4.3. Allowed Values of Phase Noise and Phase Offset for 2 dB Performance Degradation at $\bar{P}_b = 10^{-5}$

m_ϕ	σ_ϕ
0°	17.0°
10°	15.0°
15°	13.2°
20°	11.5°

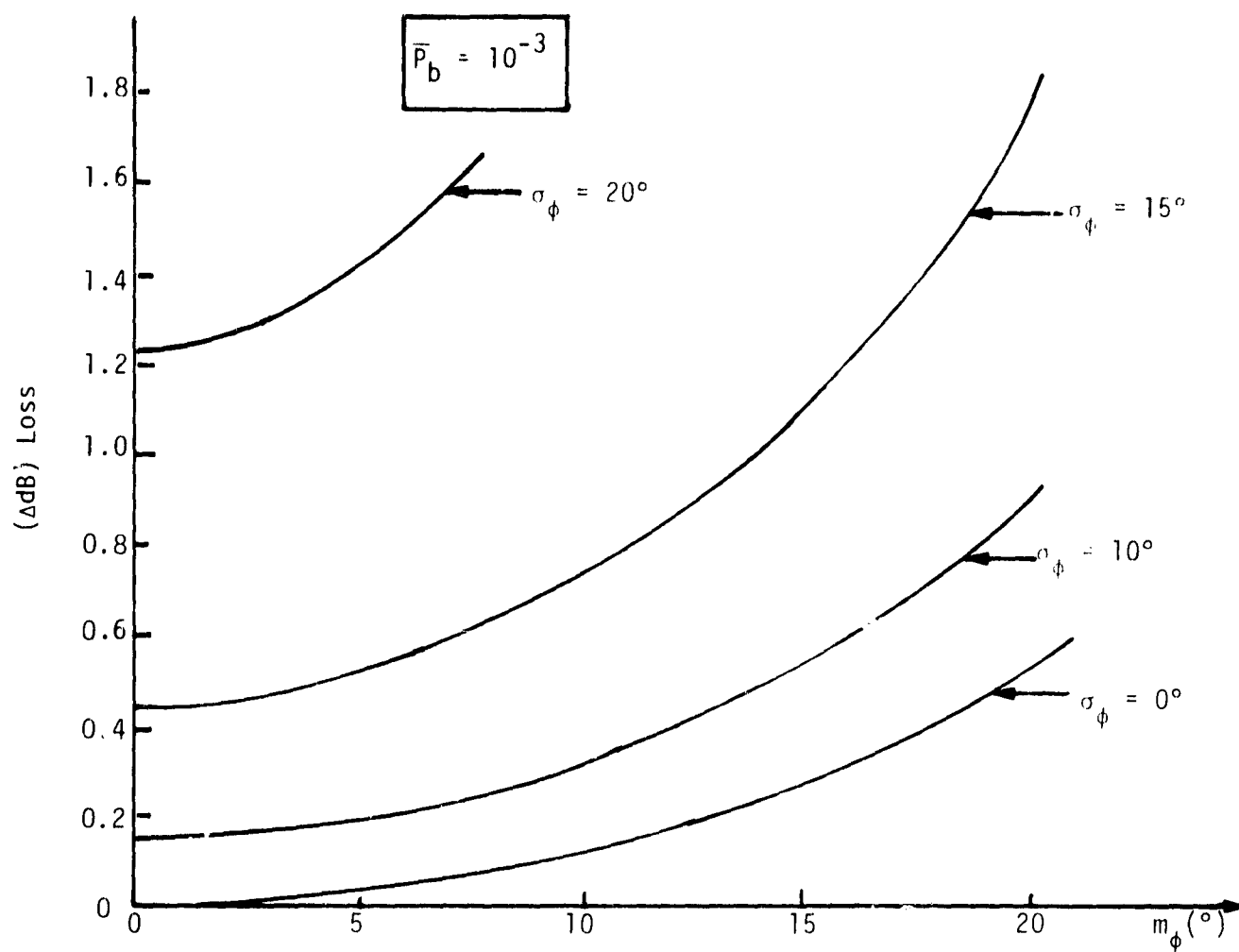


Figure 4.14. Performance Degradation versus Phase Offset at $P_b = 10^{-3}$ as a Function of Noise

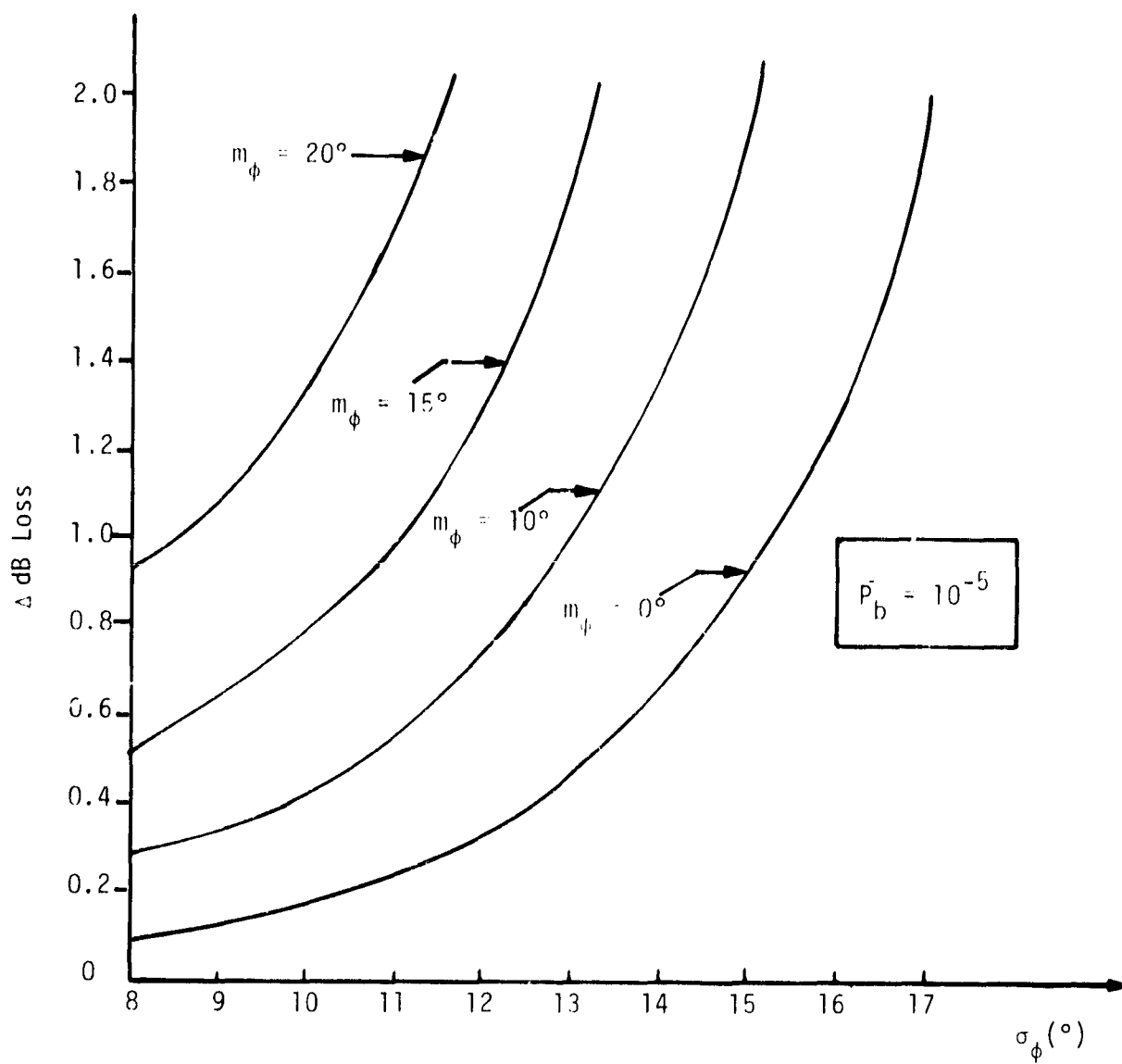


Figure 4.15. Performance Degradation versus Phase Noise at $P_b = 10^{-5}$ as a Function of Phase Offset

5.0 PAYLOAD/ORBITER/TDRSS INTERFACE STUDY

The detached or attached payload data is transmitted to the ground in one of several ways, as discussed in Section 3. As TDRSS becomes operational and the GSTDN stations are phased out, the primary on-Orbiter communication system will be the Ku-band system which transmits through the TDRS. Figure 5.1 presents the payload telemetry data signal flow and illustrates the interface with the Ku-band communication system. In the attached mode, the payload (transponder) signal processor sends telemetry directly to the payload recorder (PR), payload data interleaver (PDI), S-band FM signal processor (FMSP), or KuSP. In the detached mode, telemetry is transmitted by the payload transponder to the PI. For NASA missions with standard data formats, the telemetry data passes from the PI to the PSP, which sends it to the PDI for data handling. For DOD missions with standard data formats, the telemetry data passes from the PI to the CIU, which distributes the processed data to the PR, PDI, FMSP or KuSP for data handling. When nonstandard telemetry data formats are used in the detached mode, the PI strips off the RF carrier and sends the unprocessed data to the KuSP for transmission to the ground. This mode is called the "bent-pipe" mode since the Orbiter performs no processing of the telemetry data other than carrier translation.

The characteristics of the payload data from the detached or attached payloads which must be processed by the KuSP on the return link flow are quite varied, as shown in Table 5.1. The return link is transmitted in one of two modes which are identified by the type of carrier modulation utilized. Mode 1 implements unbalanced quadriphase-shift-keying (UQPSK) while Mode 2 implements FM. In both modes of operation, two of the channels (1 and 2) UQPSK modulate a subcarrier. Mode 1 utilizes this modulated subcarrier along with the third channel to UQPSK the carrier, as was shown in Figure 3.13. Mode 2 linearly sums the modulated subcarrier with the third channel and frequency modulates the carrier with the resultant summed signal, as was shown in Figure 3.14.

Channel 1 always (Modes 1 and 2) carries the operations data of 192 kbps. Similarly, the data on Channel 2 does not change from Mode 1 to Mode 2. Channel 2 carries the output from the PR, the operational recorder (OR) and the PSP as well as low rate data for the API and narrowband bent-pipe data from the PI. The range of data rates handled by

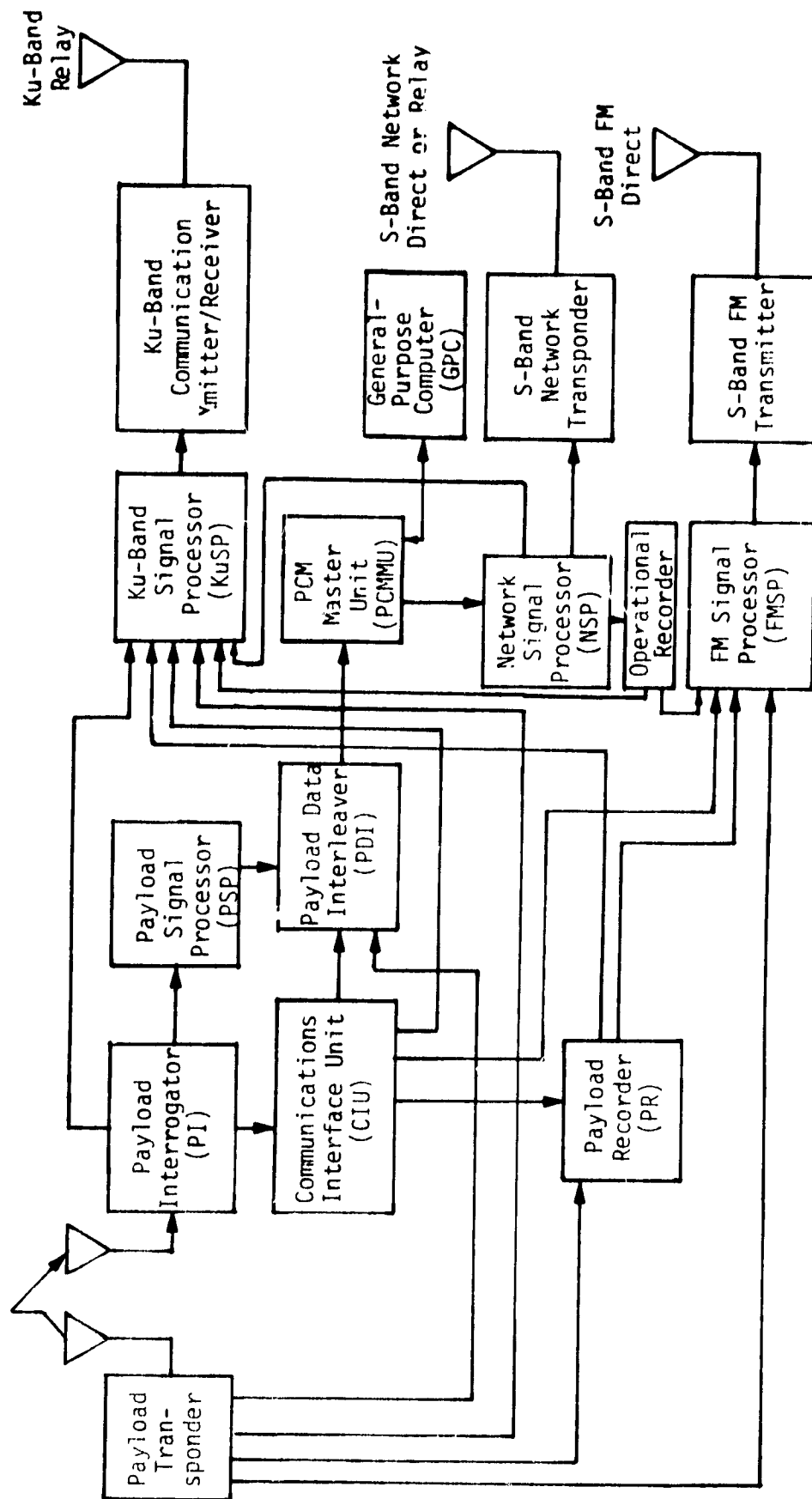


Figure 5.1. Payload/Orbiter Functional Telemetry Signal Flow

Table 5.1. Ku-Band Signal Processor Return Link Data Characteristics

KuSP Interface	Data Type	Rate or Bandwidth
RETURN LINK		
CHANNEL 1 (MODE 1/MODE 2)		
Operations Data--NSP(1,2)	Digital	192 kbps (Manchester)
CHANNEL 2 (MODE 1/MODE 2)		
Payload Recorder (PR)	Digital	25.5 - 1024 kbps (Manchester)
Operations Recorder (OR)	Digital	25.5 - 1024 kbps (Manchester)
Payload low data rate--PSP (1,2) or Attached Payload Interface (API)	Digital	16 - 2000 kbps (NRZ) 16 - 1024 kbps (Manchester)
PI(1,2) low data rate	Digital/Analog	16 - 2000 kbps (NRZ) 16 - 1024 kbps (Manchester) 0 - 2 MHz
CHANNEL 3 (MODE 1)		
Attached Payload Interface (API)	Digital	2 - 50 Mbps (NRZ)
CHANNEL 3 (MODE 2)		
PI(1,2) high data rate	Digital/Analog	16 - 4000 kbps (NRZ) 0 - 4.5 MHz
Attached Payload Interface (API)	Digital/Analog	16 - 4000 kbps (NRZ) 0 - 4.5 MHz
Video Interface Unit	Analog	0 - 4.5 MHz

the KuSP Channel 2 is shown in Table 5.1 to be 16 - 1024 kbps Manchester-coded data, 16 - 2000 kbps NRZ-coded data or DC-2 MHz analog bent-pipe data. In Mode 2, the UQPSK-modulated 8.5 MHz subcarrier is bandpass filtered and Channel 3 is lowpass-filtered, as described in Section 3, but no other processing is performed by the KuSP.

The data carried on Channel 3 in Mode 1 is digital data of 2 - 50 Mbps (NRZ) which is rate 1/2-constraint length 7, convolutionally encoded by the KuSP to maintain adequate performance margin at a bit error probability of 10^{-6} . Because the output data rate of the convolutional encoder is twice the input, the input data clock must be doubled by the KuSP. The input clock is regenerated and synchronized with the input data to compensate for phase offsets and avoid sampling the data stream near transitions. To correct for asymmetry in both the clock (specified at 20% maximum) and data (specified at 25% maximum) at the KuSP input, a very symmetric clock is regenerated and used to clock the convolutional encoder. The data bits are sampled using a pulse generated every other clock pulse. The KuSP clock regeneration circuit maintains the sample pulse in the middle of the data bit. The KuSP reduces the encoder output data asymmetry to less than 10% for all input rates and for the input clock and data asymmetry up to their maximum specified values.

Since the Ku-band communication system operates through the TDRSS, user constraints on the data characteristics and modulation formats established by the TDRSS must be met in order for the TDRSS to guarantee its specified performance. By reviewing the Orbiter subsystem processing of payload data discussed above and in Section 3, it is seen that some attached payload data is passed through the Orbiter subsystems, including the Ku-band communication system, without having the basic data characteristics modified. In these cases, the TDRSS user constraints must become payload user constraints and how well these constraints are met by the payload will determine the performance degradation of the data processed by the TDRSS.

5.1 Payload User Constraints Derived from TDRSS User Constraints

Attached payload digital data with data rates between 16 kbps and 2 Mbps can be transmitted through the TDRSS by the Ku-band Channel 2 or Channel 3 Mode 1. For either channel, the Ku-band system does not modify the basic data characteristics. Therefore, the TDRSS user constraints on data characteristics apply to this attached payload data. The TDRSS user constraints that apply are presented in Table 5.2. The data asymmetry parameter in Table 5.2 is defined for an NRZ format signal as

$$\frac{[\text{length of long bit} - \text{length of short bit}]}{[\text{length of long bit} + \text{length of short bit}]} \times 100\%$$

For a biphase format signal, data asymmetry applies to both the entire bit as well as to each half-symbol pulse. For data bits, data asymmetry is

$$\frac{[\text{length of long bit} - \text{length of short bit}]}{[\text{length of long bit} + \text{length of short bit}]} \times 100\%$$

and for half-symbol pulse, data asymmetry is

$$\frac{[\text{length of long half-symbol pulse} - \text{length of short half-symbol pulse}]}{[\text{length of long half-symbol pulse} + \text{length of short half-symbol pulse}]} \times 100\%$$

Data transition time is defined as the time required to switch from 90% of the initial data state to 90% of the final data state, as illustrated in Figure 5.2. To define data bit jitter, let ϵT be the error in seconds between the actual bit transition time and the correct transition, when T is the bit period and ϵ is a random variable. Then the data bit jitter is the square root of the variance of ϵ multiplied by 100%.

For attached payloads with data rates between 2 and 50 Mbps which are transmitted via Channel 3 (Mode 1) by the Ku-band communication system, the KuSP reclocks input data. Therefore, the payload user constraints depend only on the requirements of the KuSP to allow the data to be reclocked. Table 5.3 presents the payload user constraints for data on this channel and Table 5.4 presents the payload user constraints for clock from the payload to the KuSP.

Table 5.2. TDRSS User Constraints on Data Characteristics

Parameter	Constraint
Data Asymmetry (peak)	$\pm 3\%$
Data Transition Time (90% of initial state to 90% of final state)	$\leq 5\%$ of bit time, but no less than 800 psec
Data Bit Jitter ¹ To meet BER requirements ² ≤ 10 Mbps coded > 10 Mbps coded To meet BSR requirements ³ BSR $\leq 10^{-10}$ BSR $\leq 10^{-9}$ BSR $\leq 10^{-8}$ BSR $\leq 10^{-7}$	 $\leq 0.1\%$ $\leq 0.1\%$ $\leq 0.1\%$ $\leq 0.5\%$ $\leq 1.0\%$ $\leq 2.0\%$
Data Transitions (NRZ)	Within any sequence of 512 bits, the number of transitions will be ≥ 64 and the maximum number of consecutive bits without a transition will be ≤ 64 .
Data Rate Accuracy	Transmitted data rate will not differ from the data rate specified to TDRSS by more than 0.1%

1. Indicated percentages are the user spacecraft peak clock frequency jitter and peak jitter rate (sinusoidal or 3σ random) as a percent of the symbol clock rate. For bit jitter rates $> 0.1\%$, biphasic data format will be used. Bit jitter refers to symbol jitter when the data is coded.
2. When biphasic format is used, the 10 Mbps data rates are divided by a factor of 2.
3. BSR $\leq 10^{-9}$ does not apply to coded data > 10 Mbps or, when biphasic format is used, to coded data > 5 Mbps. BSR $\leq 10^{-8}$ and $\leq 10^{-7}$ apply only to uncoded data.

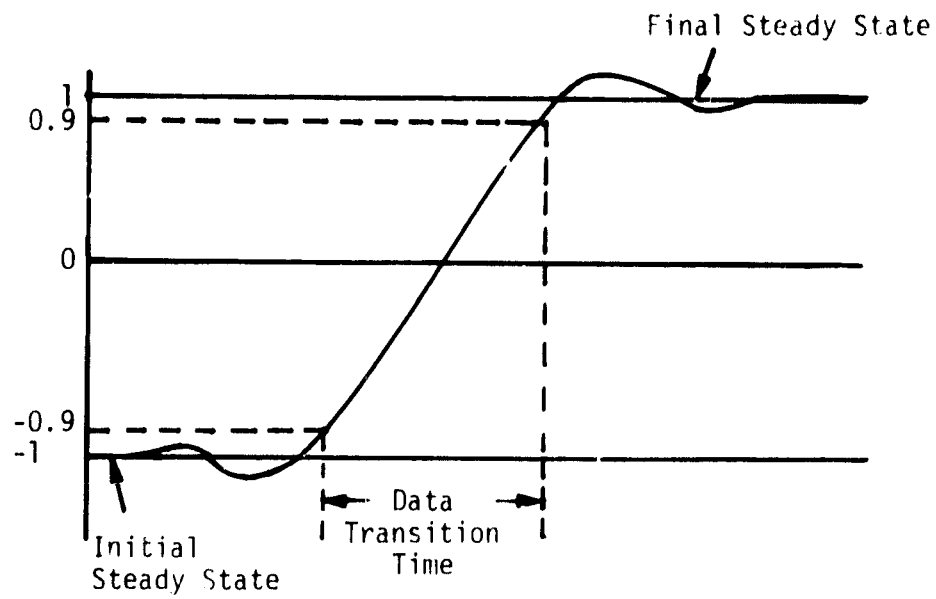


Figure 5.2. Data Transition Time Definition

Table 5.3. Payload User Constraints for Data on Ku-Band Channel 3 (Mode 1)

Parameter	Constraint
Data Level	
Peak positive level (max)	+ 6.5 V
Peak positive level (min)	+ 4.5 V
Peak negative level (max)	+ 0.5 V
Peak negative level (min)	- 0.5 V
Data-to-Clock Phase Offset	$\pm 21\%$ of bit period
Data Asymmetry	16% of bit period at 50 Mbps
Data Bit Jitter	$\pm 3\%$ of bit period
Frequency Stability (Long-Term)	$\leq 0.01\%$ of bit rate
Frequency Jitter	
RMS deviation	$\leq 0.01\%$
RMS rate	$\leq 0.01\%$
Data Transition Time	Larger of 6.0 ns or 5% of bit period

Table 5.4. Payload User Constraints for Clock to KuSP (Channel 3, Mode 1)

Parameter	Constraints
Clock Level	
Peak positive level (max)	+ 6.5 V
Peak positive level (min)	+ 4.5 V
Peak negative level (max)	+ 0.5 V
Peak negative level (min)	- 0.5 V
Clock Asymmetry	$< 30\%$ (max) of bit period at 50 Mbps
Clock Transition Time	Larger of 6.0 ns or 5% of bit period

5.2 Analysis of Cumulative Effect of TDRSS User Constraint Parameters on Bit Error Probability Performance

The TDRSS user constraints on data characteristics in Table 5.2 are analyzed in this section to determine their effect on bit error probability (BEP) performance of the low data rate attached payload data. The parameters of data transitions and data rate accuracy in Table 5.2 pertain to the TDRSS bit synchronizer's ability to acquire and maintain bit synchronization lock and are not analyzed here. The basis of this BEP analysis is the upper bound to the probability of error (or equivalently, $\Delta E_b/N_0$) below.

Let $\{p_i\}$ constitute a probability distribution and $\{u_i\}$ a set of functions of the user parameter. The unconditional bit error probability in the presence of the user parameter degradation is expressed as

$$P_E = \sum_{i=1}^N p_i Q \left\{ \sqrt{\frac{2E_b}{N_0}} u_i \right\}; \quad \sum_{i=1}^N p_i = 1 \quad (63)$$

E_b/N_0 is the bit energy-to-noise ratio; we define

$$\rho \triangleq 2E_b/N_0; \quad (64)$$

$$Q(x) \triangleq \frac{1}{\sqrt{2\pi}} \int_x^{\infty} \exp(-t^2/2) dt; \quad (65)$$

then,

$$P_E \triangleq \frac{\exp(-(E_b/N_0)D)}{\sqrt{2\pi}(2E_b/N_0)D}, \quad (66)$$

where

$$D = \frac{1}{(1 + 2E_b/N_0)} \left\{ 1 - 2 \ln \sum_{i=1}^N p_i \frac{\exp(-(E_b/N_0)u_i)}{\sqrt{u_i}} \right\} \quad (67)$$

and the SNR degradation is defined as

$$\frac{\Delta E_b}{N_0} \leq 10 \log_{10} (1/D). \quad (68)$$

In order to determine the BEP performance degradation due to the data characteristics, a model for the data modulator in the KuSP must be established. Therefore, assume that the KuSP data modulator has a channel gain imbalance G . Let

$$\eta = G_1/G_0 ; \quad \eta > 1 \text{ (arbitrarily)} , \quad (69)$$

where the subscripts 0 and 1 denote whether the data bit is -1 or +1, respectively.

Since the average power is fixed at the modulator output,

$$G_0 = \frac{2}{1+\eta} \quad \text{and} \quad G_1 = \frac{2\eta}{1+\eta} . \quad (70)$$

Now (66) gives an expression for the probability of error

$$P_E = \frac{1}{2} Q\{\sqrt{\rho G_1}\} + \frac{1}{2} Q\{\sqrt{\rho G_0}\} ; \quad (71)$$

thus

$$\begin{aligned} N &= 2 \\ p_1 &= 1/2 & u_1 &= \frac{2\eta}{1+\eta} \\ p_2 &= 1/2 & u_2 &= \frac{2}{1+\eta} \end{aligned} \quad (72)$$

For a nominal probability of error $P_E = 10^{-5}$, $E_b/N_0 = 9.6$ dB (these values are used throughout this section). The value of D is calculated using (67) and, consequently, $\Delta E_b/N_0$. Adding the effect of data asymmetry A ,

$$\begin{aligned} N &= 4 \\ p_1 &= \frac{1}{2} & u_1 &= \frac{2\eta}{1+\eta} \\ p_2 &= \frac{1}{8} & u_2 &= \frac{2}{1+\eta} \\ p_3 &= \frac{1}{4} & u_3 &= \left[\left(1 - \frac{A}{2}\right) \sqrt{\frac{2}{1+\eta}} - \frac{A}{2} \sqrt{\frac{2\eta}{1+\eta}} \right]^2 \\ p_4 &= \frac{1}{8} & u_4 &= \left[(1 - A) \sqrt{\frac{2}{1+\eta}} - A \sqrt{\frac{2\eta}{1+\eta}} \right]^2 \end{aligned} \quad (73)$$

where A is the amount of asymmetry present ($A \times 100 = \% \text{ asymmetry}$).

The parameter representing data transition time (t_r) is the ratio of transition time to bit duration: $\mu = t_r/T$. Two cases arise.

Case A: Data Transition Time Dominates Data Asymmetry

$$N = 6$$

$$\begin{aligned} p_1 &= \frac{1}{4} & u_1 &= \frac{2\eta_1}{1+\eta_1} (1 - \beta_1)^2 \\ p_2 &= \frac{1}{8} & u_2 &= \frac{2\eta_1}{1+\eta_1} (1 - 2\beta_1)^2 \\ p_3 &= \frac{1}{8} & u_3 &= \frac{2\eta_1}{1+\eta_1} \\ p_4 &= \frac{1}{4} & u_4 &= \frac{2}{1+\eta_1} (1 - \beta_0)^2 \\ p_5 &= \frac{1}{8} & u_5 &= \frac{2}{1+\eta_1} (1 - 2\beta_0)^2 \\ p_6 &= \frac{1}{8} & u_6 &= \frac{2}{1+\eta_1} \end{aligned} \quad (74)$$

$$\begin{aligned} \text{with } \beta_0 &= \frac{1}{2} \left[\frac{5}{9} \mu \sqrt{\frac{2\eta_1}{1+\eta_1}} \right] \left[1 - \frac{A/2}{\frac{5}{9} \mu \sqrt{\frac{2\eta_1}{1+\eta_1}}} \right]^2 \\ \beta_1 &= \frac{1}{2} \left[\frac{5}{9} \mu \sqrt{\frac{2\eta_1}{1+\eta_1}} \right] \left[1 - \frac{A/2}{\frac{5}{9} \mu \sqrt{\frac{2\eta_1}{1+\eta_1}}} \right]^2 \end{aligned} \quad (75)$$

Case B: Data Asymmetry Dominates Data Transition Time

$$N = 4$$

$$\begin{aligned} p_1 &= \frac{1}{2} & u_1 &= \frac{2\eta_1}{1+\eta_1} \\ p_2 &= \frac{1}{4} & u_2 &= \frac{2}{1+\eta_1} \\ p_3 &= \frac{1}{4} & u_3 &= \frac{2}{1+\eta_1} (1 - \beta_3)^2 \\ p_4 &= \frac{1}{8} & u_4 &= \frac{2}{1+\eta_1} (1 - 2\beta_3)^2 \end{aligned} \quad (76)$$

with

$$\beta_3 = \frac{1}{2} \left[\frac{5}{9} \mu \sqrt{\frac{2}{1+\eta}} \left(1 + \frac{A}{5/9 \mu \sqrt{2/(1+\eta)}} \right) + \frac{5}{9} \mu \sqrt{\frac{2\eta}{1+\eta}} \sqrt{\eta} \left(\frac{A}{5/9 \mu \sqrt{2\eta/(1+\eta)}} - 1 \right) \right] \quad (77)$$

Usually, data transition time effects are negligible when data asymmetry is dominant, but not necessarily otherwise.

Data bit jitter (Δ_D) is the random components of data asymmetry specified as being less than some peak value in % (i.e., $\Delta_D \times 100 = \text{peak value}$). The results of (74) through (77) apply with each A replaced by $A + \Delta_D$ in every u_i .

The computations of BEP performance degradation were performed for both cases, namely, where data asymmetry dominates data transition time ($A > \mu$) and vice versa.

Where $\mu > A$, the impacts of $\mu = 5\%$ and $\Delta_D = 2\%$ with varying A is shown graphically in Figure 5.3 (the results are relative to a gain imbalance of 0.5 dB). Figure 5.4 shows the effect of varying A on the cumulative degradation (relative to $\mu = 5\%$ and $\Delta_D = 2\%$); it can be seen that the two curves have approximately the same slope except at the high values of A where the individual impact is more pronounced than the impact in combination.

When $A > \mu$, the result for $A = 5\%$, $\mu = 3\%$ and $\Delta_D = 2\%$ is $\Delta E_b/N_0 = 0.728$ dB; varying μ (relative to $A = 5\%$) was found to have no appreciable effect.

5.3 Payload Data Performance Degradation due to Payload Data Asymmetry with an UQPSK Modulator

In the previous section, the digital data modulator was characterized by only a gain imbalance. In this section, the impact of payload data asymmetry on the BER performance is presented for exact implementation of the QDSB system employed in Mode 1 of the Ku-band system [4] which is a cascade of two such unbalanced QPSK systems. Of primary interest is the subcarrier QPSK system and, in particular, the version implemented via a digital phase-shift-modulated square-wave subcarrier [5].

The performance of unbalanced QPSK (UQPSK) systems in the presence of reference phase noise has been examined by a number of authors (see [6 - 10] and references therein). The general approach is to evaluate

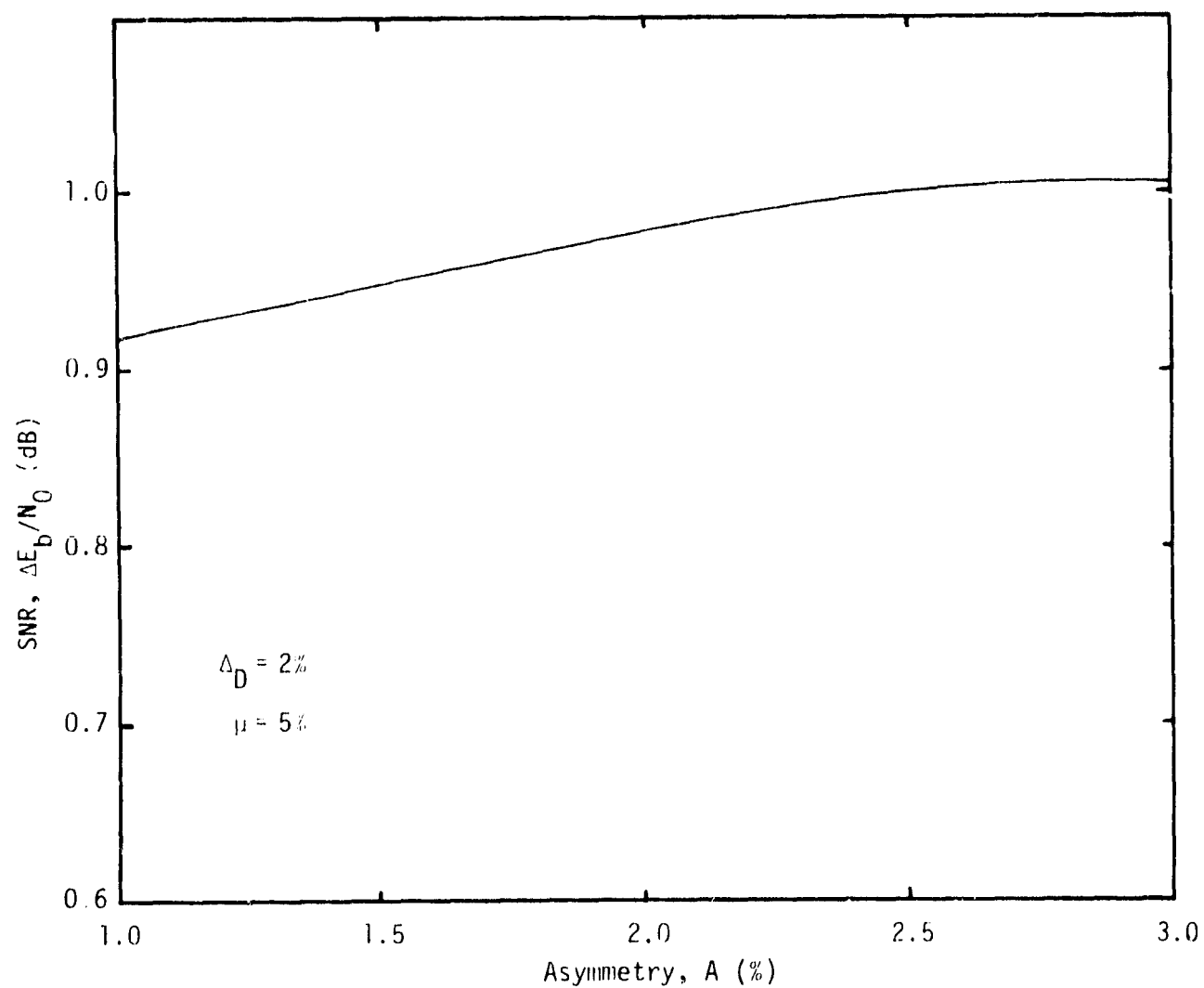


Figure 5.3. Variation of Degradation in SNR as a Function of Asymmetry When Data Transition Time Dominates Data Asymmetry (Relative to $\mu = 0.5$ dB)

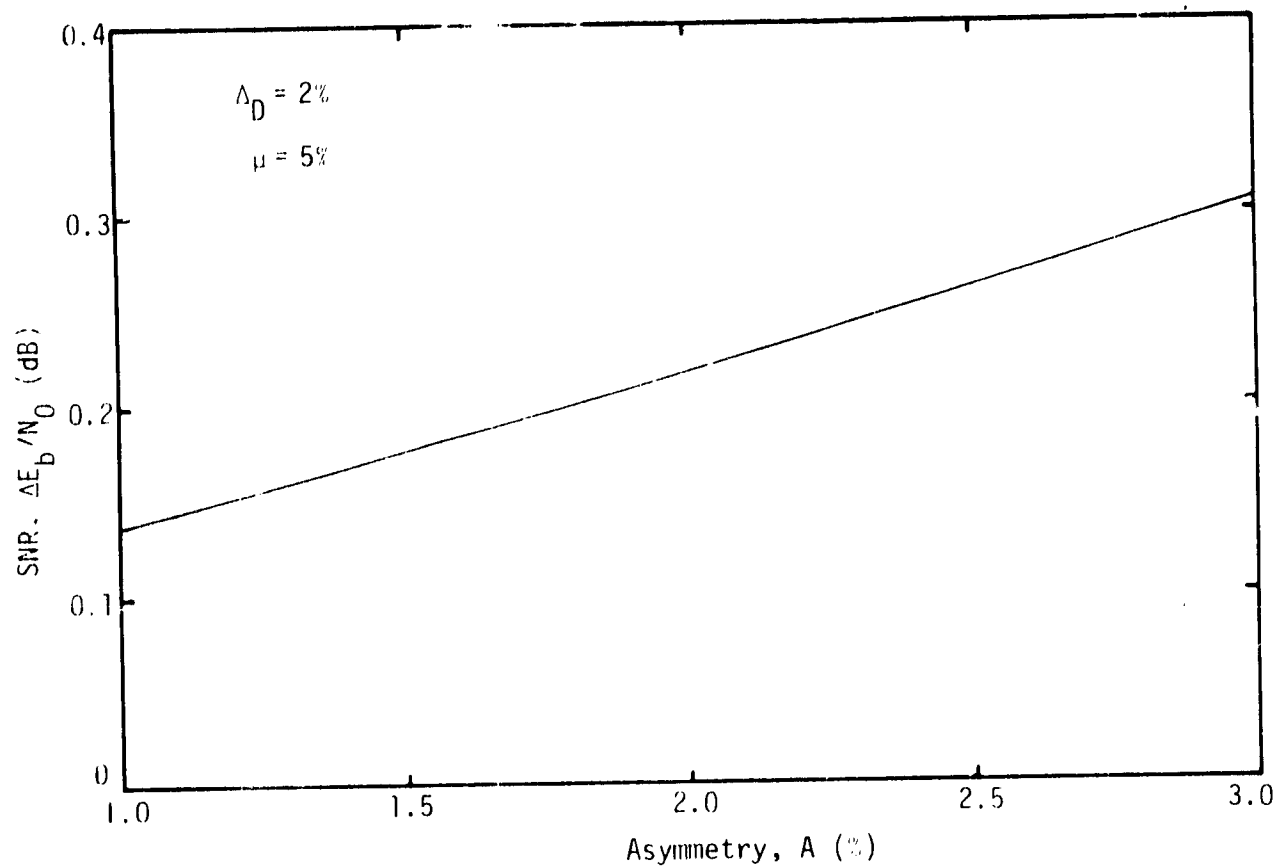


Figure 5 4 Variation of Cumulative Degradation in SNR as a Function of Asymmetry When Data Transition Time Dominates Data Asymmetry

the bit error probability conditioned on the data and the value ϕ of the phase error, then average over these variables. The marginal probability density function (p.d.f.) of ϕ strongly depends on the employed tracking loop and is, in general, difficult to accurately evaluate for sophisticated receivers. In this section, the results are based on a truncated Taylor series expansion approach, indicated in [8], which provides credible results assuming high loop signal-to-noise ratio (SNR). Regardless of the particular method used, the BEP depends on the powers and data rates of the individual channels.

The ϕ -conditioned BEP (which is a reasonable estimate of BEP for very high SNR) is an increasing function of ϕ , the reason being that an imperfect phase-lock-loop attenuates the demodulated signal power and at the same time increases interchannel crosstalk.

Data asymmetry is a potential source of performance degradation in any digital transmission system. It arises whenever the modulator spends more time at one amplitude state than the other, as a result of the misalignment of a threshold device. References [11] and [12] pertain to previous work on the issue of determining the effect of data asymmetry on the BEP of BPSK signaling ([11], for a variety of coded and uncoded data) and QPSK with equal data rates [12]. Since no crosstalk was considered in [12], the two QPSK channels are essentially two independent identical BPSK channels with different power allocation.

In this section, the performance degradation of an QPSK system due to both payload data asymmetry and noisy reference is presented. As we shall see, the degradation of each channel can qualitatively be perceived as consisting of a "self-degradation" term plus a "cross-degradation" term. The former is the superposition of a power attenuation (due to noisy reference) along with the impairment caused by asymmetry. The latter (which is actually the interchannel interference) exists because of the presence of noisy reference and also depends on the asymmetry of the companion channel data stream. Hence, the results to be derived here should coincide with those in [11] and [12] if the phase error is assumed to be zero.

The parameter of interest here is the additional signal-to-noise ratio ΔSNR (dB) required to compensate for the losses due to asymmetry and phase noise for each channel. It is defined as the difference between the

SNR required to achieve a BEP of 10^{-5} under the aforementioned conditions and the nominal value of 9.6 dB for an ideal BPSK system without impairments other than Gaussian noise.

We have assumed a power ratio of 4 and a data rate ratio of 10 for the two channels. These are typical values for the I and Q components of the subcarrier QPSK system of the Orbiter's Ku-band, which operate at 2 Mbps and 0.2 Mbps, respectively.

According to the approach taken in [13], the phase error impact is sufficiently characterized by the mean m_ϕ and the variance σ_ϕ^2 of the tracking jitter ϕ . When a biphasic Costas tracking loop is employed at the receiver, references [14] and [15] provide some (although complicated) analytic results for σ_ϕ . We feel that an extension of these results in the presence of asymmetry is a prohibitively complicated task; therefore, we can only postulate some values for m_ϕ and σ_ϕ . However, it is intuitively appealing to assume that, in the presence of small asymmetry, typical values of σ_ϕ will be slightly higher than what appears in the figure of [14] and [15]. As such, we have selected to examine the cases of $m_\phi = 0^\circ, 3^\circ, 5^\circ$ and $\sigma_\phi^2 = 0, 4, 9$ (degrees)².

Figures 5.5 through 5.7 show the plots of Δ SNR as a function of the percent asymmetry A , with m_ϕ and $\text{var } \phi$ as parameters. To gain some confidence about their correctness, let us notice that, for $\text{var } \phi = 0$ and $A = 0$ (m_ϕ is the single parameter then), the results coincide with those of Figures 9 and 10 of [9]. Also, with $m_\phi = 0$, $\sigma_\phi = 0$ and different degrees of asymmetry, the results coincide with Table 1 of [11].

In general, the SNR losses increase exponentially with the amount of asymmetry present. For the values considered, they range from 0 dB to 1.4 dB. Also notice that the plots are virtually parallel (for a fixed σ_ϕ), which means that the presence of a mean phase error shifts the curves upward. In other words, the effects of phase mean and phase variance are effectively decoupled. However, as expected, as σ_ϕ increases, the effect of phase offset becomes more and more drastic.

5.4 Payload Data Performance Degradation due to the Ku-Band System Digital Phase Modulator Phase Asymmetry

This section examines the degradation in performance of the Ku-band digital phase shift implementation of unbalanced QPSK due to modulator phase imbalance. Such a deviation from nominal operating conditions,

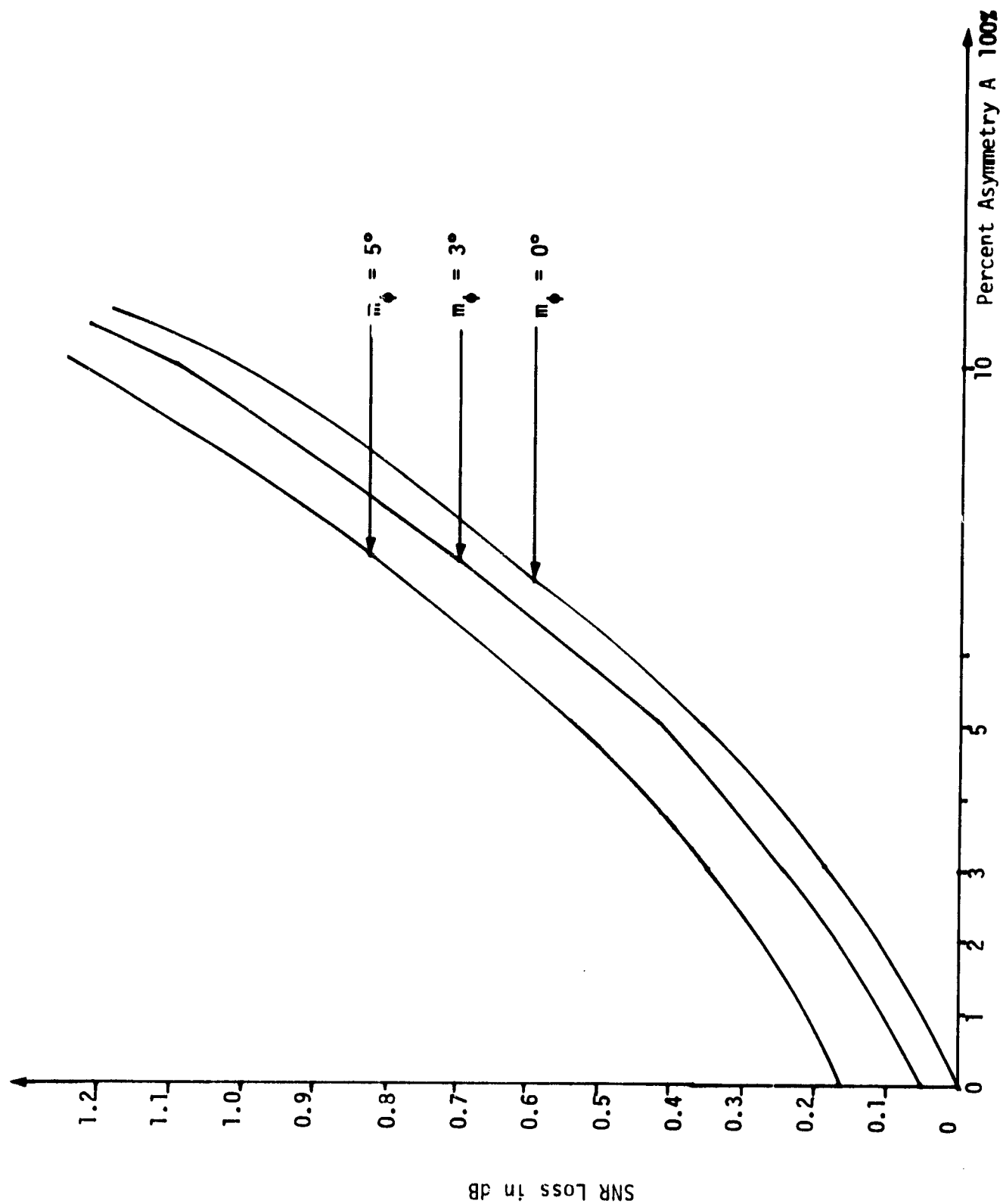


Figure 5.5. Payload Data Performance Degradation as a Function of Data Asymmetry with $\varphi = 0$

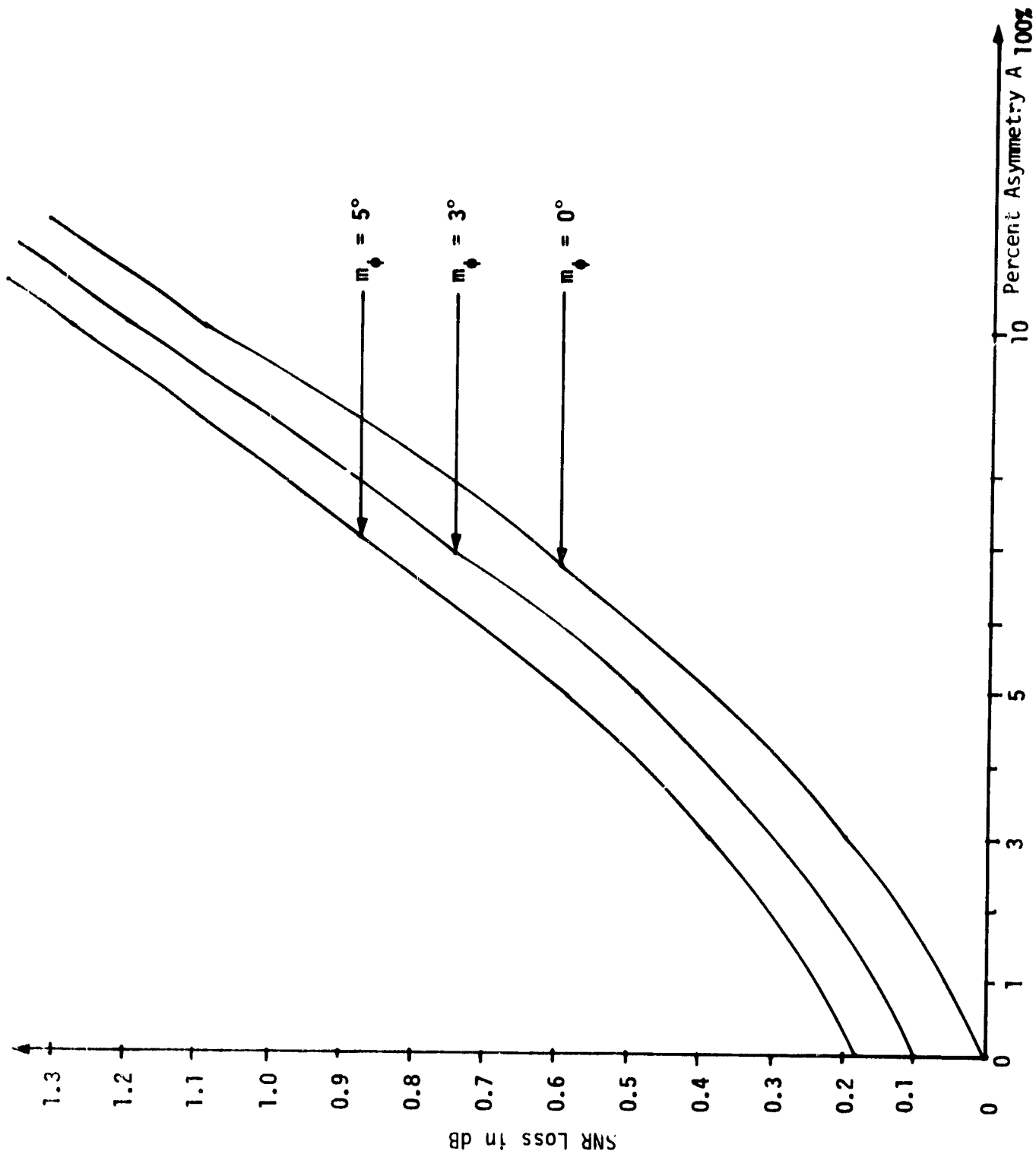


Figure 5.6. Payload Data Performance Degradation as a Function of Data Asymmetry with var $\phi = 4$

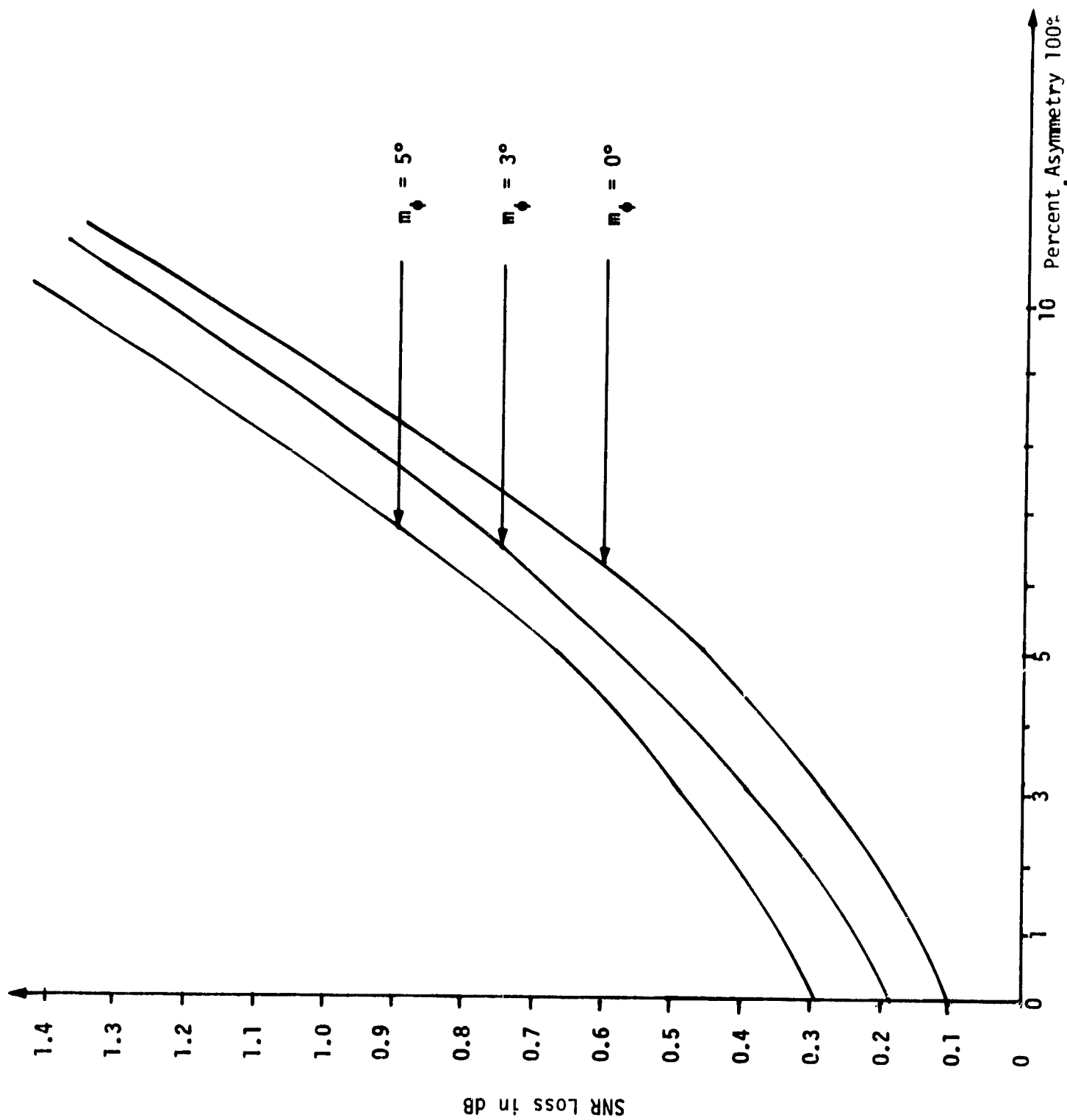


Figure 5.7. Payload Data Performance Degradation as a Function of Data Asymmetry with $\varphi = 9$

which is modeled and analyzed in Appendix IV, can possibly arise due to the different path delays involved in the digital circuitry which implements the phase selection procedure in the KuSP. A more thorough discussion and details on this transmitter structure can be found in [4] and [5].

The data asymmetry analyzed in the last section and the phase asymmetry discussed in this section belong to the same class of "timing" or "horizontal" anomalies, as opposed to the "amplitude" or "vertical" anomalies. The ultimate goal of this research would be to combine these two asymmetries although, at this point, it seems that a rigorous analysis of this sort is a very complicated task.

The degree of phase asymmetry in the digital phase shift modulator is denoted by S_θ . For unbalanced QPSK, the angle between data vectors is less than the 90° associated with balanced QPSK. Let the nominal angle between data vectors be denoted by $2\theta_0$; then S_θ is the deviation from $2\theta_0$ introduced by the digital phase shift modulator. Because there is a tracking loop phase error ϕ present at the receiver, S_θ contributes to both self-degradation and crosstalk degradation for each of the two data channels. As is shown in Appendix IV, the contribution of S_θ to the overall degradation is also a function of θ_0 . As θ_0 decreases (which means that the power split between the I and Q channels increases in favor of the stronger channel), the severity of the effect of S_θ increases proportionally to $\cot \theta_0$. Hence, for a strongly unbalanced QPSK system, the impact of modulator phase asymmetry may become quite noticeable.

The payload data BEP degradation as a function of S_θ is evaluated in Appendix IV and is presented in Figure 5.8. The degradation is parameterized by m_ϕ , the mean value of the tracking loop random variable ϕ . In Figure 5.8, the nominal value of the Ku-band system digital phase shift was assumed to be $\theta_0 = 26.6^\circ$. This value of θ_0 corresponds to the power ratio at the receiver equal to 4.

As an aside, Appendix IV also calculates the degradation of the operational data on Channel 1 of the Ku-band system return link. Figure 5.9 presents the operational data BEP degradation as a function of S and parameterized by m_ϕ . Figure 5.9 shows that the operational data is by far more sensitive to the modulator phase asymmetry than the payload data channel. This is mainly because the interchannel interference manifests itself stronger in the lower power operational data channel than in

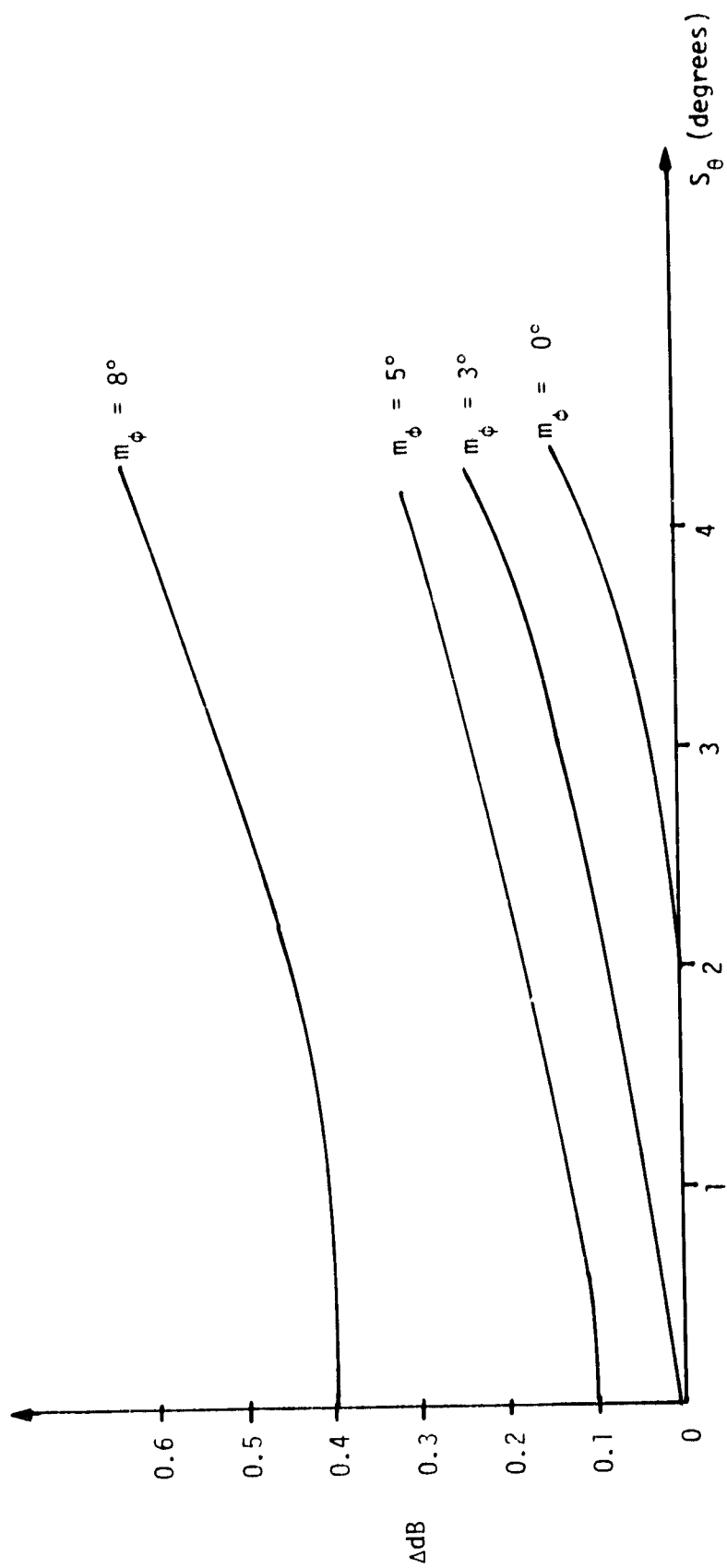


Figure 5.8. SNR Loss Versus S_θ for the Payload Data Channel 2

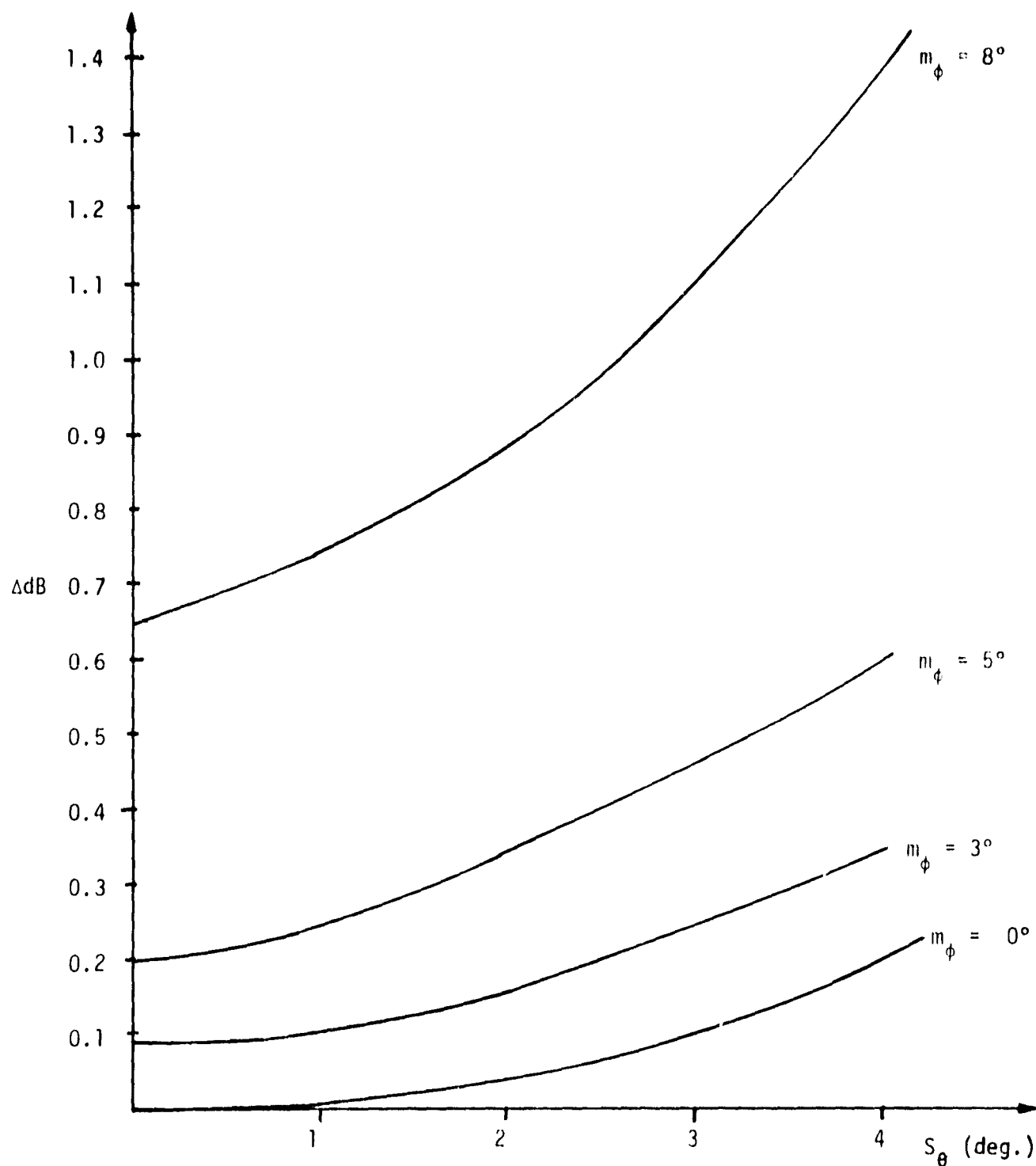


Figure 5.9. SNR Loss Versus S_θ for the Operational Data Channel 1

the higher power payload data channel. For different values of $m_\phi = 0^\circ, 3^\circ, 5^\circ$ and 8° , the range of loss in the operational data channel is 0 to 1.4 dB while, for the payload data channel, it is 0 - 0.6 dB. Notice that, for $S_\theta = 0^\circ$, the plot values coincide with the corresponding ones of Figures 9 and 10 of [9].

REFERENCES

1. J. Rutman, "Characterization of Phase and Frequency Instabilities in Precision Frequency Sources: Fifteen Years of Progress," Proceedings of the IEEE, Vol. 66, No. 9, September 1978, pp. 1048-1075.
2. W. C. Lindsey and K. Tu, "Phase Noise Effects on Space Shuttle Communication Link Performance," IEEE Trans. on Communications, Vol. COM-26, November 1978, pp. 1532-1541.
3. M. K. Simon, "The Theory of Mean-Square Phase Noise Performance of One/Two-Way Coherent Communication Links," Appendix VI to Shuttle Ku-Band and S-Band Communications Implementation Study, Axiomatix Final Report on NAS 9-15240E/F, Report No. R8005-3, May 21, 1980.
4. R. H. Cager, Jr., D. T. LaFlame, and J. C. Parode, "Orbiter Ku-Band Integrated Radar and Communications Subsystem," IEEE Transactions on Communications, November 1978, pp. 1604-1619.
5. M. K. Simon, "Power Allocation and Costas Loop Subcarrier Tracking Performance Associated with a Digital Phase Shift Implementation of the Three-Channel Orbiter Ku-Band Modulator," Axiomatix Report No. R7709-4, September 29, 1977.
6. C. L. Weber, "Candidate Receivers for Unbalanced QPSK," 1976 ITC Proceedings, Vol. XII, pp. 455-464.
7. W. R. Braun and W. C. Lindsey, "Carrier Synchronizatoin Techniques for Unbalanced QPSK Signals" (parts I and II), IEEE Transactions on Communications, September 1978, pp. 1325-1341.
8. M. K. Simon, "Error Probability Performance of Unbalanced QPSK Receivers," IEEE Trans. on Comm., September 1978, pp. 1390-1397.
9. H. C. Osborne, "Effect on Noisy Phase Reference on Coherent Detection of Unbalanced QPSK Signals," NTC '78 Proceedings, December 1978, pp. 2.2.1-2.2.6.
10. D. Divsalar and J. H. Yuen, "Performance of Unbalanced QPSK in the Presence of Noisy Reference and Cross Talk," NTC '79 Proceedings, November 1979.
11. M. K. Simon, K. Tu, and B. H. Batson, "Effects of Data Asymmetry on Shuttle Ku-Band Communications Link Performance," IEEE Trans. on Comm., November 1978, pp. 1639-1651.
12. R. S. Orr, "The Impact of Data Asymmetry on Bit Error Performance," Technical Report, Stanford Telecommunications, Inc., McLean, Virginia, July 21, 1977.
13. A. Polydoros, "Effect of Data Asymmetry on Unbalanced QPSK Signals with Noisy Phase Reference," Appendix II to Shuttle Ku-Band and S-Band Communication Implementation Study, Axiomatix Final Report on Contract NAS 9-15240E/F, Report No. R8005-3, May 21, 1980.

14. M. K. Simon and W. K. Aled, "Tracking Performance of Unbalanced QPSK Demodulators: Part I - Biphase Costas Loop with Passive Arm Filters," IEEE Trans. on Comm., August 1978, pp. 1147-1156.
15. M. K. Simon, "Tracking Performance of Unbalanced QPSK Modulators: Part II - Biphase Costas Loop with Active Arm Filters," IEEE Trans. on Comm., August 1978, pp. 1157-1166.

APPENDIX I

**PHASE NOISE SPECTRAL CALCULATIONS
FOR THE PI/IUS TWO-WAY COMMUNICATION LINK**

By

Andreas Polydorus

APPENDIX 1

PHASE NOISE SPECTRAL CALCULATIONS FOR THE PI/IUS TWO-WAY COMMUNICATION LINK

By
A. Polydoros

Here we attempt an evaluation of the phase noise spectrum $\phi_e(s)$ at the PI receiver (see Figure 1) based on the VCO, VCXO and TCXO phase noise processes, entering both in the PI and the IUS transponder. Different parameters, loop transfer functions, etc., will be defined on the way. To proceed, let us first consider the PI receiver. In the following, K_{PI} , K_{IUS} , G_f , K_1 , D , N , E and F represents constants. All other parameters represent either Laplace transforms or transfer functions, whichever is evident from Figure 1, with the variable s being suppressed.

1.0 PI RECEIVER

From Figure 1, it follows that

$$\phi_e = \phi_1 - \theta_{r2} \quad (1)$$

where

$$\phi_1 = G_4 \left\{ G_3 (\theta_{IUS} - \theta_{RX}) - 10 \left[\psi_{PI} + \frac{K_{PI}}{s} F_{PI} (\phi_1 - \theta_{r2}) \right] \right\}$$

or

$$\begin{aligned} \phi_1 + G_4 \cdot 10 \cdot \frac{K_{PI} \cdot F_{PI}}{s} \phi_1 &= G_4 G_3 (\theta_{IUS} - \theta_{RX}) \\ &\quad - \left[10 \psi_{PI} - 10 \frac{K_{PI} F_{PI}}{s} \theta_{r2} \right] G_4 \end{aligned}$$

or

$$\phi_1 = \frac{G_3 G_4 (\theta_{IUS} - \theta_{RX}) - \left[10 \psi_{PI} - 10 \frac{K_{PI} F_{PI} \cdot \theta_{r2}}{s} \right] G_4}{1 + \frac{10 \cdot G_4 \cdot F_{PI} \cdot K_{PI}}{s}} \quad (2)$$

From (1) and (2),

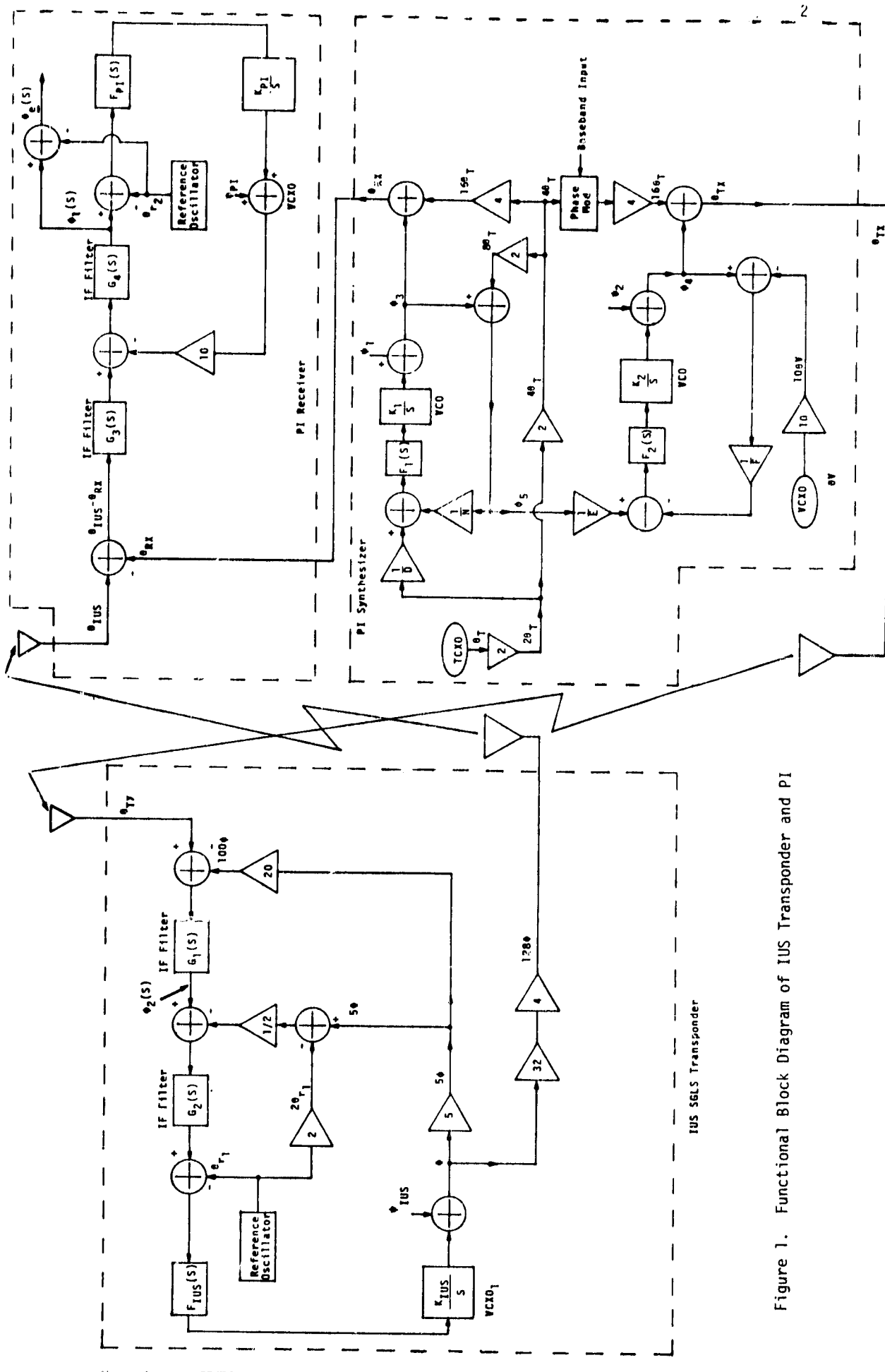


Figure 1. Functional Block Diagram of IUS Transponder and PI

$$\phi_e = (\theta_{IUS} - \theta_{RX}) \cdot \frac{G_3 \cdot G_4}{1 + \frac{10 \cdot K_{PI} \cdot G_4 \cdot F_{PI}}{s}} - \frac{10 \psi_{PI} \cdot G_4}{1 + \frac{10 K_{PI} G_4 \cdot F_{PI}}{s}} - \frac{\theta_{r_2}}{1 + \frac{10 \cdot K_{PI} \cdot G_4 \cdot F_{PI}}{s}} \quad (3)$$

Let us define

$$H_{PI}(s) \triangleq \frac{10 K_{PI} \cdot F_{PI}(s)}{s + 10 K_{PI} \cdot F_{PI}(s)} \quad (4a)$$

$$1 - H_{PI}(s) \triangleq \frac{s}{s + 10 K_{PI} \cdot F_{PI}(s)} \quad (4b)$$

Furthermore, $G_4(s)$ is assumed to be much wider than the loop filter (its bandwidth B_{G_4} is of the order of megahertz, while $B_{F_{PI}}$ is of the order of kilohertz). Hence, whenever the product $G_4(s) \cdot F_{PI}(s)$ appears, it is assumed to be equal to $F_{PI}(s)$. Using this assumption and (4), (3) simplifies to

$$\phi_e = (\theta_{IUS} - \theta_{RX}) \cdot G_3 G_4 (1 - H_{PI}) - 10 \psi_{PI} \cdot G_4 (1 - H_{PI}) - \theta_{r_2} (1 - H_{PI}) \quad (5)$$

We now proceed to evaluate $(\theta_{IUS} - \theta_{RX})$.

2.0 IUS TRANSPONDER

Note that $\theta_{IUS} = 128 \cdot \phi$; hence, $\phi(s)$ must be calculated.

$$\begin{aligned} \phi &= \psi_{IUS} + \frac{K_{IUS}}{s} \cdot F_{IUS} \left[-\theta_{r_1} + G_2 \left(\phi_2 - \frac{1}{2} (5\phi - 2\theta_{r_1}) \right) \right] \\ &= \psi_{IUS} + \frac{K_{IUS} F_{IUS}}{s} \left[-\theta_{r_1} + G_2 \phi_2 - G_2 \frac{5}{2} \phi + G_2 \theta_{r_1} \right] \\ \text{or } \phi \left[1 + \frac{5}{2} \frac{K_{IUS} \cdot F_{IUS} \cdot G_2}{s} \right] &= \psi_{IUS} + \frac{K_{IUS} F_{IUS} \cdot G_2 \cdot \phi_2}{s} + \frac{(G_2 - 1) \cdot K_{IUS} F_{IUS}}{s} \theta_{r_1} \quad (6) \end{aligned}$$

Assuming again that $B_{G_2} \gg B_{F_{IUS}}$, the product $F_{IUS} \cdot G_2$ simplifies to F_{IUS} , in which case, (6) leads to

$$\phi \left[1 + \frac{5}{2} \frac{K_{IUS} \cdot F_{IUS}}{s} \right] = \psi_{IUS} + \frac{K_{IUS} \cdot F_{IUS}}{s} \cdot \phi_2 \quad (7)$$

since, within the bandwidth of $F_{IUS}(s)$, the difference $G_2(s) - 1 = 0$ for all s . Furthermore,

$$\phi_2 = G_1 \left[\theta_{TX} - 100\phi \right] \quad (8)$$

and substitution of (8) in (7) results in

$$\phi \left[1 + \frac{5}{2} \frac{K_{IUS} \cdot F_{IUS}}{s} + \frac{100 \cdot G_1 \cdot K_{IUS} F_{IUS}}{s} \right] = \psi_{IUS} + \frac{G_1 \cdot K_{IUS} \cdot F_{IUS}}{s} \theta_{TX} \quad (9)$$

or with the same assumption, $B_{G_1} \gg B_{F_{IUS}}$, the result is

$$\phi = \frac{1}{1 + \frac{102.5 K_{IUS} F_{IUS}}{s}} \left[\psi_{IUS} + \frac{K_{IUS} F_{IUS}}{s} \theta_{TX} \right] \quad (10)$$

By defining

$$H_{IUS}(s) \triangleq \frac{102.5 K_{IUS} F_{IUS}}{s + 102.5 K_{IUS} F_{IUS}},$$

(10) simplifies to

$$\phi(s) = (1 - H_{IUS}) \psi_{IUS} + \frac{1}{102.5} H_{IUS} \theta_{TX} \quad (11)$$

Remembering that $\theta_{IUS} = 128 \cdot \phi(s)$ and substituting (11) into (5) results in

$$\begin{aligned} \phi_e(s) = & \left[128 \psi_{IUS} (1 - H_{IUS}) + \left(\frac{128}{102.5} \right) \theta_{TX} \cdot H_{IUS} - \theta_{RX} \right] G_3 G_4 (1 - H_{PI}) \\ & - 10 \psi_{PI} \cdot G_4 \cdot (1 - H_{PI}) - \theta_{r_2} (1 - H_{PI}) \end{aligned} \quad (12)$$

Comments

- (1) The ratio $\frac{128}{102.5} = \frac{256}{205} \triangleq G_f$.
- (2) Furthermore, the unknown quantities in (12) are $\theta_{TX}(s)$ and $\theta_{RX}(s)$, which are to be derived from the PI synthesizer diagram.
- (3) The quantities $1 - H_{IUS}(s)$ and $1 - H_{PI}(s)$ represent highpass filters. Hence, it is the presence of the limiting IF filters $G_3(s)$ and $G_4(s)$ which limits the variance σ^2 of $\phi_e(t)$ insofar as the contributions of the high frequencies of the spectra $\psi_{IUS}(s)$, $\theta_{RX}(s)$ and $\psi_{PI}(s)$ are concerned. In the following, we shall assume that both have a common cutoff frequency f_H (Hz) of the order of 6 MHz (hence, 12 MHz double-sided bandwidth). This is then equivalent to eliminating $G_3(s)$ and $G_4(s)$ from (12) and, instead, assuming bandlimited spectra for the aforementioned random variables (rv). Note that $\theta_{r2}(s)$ is not bandlimited in (12).

Question: What is the upper frequency of $\theta_{r2}(s)$?

From the physics of the problem, it does not seem to relate to f_H . For evaluation purposes, we have taken $(f_{\theta_{r2}})_H = f_H$, although this is not necessarily true.

3.0 PI SYNTHESIZER

The synthesizer output quantities $\theta_{RX}(s)$ and $\theta_{TX}(s)$ can be evaluated under either the coherent or noncoherent assumption, depending on the magnitude of the round-trip delay time as compared to the correlation times of the random phases θ_T and ψ_1 . (Note that ψ_2 enters only in θ_{TX} ; hence, it is of no concern in the matter of coherency, while θ_T and ψ_1 enter in the calculations of both θ_{TX} and θ_{RX} .) Hence, we distinguish between these two cases.

3.1 Coherent Case

Here θ_T and ψ_1 are common to both θ_{TX} and θ_{RX} . Furthermore, from the diagram, it follows that $\theta_{RX} = 16\theta_T + \phi_3$, where

$$\phi_3 = \psi_1 + \frac{K_1 F_1}{s} \left(\frac{2}{D} \theta_T - \frac{1}{N} (-8\theta_T + \phi_3) \right) = \psi_1 + \frac{K_1 F_1}{s} \left[\left(\frac{2}{D} + \frac{8}{N} \right) \theta_T - \frac{\phi_3}{N} \right]$$

or

$$\phi_3 \left[1 + \frac{K_1 F_1}{N \cdot s} \right] = \psi_1 + \frac{K_1 F_1}{s} \left(\frac{2}{D} + \frac{8}{N} \right) \theta_T \quad (13)$$

Substituting (13) into the previous equation yields

$$\theta_{RX} = \psi_1 \frac{1}{1 + \frac{K_1 F_1}{Ns}} + \left[16 + \frac{\frac{K_1 F_1}{s} \left(\frac{2}{D} + \frac{8}{N} \right)}{1 + \frac{K_1 F_1}{Ns}} \right] \theta_T \quad (14)$$

By defining

$$H_1(s) \triangleq \frac{K_1 F_1(s)/N}{s + K_1 F_1(s)/N}$$

equation (14) yields

$$\theta_{RX} = \psi_1 (1 - H_1) + 2 \left[8 + \left(\frac{N}{D} + 4 \right) \cdot H_1 \right] \theta_T \quad (15)$$

Similarly, we have that

$$\theta_{TX} = 16\theta_T + \phi_4 \quad (16)$$

where

$$\phi_4 = \psi_2 + \frac{K_2 F_2}{s} \left[\frac{\phi_5}{E} - \frac{1}{F} (\phi_4 - 10\theta_v) \right]$$

or

$$\phi_4 \left[1 + \frac{K_2 F_2}{Fs} \right] = \psi_2 + \frac{K_2 F_2}{Es} \phi_5 + \frac{10K_2 F_2}{Fs} \theta_v \quad (17)$$

Defining

$$H_2(s) \triangleq \frac{K_2 F_2(s)/F}{s + K_2 F_2(s)/F}$$

(17) yields

$$\phi_4 = \psi_2(1 - H_2) + \left(\frac{F}{E}\right) \cdot H_2 \cdot \phi_5 + 10H_2 \cdot \theta_v \quad (18)$$

Furthermore,

$$\begin{aligned} \phi_5 = \phi_3 - 8\theta_T &= \psi_1(1 - H_1) + 2\left(\frac{N}{D} + 4\right)H_1\theta_T - 8\theta_T \\ &= \psi_1(1 - H_1) + 2\left[\left(\frac{N}{D} + 4\right)H_1 - 4\right]\theta_T \end{aligned} \quad (19)$$

which, when substituted in (18), yields

$$\begin{aligned} \phi_4 &= \psi_2(1 - H_2) + \left(\frac{F}{E}\right) H_2 (1 - H_1) \psi_1 \\ &\quad + 2 \left(\frac{F}{E}\right) H_2 \left[\left(\frac{N}{D} + 4\right) H_1 - 4\right] \theta_T + 10H_2\theta_v \end{aligned} \quad (20)$$

Substitution of (20) into (16) finally gives

$$\begin{aligned} \theta_{TX}(s) &= \psi_2(1 - H_2) + \left(\frac{F}{E}\right) H_2(1 - H_1) \psi_1 + 10H_2\theta_v \\ &\quad + 2 \left[8 + \left(\frac{F}{E}\right) H_2 \left[\frac{N}{D} H_1 - 4(1 - H_1) \right] \right] \theta_T \end{aligned} \quad (21)$$

3.2 Noncoherent Case

Let us denote by ψ_1^i , θ_T^i , $i=T,R$ the values of the rv which are involved in the calculation of θ_{TX} and θ_{RX} , respectively. These values are assumed to be taken sufficiently temporally apart as to behave as independent rv's (i.e., ψ_1^T is independent of ψ_1^R , and the same for θ_T^i). In this case, (15) and (21) read

$$\theta_{RX}(s) = \psi_1^R (1 - H_1) + 2 \left[8 + \left(\frac{N}{D} + 4 \right) H_1 \right] \theta_T^R \quad (22)$$

and

$$\begin{aligned} \theta_{TX}(s) = & \psi_2 (1 - H_2) + \left(\frac{F}{E} \right) \cdot H_2 (1 - H_1) \psi_1^T + 10 H_2 \cdot \theta_v \\ & + 2 \left[8 + \left(\frac{F}{E} \right) H_2 \left[\left(\frac{N}{D} \right) H_1 - 4 (1 - H_1) \right] \right] \theta_T^T \end{aligned} \quad (23)$$

4.0 FINAL EXPRESSION FOR $\phi_e(s)$

The last step involves substituting (21) and (15) (for the coherent case) or (22) and (23) (for the noncoherent case) into (12). The result for the coherent case is

$$\begin{aligned} \phi_e(s) = & 128 \tilde{\psi}_{IUS} (1 - H_{IUS}) (1 - H_{PI}) - 10 \tilde{\psi}_{PI} (1 - H_{PI}) - \theta_{r_2} (1 - H_{PI}) \\ & + G_f \left(\frac{F}{E} \right) \tilde{\psi}_1 (1 - H_1) H_2 H_{IUS} (1 - H_{PI}) + G_f \tilde{\psi}_2 (1 - H_2) H_{IUS} (1 - H_{PI}) \\ & + 10 G_f \tilde{\theta}_v H_2 H_{IUS} (1 - H_{PI}) + 2 G_f \tilde{\theta}_T \left[8 + \left(\frac{F}{E} \right) H_2 \left[\frac{N}{D} H_1 - 4 (1 - H_1) \right] \right] \\ & \times H_{IUS} (1 - H_{PI}) - \tilde{\psi}_1 (1 - H_1) (1 - H_{PI}) - 2 \tilde{\theta}_T \left[8 + \left(\frac{N}{D} + 4 \right) H_1 \right] (1 - H_{PI}) \end{aligned} \quad (24)$$

or equivalently,

$$\begin{aligned} \phi_e(s) = & 128 \tilde{\psi}_{IUS}(s) (1 - H_{IUS}) (1 - H_{PI}) - 10 \tilde{\psi}_{PI}(s) (1 - H_{PI}) - \theta_{r_2}(s) (1 - H_{PI}) \\ & + G_f \tilde{\psi}_2(s) H_{IUS} (1 - H_2) (1 - H_{PI}) + 10 G_f \tilde{\theta}_v(s) H_2 H_{IUS} (1 - H_{PI}) \\ & - \tilde{\psi}_1(s) \left[1 - G_f \left(\frac{F}{E} \right) H_2 H_{IUS} \right] (1 - H_1) (1 - H_{PI}) \\ & - 2 \tilde{\theta}_T(s) \left[8 + 4 G_f \left(\frac{F}{E} \right) H_2 - 2 \right] H_{IUS} - \left(\frac{N}{D} + 4 \right) \left(G_f \cdot \frac{F}{E} \cdot H_{IUS} H_2 - 1 \right) H_1 \right] (1 - H_{PI}) \end{aligned} \quad (25)$$

Coherent Result

The corresponding result for the noncoherent case is

$$\begin{aligned}
 \phi_e(s) = & 128 \tilde{\psi}_{IUS}(s)(1 - H_{IUS})(1 - H_{PI}) - 10 \tilde{\psi}_{PI}(s)(1 - H_{PI}) - \theta_{r_2}(s)(1 - H_{PI}) \\
 & + G_f \tilde{\psi}_2(s) H_{IUS}(1 - H_2)(1 - H_{PI}) + 10 G_f \tilde{\theta}_v(s) H_2(s) H_{IUS}(1 - H_{PI}) \\
 & + G_f \left(\frac{F}{E} \right) \tilde{\psi}_1^T(s) H_2 H_{IUS}(1 - H_1)(1 - H_{PI}) + 2 G_f \tilde{\theta}_T^T(s) \\
 & \times \left[8 + \left(\frac{F}{E} \right) H_2 \left[\frac{N}{D} H_1 - 4(1 - H_1) \right] \right] H_{IUS}(1 - H_{PI}) \\
 & - \tilde{\psi}_1^R(s)(1 - H_1)(1 - H_{PI}) - 2 \tilde{\theta}_T^R(s) \left[8 + \left(\frac{N}{D} + 4 \right) H_1 \right] (1 - H_{PI})
 \end{aligned}$$

Noncoherent Result

(26)

In (25) and (26), the quantities with a \sim represent spectra which is bandlimited to $f_H = 6$ MHz. Again, $\theta_{r_2}(s)$ is not filtered.

Comment: For all three modes (STDN, DSN, SGLS), it is true that

$$G_f \frac{F}{E} = 1.$$

APPENDIX II

MEAN-SQUARE ERROR APPROXIMATION TO PHASE NOISE SPECTRA

By

Andreas Polydoros

APPENDIX II

MEAN-SQUARE ERROR APPROXIMATION TO PHASE NOISE SPECTRA

Here we wish to derive a formula for approximating a given phase noise power spectral density $S(f)$ by a power series in f^{-k} , $k \in \mathbb{N}$, in the least mean-square error sense (LMSE).

$S(f)$ is either directly available from measurements or is given in a piecewise linear form. The approximating function $\hat{S}(f)$ is assumed to be

$$\hat{S}(f) = h_0 + h_1 f^{-1} + h_2 f^{-2} + h_3 f^{-3} \quad (1)$$

where h_i ; $i = 0, 1, 2, 3$ are unknown coefficients to be determined.

The specific form of $\hat{S}(f)$ in (1) is dictated by physical considerations. The f^0 term corresponds to white phase noise, f^{-1} corresponds to white flicker noise, f^{-2} corresponds to white frequency noise, and f^{-3} serves to model flicker frequency noise. The physical significance of (1) then is that it represents the spectral superposition of the aforementioned random components, assumed independent, in the frequency band of interest.

The spectra to be approximated usually exhibit a flat portion for high frequencies. We can then assume that this value, which is directly measurable, determines h_0 . Henceforth, we will deal with the evaluation of h_k , $k \geq 1$.

The frequency band of interest will be denoted by (α, β) . We shall also assume, as is common practice, that $\beta \gg \alpha$. Indeed, customarily, α is on the order of tens of hertz while β is on the order of megahertz.

Since h_0 is known, let us define

$$S'(f) = S(f) - h_0 \quad (2)$$

The function to be minimized is

$$\begin{aligned}
 E &= \int_{\alpha}^{\beta} \left[S(f) - \left(h_0 + \frac{h_1}{f} + \frac{h_2}{f^2} + \frac{h_3}{f^3} \right) \right]^2 df \\
 &= \int_{\alpha}^{\beta} \left[S'(f) - \left(\frac{h_1}{f} + \frac{h_2}{f^2} + \frac{h_3}{f^3} \right) \right]^2 df \quad (3)
 \end{aligned}$$

Since E is a quadratic function of h_n ; $n = 1, 2, 3$, it follows that

$$\lim_{\substack{h_n \rightarrow \pm\infty \\ n=1,2,3}} E = +\infty$$

Therefore, the extremum of E , to be determined from the condition

$$\frac{\partial E}{\partial h_n} = 0, \quad n = 1, 2, 3,$$

clearly corresponds to a minimum.

Differentiating (3), we get

$$\frac{\partial E}{\partial h_n} = -2 \int_{\alpha}^{\beta} \left[S'(f) - \left(\frac{h_1}{f} + \frac{h_2}{f^2} + \frac{h_3}{f^3} \right) \right] \frac{df}{f^n} = 0$$

or

$$\int_{\alpha}^{\beta} \left[\frac{h_1}{f^{n+1}} + \frac{h_2}{f^{n+2}} + \frac{h_3}{f^{n+3}} \right] df = \int_{\alpha}^{\beta} \frac{S'(f)}{f^n} df; \quad n=1, 2, 3 \quad (4)$$

Recalling that, for $n > 1$,

$$\int_{\alpha}^{\beta} \frac{df}{f^n} = \frac{1}{(n-1)} \left[\frac{1}{\alpha^{n-1}} - \frac{1}{\beta^{n-1}} \right]$$

and inserting the assumption $\beta^{-1} \ll \alpha^{-1}$, we eventually derive from (4) the following system of equations:

$$\left. \begin{aligned} \frac{1}{\alpha} h_1 + \frac{1}{2\alpha^2} h_2 + \frac{1}{3\alpha^3} h_3 &= w_1 \\ \frac{1}{2\alpha^2} h_1 + \frac{1}{3\alpha^3} h_2 + \frac{1}{4\alpha^4} h_4 &= w_2 \\ \frac{1}{3\alpha^3} h_1 + \frac{1}{4\alpha^4} h_2 + \frac{1}{5\alpha^5} h_5 &= w_3 \end{aligned} \right\} \quad \text{I}$$

where we have defined

$$w_n \triangleq \int_{\alpha}^{\beta} \frac{S'(f)}{f^n} df ; n=1,2,3 \quad (5)$$

If we further define

$$\left. \begin{aligned} h'_n &\triangleq \frac{h_n}{\alpha^n} \\ w'_n &\triangleq \alpha^{n-1} w_n \end{aligned} \right\} \quad n=1,2,3 \quad (6)$$

the system I is written in matrix notation as

$$\begin{bmatrix} 1 & 1/2 & 1/3 \\ 1/2 & 1/3 & 1/4 \\ 1/3 & 1/4 & 1/5 \end{bmatrix} \begin{bmatrix} h'_1 \\ h'_2 \\ h'_3 \end{bmatrix} = \begin{bmatrix} w'_1 \\ w'_2 \\ w'_3 \end{bmatrix} \quad \text{II}$$

The solution of II is of the form

$$h'_n = \frac{\Delta_n}{\Lambda} \quad (7)$$

where

$$\Delta = \frac{1}{2160}$$

and

$$\Delta_1 = \frac{W_1'}{240} - \frac{W_2'}{60} + \frac{W_3'}{72} \quad (8a)$$

$$\Delta_2 = \frac{-W_1'}{60} + \frac{4W_2'}{45} - \frac{W_3'}{12} \quad (8b)$$

$$\Delta_3 = \frac{W_1'}{72} - \frac{W_2'}{12} + \frac{W_3'}{12} \quad (8c)$$

From (6), (7) and (8), it eventually follows that

$$\left. \begin{aligned} h_1 &= \alpha \left[9 W_1' - 36 W_2' + 30 W_3' \right] \\ h_2 &= 12 \alpha^2 \left[-3 W_1' + 16 W_2' - 15 W_3' \right] \\ h_3 &= 30 \alpha^3 \left[W_1' - 6 W_2' + 6 W_3' \right] \end{aligned} \right\} \quad (9)$$

where, from (5) and (6),

$$W_n' = \alpha^{n-1} \int_{\alpha}^{\beta} \left(\frac{S(f) - h_0}{f^n} \right) df; \quad n=1,2,3 \quad (10)$$

Once the W_n' is evaluated as in (10), then the h_n follows directly from (9). However, except for the unlikely case that $S(f)$ is given in a closed form, evaluation of (10) is not apparent. To circumvent this, we propose the following: assume that $S(f)$ is given by a dB-amplitude/log-frequency plot, as measured directly in the laboratory. We approximate the plot by a series of N piecewise linear segments, each valid in the region $F_i \leq f \leq F_{i+1}$; $i=1, \dots, N$, where $F_1 = \alpha$ and $F_{N+1} = \beta$. Let us also denote by S_i the value of the spectrum at F_i , i.e., $S_i = S(F_i)$. Obviously, the quality of approximation to $S(f)$ increases as N increases. The piecewise linear approximation in the log/log scale implies that $S(f)$ is

assumed to have the analytic representation

$$\left. \begin{array}{l} S(f) = S_i \left(\frac{f}{F_i} \right)^{-P_i} \\ \text{for} \\ F_i < f \leq F_{i+1} \end{array} \right\} \quad (11)$$

In (11), the exponent $-P_i$ represents the slope of the line, viz.,

$$-P_i = \frac{\text{slope of line in dB/decade}}{10} \quad (12)$$

Direct substitution of (11) into (10) gives

$$W_1' = \int_{F_1}^{F_{N+1}} \frac{S'(f)}{f} df = \sum_{i=1}^N S_i \cdot F_i^{P_i} \int_{F_i}^{F_{i+1}} \frac{df}{f^{P_i+1}} - \int_{F_1}^{F_{N+1}} \frac{h_0 df}{f}$$

or

$$W_1' = \sum_{i=1}^N \frac{S_i}{P_i} \left[1 - \left(\frac{F_i}{F_{i+1}} \right)^{P_i+1} \right] - h_0 \ln \frac{F_{N+1}}{F_1} \quad (13a)$$

Similarly, we obtain

$$W_2' = \alpha \left\{ \sum_{i=1}^N \frac{S_i}{F_i^{(P_i+1)}} \left[1 - \left(\frac{F_i}{F_{i+1}} \right)^{P_i+1} \right] - h_0 \left[\frac{1}{F_1} - \frac{1}{F_{N+1}} \right] \right\} \quad (13b)$$

and

$$w_3' = \alpha^2 \left\{ \sum_{i=1}^N \frac{S_i}{F_i^{2(P_i+2)}} \left[1 - \left(\frac{F_i}{F_{i+1}} \right)^{P_i+2} \right] - \frac{h_0}{2} \left[\frac{1}{F_1^2} - \frac{1}{F_{N+1}^2} \right] \right\} \quad (13c)$$

Note in the above that, in general, the P_i 's need not be integers.

Comment

The above theory solely derives the LMSE estimate $\hat{S}(f)$ of $S(f)$. However, no care has been taken to account for the fact that $\hat{S}(f)$ should be nonnegative as it represents a spectral density. Indeed, on some occasions, the results provide a negative $\hat{S}(f)$ for some frequency regions. In these cases, the coefficients of the LMSE estimate can serve as good starting values which, after some heuristic small perturbation, produce a good new estimate $\hat{S}^*(f)$. This new $\hat{S}^*(f)$ should also conform with the aforementioned physical constraint of positiveness. The above comments were used in Example 2 following.

Applications

We now apply the previous results to the following two examples.

Example 1

Consider the TCXO phase noise spectral density of Figure 1. The coefficients of $\hat{S}(f)$ were calculated to be

$$\begin{aligned} h_0 &= 0.31622776 \times 10^{-15} \\ h_1 &= 0.39822958 \times 10^{-9} \\ h_2 &= -0.14756626 \times 10^{-7} \\ h_3 &= 0.31740942 \times 10^{-4} \end{aligned}$$

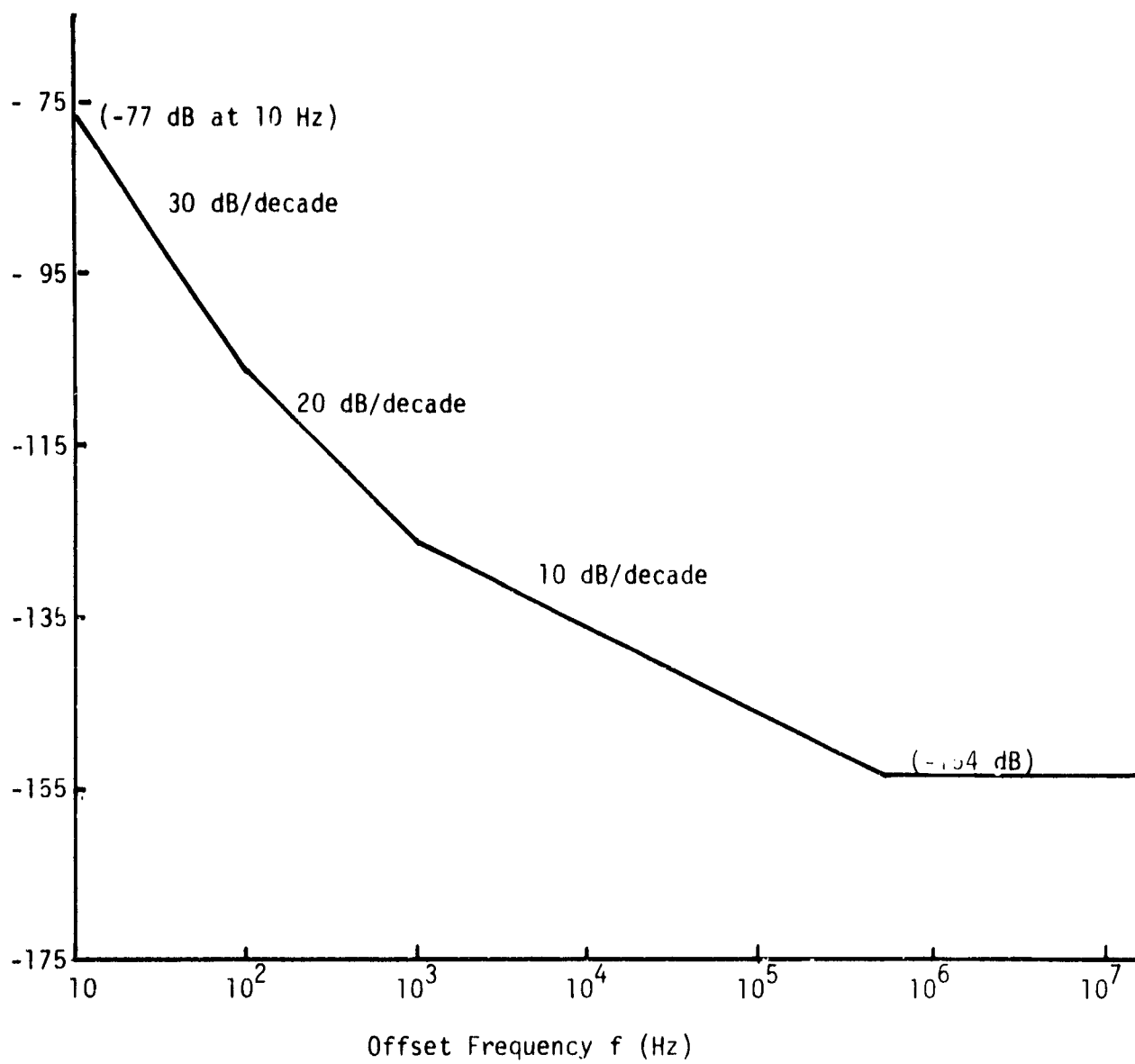


Figure 1. Phase Noise Spectrum of the PI TCXO

Table 1 following compares certain values of $S_{\text{TCXO}}(f)$ with the corresponding ones of $\hat{S}(f)$.

Table 1. Comparison of Estimated and Measured PI TCXO Phase Noise Spectra

Frequency $f(\text{Hz})$	10 Hz	100 Hz	1 kHz	10 kHz	100 kHz	1 MHz
$S_{\text{TCXO}}(f)$ (db)	-75	-105	-125	-135	-145	-155
$\hat{S}(f)$ (dB)	-75	-104.7	-123.8	-134	-144	-155

Example 2

Next we consider the VCXO phase noise spectral density, shown in Figure 2. It was approximated by three piecewise linear segments. Table 2 summarizes the characteristic values considered for the implementation of the previous algorithms.

Table 2. Piecewise Linear Segments Used for Estimating the VCXO Phase Noise Spectrum

n	1	2	3	4
F_n (Hz)	1 Hz	1 kHz	8.1 kHz	1 MHz
S_n (db)	-14	-104	-115	-
$p_n = \frac{\text{dB/decade}}{10}$ (slope)	-3	-1.4	0	-

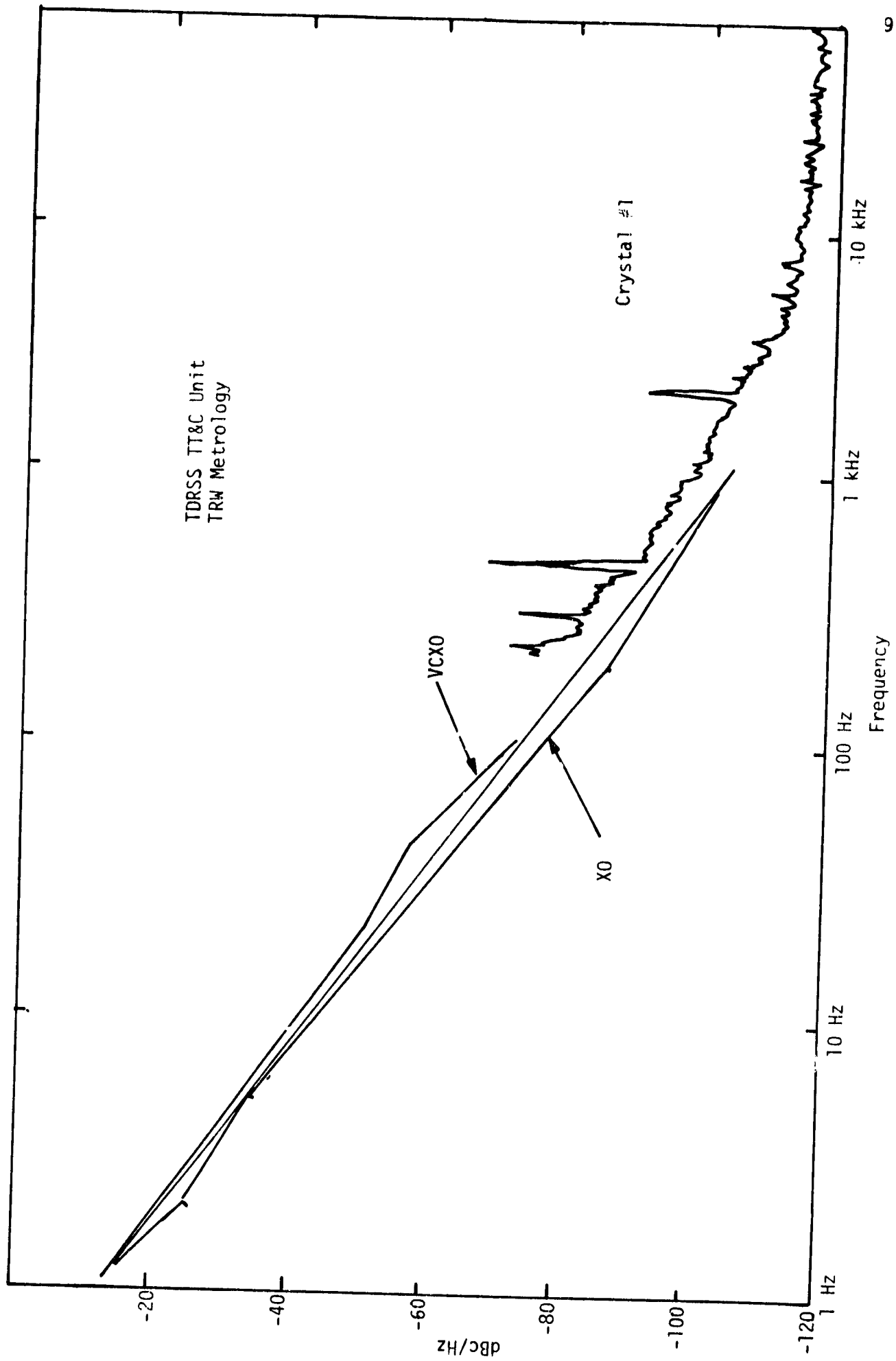


Figure 2. VCX0 Measured Phase Noise Sideband Power Spectral Density

The coefficients were found to be

$$\begin{aligned} h_0 &= 0.31622777 \times 10^{-11} \\ h_1 &= -0.3000000 \times 10^{-7} \\ h_2 &= 0.10874600 \times 10^{-3} \\ h_3 &= 0.39684600 \times 10^{-1} \end{aligned}$$

Table 3 provides a comparison between $S(f)$ and $\hat{S}(f)$ at distinct points for this case.

Table 3. Comparison of Estimated and Measured VCXO Phase Noise Spectra

Frequency $S(\text{Hz})$	1 Hz	10 Hz	100 Hz	1 kHz	10 kHz	100 kHz	1 MHz
$S(f)$ (db)	-14	-44	-74	-104	-115	-115	-115
$\hat{S}(f)$ (db)	-14	-43.9	-73	- 99.2	-118	-115.4	-115

APPENDIX III

PERFORMANCE OF A WIDEBAND PHASE DETECTOR IN THE PRESENCE OF MISMATCHED PHASE SHIFT AND PHASE NOISE

By

Andreas Polydoros

APPENDIX III

PERFORMANCE OF A WIDEBAND PHASE DETECTOR
IN THE PRESENCE OF MISMATCHED PHASE SHIFT AND PHASE NOISE

By

A. Polydoros

Consider the following scheme employed at the PI receiver in Figure 1 where the wideband phase detector is denoted by "A." The switch "S" is merely symbolic: position (a) represents the situation where data are directly phase modulated on the carrier; hence, branch (a) leads to coherent detection of these data. On the other hand, position (b) pictures the case where the data are modulating a suppressed subcarrier which, in turn, phase modulates the carrier. The received signal $r(t)$ is, in both cases, written as

$$r(t) = \sqrt{2P} \sin[\omega_c t + \theta_0 + \beta d(t)] + n(t) \quad (1)$$

where

P = the average transmitted power

ω_c = the carrier frequency

$\theta_0(t)$ = a phase noise process (including doppler, etc.) to be tracked by the receiver PLL

$\beta \triangleq \cos^{-1} m$ is the angle modulation index; m is the modulation factor; $\beta = \pi/2$ corresponds to suppressed carrier modulation

$n(t)$ = bandpass white Gaussian noise with spectral density N_0 W/Hz, and $d(t)$ depends on (a) or (b) of Figure 1.

$$\text{For (a): } d(t) = \sum_{k=-\infty}^{\infty} d_k p(t-kT)$$

where d_k is the data sequence of ± 1 's and $p(t) = \begin{cases} 1, & 0 \leq t \leq T_b \\ 0, & \text{otherwise} \end{cases}$

$$\text{For (b): } d(t) = \sum_{k=-\infty}^{\infty} a_k p(t-kT) \sin(\omega_{sc} t + \theta_{sc})$$

where $\sin(\cdot)$ is a square wave of amplitude ± 1 and a_k is the data sequence of ± 1 's. Hence, in both cases (a) and (b), it follows that $d(t) = \pm 1$ for every t . The assumption of a square-wave subcarrier facilitates the analysis

without being absolutely essential. The phase shift ϕ is required to compensate for an unwanted phase shift introduced by the crystal filter. Due to long-term drift, it inserts a constant mean phase offset at the phase detector A. Let the ϕ -shift device output be

$$z_c(t) = \sqrt{2} \cos[\omega_c t + \hat{\theta}_0]$$

where $\hat{\theta}_0$ is the loop estimate of $\theta_0(t)$. Denoting the loop phase error by $\phi = \theta_0 - \hat{\theta}_0$, we have (neglecting double-frequency terms) that

$$y(t)|_{LP} = r(t) z_c(t)|_{LP} = \sqrt{P} \sin(\beta d(t) + \phi) + n'(t) \quad (2)$$

where $n'(t)$ is lowpass white Gaussian noise with spectral density N_0 . Upon expanding (2), we get

$$y(t)|_{LP} = \sqrt{P_1} \sin \beta d(t) \cos \phi(t) + \sqrt{P_1} \cos \beta d(t) \sin \phi(t) + n'(t) \quad (3)$$

But

$$\sin \beta d(t) = d(t) \sin \beta ; \quad \cos \beta d(t) = \cos \beta$$

since $d(t) = \pm 1$. Therefore,

$$y(t)|_{LP} = \sqrt{P_1} d(t) \sin \beta \cos \phi + \sqrt{P_1} \cos \beta \sin \phi + n'(t)$$

or

$$y(t)|_{LP} = \sqrt{P_1(1-m^2)} d(t) \cos \phi + \sqrt{P_1 m^2} \sin \phi + n'(t) \quad (3')$$

Let us now make the assumption that $\phi(t)$ is relatively slowly varying with respect to $d(t)$ and $n'(t)$ and is to be considered constant, and proceed to examine case (a).

1.0 PHASE-MODULATED CARRIER BY DATA (CASE a)

The decision variable is the output of the ideal I&D filter:

$$y_{a,k} = \frac{1}{T_b} \int_0^{T_b} y(t) dt = \sqrt{(1-m^2)P_1} d_k \cos \phi + \sqrt{P_1 m^2} \sin \phi + N$$

where $N \sim G\left(0, \frac{N_0}{2T_b}\right)$. Hence, the ϕ -conditional bit error probability P_b equals

$$\begin{aligned} P_b^{(\phi)} &= \frac{1}{2} \left[P_r \{ y_{a,k} = -1 \mid d_k = 1 \} + P_r \{ y_{a,k} = 1 \mid d_k = -1 \} \right] \\ &= \frac{1}{2} \left[P_r \left\{ N > \sqrt{(1-m^2)} p_1 \cos \phi + \sqrt{p_1 m^2} \sin \phi \right\} \right. \\ &\quad \left. + P_r \left\{ N > \sqrt{(1-m^2)} p_1 \cos \phi - \sqrt{p_1 m^2} \sin \phi \right\} \right] \end{aligned}$$

or

$$P_b(\phi) = \frac{1}{2} \left\{ Q \left[\sqrt{\frac{2E}{N_0}} \cos(\phi + \psi) \right] + Q \left[\sqrt{\frac{2E}{N_0}} \cos(\phi - \psi) \right] \right\} \quad (4)$$

where $E = PT_b$ and $[\psi = \pi/2 - \beta]$. Note that $\psi = 0$ corresponds to suppressed carrier modulation.

The average \bar{P}_b is obtained by integrating (4) over the pdf of ϕ . Due to the nature of the incoming phase noise process, we can assume that ϕ is Gaussian with some mean m_ϕ (introduced by the phase shift device) and some variance (phase jitter) σ_ϕ^2 . Hence,

$$\bar{P}_b = \frac{1}{2} \int_{-\infty}^{\infty} \frac{d\phi}{\sigma_\phi \sqrt{2\pi}} \exp \left\{ -\frac{(\phi - m_\phi)^2}{2\sigma_\phi^2} \right\} \cdot \left[Q \left[\sqrt{\frac{2E}{N_0}} \cos \left(\phi + \frac{\pi}{2} - \beta \right) \right] + Q \left[\sqrt{\frac{2E}{N_0}} \cos \left(\phi - \frac{\pi}{2} + \beta \right) \right] \right] \quad (5)$$

Before evaluating (5), let us examine case (b).

2.0 PHASE-MODULATED CARRIER BY SUPPRESSED SUBCARRIER (CASE b)

Because of the assumed low-frequency context of ϕ , the broadband BPF at f_{sc} eliminates the $\sin \phi$ term in (3'). Henceforth, in order to distinguish between carrier and subcarrier phase error, we shall denote them by ϕ_c and ϕ_{sc} , respectively.

2.1 Perfect Subcarrier Tracking Loop

For simplicity, let us first assume that the Costas loop at the subcarrier performs perfect tracking, i.e.,

$$\phi_{sc}(K) \triangleq \theta_{sc} - \hat{\theta}_{sc} = 0$$

In this case (not that $n'(t)$ is narrowband Gaussian noise after the BP filter at f_{sc}). We immediately have that the ϕ_c -conditional bit error probability is

$$P_{b,sc}(\phi_c) = Q \left[\sqrt{\frac{2E^*}{N_0}} \cos \phi_c \right] \quad (6)$$

which follows from (4) by setting $\psi = 0$ and defining $E^* = E(1-m^2)$. The random variable ϕ_c always refers to the carrier loop phase error. Hence,

$$\bar{P}_{b,sc} = \frac{1}{\sigma_{\phi_c} \sqrt{2\pi}} \int_{-\infty}^{\infty} Q \left[\sqrt{\frac{2E^*}{N_0}} \cos \phi_c \right] \exp \left\{ -\frac{(\phi_c - m_{\phi_c})^2}{2\sigma_{\phi_c}^2} \right\} d\phi_c \quad (7)$$

In Addendum A, we have derived an equivalent but more manageable expression for $\bar{P}_{b,sc}$, the primary difficulty with (6) being the infinite limits of integration. The result is

$$\bar{P}_{b,sc} = Q \left[\sqrt{\frac{2E^*}{N_0}} \right] + \sqrt{\frac{E^*}{\pi N_0}} \cdot R_c(m_{\phi_c}, \sigma_{\phi_c}) \quad (8a)$$

where

$$R_c(m_{\phi_c}, \sigma_{\phi_c}) \triangleq \sum_{n=-\infty}^{\infty} \int_{-1}^1 \left[Q \left[\frac{2n\pi + \cos^{-1} x - m_{\phi_c}}{\sigma_{\phi_c}} \right] - Q \left[\frac{2(n+1)\pi - \cos^{-1} x - m_{\phi_c}}{\sigma_{\phi_c}} \right] \right] \cdot \exp \left\{ -\frac{E^*}{N_0} x^2 \right\} dx \quad (8b)$$

It is also shown in Addendum A that the limit

$$\lim_{\sigma_{\phi_c} \rightarrow 0} P_{b,sc} = Q \left[\sqrt{\frac{2E}{N_0}} \cos m_{\phi_c} \right]$$

as it should. The limits of integration in (8b) are finite, but the summation is infinite. However, it has been found that for, $m_{\phi} \geq 10^\circ$ and variance $< 10^\circ$, the $n=0$ term suffices to provide a very accurate result. With $m_{\phi}=0^\circ$ and reasonable variance, the summation is very well approximated by twice the zeroth term. At any rate, very few terms are generally sufficient for a very accurate approximation.

2.2 Imperfect Subcarrier Tracking Loop

If we now relax the assumption about the perfect subcarrier loop and denote by ϕ_{sc} the subcarrier phase error, we immediately have that

$$P_b(\phi_c, \phi_{sc}) = Q \left[\sqrt{\frac{2E^*}{N_0}} \cos \phi_c \cos \phi_{sc} \right] \quad (9)$$

Strictly speaking, the random processes ϕ_c and ϕ_{sc} are not statistically independent since ϕ_c influences the operation of the subcarrier Costas loop. However, if the phase noise power level is sufficiently smaller than the noise power level, we can argue that these two processes can be treated as independent, in which case,

$$\bar{P}_b = \int_{-\infty}^{\infty} \frac{1}{\sigma_{\phi_{sc}} \sqrt{2\pi}} \exp \left\{ -\frac{\phi_{sc}^2}{2\sigma_{\phi_{sc}}^2} \right\} \bar{P}(\phi_{sc}) d\phi_{sc} \quad (10)$$

where $\bar{P}(\phi_{sc})$ is derived from (8) by replacing $\sqrt{2E^*/N_0}$ with $\sqrt{2E^*/N_0} \cos \phi_{sc}$. Here we assume Gaussian pdf's for both ϕ_{sc} and ϕ_c , i.e.,

$$\phi_{sc} \sim G(0, \sigma_{\phi_{sc}}^2) \quad ; \quad \phi_c \sim G(m_{\phi_c}, \sigma_{\phi_c}^2)$$

Substituting (8) into (10), it follows that

$$\bar{P}_b = \mathcal{E}_{\phi_{sc}} \left\{ Q \left[\sqrt{\frac{2E^*}{N_0}} \cos \phi_{sc} \right] \right\} + \sqrt{\frac{E^*}{\pi N_0}} \cdot \mathcal{E}_{\phi_{sc}} \left\{ \cos \phi_{sc} \cdot R_c(m_{\phi_c}, \sigma_{\phi_c}) \right\} \quad (11)$$

where $\mathcal{E}_{\phi_{sc}} \{ \cdot \}$ denotes the expectation with respect to ϕ_{sc} . The first term of the right-hand side of (11) is identical to (7) if ϕ_c is replaced by ϕ_{sc} and m_{ϕ_c} is replaced by zero. Hence, substituting (8) into (11) results in

$$\bar{P}_b = Q \left[\sqrt{\frac{2E^*}{N_0}} \right] + \sqrt{\frac{E^*}{\pi N_0}} \cdot \left[R_{sc}(0, \sigma_{\phi_{sc}}) + I(m_{\phi_c}, \sigma_{\phi_c}) \right] \quad (12)$$

where

$$I(m_{\phi_c}, \sigma_{\phi_c}) \triangleq \mathcal{E}_{\phi_{sc}} \left\{ \cos \phi_{sc} \cdot R_c(m_{\phi_c}, \sigma_{\phi_c}; \phi_{sc}) \right\}$$

Unfortunately, $I(m_{\phi_c}, \sigma_{\phi_c})$ is not easily calculated. This is because here R_c is an explicit function of ϕ_{sc} also since the exponential term of (8b) is of the form

$$\exp \left\{ -\frac{E^* x^2}{N_0} \cos^2(\phi_{sc}) \right\}$$

Unless some approximation is employed, the form of I cannot be easily reduced to something analytically tractable. In that perspective, we can calculate a lower bound to the average bit error probability \bar{P}_b of (12) by using the inequality $\cos^2 \phi_{sc} \leq 1$. Indeed, in this case,

$$\exp \left\{ -\frac{E^* x^2}{N_0} \cos^2(\phi_{sc}) \right\} \geq \exp \left\{ -\frac{E^*}{N_0} x^2 \right\}$$

so that (12) reduces to

$$\bar{P}_b \geq Q \left[\sqrt{\frac{2E^*}{N_0}} \right] + \sqrt{\frac{E^*}{\pi N_0}} \left[R_{sc}(0, \sigma_{\phi_{sc}}) + \overline{\cos \phi_{sc}} \cdot R_c(m_{\phi_c}, \sigma_{\phi_c}) \right] \quad (13)$$

In (13), $\overline{\cos \phi_{sc}} \triangleq \mathcal{E}_{\phi_{sc}}\{\cos \phi_{sc}\}$, and $R_c(m_{\phi_c}, \sigma_{\phi_c})$ is given analytically by (8b). To evaluate $\overline{\cos \phi_{sc}}$, let us make use of the expansion

$$\begin{aligned} \cos \phi &= 1 - \frac{\phi^2}{2!} + \frac{\phi^4}{4!} - \dots \\ &= \sum_{n=0}^{\infty} \frac{(-1)^n \phi^{2n}}{(2n)!} \end{aligned}$$

Then,

$$\overline{\cos \phi_{sc}} = \mathcal{E} \left\{ \sum_{n=0}^{\infty} \frac{(-1)^n \phi^{2n}}{(2n)!} \right\} = \sum_{n=0}^{\infty} \frac{(-1)^n \mathcal{E}\{\phi^{2n}\}}{(2n)!}$$

and since

$$\mathcal{E}\{\phi^{2n}\} = \frac{(2n)!}{2^n \cdot n!} \cdot \sigma_{\phi}^{2n}$$

we get

$$\overline{\cos \phi_{sc}} = \sum_{n=0}^{\infty} \frac{(-1)^n}{(2n)!} \frac{(2n)!}{2^n \cdot n!} \sigma_{\phi}^{2n} = \sum_{n=0}^{\infty} \frac{\left(-\frac{\sigma_{\phi}^2}{2}\right)^n}{n!} = \exp\left\{-\frac{\sigma_{\phi}^2}{2}\right\}$$

which could also be obtained through characteristic functions. Therefore, the final result is

$$\boxed{\bar{P}_b \geq Q \left[\sqrt{\frac{2E^*}{N_0}} \right] + \sqrt{\frac{E^*}{\pi N_0}} \left[R_{sc}(0, \sigma_{\phi_{sc}}) + \exp\left\{-\frac{\sigma_{\phi_{sc}}^2}{2}\right\} \cdot R_c(m_{\phi_c}, \sigma_{\phi_c}) \right]} \quad (14)$$

where $R_{sc}(0, \phi_{sc})$ and $R_c(m_{\phi_c}, \sigma_{\phi_c})$ are given by (8b). Note that the lower bound indicated by (14) asymptotically approaches the exact value of $\overline{P_b}$ as $\sigma_{\phi_{sc}} \rightarrow 0$ because, in that case, $\cos^2 \phi_{sc} \rightarrow 1$. For small values of $\sigma_{\phi_{sc}}$, it is conjectured to be sufficiently tight.

ADDENDUM A

Consider the integral

$$P_{b,sc} = \frac{1}{\sigma_\phi \sqrt{2\pi}} \int_{-\infty}^{\infty} Q\left(\sqrt{\frac{2E}{N_0}} \cos \phi\right) \exp\left\{-\frac{(\phi-m_\phi)^2}{2\sigma_\phi^2}\right\} d\phi \quad (A1)$$

with

$$Q(x) = \frac{1}{\sqrt{2\pi}} \int_x^{\infty} \exp\left\{-\frac{z^2}{2}\right\} dz$$

Then (A1) can be rewritten as

$$P_{b,sc} = \frac{1}{2\pi\sigma_\phi} \int_{-\infty}^{\infty} \left[\int_{\sqrt{\frac{2E}{N_0}} \cos \phi}^{\infty} \exp\left\{-\tau^2/2\right\} d\tau \right] \exp\left\{-\frac{(\phi-m_\phi)^2}{2\sigma_\phi^2}\right\} d\phi \quad (A2)$$

By a careful look at the region of integration in the two-dimensional plane (τ, ϕ) , it follows that we can perform the integration in strips parallel to the ϕ axis rather than to the τ axis, as (A2) suggests. The integral can then be split into two parts, depending on the position of the strip (see Figure A.1)

$$P_{b,sc} = \frac{1}{2\pi\sigma_\phi} \int_{-\infty}^{\infty} \int_{\sqrt{\frac{2E}{N_0}} \cos \phi}^{\infty} \exp\left\{-\tau^2/2\right\} \cdot \exp\left\{-\frac{(\phi-m_\phi)^2}{2\sigma_\phi^2}\right\} d\tau d\phi$$

$$+ \sum_{n=-\infty}^{\infty} \frac{1}{2\pi\sigma_\phi} \int_{-\sqrt{\frac{2E}{N_0}}}^{\sqrt{\frac{2E}{N_0}}} \left\{ \int_{\phi_L(\tau)}^{\phi_V(\tau)} \exp\left\{-\frac{(\phi-m_\phi)^2}{2\sigma_\phi^2}\right\} d\phi \right\} \exp\left\{-\tau^2/2\right\} d\tau$$

where

$$\phi_L(\tau) = \cos^{-1}\left(\tau/\sqrt{\frac{2E}{N_0}}\right) + 2n\pi \quad ; \quad \phi_V(\tau) = (2n+1)\pi - \cos^{-1}\left(\tau/\sqrt{\frac{2E}{N_0}}\right)$$

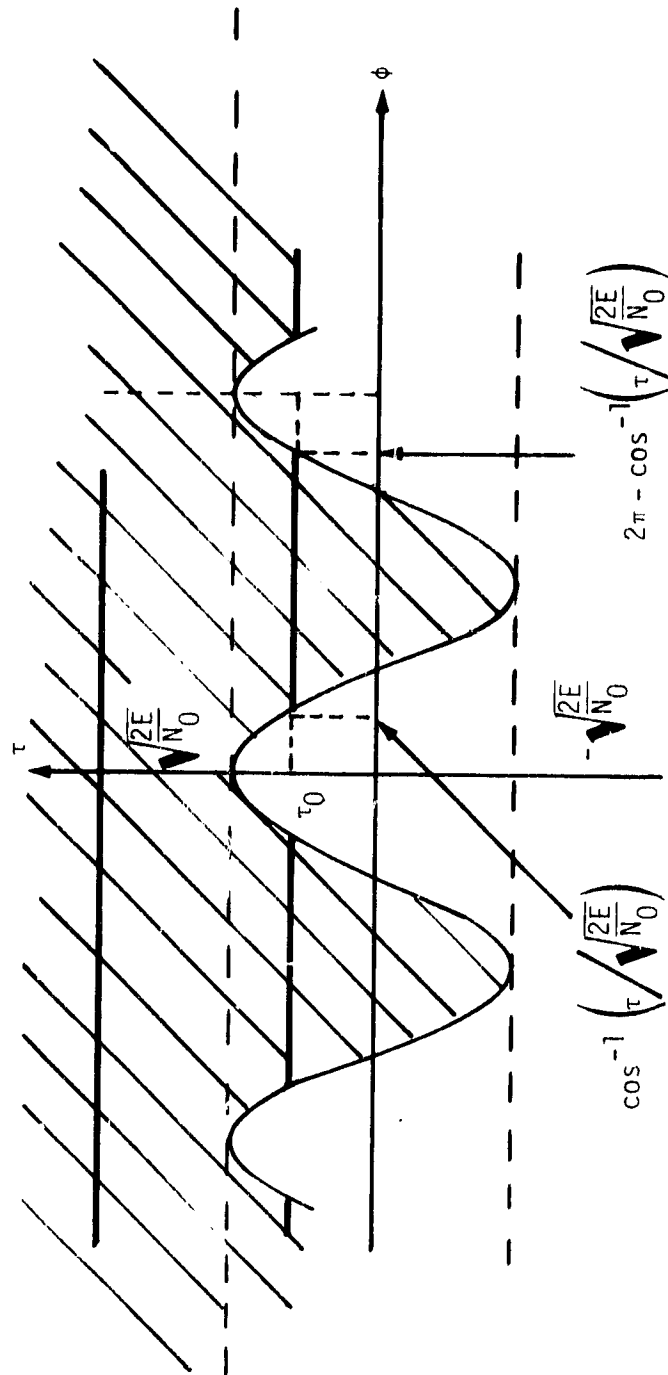


Figure A.1. Region of Integration for Equation (A2)

or

$$p_{b,sc} = Q \left[\sqrt{\frac{2E}{N_0}} \right] + \sqrt{\frac{2E}{N_0}} \sum_{n=-\infty}^{\infty} \frac{1}{2\pi\sigma_\phi} \int_{-1}^1 \left\{ \int_{\cos^{-1}x + 2n}^{(2n+1)\pi - \cos^{-1}x} \exp \left\{ -\frac{(\phi - m_\phi)^2}{2\sigma_\phi^2} \right\} d\phi \right\} \exp \left\{ -\frac{E}{N_0} \cdot x^2 \right\} dx \quad (A3)$$

since the first integral does not depend on ϕ . Finally, normalizing the random variable ϕ yields the result

$$p_{b,sc} = Q \left[\sqrt{\frac{2E}{N_0}} \right] + \sqrt{\frac{E}{\pi N_0}} \sum_{n=-\infty}^{\infty} \int_{-1}^1 \left\{ Q \left[\frac{2n\pi + \cos^{-1}x - m_\phi}{\sigma_\phi} \right] - Q \left[\frac{2(n+1)\pi - \cos^{-1}x - m_\phi}{\sigma_\phi} \right] \right\} \exp \left\{ -\frac{E}{N_0} \cdot x^2 \right\} dx \quad (A4)$$

where $\cos^{-1}x$ belongs to $[0, \pi]$.

For all practical values tested, it seemed that very fast convergence was achieved by one or, at the most, two terms of the infinite sum in (A4). Hence, this result offers a substantial reduction in computational effort as compared to the original infinite integral. To check for its validity, let us examine the limiting case where $\sigma_\phi \rightarrow 0$. In this case, the random variable ϕ degenerates to a constant m_ϕ , and the corresponding result should be

$$\overline{P}_{b,sc} = Q \left[\sqrt{\frac{2E}{N_0}} \cos m_\phi \right] \quad (A5)$$

Indeed,

$$\lim_{\sigma_\phi \rightarrow 0} \overline{P}_{b,sc} = Q \left[\sqrt{\frac{2E}{N_0}} \right] + \sqrt{\frac{E}{\pi N_0}} \lim_{\sigma_\phi \rightarrow 0} R_c(m_{\phi_c}, \sigma_{\phi_c}) \quad (A6)$$

where

$$R_c(m_{\phi_c}, \sigma_{\phi_c}) = \sum_{n=-\infty}^{\infty} \int_{-1}^1 \left\{ Q \left[\frac{2n\pi + \cos^{-1} x - m_\phi}{\sigma_\phi} \right] - Q \left[\frac{2(n+1)\pi - \cos^{-1} x - m_\phi}{\sigma_\phi} \right] \right\} \\ \times \exp \left\{ -\frac{E}{N_0} x^2 \right\} dx \quad (A7)$$

Considering $0 \leq m_\phi < \pi$, then for

$$n \geq 1 \Rightarrow \begin{cases} 2n\pi + \cos^{-1} x - m_\phi > 0 \\ 2(n+1)\pi + \cos^{-1} x - m_\phi > 0 \end{cases}$$

and

$$n \leq -1 \Rightarrow \begin{cases} 2n\pi + \cos^{-1} x - m_\phi < 0 \\ 2(n+1)\pi - \cos^{-1} x - m_\phi < 0 \end{cases}$$

Now since

$$\lim_{x \rightarrow 0^+} Q\left(\frac{\alpha}{x}\right) = \frac{1}{2} [1 - \operatorname{sgn} \alpha]$$

the $|n| \geq 1$ terms of the summation (A7) vanish as $\sigma_\phi \rightarrow 0$. The only remaining term is for $n = 0$. But

$$\lim_{\sigma_\phi \rightarrow 0} Q \left[\frac{2\pi - \cos^{-1} x - m_\phi}{\sigma_\phi} \right] = 0$$

since

$$2\pi - \cos^{-1} x - m_\phi > 0$$

Furthermore,

$$\cos^{-1} x - m_\phi = \begin{cases} > 0 ; -1 < x < \cos m_\phi \\ < 0 ; \cos m_\phi < x < 1 \end{cases}$$

so that

$$\lim_{\sigma_\phi \rightarrow 0} Q \left[\frac{\cos^{-1} x - m_\phi}{\sigma_\phi} \right] = \begin{cases} 0 ; -1 < x < \cos m_\phi \\ 1 ; \cos m_\phi < x < 1 \end{cases} \quad (A8)$$

Substituting (A8) into (A6) and (A7), it follows that

$$\begin{aligned} \lim_{\sigma_\phi \rightarrow 0} P_E &= Q \left[\sqrt{\frac{2E}{N_0}} \right] + \sqrt{\frac{E}{\pi N_0}} \int_{\cos m_\phi}^1 \exp \left\{ -\frac{E}{N_0} x^2 \right\} dx \\ &= Q \left[\sqrt{\frac{2E}{N_0}} \right] + \frac{1}{\sqrt{2\pi}} \int_{\sqrt{\frac{2E}{N_0}} \cos m_\phi}^{\sqrt{\frac{2E}{N_0}}} \exp \left\{ -z^2/2 \right\} dz \\ &= \frac{1}{\sqrt{2\pi}} \int_{\sqrt{\frac{2E}{N_0}}}^{\infty} \exp \left\{ -z^2/2 \right\} dz + \frac{1}{\sqrt{2\pi}} \int_{\sqrt{\frac{2E}{N_0}} \cos m_\phi}^{\sqrt{\frac{2E}{N_0}}} \exp \left\{ -z^2/2 \right\} dz \\ &= \frac{1}{\sqrt{2\pi}} \int_{\sqrt{\frac{2E}{N_0}} \cos m_\phi}^{\infty} \exp \left\{ -z^2/2 \right\} dz = Q \left[\sqrt{\frac{2E}{N_0}} \cos m_\phi \right] \end{aligned}$$

in agreement with (A5).

Equation (A4) suggests the following interpretation: The second term of the right-hand side represents the additional penalty in performance over the perfectly coherent Gaussian channel introduced by the presence of a noisy phase reference with Gaussian phase error.

APPENDIX IV

THE EFFECT OF TRANSMITTER PHASE ASYMMETRY ON UQPSK SYSTEMS WITH NOISY RECEIVER PHASE REFERENCE

By

Andreas Polydoros

APPENDIX IV

THE EFFECT OF TRANSMITTER PHASE ASYMMETRY ON UQPSK SYSTEMS WITH NOISY RECEIVER PHASE REFERENCE

By

Andreas Polydoros

1.0 INTRODUCTION AND SUMMARY

This appendix is a follow-up of [1], and examines the degradation in performance of a digital phase shift implementation of an unbalanced QPSK system due to transmitter phase imbalance. Such a deviation from nominal operating conditions, which is modeled and analyzed in Section 2.0, can possibly arise due to the different path delays involved in the digital circuitry which implements the phase selection procedure at the transmitter. A more thorough discussion and details on this transmitter structure can be found in [2] and [3].

Once the asymmetry model and its associated problem are formulated, the line of analysis is very similar to the one in [1]; therefore, many intermediate details will be omitted. Nevertheless, the final results for the error probability are substantially different than those in [1] although both data and phase asymmetry belong to the same class of "timing" or "horizontal" anomalies as opposed to the "amplitude" or "vertical" anomalies. The ultimate goal of this research would be to combine these two asymmetries although, at this point, it seems that a rigorous analysis of this sort is a very complicated task.

The parameter which measures the degree of asymmetry is S_θ , by which we denote the deviation from the nominal angle $2\theta_0$ between the transmitted points (see Figures 1 and 2). Because of the tracking loop phase error ϕ present at the receiver, S_θ contributes to both self-degradation and cross talk degradation for each channel. As will be shown, the contribution of S_θ to the overall degradation is also a function of θ_0 , the nominal transmission angle. As θ_0 decreases (which means that the power split between the I and Q channels increases in favor of the stronger channel), the severity of the effect of S_θ increases proportionally to $\cot \theta_0$. Hence, for a strongly unbalanced QPSK system, the impact of transmitter phase asymmetry may become quite noticeable.

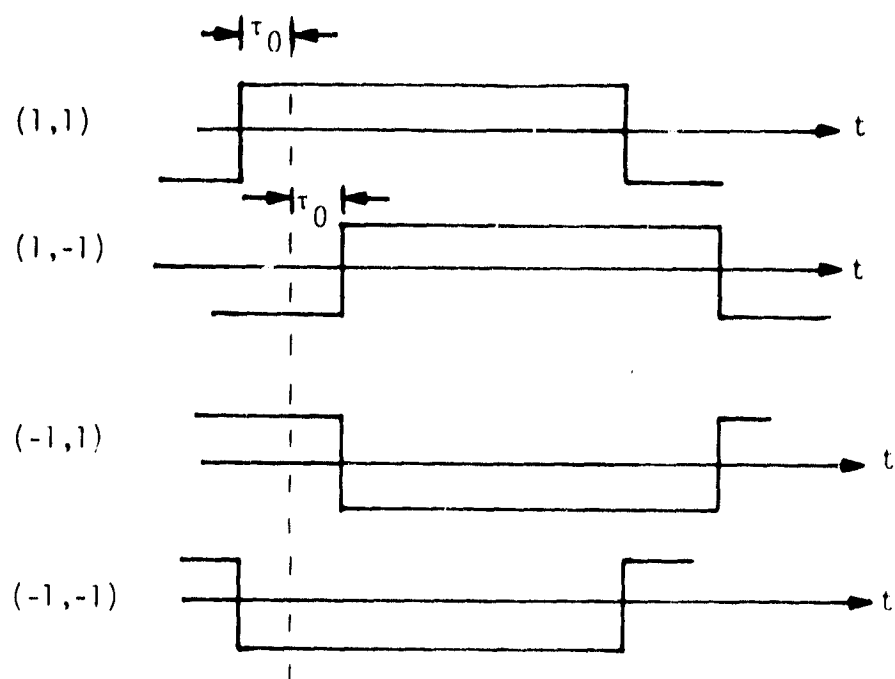


Figure 1a. Nominal Pulse Delays

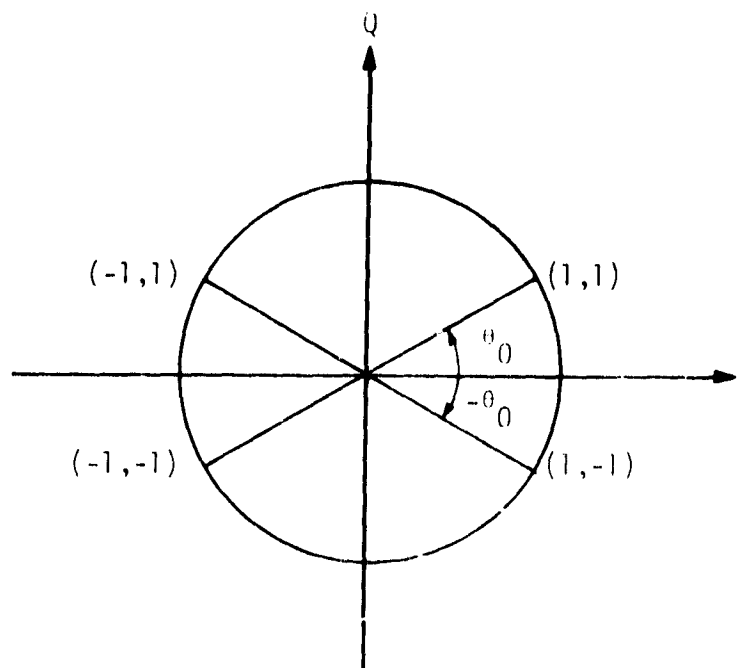


Figure 1b. Nominal Transmission Angles

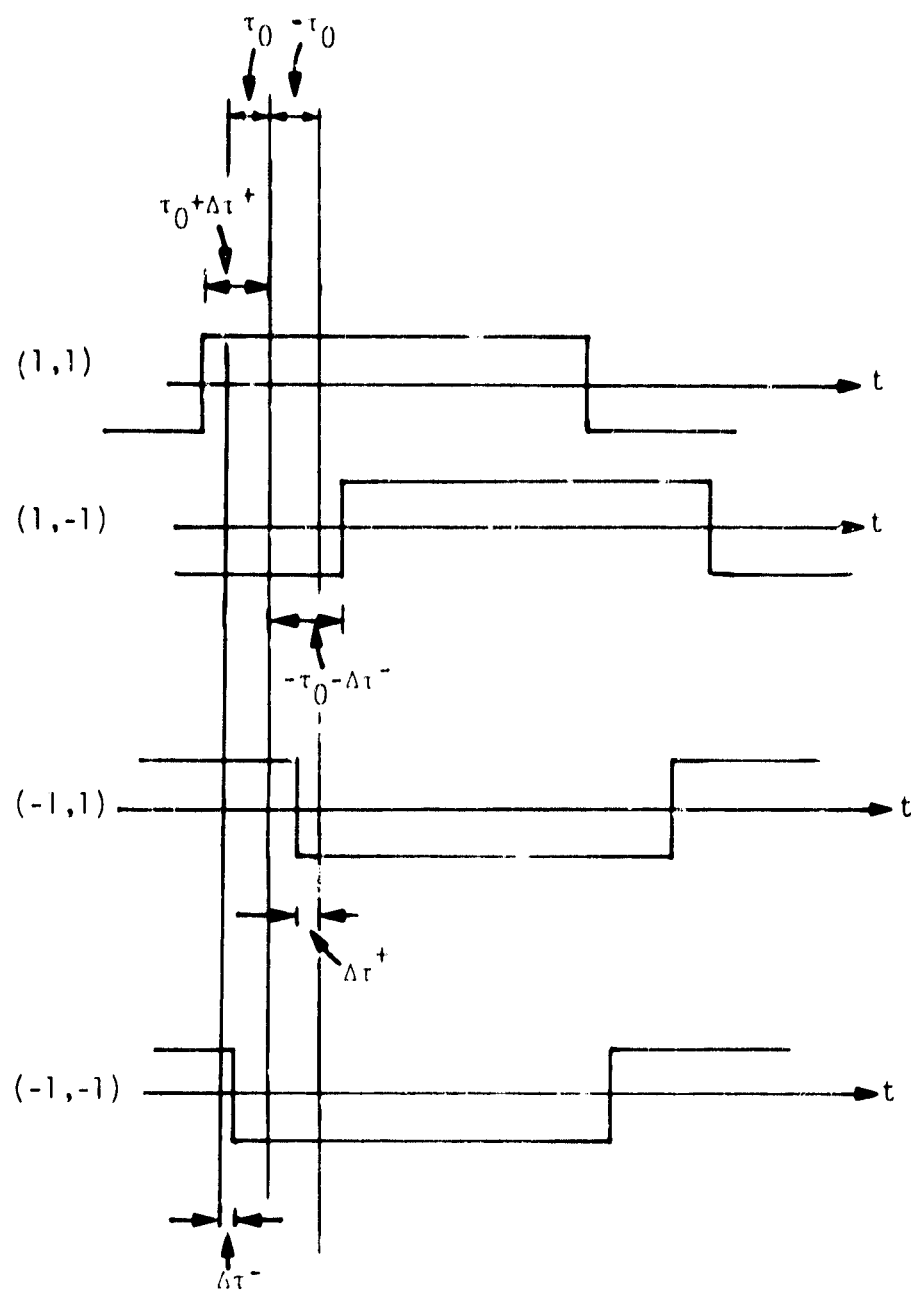


Figure 2a. Pulse Delays with Asymmetry Included

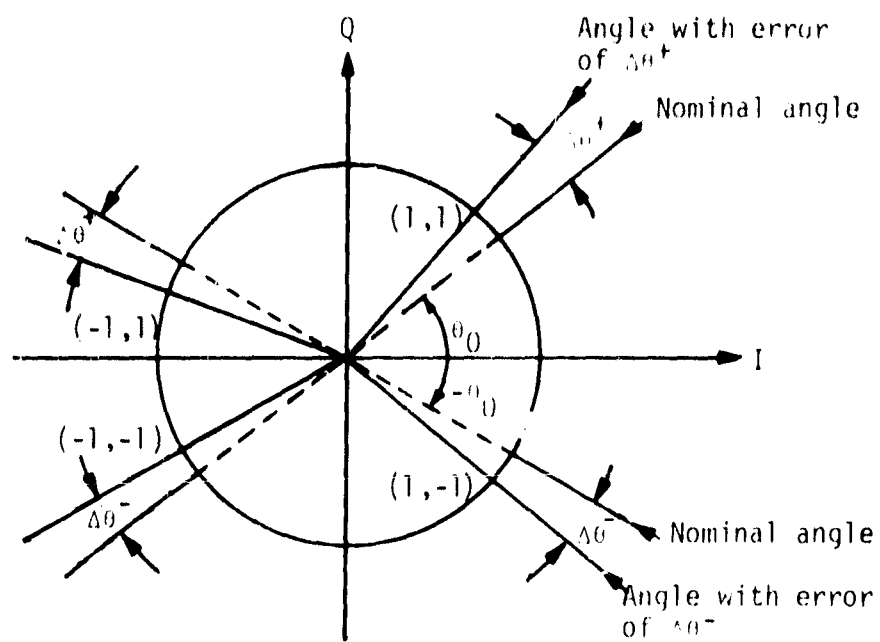


Figure 2b. Transmission Angles under Asymmetry

In the next section (2.0), we describe the asymmetry model and work out the analysis for the high and low data rate channels. The ϕ -conditional error probability is given by equations (28) and (29), respectively. Through these, the degradation in dB as a function of S_{θ} has been evaluated and is shown in Figures 3 and 4 for the two channels. The curves are parameterized by m_{ϕ} , the mean value of the random variable (RV) ϕ . To obtain the average bit error probability (BEP), one should average over the probability density function (PDF) of the RV ϕ , $P_{\phi}(\phi)$. As commented in [1], an explicit expression for $P_{\phi}(\phi)$ is rather difficult to derive for sophisticated tracking loops; hence, we have to resort to some other alternative. In [1], a truncated Taylor series expansion was used which provides credible results as long as the variance of ϕ is small. The easiest approach, however, is to assume a high signal-to-noise ratio (SNR) environment within the loop, in which case the m_{ϕ} -conditional BEP stands as a close estimate of the average BEP. We shall use the latter approach here which will provide us with a feeling for the order of degradation under different operating conditions. Judging from the results in [1], we conjecture an average increase of 20-30% in dB loss if the variance of ϕ is taken into consideration.

We should also mention here that the model encountered in this report is probably not the most general one regarding transmitter phase asymmetry. A more elaborate model would also include independent delays for points $(-1,-1)$ and $(-1,1)$ of Figure 1. The analysis of such a model, although tedious, should follow the guidelines of the present analysis in a straightforward manner.

The plots in Figures 3 and 4 are based on a typical value of $\theta_0 = 26.6^\circ$. This value of θ_0 corresponds to a power ratio at the receiver equal to 4. We should point out here that the power ratio at the transmitter is quite different (in fact, it is approximately 2.4). This difference is due to the particular digital phase shift subcarrier modulation scheme used, in combination with the bandpass (BP) filter employed in front of the subcarrier tracking loop. We will elaborate on that later.

As expected, the low data rate channel (LDRCH) is by far more sensitive to the asymmetry than the high data rate channel (HDRCH). This is mainly because the interchannel interference manifests itself stronger

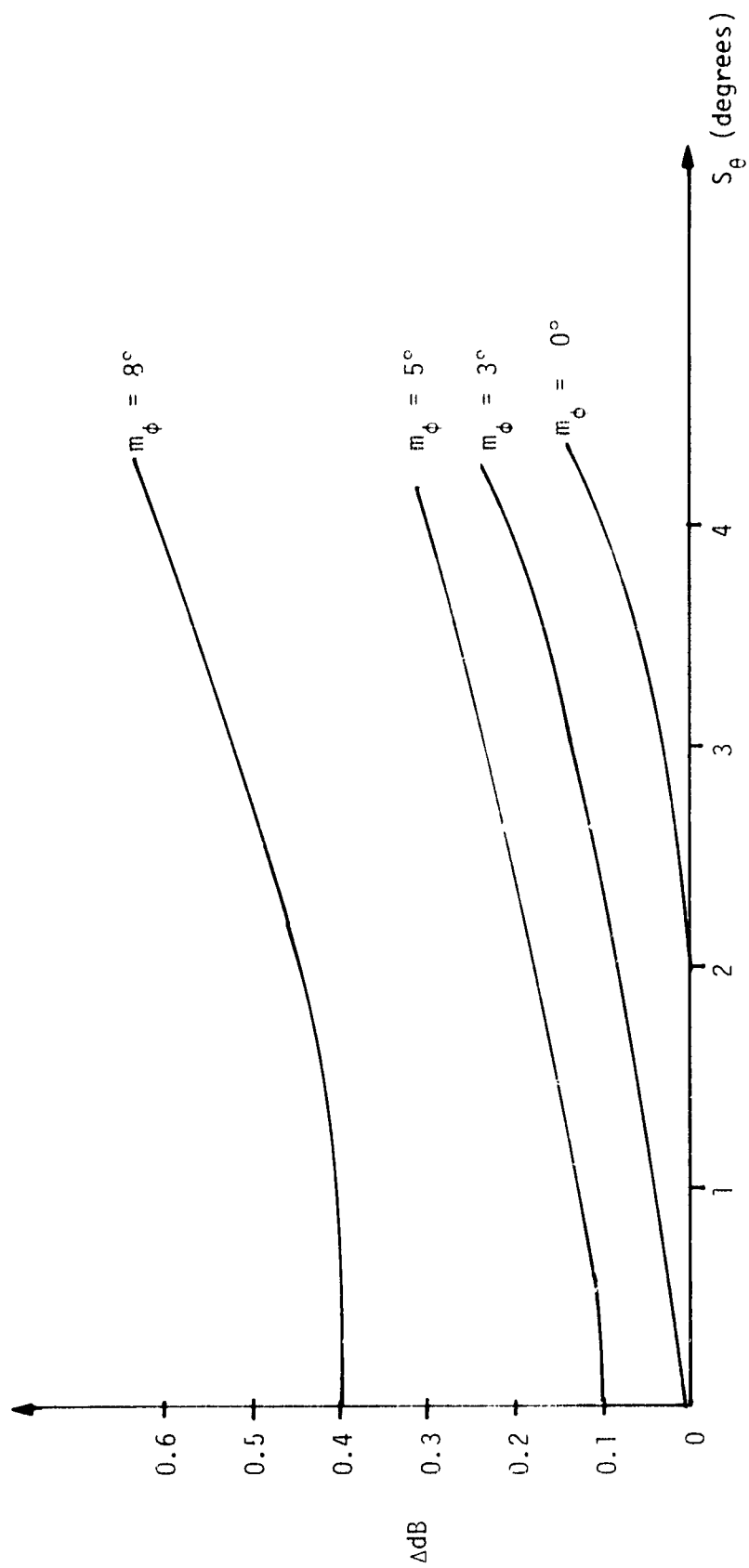


Figure 3. ΔdB Loss Versus S_θ for the High Data Rate Channel 2

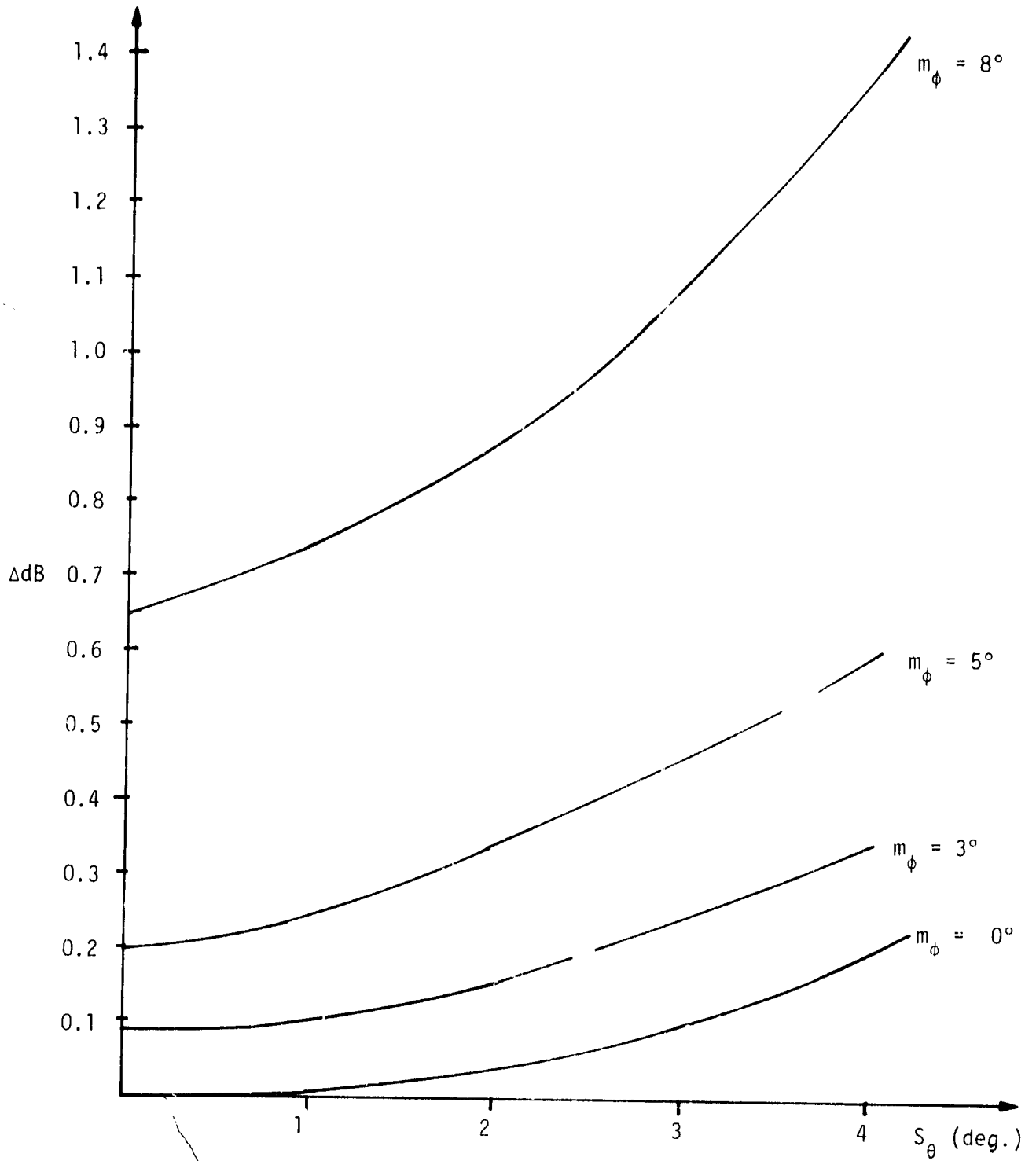


Figure 4. ΔdB Loss Versus S_θ for the Low Data Rate Channel 1

in the LDRCH than in the HDRCH. For different values of $m_\phi = 0^\circ, 3^\circ, 5^\circ$, and 8° , the range of loss for the LDRCH is 0-1.4 dB while, for the HDRCH, it is 0-0.6 dB (see Figures 3 and 4). Notice that, for $S_\theta = 0^\circ$, the plot values coincide with the corresponding ones of Figures 9 and 10 of [4].

2.0 ASYMMETRY MODEL AND ANALYSIS

Under nominal transmitting conditions for the digital phase shift subcarrier modulation scheme, the modulator output is

$$C(t) = \sqrt{P_s} \sum \sin [\omega_{sc} t + \theta(t)] \quad (1)$$

where

$$\theta(t) \triangleq m_2(t) m_3(t) \theta_0 - \left(\frac{m_2(t)-1}{2} \right) \cdot \pi \quad (2)$$

The nominal transmission angle θ_0 is shown in Figure 1b. It corresponds to a nominal pulse delay of τ_0 sec, as shown in Figure 1a. The functions $m_2(t)$ and $m_3(t)$ represent the digital data streams for the two channels, respectively.

We now adopt the following asymmetry model. We assume that the delay of the (1,1) and (-1,1) pulses are distorted by an additional amount of $\Delta\tau^+$ sec in the manner shown in Figure 2a. Similarly, we assume that the the pulses (1,-1) and (-1,-1) are delayed by an additional $\Delta\tau^-$ sec, also shown in Figure 2a. We furthermore assume that the two parameters $\Delta\tau^+$ and $\Delta\tau^-$ are independent and of arbitrary (but small, compared to τ_0) value. Although a more elaborate model would include individual delays for each pulse, the present model does provide sufficient insight about the problem. The corresponding phase deviations are denoted by $\Delta\theta^+$ and $\Delta\theta^-$, respectively, and are shown in Figure 2b.

In the presence of asymmetry, the transmitted subcarrier signal is again

$$C_a(t) = \sqrt{P_s} \sum \sin (\omega_{sc} t + \theta_a(t)) \quad (3)$$

where now

$$\theta_a(t) \triangleq m_2(t)m_3(t) - \left(\frac{m_2(t)-1}{2}\right)\pi + \left(\frac{m_3(t)+1}{2}\right) \cdot \Delta\theta^+ + \left(\frac{m_3(t)-1}{2}\right) \cdot \Delta\theta^- \quad (4)$$

or, using (2),

$$\theta_a(t) = \theta(t) + m_3(t) \cdot S_\theta + \Delta\theta \quad (5)$$

where we have defined the average (phase) distortion sum S_θ and the average distortion difference $\Delta\theta$ by

$$S_\theta = \frac{\Delta\theta^+ + \Delta\theta^-}{2} \quad (6a)$$

and

$$\Delta\theta = \frac{\Delta\theta^+ - \Delta\theta^-}{2} \quad (6b)$$

Since we assume that the carrier modulation and demodulation process are perfectly performed (i.e., we do not consider any carrier-tracking loop phase error appearing in our model), we can focus on the following received signal just after the bandpass filter at the input of the subcarrier tracking loop (see Figure 4 of [1]):

$$x(t) = C_1(t) + n_{BP}(t) \quad (7)$$

where $C_1(t)$ is the bandpass-filtered version of $C(t)$ (where only the fundamental is retained) and $n_{BP}(t)$ is bandpass noise represented by

$$n_{BP}(t) = \sqrt{2} \left[N_C(t) \cos(\omega_{SC}t + \Delta\theta) - N_S(t) \sin(\omega_{SC}t + \Delta\theta) \right] \quad (8)$$

In (8), $N_C(t)$ and $N_S(t)$ are approximately statistically independent white Gaussian noise processes with single-sided spectral density N_0 W/Hz and single-sided bandwidth $B_H < \omega_{SC}/2\pi$ Hz.

If we expand $\sin(\cdot)$ into a Fourier series and keep only the first harmonic, (1) gives

$$\begin{aligned} C_1(t) &= \sqrt{P_s} \cdot \frac{4}{\pi} \cdot \sin \left[\omega_{sc} t + \theta_a(t) \right] \\ &= \frac{4\sqrt{P_s}}{\pi} \left[\sin \omega_{sc} t \cos \theta_a(t) + \cos \omega_{sc} t \sin \theta_a(t) \right] \end{aligned} \quad (9)$$

From (5), it follows that

$$\begin{aligned} \cos \theta_a(t) &= \cos \left[\theta(t) + S_\theta \cdot m_3(t) + \Delta\theta \right] \\ &= \cos \left[\theta(t) + S_\theta m_3(t) \right] \cos \Delta\theta - \sin \left[\theta(t) + S_\theta m_3(t) \right] \sin \Delta\theta \end{aligned} \quad (10a)$$

and

$$\sin \theta_a(t) = \sin \left[\theta(t) + S_\theta m_3(t) \right] \cos \Delta\theta + \cos \left[\theta(t) + S_\theta m_3(t) \right] \sin \Delta\theta \quad (10b)$$

Furthermore,

$$\begin{aligned} \sin \left[\theta(t) + S_\theta m_3(t) \right] &= \sin \theta(t) \cos (S_\theta m_3(t)) + \cos \theta(t) \sin (S_\theta m_3(t)) \\ &= \sin \theta(t) \cos S_\theta + m_3(t) \cos \theta(t) \sin S_\theta \end{aligned} \quad (11a)$$

and

$$\begin{aligned} \cos \left[\theta(t) + S_\theta m_3(t) \right] &= \cos \theta(t) \cos (S_\theta m_3(t)) - \sin \theta(t) \sin (S_\theta m_3(t)) \\ &= \cos \theta(t) \cos S_\theta - m_3(t) \sin \theta(t) \sin S_\theta \end{aligned} \quad (11b)$$

Also, from (2), it follows that

$$\begin{aligned} \cos \theta(t) &= \cos \left[m_2(t) m_3(t) \theta_0 \right] \cos \left[\frac{m_2(t)-1}{2} \cdot \pi \right] \\ &\quad + \sin \left[m_2(t) m_3(t) \theta_0 \right] \sin \left[\frac{m_2(t)-1}{2} \cdot \pi \right] \end{aligned} \quad (12)$$

But

$$\cos \left[\frac{\bar{m}_2(t)-1}{2} \cdot \pi \right] = m_2(t) \quad (13a)$$

and

$$\sin \left[\frac{\bar{m}_2(t)-1}{2} \cdot \pi \right] = 0 \quad (13b)$$

From (12) and (13), we get

$$\cos \theta(t) = m_2(t) \cos \theta_0 \quad (14a)$$

Similarly, we have [using (13)] that

$$\begin{aligned} \sin \theta(t) &= \sin \left[m_2(t) m_3(t) \theta_0 \right] \cos \left[\frac{\bar{m}_2(t)-1}{2} \cdot \pi \right] \\ &\quad + \cos \left[m_2(t) m_3(t) \theta_0 \right] \cdot \sin \left[\frac{\bar{m}_2(t)-1}{2} \cdot \pi \right] \\ &= m_2^2(t) m_3(t) \sin \theta_0 = m_3(t) \sin \theta_0 \end{aligned} \quad (14b)$$

Equations (11) and (14) combined yield

$$\cos \left[\theta(t) + S_\theta m_3(t) \right] = m_2(t) \cos \theta_0 \cos S_\theta - \sin \theta_0 \sin S_\theta \triangleq A_2^* \quad (15a)$$

and

$$\sin \left[\theta(t) + S_\theta m_3(t) \right] = m_3(t) \sin \theta_0 \cos S_\theta + m_2(t) m_3(t) \cos \theta_0 \sin S_\theta \triangleq A_3^* \quad (15b)$$

Substituting (15) back into (10) gives

$$\cos \theta_a(t) = A_2^* \cos \Delta \theta - A_3^* \sin \Delta \theta \quad (16a)$$

and

$$\sin \theta_a(t) = A_3^* \cos \Delta \theta + A_2^* \sin \Delta \theta \quad (16b)$$

Then, from (9) and (16), we get

$$\begin{aligned} C_1(t) &= \frac{4\sqrt{P_s}}{\pi} \left[A_2^* \cos \Delta \theta \sin \omega_{sc} t - A_3^* \sin \Delta \theta \sin \omega_{sc} t + A_3^* \cos \Delta \theta \cos \omega_{sc} t \right. \\ &\quad \left. + A_2^* \sin \Delta \theta \cos \omega_{sc} t \right] \\ &= \frac{4\sqrt{P_s}}{\pi} \left[A_2^* \sin(\omega_{sc} t + \Delta \theta) + A_3^* \cos(\omega_{sc} t + \Delta \theta) \right] \end{aligned} \quad (17)$$

In order to parallel the present results with the corresponding ones in [1], let us define

$$P_{2r} = \left[\frac{1}{2} \left(\frac{4}{\pi} \right)^2 \cdot \cos^2 \theta_0 \right] P_s \quad (18a)$$

and

$$P_{3r} = \left[\frac{1}{2} \left(\frac{4}{\pi} \right)^2 \sin^2 \theta_0 \right] P_s \quad (18b)$$

in accordance with (13) and (14) of [1]. Then, using the definitions in (15) along with (18), (17) is reformed to

$$C_1(t) = \sqrt{2P_{2r}} \cdot A_2 \cdot \sin[\omega_{sc} t + \Delta \theta] + \sqrt{2P_{3r}} \cdot A_3 \cdot \cos[\omega_{sc} t + \Delta \theta] \quad (19)$$

where we have defined

$$A_2 \triangleq m_2(t) \cos S_\theta - \tan \theta_0 \cdot \sin S_\theta \quad (20a)$$

and

$$A_3 \triangleq m_3(t) \cos S_\theta + m_2(t) m_3(t) \cdot \cot \theta_0 \cdot \sin S_\theta \quad (20b)$$

Certain interesting comments can be made about the form of $C_1(t)$ as in (19), particularly in connection with the corresponding waveform $C_1(t)$ of (15) in [1]. First, let us note that the nominal power ratio at the receiver (i.e., with $S_\theta = 0$) is again

$$\frac{P_{2r}}{P_{3r}} = \left(\frac{P_2}{P_3} \right)_{\text{receiver}} = \cot^2 \theta_0$$

while the transmitted power ratio for this particular implementation can be shown to be [1]

$$\left(\frac{P_2}{P_3} \right)_{\text{transmitter}} = \frac{1 - \frac{2\theta_0}{\pi}}{\frac{2}{\pi} \theta_0} \quad ; \quad \theta_0 \text{ in radians}$$

For a nominal transmission angle $\theta_0 = 26.6^\circ$, the receiver power ratio is 4 while the transmitter power ratio is approximately 2.4. In other words, the cascade of the digital phase shift realization of the transmitter and bandpass filter at the receiver creates a power shift which favors the stronger channel, and this fact should be taken into account when designing the system. Furthermore, the appearance of the phase asymmetry slightly changes the power imbalance. To show this, let us observe that, under nominal conditions ($S_\theta = 0$), the ratio

$$\frac{\text{var}\{A_2\}}{\text{var}\{A_3\}} = \frac{\cos^2 S_\theta \cdot E\{m_2^2(t)\}}{\cos^2 S_\theta \cdot E\{m_3^2(t)\}} = 1$$

where $E\{\cdot\}$ means "expected value of (\cdot) ." When $S_\theta \neq 0$, it follows from (20) that

$$\text{var}\{A_2\} = \cos^2 S_\theta$$

while

$$\begin{aligned} \text{var}\{A_3\} &= E\left\{m_3^2(t) \cdot (\cos S_\theta + m_2(t) \cot \theta_0 \cdot \sin S_\theta)^2\right\} \\ &= \cos^2 S_\theta + \cot^2 \theta_0 \cdot \sin^2 S_\theta \end{aligned}$$

so that the ratio is

$$\frac{\text{var}\{A_2\}}{\text{var}\{A_3\}} = \frac{\cos^2 S_\theta}{\cos^2 S_\theta + \cot^2 \theta_0 \sin^2 S_\theta} \quad (21)$$

as shown in Figure 5.

For $\theta_0 = 26.6^\circ$ and S_θ in the range of interest $0-4^\circ$, the ratio varies between 1 and 0.98. Hence, we conclude that, for this particular case, the power imbalance due to phase asymmetry is negligible.

It is also interesting to note that, in contrast with (1b) of [1], the coefficient A_3 of the in-phase component of the subcarrier depends on both data streams $m_2(t)$ and $m_3(t)$. This will inevitably affect the final expression for the average biphase error probability, to be derived later.

Finally, we see from (19) that the subcarrier phase has been altered by an amount of $\Delta\theta^\circ$. We then expect that the tracking loop will lock at $\Delta\theta$ with a phase error $\phi(t)$, which we assume to be very slowly varying so that it can be treated as a constant over the baud intervals. The coherent reference signals are assumed to be of the form

$$r_c(t) = \cos[\omega_{sc}t + \Delta\theta - \phi] \quad (22a)$$

$$r_s(t) = \sin[\omega_{sc}t + \Delta\theta - \phi] \quad (22b)$$

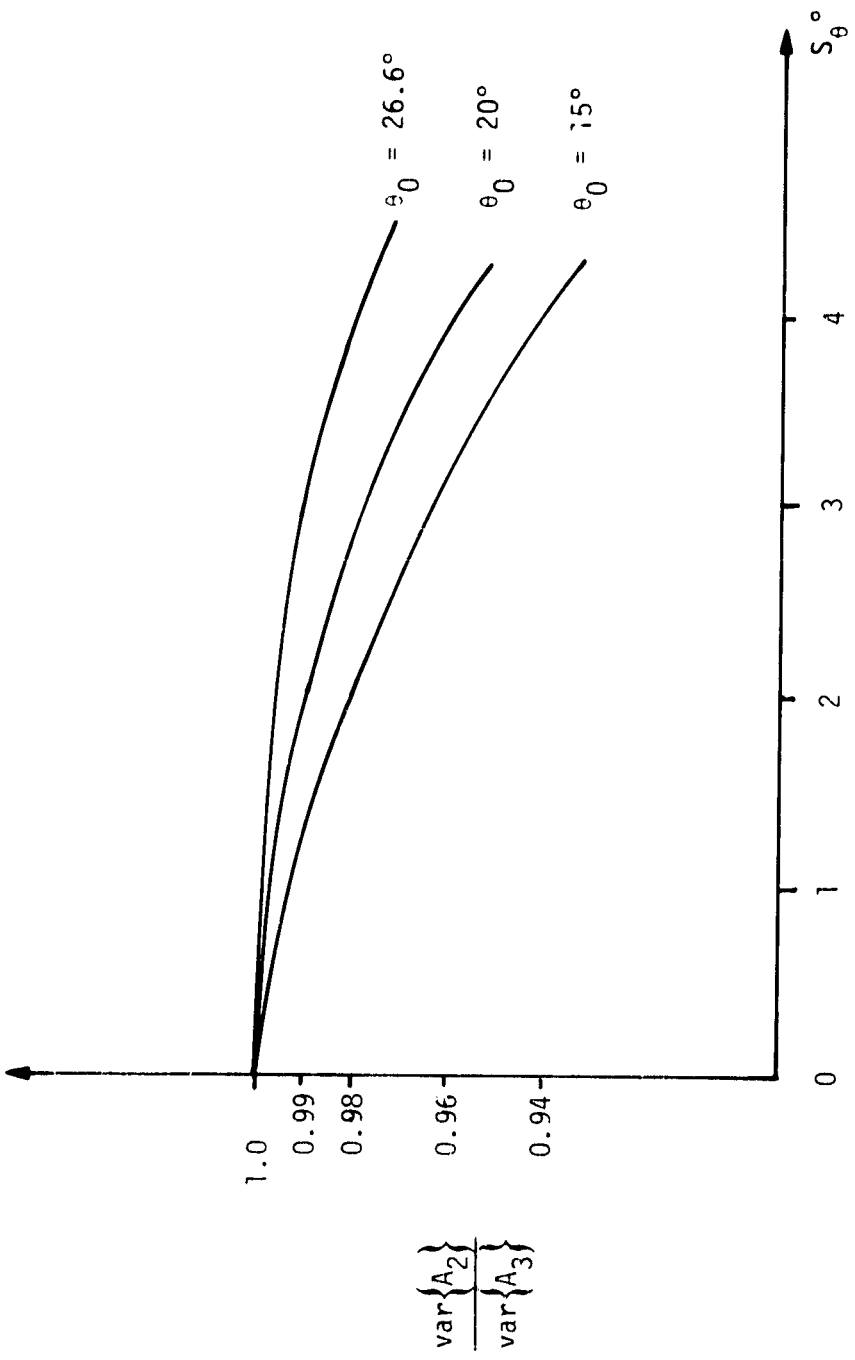


Figure 5. Ratio $\frac{\text{var}\{A_2\}}{\text{var}\{A_3\}}$ Versus Asymmetry S_θ°

Upon correlating these reference signals with

$$\begin{aligned} x(t) &= C_1(t) + n_{BP}(t) \\ &= \sqrt{2} \left\{ \left[\sqrt{P_2} A_3 + N_c(t) \right] \cos(\omega_{sc} t + \Delta\theta) + \left[\sqrt{P_3} A_2 - N_s(t) \right] \sin(\omega_{sc} t + \Delta\theta) \right\}, \end{aligned}$$

normalizing and retaining only the first harmonic, we obtain

$$e_c(t) = x(t) \cdot r_c(t) \Big|_{LP} = \left(\sqrt{P_3} A_3 + N_c(t) \right) \cos\phi + \left(\sqrt{P_2} A_2 - N_s(t) \right) \sin\phi$$

and

$$e_s(t) = x(t) \cdot r_s(t) \Big|_{LP} = \left(\sqrt{P_2} A_2 - N_s(t) \right) \cos\phi - \left(\sqrt{P_3} A_3 + N_c(t) \right) \sin\phi$$

Waveforms $e_c(t)$ and $e_s(t)$ are the inputs to the integrate-and-dump circuits shown in Figure 4 of [1], and the corresponding filter outputs at the end of the k th and l th signaling interval of each channel are given by

$$D_2 = \frac{1}{T_2} \int_{(k-1)T_2 + \epsilon_2}^{kT_2 + \epsilon_3} e_s(t) P_2(t - (k-1)T_2 - \epsilon_2) dt$$

and

$$D_3 = \frac{1}{T_3} \int_{(l-1)T_3 + \epsilon_3}^{lT_3 + \epsilon_3} e_c(t) P_3(t - (l-1)T_3 - \epsilon_3) dt$$

where $P_i(t)$; $i=2,3$ is the basic unit power symbol pulse in the i th data stream, $m_i(t)$, and is defined to be nonzero only in the interval $(0, T_i)$. Finally, the random variables D_2 and D_3 are fed into a zero-level threshold device which outputs a decision according to the sign of D_i at each time interval:

$$\hat{a}_i = \text{sgn}\{D_i\} \quad i = 2, 3$$

The above scheme has been thoroughly analyzed in [1]. Following identical steps, we find that the conditional probability of error for each channel is

$$P(e_2/\tilde{m}_{22}, \tilde{m}_{32}, \phi) = Q \left[(\text{sgn } \tilde{m}_{22}) \cdot \left(\sqrt{R_2} \tilde{m}_{22} \cos \phi - \sqrt{\frac{R_3}{N_T}} \tilde{m}_{32} \sin \phi \right) \right] \quad (23a)$$

and

$$P(e_3/\tilde{m}_{33}, \tilde{m}_{23}, \phi) = Q \left[(\text{sgn } \tilde{m}_{33}) \cdot \left(\sqrt{R_3} \tilde{m}_{33} \cos \phi + \sqrt{R_2 N_T} \tilde{m}_{23} \sin \phi \right) \right] \quad (23b)$$

and

$$Q(x) = \frac{1}{\sqrt{2\pi}} \int_x^\infty \exp \left\{ -\frac{x^2}{2} \right\} dx$$

where the parameters appearing in (23) are defined below:

$$R_2 \triangleq \frac{2P_2 r T_2}{N_0} \quad (\text{SNR for channel 2}) \quad (24a)$$

$$R_3 \triangleq \frac{2P_3 r T_3}{N_0} \quad (\text{SNR for channel 1}) \quad (24b)$$

$$N_T \triangleq \frac{T_3}{T_2} \quad (\text{Data rates ratio}) \quad (24c)$$

$$\tilde{m}_{22} = \frac{1}{T_2} \int_{(k-1)T_2}^{kT_2} A_2 \cdot P_2(t - (k-1)T_2) dt \quad (24d)$$

$$\tilde{m}_{32} = \frac{1}{T_2} \int_{(k-1)T_2}^{kT_2} A_3 \cdot P_2(t - (k-1)T_2) dt \quad (24e)$$

$$\tilde{m}_{33} = \frac{1}{T_3} \int_{(\ell-1)T_3}^{\ell T_3} A_3 \cdot P_3(t - (\ell-1)T_3) dt \quad (24f)$$

$$\tilde{m}_{23} = \frac{1}{T_3} \int_{(i-1)T_3}^{iT_3} A_2 \cdot P_3(t - (i-1)T_3) dt \quad (24g)$$

and the data dependent quantities A_2 and A_3 have been defined in (20).

In deriving (24), the assumption has been implicitly made that the epoch difference $\epsilon_2 - \epsilon_3$ between the two channels is zero. Although this is a rather strict assumption from a practical standpoint, it can be argued that, for large N_T , the effect of the epoch difference is negligible.

In the following, we consider the case where the data are NRZ for both channels and the ratio N_T is an integer.

The ϕ -conditional error probability of either channel is obtained by properly removing the conditioning on the parameters \tilde{m}_{ij} ; $i, j=2, 3$ which depend on the data. This is done in the following two subsections.

2.1 BEP for Channel 2 (HDRCH)

Let us assume that the data streams $m_i(t)$ are of the form

$$m_i(t) = \sum_{n=-\infty}^{\infty} a_{n_i} P_i(t - nT_i) ; \quad i = 2, 3 \quad (25)$$

where a_{n_i} are sequences of ± 1 with the properties

$$E\{a_{n_i} a_{m_i}\} = \delta_{nm} \quad (26a)$$

$$E\{a_{n_i} a_{m_j}\} = 0 \quad \text{for } i \neq j \quad (26b)$$

Then, combining (20), (24) and (25) res.

$$\tilde{m}_{22} = a_{(k-1)_2} \cdot \cos S_\theta - \tan \theta_0 \cdot \sin S_\theta \quad (27a)$$

and

$$m_{32} = a_{(\ell-1)_3} \left[\cos S_\theta + a_{(k-1)_2} \cdot \cot \theta_0 \cdot \sin S_\theta \right] \quad (27b)$$

by considering all four possible combinations for $a_{(k-1)_2}$ and $a_{(\ell-1)_3}$, the following expression for the ϕ -conditional channel-2 BEP is derived:

$$\begin{aligned} P(e_2/\phi) = & \frac{1}{4} Q \left[\sqrt{R_2} \cos \phi (\cos S_\theta - \sin S_\theta \tan \theta_0) - \sqrt{\frac{R_3}{N_T}} \sin \phi (\cos S_\theta + \sin S_\theta \cot \theta_0) \right] \\ & + Q \left[\sqrt{R_2} \cos \phi (\cos S_\theta - \sin S_\theta \tan \theta_0) + \sqrt{\frac{R_3}{N_T}} \sin \phi (\cos S_\theta + \sin S_\theta \cot \theta_0) \right] \\ & + Q \left[\sqrt{R_2} \cos \phi (\cos S_\theta + \sin S_\theta \tan \theta_0) + \sqrt{\frac{R_3}{N_T}} \sin \phi (\cos S_\theta - \sin S_\theta \cot \theta_0) \right] \\ & + Q \left[\sqrt{R_2} \cos \phi (\cos S_\theta + \sin S_\theta \tan \theta_0) - \sqrt{\frac{R_3}{N_T}} \sin \phi (\cos S_\theta - \sin S_\theta \cot \theta_0) \right] \end{aligned} \quad (28)$$

In deriving (28), we have assumed that $|S_\theta| \ll 45^\circ$ so that $\text{sgn } \tilde{m}_{22} = a_{(k-1)_2}$. This assumption is fully justified since S_θ represents asymmetry and is expected to be on the order of $4-5^\circ$. The additional dB in SNR required to achieve the nominal BEP of 10^{-5} is shown in Figure 3 as a function of the asymmetry parameter S_θ .

2.2 BEP for Channel 1 (LDRCH)

We have considered the case where exactly N_T pulses $P_2(t)$ exist in one P_3 pulse. Assume that k of them are positive, with $0 \leq k \leq N_T$. Then, from (20) and (24g), it follows that

$$\tilde{m}_{23} = \frac{1}{T_3} \cos S_\theta \int_{(\ell-1)T_3}^{\ell T_3} m_2(t - (\ell-1)T_3) dt - \tan \theta_0 \cdot \sin S_\theta \quad (29)$$

C-3

Since there exists k positive and $N_T - k$ negative pulses in T_3 seconds, the integral in (29) equals

$$\frac{1}{T_3} \int_{(\ell-1)T_3}^{\ell T_3} m_2(t - (\ell-1)T_3) dt = \frac{2k - N_T}{N_T} \quad (30)$$

from (29) and (30),

$$\tilde{m}_{23} = \left(\frac{2k - N_T}{N_T} \right) \cdot \cos S_\theta - \tan \theta_0 \cdot \sin S_\theta \quad (31)$$

Also, from (20) and (24f), we get

$$\tilde{m}_{33} = a_{(\ell-1)3} \left[\cos S_\theta + \left(\frac{2k - N_T}{N_T} \right) \cdot \cot \theta_0 \cdot \sin S_\theta \right] \quad (32)$$

Furthermore, for typical values of θ_0 and S_θ , it immediately follows that $\sin \tilde{m}_{33} = a_{(\ell-1)3}$. Combining (23b), (30) and (32) and the law of total probability results in

$$P(e_3 / a_{(\ell-1)3}, \phi) = \sum_{k=0}^{N_T} P(k) \cdot Q \left\{ \sqrt{R_3} \cos \phi \cdot a_{(\ell-1)3} \left(\cos S_\theta + \left(\frac{2k - N_T}{N_T} \right) \cot \theta_0 \cdot \sin S_\theta \right) + \sqrt{R_2 N_T} \sin \phi \left(\left(\frac{2k - N_T}{N_T} \right) \cos S_\theta - \tan \theta_0 \cdot \sin S_\theta \right) \right\} \quad (33)$$

where $P(k)$ is the probability of having k positive pulses in N_T slots, i.e., k follows the binominal distribution:

$$P(k) = \frac{1}{2^{N_T}} \binom{N_T}{k} \quad (34)$$

Finally, considering the two possibilities for $a_{(\ell-1)3}$ along with (33) and (34), we derive the final expression for the channel l ϕ -conditional error probability:

$$\begin{aligned}
 P(e_3/\phi) = \frac{1}{2^{N_T+1}} & \left\{ \sum_{k=0}^{N_T} \binom{N_T}{k} \left\{ Q \left[\sqrt{R_3} \cos \phi \left(\cos S_\theta + \left(\frac{2k-N_T}{N_T} \right) \cot \theta_0 \sin S_\theta \right) \right. \right. \right. \\
 & \left. \left. + \sqrt{R_2 N_T} \sin \phi \left(\left(\frac{2k-N_T}{N_T} \right) \cos S_\theta - \tan \theta_0 \sin S_\theta \right) \right] \right. \\
 & \left. + Q \left[\sqrt{R_3} \cos \phi \left(\cos S_\theta + \left(\frac{2k-N_T}{N_T} \right) \cot \theta_0 \sin S_\theta \right) \right. \right. \\
 & \left. \left. - \sqrt{R_2 N_T} \sin \phi \left(\left(\frac{2k-N_T}{N_T} \right) \cos S_\theta - \tan \theta_0 \sin S_\theta \right) \right] \right\} \right\} \quad (35)
 \end{aligned}$$

where again we assumed that $|S_\theta| \ll 45^\circ$ so that $\text{sgn } \tilde{m}_{33} = a_{(\ell-1)3}$. The loss in dB resulting from (35) as a function of S_θ for a nominal 10^{-5} BEP is plotted in Figure 4.

REFERENCES

1. Polydoros, A., "Effect of Data Asymmetry on Unbalanced QPSK Signals with Noisy Phase Reference," Appendix II to Shuttle Ku-Band and S-Band Communication Implementation Study, Axiomatix Final Report on NAS 9-15240E/F, Report No. R8005-3, May 21, 1980.
2. Caper, R. H., Jr., LaFlame, D. T., and Parode, L. C., "Orbiter Ku-Band Integrated Radar and Communications Subsystem," IEEE Transactions on Communications, November 1978, pp 1604-1619.
3. Simon, M. K., "Power Allocation and Costas Loop Subcarrier Tracking Performance Associated with a Digital Phase Shift Implementation of the Three-Channel Orbiter Ku-Band Modulator," Axiomatix Report No. R7709-4, September 29, 1977.
4. Osborne, H. C., "Effect of Noisy Phase Reference on Coherent Detection of Unbalanced QPSK Signals," NTC 78 Proceedings, December 1978, pp 2.2.1-2.2.6.